# MRI-based Biomechanical Modeling of Carotid Atherosclerotic Plaques

## – The Stable Plaque Paradigm –

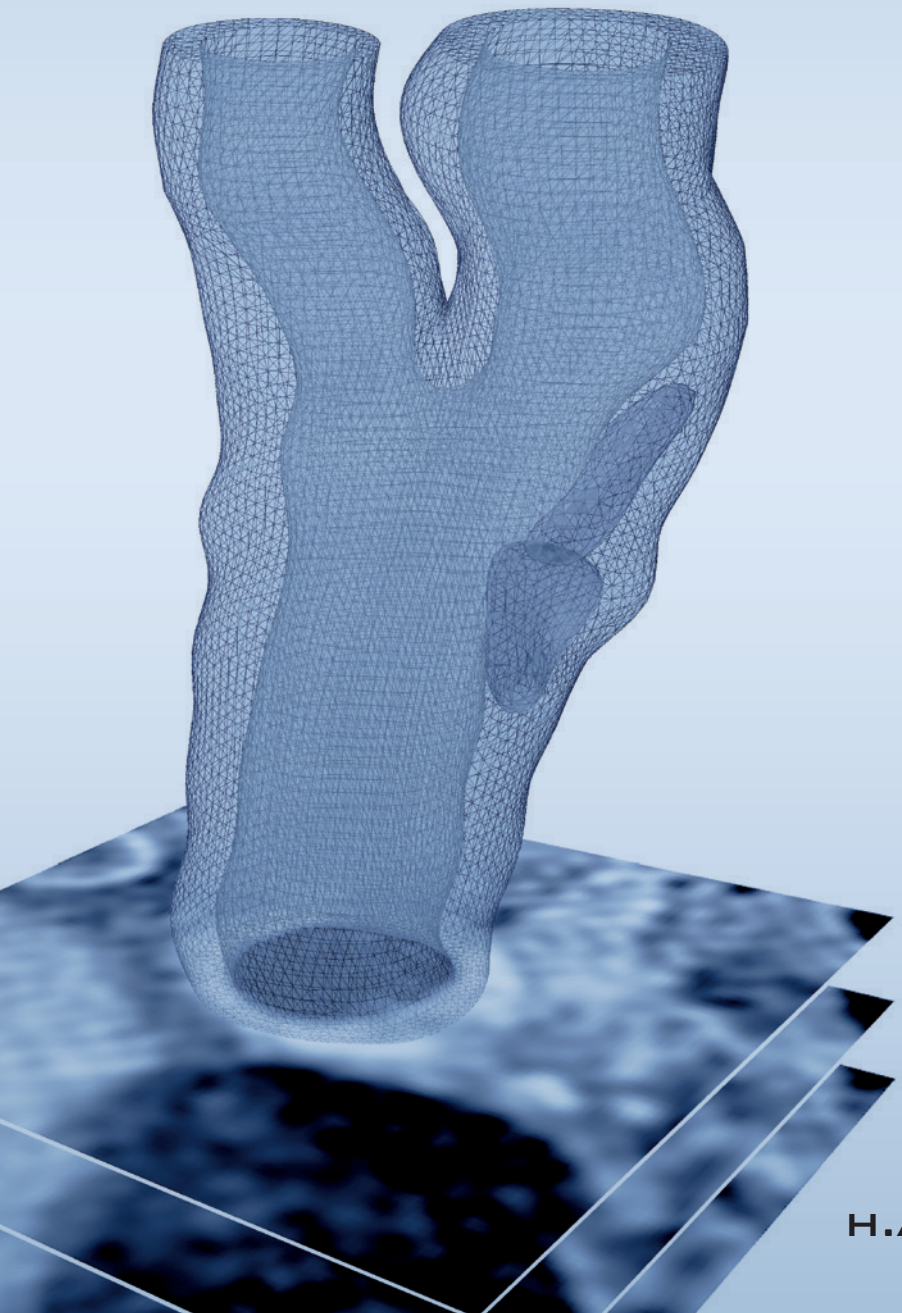

H.A. Nieuwstadt

# MRI-based Biomechanical Modeling of Carotid Atherosclerotic Plaques

## – The stable plaque paradigm –

Harm Nieuwstadt

2015




Financial support by the Dutch Heart Foundation for the publication of this thesis is gratefully acknowledged. Additional financial support for the printing of this thesis was kindly provided by Cardialysis and Philips Healthcare.

This research was performed within the framework of CTMM, the Center for Translational Molecular Medicine, project PARISk (grant 01C-202), and supported by a grant of the Dutch Heart Foundation (DHF-2008T094).

A full color, open-access (free of charge) electronic version of this thesis is publicly available at the institutional repository of the Erasmus University Rotterdam: http://repub.eur.nl/

Printed in the Netherlands by Ridderprint BV
ISBN: 978-94-6299-043-2

# MRI-based Biomechanical Modeling of Carotid Atherosclerotic Plaques

## – The stable plaque paradigm –

MRI-gebaseerde biomechanische modelvorming
van atherosclerotische halsslagaderplaques

– Het stabiele plaque paradigma –

## Thesis

to obtain the degree of Doctor
from the Erasmus University Rotterdam
by command of the rector magnificus

Prof.dr. H.A.P. Pols

and in accordance with the decision of the Doctoral Board

The public defense shall be held on
Wednesday April 22nd 2015 at 13.30 hours by

**Harm Aarnout Nieuwstadt**
born in Utrecht, the Netherlands

## Doctoral Committee

| | |
|---|---|
| **Promotor:** | Prof.dr.ir. A.F.W. van der Steen |
| **Other members:** | Prof.dr. H.J.M. Verhagen |
| | Prof.dr. M.J.A.P. Daemen |
| | Prof.dr.ir. M. Breeuwer |
| **Copromotor:** | Dr.ir. F.J.H. Gijsen |

# Table of Contents

# Preface

We are natural-born conceptualizers. Our ability to formulate concepts such as “time”, “zero”, “$\hbar$”, and “deoxyribonucleic acid” is a curiosity-fueled skill that has rocketed us all the way to the moon, and beyond. Conceptual modeling, through which we seek to make some sense of the ungraspable universe, may very well be one of the defining features of our species, and certainly one of our greatest accomplishments. Our insatiable desire for understanding has led us to develop models that not only provide the answers but also the questions. Conceptual models form the foundations of the cognitive structures we build, from language and philosophy to the social and physical sciences. But models need to be used responsibly if we are not to lose touch with reality. When should a cow cease to be a cow and become just a black and white patterned sphere in a vacuum? At what speed does an apple need to fall from a tree before it will obey a different set of made-up rules? What do concepts such as “good”, “bad”, and “ugly” really mean, and why should they mean anything at all? Unfortunately, we often have a tendency to overconceptualize for ease of mind. Sometimes a rock is just a rock, yet we are intrinsically devoted to assigning it a purpose.

Nevertheless, if scientific models can be helpful in deciding where to aim your wayward darts (see the appendix of this thesis), then they might also be helpful in deciding on which patients with atherosclerotic carotid artery disease to operate. In this thesis we will set off on a yellow-brick-road scientific modeling journey that will introduce us along the way to the nature of atherosclerosis, the concept of the “vulnerable plaque”, cardiovascular biomechanics, magnetic resonance imaging, and ultrasound strain imaging. Whether we have the brains, heart, and courage to ever complete this journey and to discover the wizard's true identity, I cannot say. But we will see that, once again, it’s not about giving the right answers. It’s about asking the right questions.

# Introduction 1

## STROKE

A stroke occurs when the blood supply to brain cells is blocked or interrupted [1]. This results in a rapid loss of brain function as brain cells are dying because they no longer receive enough oxygen. The typical symptoms of this acute medical emergency are a sudden feeling of numbness on one side of the body, confusion, dizziness, and impaired speech. If the blockage is temporary and self-resolving, one speaks of a transient ischemic attack. More than 15 million people suffer a stroke or transient ischemic attack annually worldwide. Roughly 5 million of them become permanently disabled and another 5 million do not survive, making stroke a major cause of disability and the second largest cause of death worldwide [2-5]. The most common type of stroke is an ischemic stroke which occurs when one or more blood vessels leading to the brain are suddenly blocked [3,6]. This occlusion is usually caused by a blood thrombus which was formed after atherosclerotic plaque rupture: an acute manifestation of atherosclerosis [7-10].

## ATHEROSCLEROSIS

Atherosclerosis is a cardiovascular disease which is characterized by a local thickening of the walls of arteries due to a slow build-up of cholesterol, lipids, calcium, and other debris within the wall [11]. Such parts of the vessel wall are referred to as atherosclerotic plaques, also known as atheromas or lesions [12,13]. While factors such as genetics influence the tendency to develop plaques, lifestyle habits such as an unhealthy diet, smoking, and lack of physical exercise have a major influence as well [14-17]. Plaques are usually present at locations where arteries curve or bifurcate, because the blood flow patterns at these sites make the vessel wall more susceptible to the disease [18-21]. One of the biggest practical challenges with atherosclerosis is that it can remain completely unnoticed (asymptomatic) until a sudden symptomatic plaque rupture occurs [22]. Rupture of atherosclerotic plaques in the carotid artery (Figure 1) or in other arteries leading to the brain can cause a stroke, whereas rupture of coronary artery plaques in the heart can cause a heart attack.

The initial phase of atherosclerosis consists of an accumulation of low-density lipoprotein particles inside the intima, which is the inner layer of the vessel wall [11]. This is caused by dysfunction of the endothelial cells which are the cells in contact with the lumen through which the blood flows [23-25]. The endothelial cells are stimulated to attract monocytes which migrate into the intima, proliferate, and become macrophages [26,27]. This is, in essence, a process of inflammation [28,29]. The macrophages engulf the low-density lipoprotein which transforms them into fat-rich

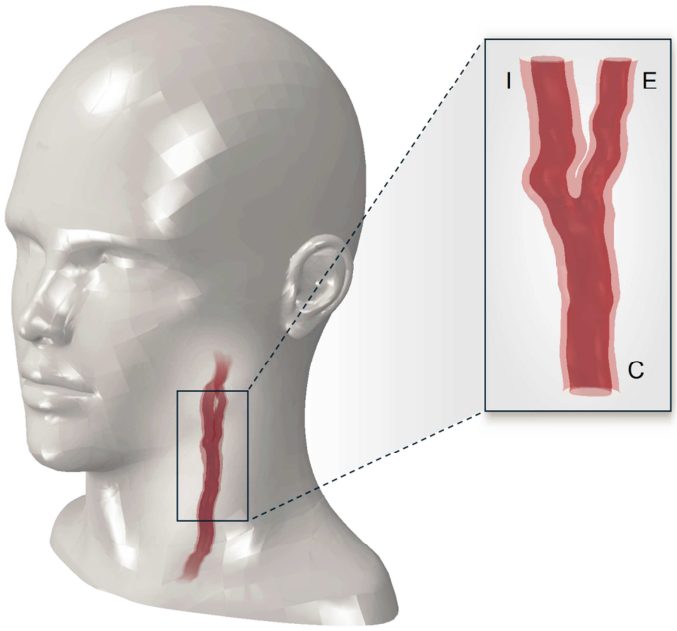


**Figure 1.** Location of the left carotid artery bifurcation where the common carotid (C) splits off in the internal (I) and external (E) carotid arteries. Disturbed blood flow patterns at this site make the vessel wall susceptible to the development of an atherosclerotic carotid plaque which can cause an ischemic stroke.

foam cells. When foam cells eventually die, the dead fatty material is deposited as an extracellular lipid-rich necrotic core (Figure 2) [30]. The soft lipid-rich necrotic core is separated from the lumen by a layer of stiffer, fibrous-rich tissue called the fibrous cap [31]. Activated macrophages, vascular smooth muscle cells, and so-called matrix metalloproteinases inside the cap have effect on its structural integrity [26,32]. They influence the break-down of elastin and collagen fibers in the extracellular matrix [33]. This causes both thinning and weakening of the fibrous cap [34-36]. Initially, plaques grow outwards to maintain the original lumen diameter (outward remodeling) but this only occurs up to a certain point [37,38]. If a plaque grows too large, the lumen starts to become narrowed, also termed stenosis. In more advanced plaques, bleedings can occur inside lipid-rich necrotic core due to leaky vasa vasorum, which is the small vasculature within the walls of large vessels [39]. Such bleedings are referred to as intraplaque hemorrhage [40-42]. For older plaques, necrotic areas can calcify [43]. The process of plaque growth usually takes years or even decades, which makes atherosclerosis a disease of vascular aging [44]. Despite the current level of

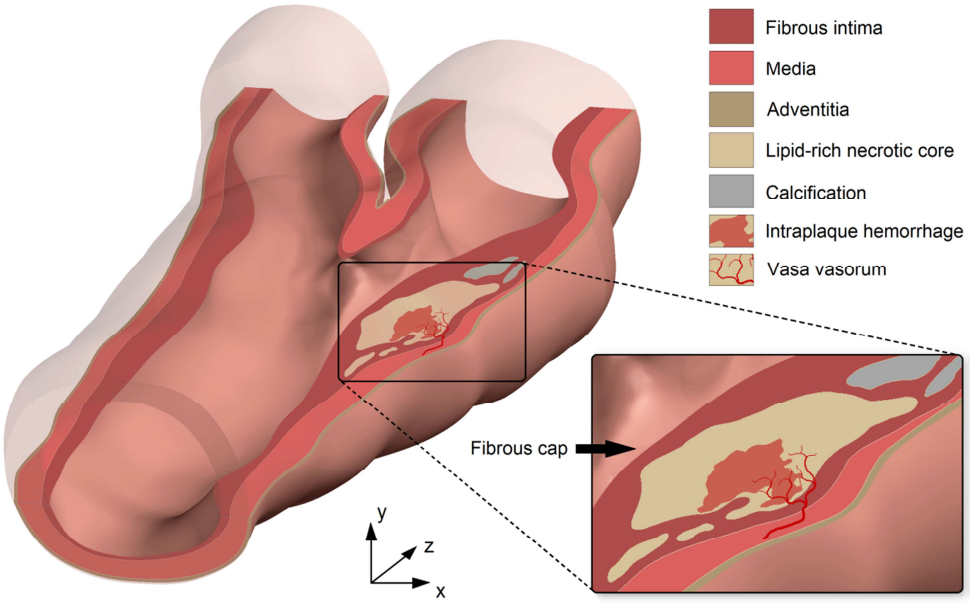


**Figure 2.** Illustrative longitudinal cross section of an advanced atherosclerotic plaque at an artery bifurcation. The fibrous cap is the tissue separating the lipid-rich necrotic core from the flowing blood within the lumen.

understanding, much remains unknown about the pathophysiology and the natural course of atherosclerosis such as the processes governing plaque growth or decay [45].

At a certain moment a plaque can rupture [46]. A rupture occurs when the fibrous cap breaks and the lipid-rich necrotic core gets in direct contact with the blood. Because the body does not recognize the necrotic material, it initiates a thrombotic response. The resulting thrombus (blood clot) and/or material from the plaque can cause an embolism (vessel occlusion) which was noted earlier as the cause of ischemic stroke. This blockage can occur at the site of rupture or further downstream.

## STROKE TREATMENT

Stroke patients first need medical treatment to resolve their current stroke. They then need treatment to help prevent future (re-current) strokes or transient ischemic attacks. An ischemic stroke can be diagnosed with a computed tomography (CT) or magnetic resonance imaging (MRI) scan and immediately treated in the emergency room by intravenous administration of a protein that can break down blood clots to

resolve the blockage [47,48]. This is called intravenous thrombolytic therapy [49,50]. Stroke patients are often left permanently disabled, for example post-stroke paralysis. In that case they would also need physical therapy as a result of their stroke [3].

In current clinical practice, all symptomatic stroke or transient ischemic attack patients, as well as some of the people who are at an increased risk of carotid artery disease, undergo a routine ultrasound evaluation of the left and right carotid arteries. With an ultrasound scan the blood flow through the carotid artery bifurcation and the degree of stenosis can be measured [51,52]. In general, guidelines state that if the stenosis-degree is higher than 70%, the patient should get an intervention through either carotid angioplasty with stenting or carotid endarterectomy [53-59]. The latter is a surgical procedure in which the artery is cut open and the plaque is removed. This surgery is expensive and risky [60,61]. The benefit is that the possible future rupture of that particular plaque has been prevented. Regardless of the need for surgery, carotid artery disease patients receive medication therapy such as aspirin and drugs that lower the blood pressure and cholesterol levels [62,63].

There are shortcomings to this current approach. Many carotid plaques remain unnoticed until acute symptoms occur because mass screening for carotid plaques in asymptomatic patients is currently not feasible [64,65]. But besides that, there are other issues as well. The degree of stenosis is insufficient as the sole determinant for plaque rupture-risk [66,67]. Numerous plaque-specific factors such as local hemodynamics, inflammation, calcifications, lipid content, vasa vasorum, intraplaque hemorrhage, or the fibrous cap thickness are not taken into account. Some plaques that do not induce much stenosis because of outward remodeling might also rupture, while some plaques that do induce severe stenosis might not [68,69]. In effect, a substantial number of carotid plaques that would not rupture are currently surgically treated at unnecessary cost and risk, while many carotid plaques that will rupture are left untreated [70,71]. The guidelines for carotid plaque surgical intervention need to be improved. In order to do so, one first needs to ask the question: what is it that makes a plaque prone to rupture?

## THE VULNERABLE PLAQUE

A vulnerable plaque is defined as a plaque that is unstable and susceptible to rupture, or more precisely: thrombosis-prone [72-74]. As of now, it is unknown what exactly makes a plaque vulnerable or stable [45,75,76]. However, histological studies of plaques have provided important insights [77-79]. In a histological examination, excised plaques are cut in thin slices, stained for various cells/tissues to give them different colors, and then examined through microscopy. Ruptured plaques have been found to generally

contain a large lipid-rich necrotic core with a ruptured thin fibrous cap. Inflammation in the fibrous cap in the form of activated macrophages and the presence of intraplaque hemorrhage have also been linked to an increased rupture-risk [35,80]. Approximately 15 years ago, Virmani and colleagues introduced a plaque morphological classification scheme based on histopathological examinations [31]. Plaques with a thin fibrous cap (less than 0.2 mm thickness for carotid plaques [81]), a large lipid-rich necrotic core, infiltration by macrophages, and usually presence of intraplaque hemorrhage and/or vasa vasorum were classified as a thin cap fibroatheroma [82]. In their experience these thin fibrous cap atheromas were more likely to rupture, and this was later confirmed by many other researchers [45,83-85]. The concept of the "vulnerable plaque", which was actually already introduced in 1989 [86], is nowadays almost always directly linked to the thin fibrous cap atheroma classification.

But caution is called for at this point. Directly linking the two concepts is misleading as it would incorrectly suggest that the answer is there while it is not [87]. Certainly, morphological studies of plaques have greatly increased our understanding of plaque rupture [31,88,89]. But not all, and not only, thin fibrous cap atheromas are vulnerable. Carotid endarterectomy specimens have been found with intact caps much thinner than 0.2 mm and without thrombosis [81,90]. These plaques apparently did not rupture. And for the other way around: there is evidence that plaques histologically classified differently can also rupture [91]. Most research lines within the field of atherosclerosis focus at both a better fundamental understanding of plaque vulnerability and at an improved rupture-risk stratification in the clinic [45,92-94]. One such approach, and a topic of extensive investigation, is the use of cardiovascular biomechanics for plaque stress modeling.

## PLAQUE BIOMECHANICS

Plaque rupture is essentially a phenomenon of mechanical failure which can be approached from an engineering point-of-view. The underlying concept is that the fibrous cap ruptures when the stress within the cap exceeds the strength [95]. The highest stress in the cap –the peak cap stress– can be regarded as a measure for rupture-risk. Plaques with a high peak cap stress have been shown to be more vulnerable [96-100].

Stresses relate to the internal forces acting throughout the material and can be described mathematically in terms of a stress tensor $\sigma$ [101,102]. This tensor enables the evaluation of the normal and shear components of the force relative to any given orientation of the area on which it is acting. It is often convenient to characterize the stresses at a certain location by a single scalar quantity. One way to achieve this is by

computing the maximum principal stress. This scalar is determined from tensor invariants expressed in terms of the eigenvalues of the tensor. Stresses in soft materials can lead to deformations, causing compression and expansion in different directions [103]. The internal strains associated with such deformations can be described by a strain tensor $\varepsilon$.

Unfortunately, stresses cannot be measured directly. However, by modeling the underlying physics it is possible to predict, through numerical calculation, the values of stresses and corresponding strains. The most basic example one can use to illustrate stress/strain modeling is the extension of a spring by application of a tensile force. To model this, or any other mechanical scenario, one needs to know four things. First, the external loading condition needs to be determined. In the example of a spring it is the force applied on one end of the spring. Second, it is necessary to specify boundary and initial conditions that describe features of stresses and strains at interfaces. When pulling one end of the spring, one could specify that the other end is not able to move. Third, the material models in the form of constitutive relationships must be specified, together with appropriate values for any parameters appearing within these models. Constitutive models relate stresses to strains. For a spring behaving linearly one can use Hooke's law, which, in its simplest form, is given by $\sigma = C\varepsilon$. The model constant $C$ specifies the stiffness (elasticity) of the material. Fourth, it is necessary to define the shape/geometry of the object(s) one is modeling. A spring can often be sufficiently characterized in a mechanical sense as a one-dimensional object.

When modeling plaques instead of a spring, the loading condition becomes the blood pressure within the lumen exerting forces on the inside of the vessel wall. An example of a boundary condition is a plane strain assumption for a two-dimensional cross-sectional plaque model. While a material model in the form Hooke's law works well to illustrate the concept of stiffness, this type of linear relationship does not accurately model biological soft tissues which generally exhibit nonlinear stress-strain relationships [104-106]. Alternative constitutive models, for example the nonlinear neo-Hookean model, are used when modeling biological tissues [107,108]. Typically, group-averaged data from *ex vivo* plaque material testing studies are used to define the parameter values in constitutive models [109-111]. Finally, the plaque geometry needs to be specified. The geometry can be obtained in various ways depending on the type of study and/or the available medical imaging modalities [98,112].

Because the plaque geometry is complex and tissues behave nonlinearly, the resulting model does not allow an analytical evaluation of peak cap stress. Instead, a numerical approach known as finite element analysis can be used to compute an approximation to the stress distribution in plaques [99,113,114]. In finite element analysis, the geometry is divided up into a mesh (Figure 3) consisting of a large

number of elements having a prescribed shape, for instance a convex polygon such as a triangle. Since the individual elements are relatively small it is possible to approximate, in a simple fashion, the form of the spatial variation of the stresses within each element. This representation provides the basis of the subsequent numerical computation. In steady-state simulations where viscoelasticity effects are neglected, the solution for the stress/strain field is obtained by iteratively solving the differential equations for the material constitutive laws while maintaining a force balance for the loaded, now-deformed geometry.

In essence, plaque biomechanical models can incorporate numerous features such as plaque morphology, tissue composition, and hemodynamic conditions by mapping their influence onto one meaningful physical quantity which is directly related to plaque rupture: the peak cap stress. Studies on plaque biomechanics have provided important fundamental insights on plaque vulnerability. The peak cap stress is closely related to the fibrous cap thickness and has been directly associated with plaque

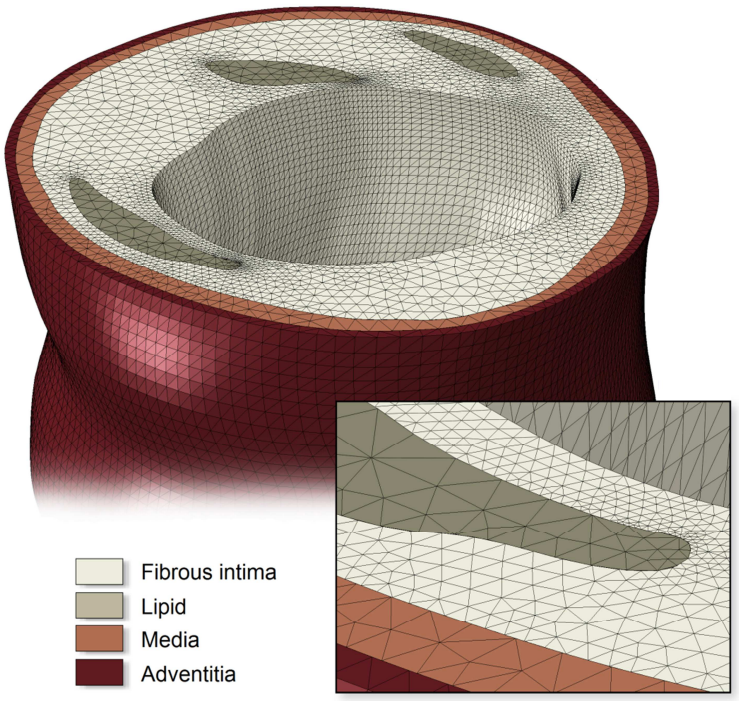


**Figure 3.** Three-dimensional atherosclerotic plaque biomechanical model for finite element analysis. Note the localized refinement of the unstructured mesh at the fibrous cap regions and the use of mesh-independent surface ties between different tissues.

rupture [98,115-117]. Plaque stresses and strains have been linked to plaque biological processes [118-122], shape [123,124], and composition such as the presence of (micron-size) calcifications [125-129], lipids, and intraplaque hemorrhage [130-134]. Numerous experimental studies focused on measuring the material properties of plaque tissues. For a reliable rupture-risk assessment, the fibrous cap strength needs to be known in addition to the peak cap stress. The cap strength of plaque specimens can be estimated *ex vivo* with mechanical failure testing. Early studies reported a cap strength threshold of 300 kPa [98].

Plaque biomechanical modeling can also be used as an applied clinical tool to help decide if a patient needs treatment [97,100,114,135,136]. One can compute the *in vivo* peak cap stress of a plaque to use it as a more meaningful diagnostic marker for plaque vulnerability than merely the plaque burden or the degree of stenosis. This could greatly improve the targeting of patients at increased risk which would benefit from a surgical procedure. For finite element analysis to produce realistic results it is essential that the plaque geometry is accurately represented within the computational model. In this respect a carotid ultrasound scan which is currently used in clinical practice is inadequate, mainly because of the poor soft tissue contrast. Only MRI can noninvasively image carotid plaques to obtain their three-dimensional geometry/morphology [137,138]. The fact that MRI is noninvasive (i.e., not requiring an intravascular catheter) facilitates clinical applicability. By performing image segmentation on MRI a geometrical computer model of the plaque can be reconstructed and used for finite element analysis [97,139-144]. It is worth noting that, because plaque tissue material properties used in MRI-based biomechanical studies are typically based on values reported in the literature, it is often only the MRI-derived plaque geometry that actually remains patient-specific. In either case, MRI plays a crucial role by providing the carotid plaque geometry for a noninvasive biomechanical analysis to assess the rupture-risk.

## CAROTID MAGNETIC RESONANCE IMAGING

Magnetic resonance imaging (MRI) is a medical imaging modality which employs the magnetic properties of protons to form an image. The basis of MRI is the principle that biological tissue contains water, water contains protons, and protons have a nonzero quantum-mechanical spin: up or down [145]. This makes their magnetic moments precess about any externally applied magnetic field. Hitting the protons in that condition with an electromagnetic wave at their resonance frequency will induce precession-phase coherence, allowing a net-magnetization in the transverse plane. This resonance frequency is proportional to the external field strength. After taking the hit,

it takes a while for the longitudinal magnetization to recover (characterized by $T_1$), and the transverse magnetization to decay (characterized by $T_2$) [146]. Both these times are tissue-dependent and roughly range from $10^{-2}$ to $10^{0}$ seconds. During the relaxation the protons release their energy through radiofrequency waves of which the magnitude (the rotating net transverse magnetization at the readout-time of choosing [147]) and phase can be measured. Because only protons at a resonance-inducing external field give a signal, some clever spatial field strength variations can be applied during the process, which is called a pulse sequence [148]. One can now control and measure the signal of proton spins locally, while the signal strength depends on the specific relaxation times of the biological tissue [149]. This, in a nutshell, is MRI.

MRI is one of the finest gifts of physics to modern medicine. It has become an established research field on its own and now has countless applications as a medical imaging modality [150]. The physics behind MRI give it distinct advantages over other medical imaging modalities, such as being noninvasive, nonionizing, and having high soft-tissue contrast. Unfortunately, the long relaxation times of the magnetization demand relatively long scan times in order to acquire an image with sufficient diagnostic quality. This long scan time is, despite continuous improvements, one of the main limitations of MRI. Other limitations are, besides the relatively high costs, the various image artifacts and the unavoidable trade-off between the field-of-view, scan time, image resolution, and image noise [149].

When it comes specifically to imaging carotid atherosclerosis [138,151-154], MRI is currently the only noninvasive modality to image individual carotid plaque components, namely fibrous, hemorrhagic, lipid, calcified, and thrombotic tissues (Figure 4) [155-158]. For clinical carotid MRI using a 3T whole-body system with neck coils, the typical in-plane acquired voxel dimension is currently about 0.5 mm and the slice thickness is about 2 mm, yielding anisotropic voxels [159]. All the signals from the individual protons within a voxel are averaged out, which is referred to as the partial volume effect [160]. In order to facilitate visualization of various plaque tissues, a number of different pulse sequences can be applied in a series, called a multicontrast protocol. A T1-weighted sequence creates image contrast based on tissue $T_1$ times, a T2-weighted sequence based on tissue $T_2$ times, and a proton-density sequence based on the density of protons in tissues [161]. A higher proton density results in a stronger magnetization and, in effect, a higher signal. The typical scan time of one carotid MRI pulse sequence is in the order of minutes. To improve visualization of the vessel wall, the signal from the flowing blood inside the artery is often suppressed by adding a black-blood preparation within a pulse sequence [162]. In addition, a contrast-enhanced scan can be made by intravenously administrating a contrast agent such as gadolinium a few minutes before scanning [163-165]. Gadolinium is absorbed by the fibrous cap and

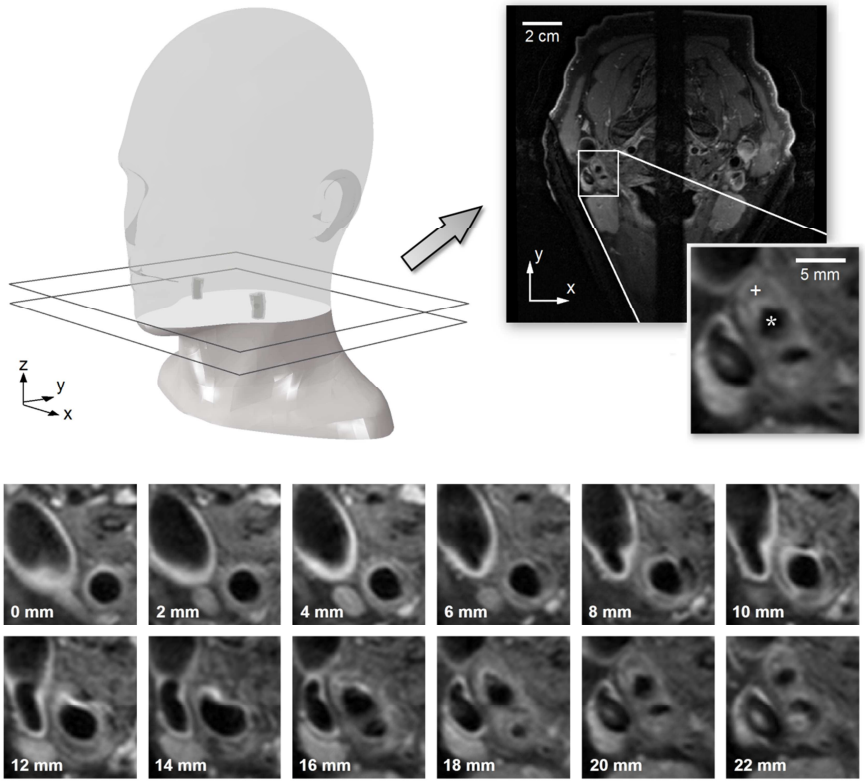


**Figure 4.** Carotid magnetic resonance imaging (MRI). Twelve axial cross-sectional slices are positioned around the carotid bifurcation. The example shows a carotid plaque causing less than 70% stenosis in a 58 year-old male who had recently suffered an ischemic stroke. Lipid-rich necrotic core indicated in the inset by the (+) symbol, lumen by the (*) symbol. (T1-weighted, 2D pulse sequence with contrast enhancement and black-blood preparation on a Philips 3T system)

lowers its $T_1$ which increases its signal on a T1-weighted scan [166]. Upon performing MRI, the carotid artery geometry, including the plaque and its components, can be reconstructed through (automated) image segmentation [167-171].

## THESIS OUTLINE

Stroke is a major cause of disability and death worldwide. The current stenosis-degree guidelines for intervention in the case of atherosclerotic carotid plaque presence in order to prevent an ischemic event are imperfect. This is because they insufficiently

target plaque vulnerability. The vast majority of surgeries, with accompanying risk and costs, are ultimately unnecessary while many vulnerable plaques remain untreated. A biomechanical plaque stress analysis based on MRI is a highly promising noninvasive method to provide a much more meaningful carotid plaque vulnerability assessment in the clinic.

*The main aim of this thesis was to investigate the feasibility of MRI-based biomechanical stress modeling of carotid atherosclerotic plaques for rupture-risk assessment.*

First, we focused on quantifying the influence of the MRI spatial resolution on the accuracy of plaque segmentation, fibrous cap assessment, and biomechanical stress computations. Second, we introduced and investigated new methods to achieve an improved estimation of the mechanical properties of plaque tissues. Third, we studied the implications of our findings for a noninvasive MRI-based carotid plaque vulnerability assessment in a clinical setting. These implications resulted in the subtitle of this dissertation: "The stable plaque paradigm".

In **Chapter 2**, the effects of MRI segmentation errors on the quantification of carotid plaque components such as the lipid-rich necrotic core size and the minimum fibrous cap thickness are investigated. In order to investigate these effects, a new technique consisting of numerical simulations of carotid MRI is used.

In **Chapter 3**, numerical simulations of MRI are used to investigate fibrous cap imaging. The effects of localized scan plane angulations on fibrous cap contrast when acquiring anisotropic voxels are studied.

In **Chapter 4**, the influence of the MRI slice thickness and in-plane voxel size on the accuracy of plaque segmentation and peak cap stress computations is studied.

In **Chapter 5**, the influence of the axial sampling resolution of cross-sectional plaque geometrical data on the computed plaque stresses in reconstructed models is studied. In addition, two-dimensional cross-sectional plaque stress computations are compared with three-dimensional computations.

In **Chapter 6**, the influence of MRI segmentation errors on the computed peak cap stress is quantified. This study also uses the numerical MRI simulation approach introduced in chapter 2.

In **Chapter 7**, an *ex vivo* experimental study is described in which plaque tissue mechanical properties are estimated through a combination of arterial inflation experiments, ultrasound strain imaging, histological processing, and inverse finite element analysis.

In **Chapter 8**, a new clinically-practicable method to noninvasively estimate plaque component elasticity *in vivo* is presented. The feasibility of the method, which combines MRI, ultrasound strain imaging, and inverse finite element analysis, is investigated by means of a numerical approach.

In **Chapter 9**, a morphology-based plaque classification scheme is compared with the computed peak cap stress for a large set of carotid plaque cross sections. We demonstrate the profound influence of inaccuracies in computed stress due to noninvasive MRI on such a comparison, and we assess the implications for a diagnosis of plaque vulnerability in clinical practice.

In **Chapter 10**, the main findings of this thesis and their implications are discussed. A future perspective is presented as well.

## REFERENCES


1. Mohr JP, Grotta JC, Wolf PA, Moskowitz MA, Mayberg MR, Von Kummer R. Stroke: pathophysiology, diagnosis, and management. 1520 pages, Saunders, Philadelphia, 2011.
2. World Health Organization. Fact sheet N°310: the ten leading causes of death in the world in 2012. Updated May 2014.
3. Go AS et al. Heart disease and stroke statistics - 2014 update: a report from the American heart association. Circulation 2014;129:e228-e292.
4. Mackay J, Mensah G editors. The atlas of heart disease and Stroke, sheet N°15: global burden of stroke. World Health Organization, Geneva, 2004.
5. Mendis S, Puska P, Norrving B editors. Global atlas on cardiovascular disease prevention and control. World Health Organization, Geneva, 2011.
6. Dirnagl U, Iadecola C, Moskowitz MA. Pathobiology of ischaemic stroke: an integrated view. Trends Neurosci 1999;22:391-397.
7. Fisher M, Paganini-Hill A, Martin A, Cosgrove M, Toole JF, Barnett HJ, Norris J. Carotid plaque pathology: thrombosis, ulceration, and stroke pathogenesis. Stroke 2005;36:253-357.
8. Thim T, Hagensen MK, Bentzon JF, Falk E. From vulnerable plaque to atherothrombosis. J Intern Med 2008;263:506-516.
9. Yuan C, Zhang SX, Polissar NL, Echelard D, Ortiz G, Davis JW, Ellington E, Ferguson MS, Hatsukami TS. Identification of fibrous cap rupture with magnetic resonance imaging is highly associated with recent transient ischemic attack or stroke. Circulation 2002;105:181-185.
10. Saam T, Cai J, Ma L, Cai YQ, Ferguson MS, Polissar NL, Hatsukami TS, Yuan C. Comparison of symptomatic and asymptomatic atherosclerotic carotid plaque features with in vivo MR imaging. Radiology 2006;240:464-472.
11. Falk E. Pathogenesis of atherosclerosis. J Am Coll Cardiol 2006;47:C7–12.

12. Stary HC et al. A definition of initial, fatty streak, and intermediate lesions of atherosclerosis. A report from the Committee on Vascular Lesions of the Council on Arteriosclerosis, American Heart Association. Circulation 1994;89:2462-2478.
13. Stary HC et al. A definition of advanced types of atherosclerotic lesions and a histological classification of atherosclerosis. A report from the Committee on Vascular Lesions of the Council on Arteriosclerosis, American Heart Association. Circulation 1995;92:1355-1374.
14. Canto JG, Iskandrian AE. Major risk factors for cardiovascular disease: debunking the "only 50%" myth. JAMA 2003;290:947-949.
15. Winter Y, Rohrmann S, Linseisen J, Lanczik O, Ringleb PA, Hebebrand J, Back T. Contribution of obesity and abdominal fat mass to risk of stroke and transient ischemic attacks. Stroke 2008;39:3145-3151.
16. Willey JZ, Moon YP, Paik MC, Boden-Albala B, Sacco RL, Elkind MS. Physical activity and risk of ischemic stroke in the Northern Manhattan Study. Neurology 2009;73:1774-1779.
17. Shah RS, Cole JW. Smoking and stroke: the more you smoke the more you stroke. Expert Rev Cardiovasc Ther 2010;8:917-932.
18. Zarins CK, Giddens DP, Bharadvaj BK, Sottiurai VS, Mabon RF, Glagov S. Carotid bifurcation atherosclerosis. Quantitative correlation of plaque localization with flow velocity profiles and wall shear stress. Circ Res 1983;53:502-514.
19. Malek AM, Alper SL, Izumo S. Hemodynamic shear stress and its role in atherosclerosis. JAMA 1999;282:2035-2042.
20. Slager CJ, Wentzel JJ, Gijsen FJ, Schuurbiers JC, van der Wal AC, van der Steen AF, Serruys PW. The role of shear stress in the generation of rupture-prone vulnerable plaques. Nat Clin Pract Cardiovasc Med 2005;2:401-407.
21. Cheng C, Tempel D, van Haperen R, van der Baan A, Grosveld F, Daemen MJ, Krams R, de Crom R. Atherosclerotic lesion size and vulnerability are determined by patterns of fluid shear stress. Circulation 2006;113:2744-2753.
22. Naghavi M editor. Asymptomatic atherosclerosis: pathophysiology, detection and treatment. 737 pages, Humana Press, New York, 2011.
23. Stary HC et al. A definition of the intima of human arteries and of its atherosclerosis-prone regions. A report from the Committee on Vascular Lesions of the Council on Arteriosclerosis, American Heart Association. Circulation 1992;85:391-405.
24. Dirksen MT, van der Wal AC, van den Berg FM, van der Loos CM, Becker AE. Distribution of inflammatory cells in atherosclerotic plaques relates to the direction of flow. Circulation 1998;98:2000-2003.
25. Davignon J, Ganz MP. Role of endothelial dysfunction in atherosclerosis. Circulation 2004;106:III-27-32.
26. Moreno PR, Falk E, Palacios IF, Newell JB, Fuster V, Fallon JT. Macrophage infiltration in acute coronary syndromes. Implications for plaque rupture. Circulation 1994;90:775-778.
27. Moore KJ, Sheedy FJ, Fisher EA. Macrophages in atherosclerosis: a dynamic balance. Nat Rev Immunol 2013;13:709-721.
28. Libby P. Inflammation in atherosclerosis. Nature 2002;420:868-874.
29. Libby P. Atherosclerosis: the new view. Sci Am 2002;286:46-55.
30. Guyton JR, Klemp KF. Development of the lipid-rich core in human atherosclerosis. Arterioscler Thromb Vasc Biol 1996;16:4-11.
31. Virmani R, Kolodgie FD, Burke AP, Farb A, Schwartz SM. Lessons from a sudden coronary death: a comprehensive morphological classification scheme for atherosclerotic lesions. Arterioscler Thromb Vasc Biol 2000;20:1262-1275.
32. Galis ZS, Khatri JJ. Matrix metalloproteinases in vascular remodeling and atherogenesis: the good, the bad, and the ugly. Circ Res 2002;90:251-262.
33. Galis ZS, Sukhova GK, Kranzhöfer R, Clark S, Libby P. Macrophage foam cells from experimental atheroma constitutively produce matrix-degrading proteinases. Proc Natl Acad Sci 1995;92:402-406.
34. Burleigh MC, Briggs AD, Lendon CL, Davies MJ, Born GV, Richardson PD. Collagen types I and III, collagen content, GAGs and mechanical strength of human atherosclerotic plaque caps: span-wise variations. Atherosclerosis 1992;96:71-81.
35. Lendon CL, Davies MJ, Born GV, Richardson PD. Atherosclerotic plaque caps are locally weakened when macrophages density is increased. Atherosclerosis 1991;87:87-90.
36. Newby AC, Zaltsman AB. Fibrous cap formation or destruction--the critical importance of vascular smooth muscle cell proliferation, migration and matrix formation. Cardiovasc Res 1999;41:345-360.

37. Glagov S, Weisenberg E, Zarins CK, Stankunavicius R, Kolettis GJ. Compensatory enlargement of human atherosclerotic coronary arteries. N Engl J Med 1987;16:1371-1375.
38. Ward MR, Pasterkamp G, Yeung AC, Borst C. Arterial remodeling. Mechanisms and clinical implications. Circulation 2000;102:1186-1191.
39. Moreno PR, Purushothaman KR, Sirol M, Levy AP, Fuster V. Neovascularization in human atherosclerosis. Circulation 2006;113:2245-2252.
40. Kolodgie FD, Gold HK, Burke AP, Fowler DR, Kruth HS, Weber DK, Farb A, Guerrero LJ, Hayase M, Kutys R, Narula J, Finn AV, Virmani R. Intraplaque hemorrhage and progression of coronary atheroma. N Engl J Med 2003;349:2316-2325.
41. Takaya N, Yuan C, Chu B, Saam T, Polissar NL, Jarvik GP, Isaac C, McDonough J, Natiello C, Small R, Ferguson MS, Hatsukami TS. Presence of intraplaque hemorrhage stimulates progression of carotid atherosclerotic plaques: a high-resolution magnetic resonance imaging study. Circulation 2005;111:2768-2775.
42. Virmani R, Kolodgie FD, Burke AP, Finn AV, Gold HK, Tulenko TN, Wrenn SP, Narula J. Atherosclerotic plaque progression and vulnerability to rupture: angiogenesis as a source of intraplaque hemorrhage. Arterioscler Thromb Vasc Biol 2005;25:2054-2061.
43. Otsuka F, Sakakura K, Yahagi K, Joner M, Virmani R. Has our understanding of calcification in human coronary atherosclerosis progressed? Arterioscler Thromb Vasc Biol 2014;34:724-736.
44. Thompson et al. Atherosclerosis across 4000 years of human history: the Horus study of four ancient populations. Lancet 2013;381:1211-1222.
45. Bentzon JF, Otsuka F, Virmani R, Falk E. Mechanisms of plaque formation and rupture. Circ Res 2014;114:1852-1866.
46. Falk E. Why do plaques rupture? Circulation 1992;86:III-30-42.
47. Muir KW, Buchan A, von Kummer R, Rother J, Baron JC. Imaging of acute stroke. Lancet Neurol 2006;5:755-768.
48. Chalela JA, Kidwell CS, Nentwich LM, Luby M, Butman JA, Demchuk AM, Hill MD, Patronas N, Latour L, Warach S. Magnetic resonance imaging and computed tomography in emergency assessment of patients with suspected acute stroke: a prospective comparison. Lancet 2007;369:293-298.
49. Adams et al. Guidelines for thrombolytic therapy for acute stroke: a supplement to the guidelines for the management of patients with acute ischemic stroke. Stroke 1996;27:1711-1718.
50. Wardlaw JM, Murray V, Berge E, del Zoppo G, Sandercock P, Lindley RL, Cohen G. Recombinant tissue plasminogen activator for acute ischaemic stroke: an updated systematic review and meta-analysis. Lancet 2012;379:2364-2372.
51. Sidhu PS, Allan PL. Ultrasound assessment of internal carotid artery stenosis. Clin Radiol. 1997;52:654-658.
52. Staikov IN, Arnold M, Mattle HP, Remonda L, Sturzenegger M, Baumgartner RW, Schroth G. Comparison of the ECST, CC, and NASCET grading methods and ultrasound for assessing carotid stenosis. European Carotid Surgery Trial. North American Symptomatic Carotid Endarterectomy Trial. J Neurol 2000;247:681-686.
53. Hobson RW et al. Management of atherosclerotic carotid artery disease: clinical practice guidelines of the Society for Vascular Surgery. J Vasc Surg 2008;48(2):480-486.
54. Mas JL et al. Endarterectomy versus stenting in patients with symptomatic severe carotid stenosis. New Engl J Med 2006;355:1660-1671.
55. Yadav JS, et al. Protected carotid-artery stenting versus endarterectomy in high-risk patients. New Engl J Med 2004;351:1493-1501.
56. Ferguson GG, Eliasziw M, Barr HW, Clagett GP, Barnes RW, Wallace MC, Taylor DW, Haynes RB, Finan JW, Hachinski VC, Barnett HJ. The North American Symptomatic Carotid Endarterectomy Trial: surgical results in 1415 patients. Stroke 1999;30:1751-1758.
57. Halliday A, Mansfield A, Marro J, Peto C, Peto R, Potter J, Thomas D; MRC Asymptomatic Carotid Surgery Trial (ACST) Collaborative Group. Prevention of disabling and fatal strokes by successful carotid endarterectomy in patients without recent neurological symptoms: randomised controlled trial. Lancet 2004;363:1491-1502.
58. Diethrich EB, Ndiaye M, Reid DB. Stenting in the carotid artery: initial experience in 110 patients. J Endovasc Surg 1996;3:42-62.
59. Barnett HJM, et al. Benefit of carotid endarterectomy in patients with symptomatic moderate or severe stenosis. New Engl J Med 1998;339:1415-1425.

60. Rothwell PM, Goldstein LB. Carotid endarterectomy for asymptomatic carotid stenosis: asymptomatic carotid surgery trial. Stroke 2004;35:2425-2427.
61. Rerkasem K, Rothwell PM. Systematic review of the operative risks of carotid endarterectomy for recently symptomatic stenosis in relation to the timing of surgery. Stroke 2009;40:e564-572.
62. Roncaglioni MC; Collaborative Group of the Primary Prevention Project. Low-dose aspirin and vitamin E in people at cardiovascular risk: a randomised trial in general practice. Lancet 2001;357:89-95.
63. Crisby M, Nordin-Fredriksson G, Shah PK, Yano J, Zhu J, Nilsson J. Pravastatin treatment increases collagen content and decreases lipid content, inflammation, metalloproteinases, and cell death in human carotid plaques: implications for plaque stabilization. Circulation 2001;103:926-933.
64. Mughal MM, Khan MK, DeMarco JK, Majid A, Shamoun F, Abela GS. Symptomatic and asymptomatic carotid artery plaque. Expert Rev Cardiovasc Ther 2011;9:1315-1330.
65. Sillesen H, Falk E. Why not screen for subclinical atherosclerosis? Lancet 2011;378:645-646.
66. Kolodgie FD, Virmani R, Burke AP, Farb A, Weber DK, Kutys R, Finn AV, Gold HK. Pathologic assessment of the vulnerable human coronary plaque. Heart 2004;90:1385-1391.
67. Zhao X, Underhill HR, Zhao Q, Cai J, Li F, Oikawa M, Dong L, Ota H, Hatsukami TS, Chu B, Yuan C. Discriminating carotid atherosclerotic lesion severity by luminal stenosis and plaque burden: a comparison utilizing high-resolution magnetic resonance imaging at 3.0 Tesla. Stroke 2011;42:347-353.
68. Ballotta E, Angelini A, Mazzalai F, Piatto G, Toniato A, Baracchini C. Carotid endarterectomy for symptomatic low-grade carotid stenosis. J Vasc Surg 2014;59:25-31.
69. Niccoli G, Stefanini GG, Capodanno D, Crea F, Ambrose JA, Berg R. Are the culprit lesions severely stenotic? JACC Cardiovasc Imaging 2013;6:1108-1114.
70. Rothwell PM, Warlow CP. Prediction of benefit from carotid endarterectomy in individual patients: a risk-modelling study. European Carotid Surgery Trialists' Collaborative Group. Lancet 1999;353:2105-2110.
71. Naylor AR. Time to rethink management strategies in asymptomatic carotid artery disease. Nat Rev Cardiol 2011;9:116-124.
72. Schaar JA, Muller JE, Falk E, Virmani R, Fuster V, Serruys PW, Colombo A, Stefanadis C, Ward Casscells S, Moreno PR, Maseri A, van der Steen AF. Terminology for high-risk and vulnerable coronary artery plaques. Report of a meeting on the vulnerable plaque, June 17 and 18, 2003, Santorini, Greece. Eur Heart J 2004;25:1077-1082.
73. Naghavi M et al. From vulnerable plaque to vulnerable patient: a call for new definitions and risk assessment strategies: Part I. Circulation 2003;108:1664-1672.
74. Naghavi M et al. From vulnerable plaque to vulnerable patient: a call for new definitions and risk assessment strategies: Part II. Circulation 2003;108:1772-1778.
75. Lutgens E, van Suylen RJ, Faber BC, Gijbels MJ, Eurlings PM, Bijnens AP, Cleutjens KB, Heeneman S, Daemen MJ. Atherosclerotic plaque rupture: local or systemic process? Arterioscler Thromb Vasc Biol 2003;23:2123-2130.
76. Arroyo LH, Lee RT. Mechanisms of plaque rupture: mechanical and biologic interactions. Cardiovasc Res 1999;41:369-375.
77. Virmani R, Burke AP, Farb A, Kolodgie FD. Pathology of the unstable plaque. Prog Cardiovasc Dis 2002;44:349-356.
78. Fisher M, Paganini-Hill A, Martin A, Cosgrove M, Toole JF, Barnett HJ, Norris J. Carotid plaque pathology: thrombosis, ulceration, and stroke pathogenesis. Stroke 2005;36:253-257.
79. Schwartz SM, Galis ZS, Rosenfeld ME, Falk E. Plaque rupture in humans and mice. Arterioscler Thromb Vasc Biol 2007;27:705-713.
80. Michel JB, Virmani R, Arbustini E, Pasterkamp G. Intraplaque haemorrhages as the trigger of plaque vulnerability. Eur Heart J 2011;32:1977-1985.
81. Redgrave JN, Gallagher P, Lovett JK, Rothwell PM. Critical cap thickness and rupture in symptomatic carotid plaques. Stroke 2008;39:1722-1729.
82. Virmani R, Burke AP, Farb A, Kolodgie FD. Pathology of the vulnerable plaque. J Am Coll Cardiol 2006;47:C13-18.
83. Golledge J, Greenhalgh RM, Davies AH. The symptomatic carotid plaque. Stroke 2000;31:774-781.
84. Ota H, Yu W, Underhill HR, Oikawa M, Dong L, Zhao X, Polissar NL, Neradilek B, Gao T, Zhang Z, Yan Z, Guo M, Zhang Z, Hatsukami TS, Yuan C. Hemorrhage and large lipid-rich necrotic cores are independently associated with thin or ruptured fibrous caps: an in vivo 3T MRI study. Arterioscler Thromb Vasc Biol 2009;29:1696-1701.

85. Redgrave JN, Lovett JK, Gallagher PJ, Rothwell PM. Histological assessment of 526 symptomatic carotid plaques in relation to the nature and timing of ischemic symptoms: the Oxford plaque study. Circulation 2006;113:2320-2328.
86. Muller JE, Tofler GH, Stone PH. Circadian variation and triggers of onset of acute cardiovascular disease. Circulation 1989;79:733-743.
87. Finn AV, Nakano M, Narula J, Kolodgie FD, Virmani R. Concept of vulnerable/unstable plaque. Arterioscler Thromb Vasc Biol 2010;30:1282-1292.
88. van der Wal AC, Becker AE. Atherosclerotic plaque rupture--pathologic basis of plaque stability and instability. Cardiovasc Res 1999;41:334-344.
89. Moreno PR, Purushothaman KR, Fuster V, Echeverri D, Truszczynska H, Sharma SK, Badimon JJ, O'Connor WN. Plaque neovascularization is increased in ruptured atherosclerotic lesions of human aorta: implications for plaque vulnerability. Circulation 2004;110:2032-2038.
90. Virmani R, Ladich ER, Burke AP, Kolodgie FD. Histopathology of carotid atherosclerotic disease. Neurosurgery 2006;59:S219-227.
91. Tanaka A et al. Morphology of exertion-triggered plaque rupture in patients with acute coronary syndrome: an optical coherence tomography study. Circulation 2008;118:2368-2373.
92. Granada JF, Kaluza GL, Raizner AE, Moreno PR. Vulnerable plaque paradigm: prediction of future clinical events based on a morphological definition. Catheter Cardiovasc Interv 2004;62:364-374.
93. Vancraeynest D, Pasquet A, Roelants V, Gerber BL, Vanoverschelde JL. Imaging the vulnerable plaque. J Am Coll Cardiol 2011;57:1961-1979.
94. Nighoghossian N, Derex L, Douek P. The vulnerable carotid artery plaque: current imaging methods and new perspectives. Stroke 2005;36:2764-2772.
95. Richardson PD, Davies MJ, Born GVR. Influence of plaque configuration and stress distribution on fissuring of coronary atherosclerotic plaques. Lancet 1989;2:941-944.
96. Tang D, Yang C, Zheng J, Woodard PK, Saffitz JE, Petruccelli JD, Sicard GA, Yuan C. Local maximal stress hypothesis and computational plaque vulnerability index for atherosclerotic plaque assessment. Ann Biomed Eng 2005;33:1789-1801.
97. Tang D, Teng Z, Canton G, Yang C, Ferguson M, Huang X, Zheng J, Woodard PK, Yuan C. Sites of rupture in human atherosclerotic carotid plaques are associated with high structural stresses: an in vivo MRI-based 3D fluid-structure interaction study. Stroke 2009;40:3258-3263.
98. Cheng GC, Loree HM, Kamm RD, Fishbein MC, Lee RT. Distribution of circumferential stress in ruptured and stable atherosclerotic lesions. A structural analysis with histopathological correlation. Circulation 1993;87:1179-1187.
99. Sadat U, Teng Z, Gillard JH. Biomechanical structural stresses of atherosclerotic plaques. Expert Rev Cardiovasc Ther 2010;8:1469-1481.
100. Teng Z, Brown AJ, Calvert PA, Parker RA, Obaid DR, Huang Y, Hoole SP, West NE, Gillard JH, Bennett MR. Coronary plaque structural stress is associated with plaque composition and subtype and higher in acute coronary syndrome: the BEACON I (Biomechanical Evaluation of Atheromatous Coronary Arteries) study. Circ Cardiovasc Imaging 2014;7:461-470
101. Humprey JD. Cardiovascular solid mechanics: cells, tissues, and organs, 757 pages, Springer, New York, 2002.
102. Oomens C, Brekelmans M, Baaijens F. Biomechanics: concepts and computation, 348 pages. Cambridge University Press, Cambridge, 2010.
103. Holzapfel GA. Nonlinear Solid Mechanics: A continuum approach for engineering, 455 pages. Wiley, Hoboken, 2000.
104. Maher E, Creane A, Sultan S, Hynes N, Lally C, Kelly DJ. Tensile and compressive properties of fresh human carotid atherosclerotic plaques. J Biomech 2009;42:2760-2767.
105. Akyildiz AC, Speelman L, Gijsen FJ. Mechanical properties of human atherosclerotic intima tissue. J Biomech 2014;47:773-783.
106. Walsh MT, Cunnane EM, Mulvihill JJ, Akyildiz AC, Gijsen FJ, Holzapfel GA. Uniaxial tensile testing approaches for characterisation of atherosclerotic plaques. J Biomech 2014;47:793-804.
107. Barrett SR, Sutcliffe MP, Howarth S, Li ZY, Gillard JH. Experimental measurement of the mechanical properties of carotid atherothrombotic plaque fibrous cap. J Biomech 2009;42:1650-1655.
108. Holzapfel GA, Sommer G, Regitnig P. Anisotropic mechanical properties of tissue components in human atherosclerotic plaques. J Biomech Eng 2004;126:657-665.

109. Lawlor MG, O'Donnell MR, O'Connell BM, Walsh MT. Experimental determination of circumferential properties of fresh carotid artery plaques. J Biomech 2011;44:1709-1715.
110. Chai CK, Speelman L, Oomens CW, Baaijens FP. Compressive mechanical properties of atherosclerotic plaques--indentation test to characterise the local anisotropic behaviour. J Biomech 2014;47:784-792.
111. Holzapfel GA, Mulvihill JJ, Cunnane EM, Walsh MT. Computational approaches for analyzing the mechanics of atherosclerotic plaques: a review. J Biomech 2014;47:859-869.
112. Coombs BD, Rapp JH, Ursell PC, Reilly LM, Saloner D. Structure of plaque at carotid bifurcation: high-resolution MRI with histological correlation. Stroke 2001;32:2516-2521.
113. Braess D. Finite elements: theory, fast solvers, and applications in solid mechanics, 384 pages, Cambridge University Press, Cambridge, 2007.
114. Tang D, Kamm RD, Yang C, Zheng J, Canton G, Bach R, Huang X, Hatsukami TS, Zhu J, Ma G, Maehara A, Mintz GS, Yuan C. Image-based modeling for better understanding and assessment of atherosclerotic plaque progression and vulnerability: data, modeling, validation, uncertainty and predictions. J Biomech 2014;47:834-846.
115. Li ZY, Howarth SP, Tang T, Gillard JH. How critical is fibrous cap thickness to carotid plaque stability? A flow-plaque interaction model. Stroke 2006;37:1195-1199.
116. Loree HM, Kamm RD, Stringfellow RG, Lee RT. Effects of fibrous cap thickness on peak circumferential stress in model atherosclerotic vessels. Circ Res 1992;71:850-858.
117. Gao H, Long Q, Das SK, Sadat U, Graves M, Gillard JH, Li ZY. Stress analysis of carotid atheroma in transient ischemic attack patients: evidence for extreme stress-induced plaque rupture. Ann Biomed Eng 2011;39:2203-2212.
118. Hallow KM, Taylor WR, Rachev A, Vito RP. Markers of inflammation collocate with increased wall stress in human coronary arterial plaque. Biomech Model Mechanobiol 2009;8:473-486.
119. Kilpatrick D, Xu C, Vito RP. Correlation of mechanical behavior and MMP-1 presence in human atherosclerotic plaque. J Mech Med Biol 2002:1:1-7.
120. Lee RT, Schoen FJ, Loree HM, Lark MW, Libby P. Circumferential stress and matrix metalloproteinase 1 in human coronary atherosclerosis. Implications for plaque rupture. Arterioscler Thromb Vasc Biol 1996;16:1070-1073.
121. Wang Y, Johnson JA, Fulp A, Sutton MA, Lessner SM. Adhesive strength of atherosclerotic plaque in a mouse model depends on local collagen content and elastin fragmentation. J Biomech 2013;46:716-722.
122. Nguyen CM, Levy AJ. The mechanics of atherosclerotic plaque rupture by inclusion/matrix interfacial decohesion. J Biomech 2010;43:2702-2708.
123. Teng Z, Sadat U, Li Z, Huang X, Zhu C, Young VE, Graves MJ, Gillard JH. Arterial luminal curvature and fibrous-cap thickness affect critical stress conditions within atherosclerotic plaque: an in vivo MRI-based 2D finite-element study. Ann Biomed Eng 2010;38:3096-3101.
124. Teng Z, Sadat U, Ji G, Zhu C, Young VE, Graves MJ, Gillard JH. Lumen irregularity dominates the relationship between mechanical stress condition, fibrous-cap thickness, and lumen curvature in carotid atherosclerotic plaque. J Biomech Eng 2011;133:034501.
125. Creane A, Maher E, Sultan S, Hynes N, Kelly DJ, Lally C. Prediction of fibre architecture and adaptation in diseased carotid bifurcations. Biomech Model Mechanobiol 2011;10:831-843.
126. Mulvihill JJ, Cunnane EM, McHugh SM, Kavanagh EG, Walsh SR, Walsh MT. Mechanical, biological and structural characterization of in vitro ruptured human carotid plaque tissue. Acta Biomater 2013;9:9027-9035.
127. Gasser TC, Ogden RW, Holzapfel GA. Hyperelastic modelling of arterial layers with distributed collagen fibre orientations. J R Soc Interface 2006;3:15-35.
128. Huang H, Virmani R, Younis H, Burke AP, Kamm RD, Lee RT. The impact of calcification on the biomechanical stability of atherosclerotic plaques. Circulation 2001;103:1051-1056.
129. Vengrenyuk Y, Carlier S, Xanthos S, Cardoso L, Ganatos P, Virmani R, Einav S, Gilchrist L, Weinbaum S. A hypothesis for vulnerable plaque rupture due to stress-induced debonding around cellular microcalcifications in thin fibrous caps. Proc Natl Acad Sci 2006;103:14678-14683.
130. Gao H, Long Q. Effects of varied lipid core volume and fibrous cap thickness on stress distribution in carotid arterial plaques. J Biomech 2008;41:3053-3059.
131. Teng Z, Sadat U, Wang W, Bahaei NS, Chen S, Young VE, Graves MJ, Gillard JH. Intraplaque stretch in carotid atherosclerotic plaque--an effective biomechanical predictor for subsequent cerebrovascular ischemic events. PLoS One 2013;8:e61522.

132. Teng Z, He J, Degnan AJ, Chen S, Sadat U, Bahaei NS, Rudd JH, Gillard JH. Critical mechanical conditions around neovessels in carotid atherosclerotic plaque may promote intraplaque hemorrhage. Atherosclerosis 2012;223:321-326.
133. Teng Z, Sadat U, Brown AJ, Gillard JH. Plaque hemorrhage in carotid artery disease: pathogenesis, clinical and biomechanical considerations. J Biomech 2014;47:847-858.
134. Huang X, Teng Z, Canton G, Ferguson M, Yuan C, Tang D. Intraplaque hemorrhage is associated with higher structural stresses in human atherosclerotic plaques: an in vivo MRI-based 3D fluid-structure interaction study. Biomed Eng Online 2010;9:86.
135. Chau AH, Chan RC, Shishkov M, MacNeill B, Iftimia N, Tearney GJ, Kamm RD, Bouma BE, Kaazempur-Mofrad MR. Mechanical analysis of atherosclerotic plaques based on optical coherence tomography. Ann Biomed Eng 2004;32:1494-1503.
136. Sadat U, Teng Z, Young VE, Walsh SR, Li ZY, Graves MJ, Varty K, Gillard JH. Association between biomechanical structural stresses of atherosclerotic carotid plaques and subsequent ischaemic cerebrovascular events--a longitudinal in vivo magnetic resonance imaging-based finite element study. Eur J Vasc Endovasc Surg 2010;40:485-491.
137. Toussaint J, LaMuraglia GM, Southern JF, Fuster V, Kantor HL. Magnetic resonance images lipid, fibrous, calcified, hemorrhagic, and thrombotic components of human atherosclerosis in vivo. Circ 1996;94:932-938.
138. Sanz J, Fayad ZA. Imaging of atherosclerotic cardiovascular disease. Nature 2008;451:953-957.
139. Li Z, Howarth S, Trivedi RA, U-King-Im JM, Graves MJ, Brown A, Wang L, Gillard JH. Stress analysis of carotid plaque rupture based on in vivo high resolution MRI. J of Biomech 2006;39:2611-2622.
140. Li ZY, Howarth SP, Tang T, Graves MJ, U-King-Im J, Trivedi RA, Kirkpatrick PJ, Gillard JH. Structural analysis and magnetic resonance imaging predict plaque vulnerability: a study comparing symptomatic and asymptomatic individuals. J Vasc Surg 2007;45:768-775.
141. Kaazempur-Mofrad MR, Isasi AG, Younis HF, Chan RC, Hinton DP, Sukhova G, LaMuraglia GM, Lee RT, Kamm RD. Characterization of the atherosclerotic carotid bifurcation using MRI, finite element modeling, and histology. Ann Biomed Eng 2004;32:932-946.
142. Gao H, Long Q, Graves M, Gillard JH, Li Z. Carotid arterial plaque stress analysis using fluid–structure interactive simulation based on in-vivo magnetic resonance images of four patients. J of Biomech 2009;42:1416-1423.
143. Gao H, Long Q, Graves M, Gillard JH, Li Z. Study of Reproducibility of human arterial plaque reconstruction and its effects on stress analysis based on multispectral in vivo magnetic resonance imaging. J Magn Reson Imaging 2009;30:85-93.
144. Sadat U, Teng Z, Young VE, Graves MJ, Gaunt ME, Gillard JH. High-resolution magnetic resonance imaging-based biomechanical stress analysis of carotid atheroma: a comparison of single transient ischaemic attack, recurrent transient ischaemic attacks, nondisabling stroke and asymptomatic patient groups. Eur J Vasc Endovasc Surg 2011;41:83-90.
145. Griffiths DJ. Introduction to quantum mechanics. 480 pages, Pearson Prentice Hall, Upper Saddle River, 2004.
146. de Graaf RA. In vivo NMR spectroscopy: principles and techniques. 592 pages, Wiley, Hoboken, 2007.
147. Griffiths DJ. Introduction to electrodynamics. 624 pages, Addison-Wesley, Boston, 2012.
148. Bernstein MA, King KF, Zhou XJ. Handbook of MRI pulse sequences. 1040 pages, Academic Press, Waltham, 2004.
149. Hashemi RH, Bradley GW, Lisanti CJ. MRI: the basics. 400 pages, Lippincott Williams & Wilkins, Philadelphia, 2010.
150. Westbrook C, Roth CK, Talbot J. MRI in practice. 456 pages, Wiley-Blackwell, Hoboken, 2011.
151. Underhill HR, Hatsukami TS, Fayad AZ, Fuster V, Yuan C. MRI of carotid atherosclerosis: clinical implications and future directions. Nat Rev Cardiol 2010;7:165–173.
152. Cai JM, Hatsukami TS, Ferguson MS, Small R, Polissar NL, Yuan C. Classification of human carotid atherosclerotic lesions with in vivo multicontrast magnetic resonance imaging. Circulation 2002;106:1368-1373.
153. Corti R, Fuster V. Imaging of atherosclerosis: magnetic resonance imaging. Eur Heart J 2011;32:1709-1719.
154. Watanabe Y, Nagayama M. MR plaque imaging of the carotid artery. Neuroradiology 2010;52:253–274.
155. Yuan C, Mitsumori LM, Ferguson MS, Polissar NL, Echelard D, Ortiz G, Small R, Davies JW, Kerwin WS, Hatsukami TS. In vivo accuracy of multispectral magnetic resonance imaging for identifying lipid-rich

necrotic cores and intraplaque hemorrhage in advanced human carotid plaques. Circulation 2001;104:2051-2056.
156. Yuan C, Kerwin WS. MRI of atherosclerosis. J Magn Reson Imaging 2004;19:710-719.
157. Cai J, Hatsukami TS, Ferguson MS, Kerwin WS, Saam T, Chu B, Takaya N, Polissar NL, Yuan C. *In vivo* quantitative measurement of intact fibrous cap and lipid-rich necrotic core size in atherosclerotic carotid plaque: comparison of high-resolution, contrast-enhanced magnetic resonance imaging and histology. Circulation 2005;112:3437-3444.
158. Saam T, Ferguson MS, Yarnykh VL, Takaya N, Xu D, Polissar NL, Hatsukami TS, Yuan C. Quantitative evaluation of carotid plaque composition by in vivo MRI. Arterioscler Thromb Vasc Biol 2005;25:234-239.
159. Wang J, Balu N, Canton G, Yuan C. Imaging biomarkers of cardiovascular disease. J Magn Reson Imag 2010;32:502–515.
160. González Ballester MA, Zisserman AP, Brady M. Estimation of the partial volume effect in MRI. Med Image Anal 2002;6:389-405.
161. Chu B, Ferguson MS, Chen H, Hippe DS, Kerwin WS, Canton G, Yuan C, Hatsukami TS. Magnetic resonance imaging features of the disruption-prone and the disrupted carotid plaque. JACC Cardiovasc Imaging 2009;2:883-896.
162. Yarnykh VL, Yuan C. T1-insensitive flow suppression using quadruple inversion-recovery. Magn Reson Med 2002;48:899-905.
163. Yuan C, Kerwin WS, Ferguson MS, Polissar N, Zhang S, Cia J, Hatsukami TS. Contrast-enhanced high resolution MRI for atherosclerotic carotid artery tissue characterization. J Magn Reson Imaging 2002;15:62–67.
164. Kerwin WS, Zhao X, Yuan C, Hatsukami TS, Maravilla KR, Underhill HR, Zhao X. Contrast-enhanced MRI of carotid atherosclerosis: dependence on contrast agent. J Magn Reson Imaging 2009;30:35-40.
165. Millon A, Boussel L, Brevet M, Mathevet JL, Canet-Soulas E, Mory C, Scoazec JY, Douek P. Clinical and histological significance of gadolinium enhancement in carotid atherosclerotic plaque. Stroke 2012;43:3023-3028.
166. Kwee RM, van Engelshoven JM, Mess WH, ter Berg JW, Schreuder FH, Franke CL, Korten AG, Meems BJ, van Oostenbrugge RJ, Wildberger JE, Kooi ME. Reproducibility of fibrous cap status assessment of carotid artery plaques by contrast-enhanced MRI. Stroke 2009;40:3017-3021.
167. Li F, Yarnykh VL, Hatsukami TS et al. Scan-rescan reproducibility of carotid atherosclerotic plaque morphology and tissue composition measurements using multicontrast MRI at 3T. J Magn Reson Imag 2010;31:168–176.
168. Clarke LP, Velthuizen RP, Camacho MA, Heine JJ, Vaidyanathan M, Hall LO, Thatcher RW, Silbiger ML. MRI segmentation: methods and applications. Magn Reson Imaging 1995;13:343-368.
169. Adame IM, van der Geest RJ, Wasserman BA, Mohamed MA, Reiber JHC, Lelieveldt BPF. Automatic segmentation and plaque characterization in atherosclerotic carotid artery MR images. MAGMA 2004;16: 227–234.
170. Hofman JMA, Branderhorst WJ, ten Eikelder HMM, Cappendijk VC, Heeneman S, Kooi ME, Hilbers PAJ, ter Haar Romeny BM. Quantification of atherosclerotic plaque components using in vivo MRI and supervised classifiers. Magn Reson Med 2006;55:790–799.
171. Liu F, Xu D, Ferguson MS, Chu B, Saam T, Takaya N, Hatsukami TS, Yuan C, Kerwin WS. Automated *in vivo* segmentation of carotid plaque MRI with morphology-enhanced probability maps. Magn Reson Med 2006:55:659–668.

# Numerical simulations of carotid MRI quantify the accuracy in measuring atherosclerotic plaque components in vivo

# 2

**Abstract** | Atherosclerotic carotid plaques can be quantified *in vivo* by magnetic resonance imaging (MRI). However, the accuracy in segmentation and quantification of components such as the thin fibrous cap (FC) and lipid-rich necrotic core (LRNC) remains unknown due to the lack of a submillimeter scale ground truth. A novel approach was taken by numerically simulating *in vivo* carotid MRI providing a ground truth comparison. Upon evaluation of a simulated clinical protocol, three MR readers segmented simulated images of cross-sectional plaque geometries derived from histological data of 12 patients. The MR readers showed high correlation (R) and intraclass correlation (ICC) in measuring the luminal area (R = 0.996, ICC = 0.99), vessel wall area (R = 0.96, ICC = 0.94) and LRNC area (R = 0.95, ICC = 0.94). LRNC area was underestimated (mean error, -24%). Minimum FC thickness showed a mediocre correlation and intraclass correlation (R = 0.71, ICC = 0.69). It can be concluded that current clinical MRI can quantify carotid plaques but shows limitations for thin FC thickness quantification. These limitations could influence the reliability of carotid MRI for assessing plaque rupture risk associated with FC thickness. Overall, MRI simulations provide a feasible methodology for assessing segmentation and quantification accuracy, as well as for improving scan protocol design.

**This chapter is based on:** Nieuwstadt HA, Geraedts TR, Truijman MTB, Kooi ME, van der Lugt A, van der Steen AFW, Wentzel JJ, Breeuwer M, Gijsen FJH. Numerical simulations of carotid MRI quantify the accuracy in measuring atherosclerotic plaque components in vivo. Magnetic Resonance in Medicine 2014;72:188-201.

## INTRODUCTION

Carotid atherosclerosis is a cardiovascular disease characterized by plaque formation in the arterial wall. Vulnerable plaques, consisting of a large lipid-rich necrotic core (LRNC) separated by a thin fibrous cap (FC) from the lumen, are most prone to rupture [1,2]. Rupture of the FC and subsequent embolization of thrombus and/or atherosclerotic debris can lead to ischemic stroke, which continues to rank among the leading causes of mortality and morbidity in Western countries [3]. By virtue of the high contrast for plaque components, carotid magnetic resonance imaging (MRI) has proven to be an effective noninvasive tool for assessing plaque composition *in vivo* in a clinical setting [4-8]. Plaque quantification can be performed via (automated) segmentation of the lumen and/or outer vessel wall and of components such as the FC, LRNC, calcifications and intraplaque hemorrhage [9-15]. Contours obtained from segmented carotid MRI data are increasingly being used as input for biomechanics-based carotid plaque studies using finite element analysis (FEA) and/or computational fluid dynamics [16-20].

A crucial component of a vulnerable plaque is the FC. Numerous studies have focused on the capabilities of carotid MRI with regard to FC imaging. Whereas most studies perform a qualitative assessment (i.e., thick versus thin) of the cap [21-24], the studies that provide quantitative data report parameters such as FC length and FC/LRNC ratios [25-27] or thickness measurements only for caps thicker than ~1 mm [28,29]. Consequently, there are no *in vivo* MR studies reporting FC thickness measurements for caps with a thickness of 0.1–1.0 mm, which are especially related to vulnerable plaques [30-32]. The reason for this can be found in the in-plane acquired voxel size that can be achieved currently with *in vivo* carotid MRI. Typically around 0.5–0.6 mm (8), this spatial resolution is limited concerning imaging of submillimeter FCs [24,28]. This raises concern because biomechanical FEA studies have shown that the minimum FC thickness, together with the LRNC size, is among the most important morphological parameters influencing computed peak cap stress, which is a marker for plaque vulnerability [33-36]. For these reasons, it is important to assess the accuracy and precision of *in vivo* carotid MRI with regard to plaque segmentation and, in particular, minimum FC thickness quantification.

The challenge of validating carotid MRI for this particular purpose is the lack of a ground truth (i.e., knowledge of the object being imaged) on the submillimeter scale. Histological sections from carotid endarterectomy (CEA) specimens are most commonly used as a gold standard [12,23,37,38]. However, they suffer from deformation artifacts such as shrinkage [39]. An additional limitation of histological validation is that cross-sectional *in vivo* carotid MRI data cannot be directly compared with thin (~5–10 µm)

histological sections due to the fact that carotid MR data have highly anisotropic voxels. A slice thickness in the order of 2–3 mm, as is common practice [8,12], results in severe partial volume effects (intravoxel signal averaging) within the entire slice in the axial direction, whereas carotid plaques can express considerable morphological changes over submillimeter axial distances [40]. To study the accuracy of *in vivo* carotid MRI in quantifying small features such as FCs, a different method needs to be developed that circumvents this problem by allowing a ground truth comparison on a submillimeter scale. The method presented here is a novel approach that involves numerically simulating *in vivo* carotid MRI using the modern open-source Jülich extensible MRI simulator (JEMRIS) [41].

The aim of our study was two-fold: (1) to implement and evaluate a typical clinical carotid MRI protocol in JEMRIS and simulate *in vivo* T1-weighted (T1W) contrast-enhanced (CE) carotid plaque imaging and (2) to apply this simulated carotid MRI protocol to a separate set of histology-derived ground truth plaque models to assess the accuracy and precision of current clinical carotid MRI in quantifying vulnerable plaque components via manual segmentation. We focused on the luminal area, vessel wall area, LRNC area, and minimum thickness of FCs thinner than 1 mm. Additionally, in order to provide guidance for improving carotid MRI FC quantification, we also explored the trade-off between scan time, resolution, and noise.

## METHODS

To fulfill the first aim of our study, we simulated a current clinically applied T1W CE carotid MR protocol that is used to visualize the FC [24]. A set of patient images from this clinical protocol was used; first, to derive apparent $T_1$ relaxation times of plaque components (which were used for the simulations), and second, to evaluate simulated images. To fulfill the second aim of our study, we applied the simulated MR protocol to a separate set of ground truth plaque models.

### Clinical MRI protocol

Six symptomatic patients with 30-69% carotid stenosis were positioned supinely in a 3.0T Philips Achieva TX System (Philips Healthcare, Best, the Netherlands) equipped with an eight-channel carotid RF coil (Shanghai Chenguan Medical Technologies Co., Shanghai, China). The patients were selected for presence of LRNC and an intact FC. After a non-contrast MR angiography scout scan, the carotid bifurcation containing the plaque was imaged using a fat-suppressed two-dimensional (2D) quadruple inversion recovery (QIR) T1W turbo spin echo (TSE) sequence (Table 1). This was done 6

minutes after intravenous injection of a gadolinium-based contrast agent (Gadovist; Bayer, Berlin, Germany [dose 0.1 mmol/kg body weight]) used to enhance the signal from the fibrous tissue, and thus the FC, by lowering the $T_1$ relaxation time [42-44]. Fifteen adjoining 2-mm-thick slices were positioned transversely around the site with

**Table 1**
Scan parameters for the clinical and simulated MRI protocols.

| Scan parameter | Clinical protocol | Simulated protocol |
|---|---|---|
| Pulse sequence | TSE | TSE |
| Weighting | T1W | T1W |
| Image mode, scan plane | 2D, axial | 2D, axial |
| FOV (mm) | 160 x 150 | 37 x 37 |
| Contrast enhanced | Yes (gadolinium) | n/a |
| Acquisition matrix size | 260 x 240 | 60 x 60 |
| Reconstructed matrix size | 520 x 480 | 120 x 120 |
| TSE factor | 10 | 10 |
| Slice thickness (mm) | 2 (adjoining) | n/a |
| Number of slices | 12 | 1 |
| Blood suppression | QIR | No |
| Eddy current compensation | Yes | No |
| Spin discretization $\delta$ | n/a | 10–30 µm |
| TR (ms), TE (ms) | 800, 10 | 800, 10 |
| Acquisition voxel size (mm) | 0.62 x 0.62 x 2.00 | 0.62 x 0.62 |
| Reconstructed voxel size (mm) | 0.31 x 0.31 x 2.00 | 0.31 x 0.31 |
| Scan technique | Full scan | Full scan |
| ECG gating (motion correction) | No | n/a |
| k-space filling order | Centric (low-high) | Centric (low-high) |
| NSA | 1 | 1 |
| Scan duration (min:s) | 5:12 | n/a |

TSE, turbo spin-echo; FOV, field of view; QIR, quadruple inversion-recovery; TR, repetition time; TE, echo time; ECG, electrocardiogram; NSA, number of signal averages; n/a, not applicable.

the maximum carotid stenosis in such a manner that the entire plaque was always within the slice package. Two patients had plaque formation in both the left and right carotid bifurcation. From each plaque (n = 8), one slice containing at least one clearly delineable LRNC was selected and used for this study. The *in vivo* images from the clinical protocol are hereafter referred to as the patient images and were used for the first aim of our study.

### Simulated MRI protocol

The choice of JEMRIS was motivated by several particular advantages of this MRI simulator over others, namely its fast parallel computing options and easy to use graphical user interfaces (GUIs) for pulse sequence implementation and sample model (input) simulations. The protocol implemented in JEMRIS had the same timings, TSE factor, k-space filling, and in-plane spatial resolution as the clinical protocol (Table 1). The centric low-high order k-space filling first filled the lower half of k-space from the center outwards, interleaved with half the number of shots, and repeated this pattern for the upper half. We performed single-slice MRI simulations because the simulation input samples, hereafter referred to as the sample models, were 2D models. This choice was made so that we could simulate a best-case imaging scenario wherein the plaque

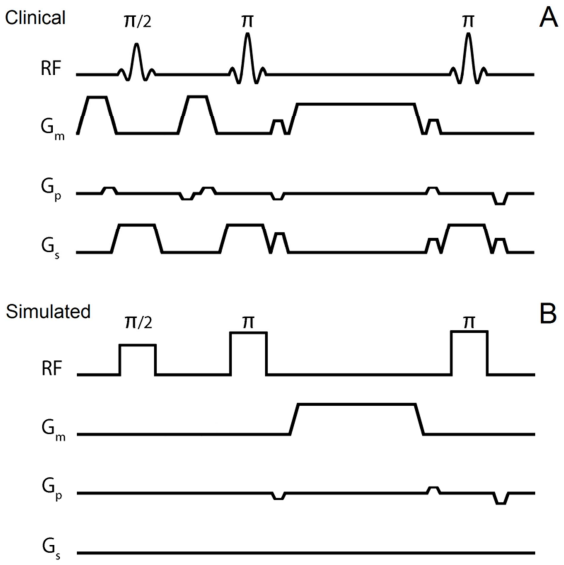


**Figure 1.** (A) Clinical pulse sequence diagram. (B) Simulated pulse sequence diagram. RF = radio frequency pulse, $G_m$ = measurement/frequency encoding gradient, $G_p$ = phase encoding gradient, $G_s$ = slice selection gradient.

morphology would be entirely uniform in the axial direction within a 2-mm slice. For the same reason, we also chose not to simulate arterial motion. This best-case scenario allowed us to quantify the upper limits of the accuracy and precision in plaque quantification. Because the sample model would thus be treated as a fully excited 2D slab, the need for selective radio frequency (RF) pulses became obsolete, and they were thus replaced by full excitation hard RF pulses (Figure 1). Gradient spoilers used to spoil unwanted signal coherences from imperfect selective RF pulses were discarded. Fat-suppressing and QIR black-blood pre-pulses were omitted due to the absence of neck tissue and flowing blood, respectively. Instead, for all sample models, the net magnetization $M_0$ of the lumen was set to zero to model black-blood imaging. Dummy gradients mimicking eddy current behavior in front of RF pulses were discarded because eddy currents do not occur in simulations. Due to the smaller size of the carotid plaque sample models compared with a full scale neck, the field of view (FOV) was reduced by using fewer shots. The FOV was kept large in comparison to the sample model to prevent the influence of ghosting artifacts in the phase direction. Note that the use of a reduced FOV by fewer k-space acquisitions reduces the image signal-to-noise ratio (SNR) in clinical MR systems. However, because noise will be artificially superimposed on the simulated image space, this effect can be discarded. JEMRIS simulations are based on spatially discretizing a sample model to a finite number of spins, given here by the distance parameter $\delta$. Simulated images were found to be independent of $\delta$ for $\delta < 30$ µm, thus resulting in $> 1.5 \cdot 10^6$ simulated spins for the FOV used in the simulations.

In post-processing, the k-space was zero-padded prior to Fourier transforming in order to double the reconstructed matrix size. This affects the discrete point spread function (PSF) in image space, which is –in contrast to merely the reconstructed in-plane voxel size (0.31 mm)– the actual measure for resolving small features [45]. Simulations on a single spin at the center of the FOV provided the PSF. The full-width at half-maximum in the image space was 3.6 voxels (1.8 acquired voxels, 1.1 mm) in the phase direction and 2.8 voxels (1.4 acquired voxels, 0.9 mm) in the frequency direction. The PSF, when normalized, was found to be independent of $\delta$ for $\delta < 30$ µm. These ranges indicate substantial out-of-voxel signal spreading of high intensity signals. As a last step in post-processing, Rician distributed noise was superimposed on the simulated image space to match the SNR in patient MR images [46]. For this, the noise standard deviation ($\sigma_n$) was estimated using the maximum-likelihood estimator for the Rayleigh distribution valid at non-signal areas in all the patient MR images [47]. Pixel data were obtained from various regions of interest (ROIs) containing $> 1 \cdot 10^4$ pixels in total at the non-signal areas in the vicinity of a neck RF coil providing an estimation of minimal noise for our best-case imaging

scenario. This yielded a $\sigma_n$ of 0.06, and hence an SNR of 16.7, when patient image intensities were normalized to the mean intensity of the sternocleidomastoid (SCM) muscle.

### Apparent $T_1$ relaxation times

Because $T_1$ relaxation times of carotid plaque components *in vivo* at 3.0T have not, to our knowledge, been reported in the literature, and because the clinical MR protocol is gadolinium CE, the apparent $T_1$ values for the plaque components to be used for the MRI simulations were reverse-engineered. We chose to model two essential plaque components: fibrous tissue and LRNC. The apparent $T_1$ values were determined such that fibrous tissue and LRNC had the same mean intensity relative to the adjacent SCM muscle as in the clinical MR images. The SCM muscle, with a known $T_1$ of 1412 ms at 3.0T [48], served as an adequate reference and as background tissue for the simulations. First, simulations were performed on sample models consisting of tissues with predefined $T_1$ relaxation times ranging from 100–1700 ms, and the resulting image intensity was measured. Second, signal intensities were measured in all patient images by averaging $N$ pixel values ($N > 1 \cdot 10^3$ pixels) from user-defined ROIs well within LRNC, fibrous tissue, and SCM regions. The simulated intensities were then used to determine the apparent T1 relaxation times of plaque components taking the SCM muscle as a reference. Because the simulated protocol is T1W, the $T_2$ relaxation time was set at 50 ms for all plaque components [49].

### Evaluation of simulated images

To evaluate whether the simulated *in vivo* MR images were realistic for segmentation analysis, the set of patient MR images was used. The inner and outer vessel wall and LRNC were delineated in the patient images based on previous validations of component contrasts to create 2D plaque sample models [7]. The models were assigned the earlier derived apparent $T_1$ relaxation times and then reimaged with MRI simulations. To assess similarity in image appearance, we focused on component edges because plaque segmentation is often based on edge detection by means of intensity differences as well as intensity gradients [14,50,51]. The patient images and their simulated counterparts were therefore compared by means of the intensity *I,* the 1-norm intensity gradient $|\nabla I| = |\partial I / \partial \mathrm{x}| + |\partial I / \partial \mathrm{y}|$, and intensity profile (line scan) plots. The pixel intensity distributions of the plaque components were compared by means of statistical analysis. The patient images and their simulated counterparts were normalized to the SCM tissue intensity (background in simulated images) for all quantitative comparisons.

### Quantification of plaque components

The second aim of this study was to use MRI simulations to assess the accuracy in carotid plaque quantification. For this purpose, we used histology of excised plaques to obtain a set of realistic 2D ground truth carotid plaque sample models for the simulations. Plaques from twelve (n = 12) symptomatic patients with >70% carotid stenosis scheduled for CEA were surgically removed and kept as intact as possible. The specimens were decalcified and embedded in paraffin for histological processing, which consisted of cutting 10 axial slices with a thickness of 5 µm at intervals of 1 mm. The slices were stained with an Elastica van Gieson stain (for details, see van Engelen et al. [52]). From each patient, two to four undamaged sections were selected that characterized the cross-sectional morphology of a typical carotid plaque with at least one LRNC and one FC < 1 mm. Each of the 33 selected sections displayed a different cross-sectional plaque morphology. Manual delineation of fibrous tissue and LRNC was performed on high-resolution microscopic digitized images. The shapes of the histological plaque models were then converted to mimic *in vivo* shapes. To obtain a more realistic arterial pressurized *in vivo* shape, each cross section was subjected to a 2D FEA computation (Abaqus Standard 6.11, Dassault Systèmes Simulia Corp., Providence, Rhode Island, USA) with incompressible, isotropic, neo-Hookean material models to compute the arterial deformation at a luminal pressure of 100 mmHg as the loading condition. The values for the material constant (~half the shear modulus) were taken as 167 kPa for fibrous tissue and 1 kPa for LRNC (for details, see Nieuwstadt et al. [53]). It should be noted that the FEA was not applied to determine the stress/strain distribution in the plaques but only to create a more realistic, *in vivo*, geometry. The resulting 33 deformed plaque cross sections became the 2D ground truth sample models for the MRI simulations. Plaque components were assigned the earlier derived mean $T_1$ relaxation times. Segmentation of simulated MR images was performed independently by three expert MR readers (M.B., G.H., and J.S. with respectively 16, 8 and 8 years of experience in the field). All readers were blinded to the ground truth and worked with preset contrast-brightness (i.e., window level) settings. Those settings were determined by averaging the settings preferred by four other experienced MR readers. Luminal area, vessel wall area (outer contour area minus lumen contour area), LRNC area and minimum FC thickness were compared with the ground truth. The Pearson correlation coefficient (R) was used to assess correlation. As a more strict measure for delineation accuracy, the ground truth of each area-based plaque component was superimposed on its segmented counterpart, and the percentage of nonoverlapping area relative to the ground truth was computed. To assess the consistency in measurements between the readers, the single measure intraclass correlation coefficient (ICC) with the two-way mixed effect model (absolute agreement)

was used. Data are expressed as the mean (μ) ± standard deviation ($\sigma$). R and ICC are significant when reported with $p < 10^{-3}$.

### Trade-off between scan time, resolution, and SNR

We performed an additional study to provide guidance for carotid MRI protocol design to improve LRNC area and FC thickness quantification. We explored the trade-off between scan time, resolution, and SNR by simulating two modifications of the original protocol. Both modified protocols had a doubling of the original scan time. The SNR equation was used to calculate changes in SNR [54]. The first modification (protocol A) was designed to only decrease the noise by setting the number of signal averages (NSA) at 2 with the same resolution, gaining a factor of $\sqrt{2}$ higher SNR. The second modification (protocol B) was designed to double the spatial resolution (acquired in-plane voxel size of 0.31 x 0.31 mm$^2$) by doubling the number of phase encoding steps. According to the SNR equation, for protocol B the SNR decreases with a factor of $\sqrt{8}$ (NSA = 1). There is a factor 4 loss in SNR due to the reduction in voxel size together with a factor $\sqrt{2}$ gain in SNR due to doubling of the number of phase encoding steps, together resulting in a decrease in SNR of $¼ \cdot \sqrt{2} = 1/\sqrt{8}$. Simulated images obtained from these two modified protocols were manually segmented by one expert (M.B.). Groups of data were compared using a one-tailed Mann-Whitney $U$ test ($p < 0.01$ was considered significant). Note that we did not evaluate the effects of scan time, resolution, and SNR separately, but rather their combined effect. We investigated whether (1) a doubling of the scan time can lead to better measurements and (2) if so, whether this could be achieved by investing the additional scan time in a factor $\sqrt{2}$ higher SNR (with the same resolution) or a doubling in resolution (but accompanied by a factor $\sqrt{8}$ lower SNR).

## RESULTS

### Apparent $T_1$ relaxation times

The simulated intensity of a sample model tissue is plotted as a function of its predefined $T_1$ value in Figure 2A. Plaque component intensities were measured in the patient images entirely within the fibrous tissue, LRNC, and SCM muscle, averaged, and divided by averaged SCM muscle intensity. This resulted in the intensity ratios $I_{SCM}/I_{SCM} = 1.00$, $I_{FT}/I_{SCM} = 1.48 \pm 0.15$, and $I_{LRNC}/I_{SCM} = 1.09 \pm 0.14$. On the patient images (Figure 2B), the fibrous tissue was found to be hyperintense with the highest intensity (shortest $T_1$), whereas LRNC had a lower intensity, consistent with

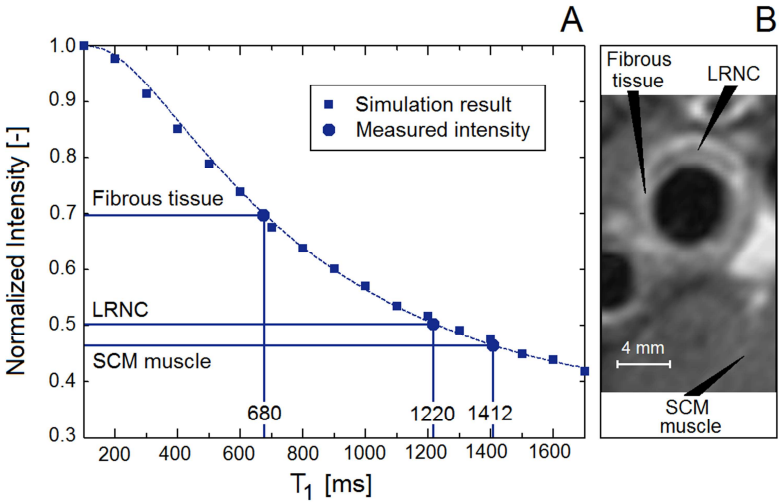


**Figure 2.** (A) Simulated image intensity as a function of phantom tissue $T_1$ (normalized on $T_1 = 100$ ms). The graph is used to determine the apparent $T_1$ relaxation time of plaque components based on their measured intensity in patient images. (B) Example of a patient image with the various components indicated.

previous studies [7,8]. By employing the graph in Figure 2A, we determined an apparent $T_1 = 680 \pm 135$ ms for fibrous tissue and an apparent $T_1 = 1220 \pm 280$ ms for LRNC, given the known $T_1 = 1412$ ms of SCM muscle. The means of these apparent relaxation times were used for the remainder of the study.

### Evaluation of simulated images

Patient versus simulated carotid MR images from three different patients are shown in Figure 3. Line scans were taken across all plaque components for the patient and simulated images to compare intensity profiles at the transition regions between plaque components (e.g., lumen–FC, FC–LRNC, etc.). The simulated images all had intensity levels and intensity gradients similar to those of the patient images (Figure 3). Fibrous tissue was simulated as hyperintense and LRNC as hypointense, which was in agreement with the patient images. Moreover, the line scan intensity profiles indicated that the simulations provided a quantitatively similar intensity profile at plaque component transition regions. The line scan intensity profiles from the simulated and patient images were compared quantitatively by computing the mean error ($\varepsilon$) ± standard deviation of the error for each profile, with the error defined as $\varepsilon = I_{\text{simulated}} - I_{\text{patient}}$. This resulted in $\varepsilon = 0.00 \pm 0.15$ for patient 1, $-0.05 \pm 0.16$ for patient 2, and $+0.05 \pm 0.20$ for patient 3.

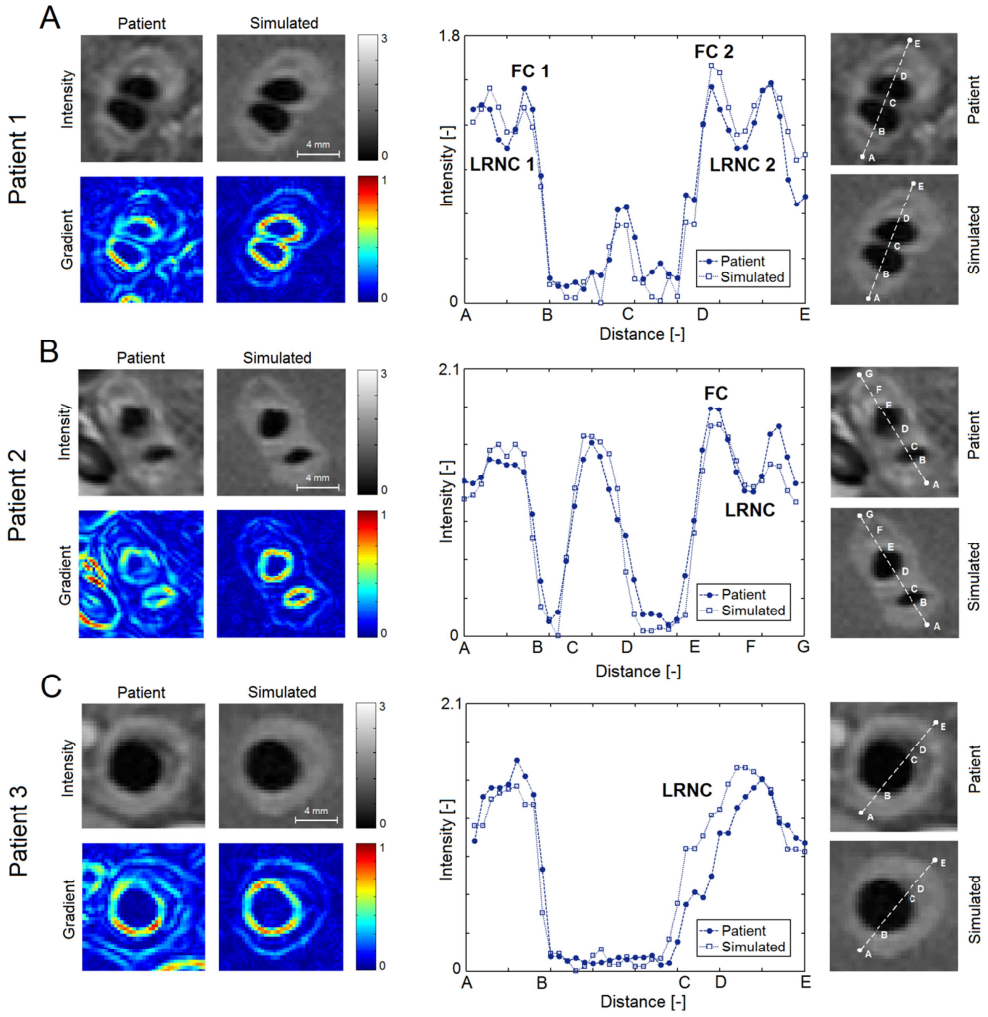


**Figure 3.** (A-C) Evaluation of carotid plaque MRI simulations for three images, each from a different patient. Intensity images together with absolute intensity gradient images are shown on the left. Line scan intensity profile plots are shown on the right. Transition regions are marked by capital letters, and LRNC and FC are indicated in the line scan plots. Simulated images were normalized to the background, patient images were normalized to SCM muscle tissue.

Histograms of pixel intensities within segmented regions of plaque components for all simulated versus patient images are shown in Figure 4 (μ and $\sigma$ indicated in the histograms). Simulations resulted in a smaller spread in within-component pixel intensities, most notably for LRNC. Simulated fibrous tissue pixel intensities had a

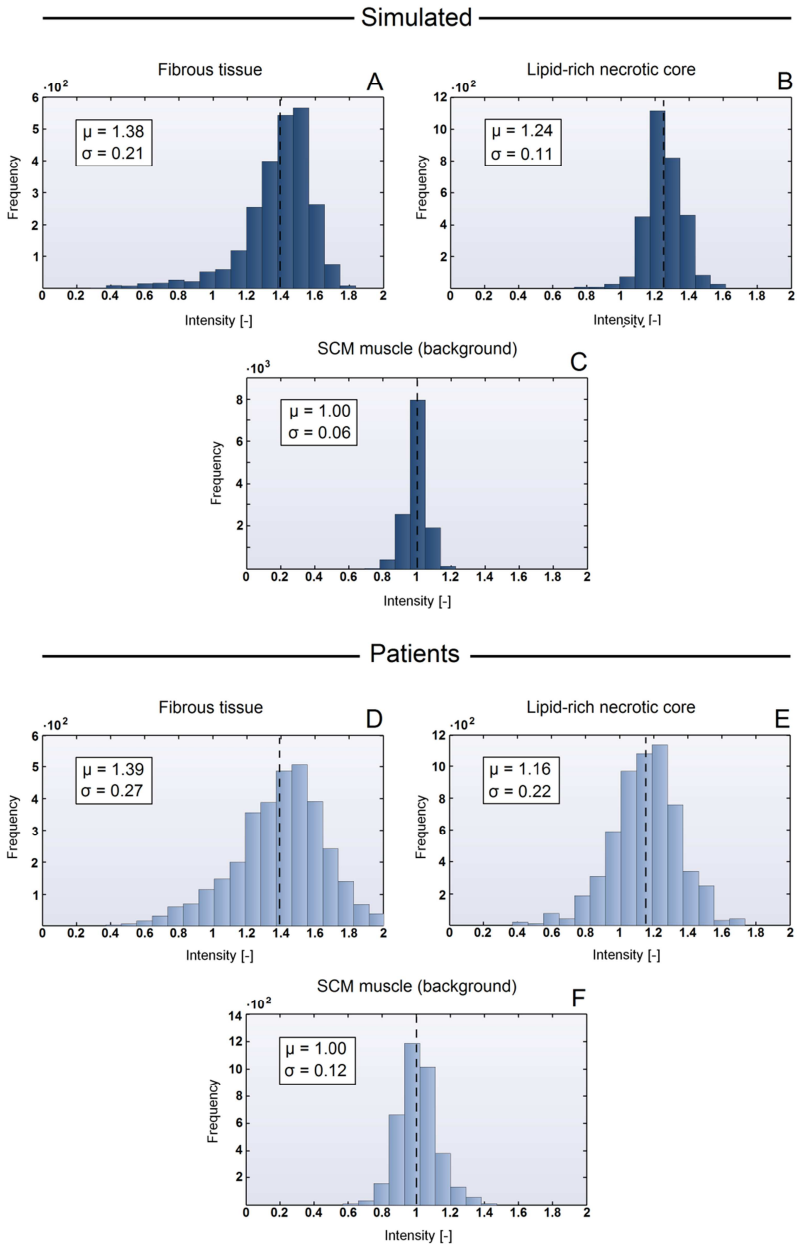


**Figure 4.** Histograms of fibrous tissue, LRNC, and SCM muscle pixel intensities within segmented regions. (A-C) Data from simulated images. (D-F) Data from patient images. The mean ($\mu$, dotted line) and standard deviation ($\sigma$) are indicated. Simulated images were normalized to the background, patient images were normalized to SCM muscle tissue.

distribution, mean, and standard deviation similar to those of patient images. It is notable that the mean LRNC pixel intensities were higher (1.24 in simulated images and 1.16 in patient images) than the imposed $I_{LRNC}/I_{SCM} = 1.09$ ratio from the $T_1$ relaxation time study, whereas the mean fibrous tissue intensities (1.38 and 1.39) were lower than the $I_{FT}/I_{SCM} = 1.48$ ratio.

## Quantification of plaque components

The procedure of forming ground truth sample models based on histological cross sections is outlined in Figure 5. Histological sections (Figure 5A) were segmented (Figure 5B) and formed ground truth sample models after computational FEA pressurization (Figure 5C). These ground truth sample models were then subjected to an MRI simulation (Figure 5D). The complete data set containing 33 ground truth sample models covered a wide range of vulnerable plaque morphologies. The minimum FC thickness in the data set was 0.34 ± 0.27 mm. All ground truth minimum FC thicknesses were on a submillimeter scale, the maximum being 0.87 mm and the minimum being 0.04 mm. The ground truth luminal areas were 16.7 ± 12.6 $mm^2$, the LRNC areas were 12.4 ± 9.4 $mm^2$, and the vessel wall areas were 31.3 ± 10.6 $mm^2$.

Three examples of ground truth sample models of different morphologies, their simulated MR images, and the segmentation of each MR reader are given in Figure 6. Small morphological plaque features in the ground truth models were obscured in the

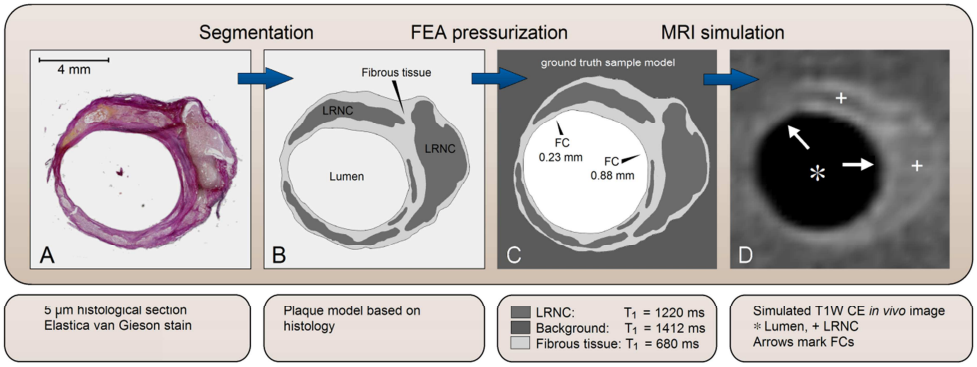


**Figure 5.** The creation of a simulated MR image from a histological section illustrated by an example. (A) Histological plaque cross section. (B) Segmentation by delineating fibrous tissue and LRNCs to form the computational model for 2D FEA. (C) The resulting pressurized *in vivo* plaque model at 100 mmHg is assigned an apparent $T_1$ relaxation time per component and defined as the ground truth sample model. (D) A simulation in JEMRIS results in a simulated *in vivo* TW1 CE carotid MR image. Details are noted in the boxes below each image.

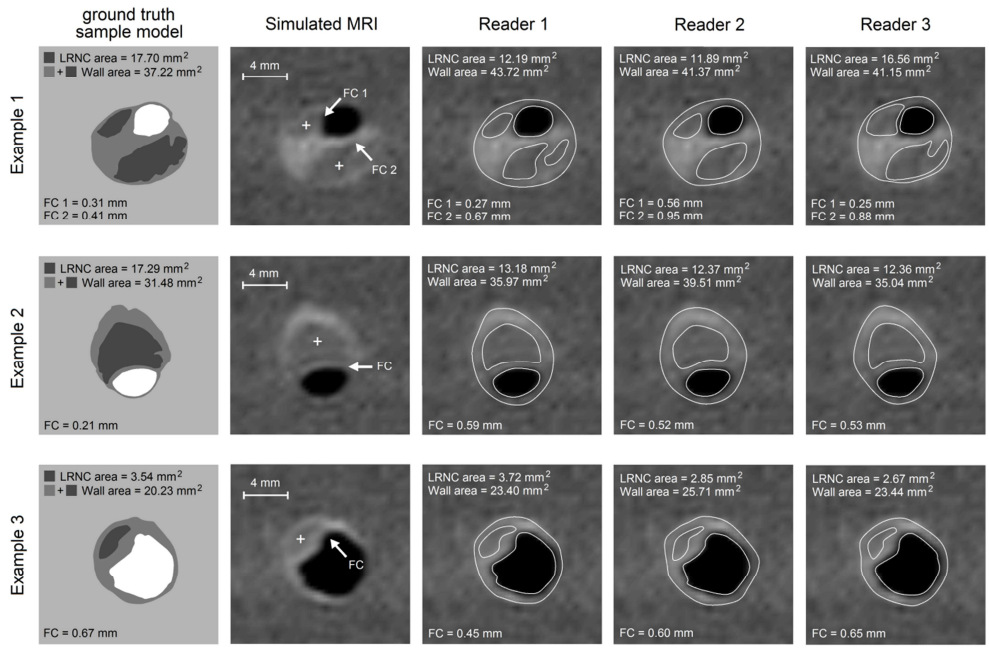


**Figure 6.** Three examples show the ground truth sample model (first column), the resulting simulated MR image (second column), and the segmentations from the three MR readers (third through fifth column). Quantitative plaque component values are given in the images. FCs are denoted by arrows; LRNCs are denoted by plus symbols (+) in MR images.

MR images due to the limited spatial resolution, PSF signal spreading, and noise. In the three examples, readers showed qualitative agreement and accuracy in delineating the lumen and outer vessel walls. In example 1, readers exhibited disagreement in LRNC segmentation. Upon analysis, all readers tended to be inaccurate in measuring component areas: the total LRNC area was on average underestimated, while the vessel wall area was overestimated. The readers showed poor precision in quantifying minimum FC thickness. Although the spatial resolution and contrast were sufficient to distinguish the second FC in example 1, its minimum thickness was severely overestimated by all readers. The thin FC in example 2 was also overestimated in thickness, whereas the relatively thick cap in example 3 was quantified more accurately.

Regarding the entire dataset of sample models, the readers qualitatively agreed in segmentation in almost all plaque models. Of all LRNCs in the ground truth ($n = 47$), the readers successfully identified 34 (73%). The 13 LRNCs that were missed by one or more readers were very small, with an area of only $1.40 \pm 1.35$ mm$^2$. An

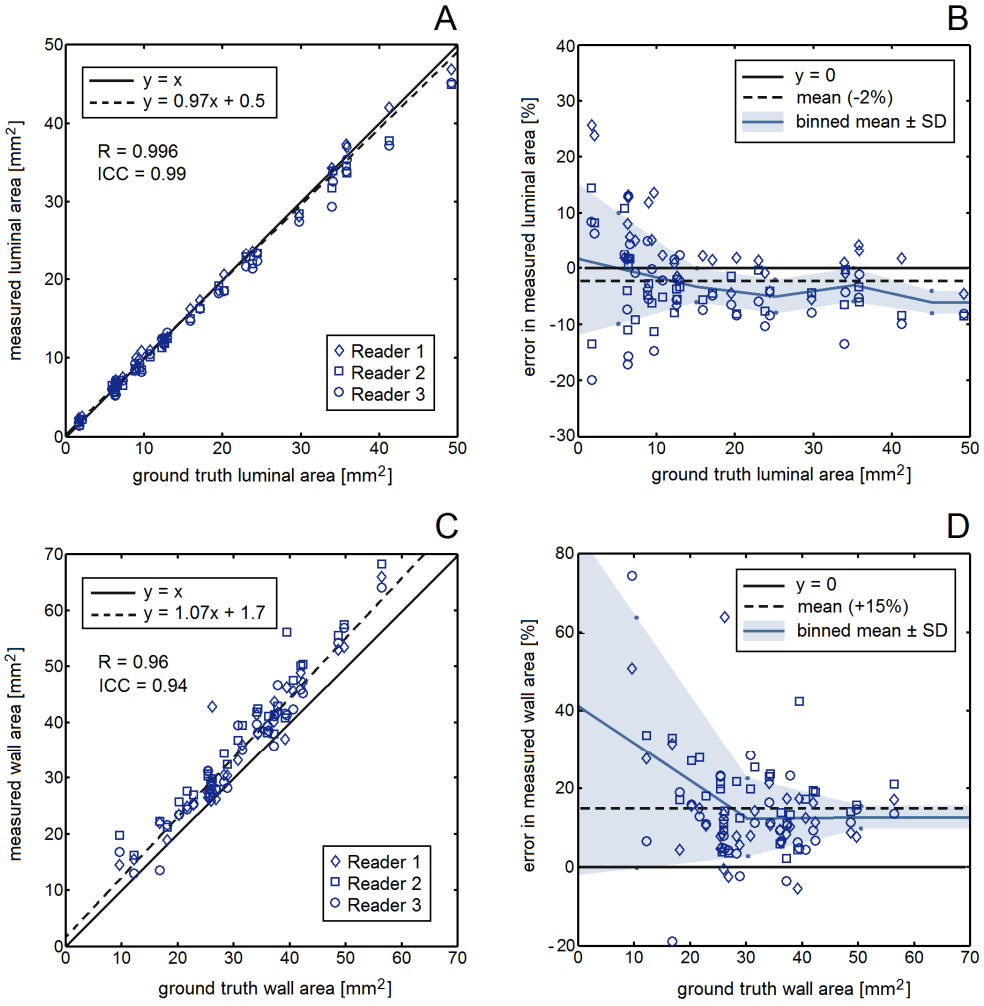


**Figure 7.** (A) Measured luminal area as a function of ground truth value. (B) Relative error [%] in measured luminal area as a function of ground truth value. (C) Measured wall area as a function of ground truth value. (D) Relative error [%] in measured wall area as a function of ground truth value. Bin size is 10 mm$^2$ for (B) and 20 mm$^2$ for (D). $p < 10^{-3}$ for all R and ICC.

example where small LRNCs were unidentifiable in the simulated MR image can be seen in Figure 5C and 5D. In five cases, a reader false-positively segmented a relatively small LRNC (area of 3.27 ± 1.36 mm$^2$) which was nonexistent in the ground truth. In Figures 7 and 8, the measured value and the relative error [%] are plotted as functions of the ground truth value for the luminal area (Figure 7A and 7B), the vessel wall area

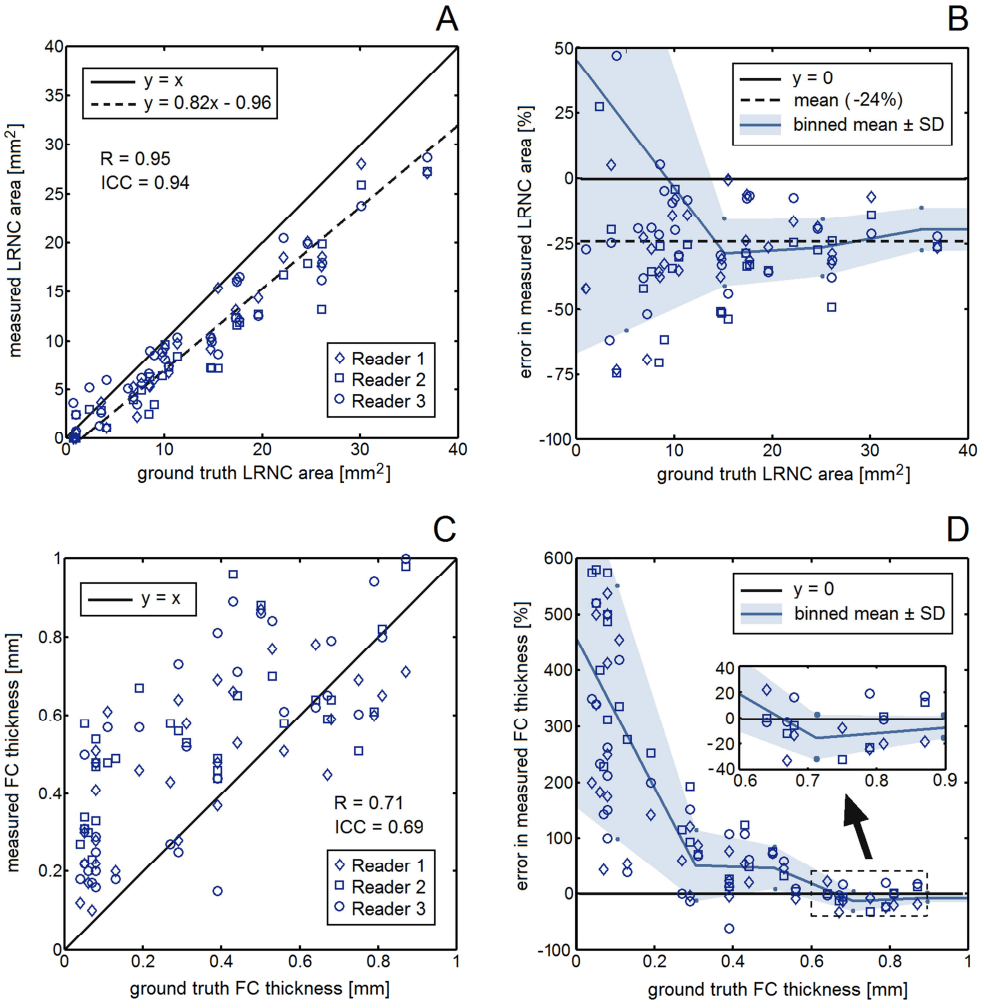


**Figure 8.** (A) Measured LRNC area as a function of ground truth value. (B) Relative error [%] in measured LRNC area as a function of ground truth value. (C) Measured minimum FC thickness as a function of ground truth value. (D) Relative error [%] in measured minimum FC thickness as a function of ground truth value. Bin size is 10 $mm^2$ for (B) and 0.2 mm for (D). $p < 10^{-3}$ for all R and ICC.

(Figure 7C and 7D), the LRNC area (Figure 8A and 8B) and the minimum FC thickness (Figure 8C and 8D) for all sample models and all MR readers. In Table 2, the relative error in FC thickness measurements for FCs thinner and thicker than 0.62 mm (in-plane acquisition voxel size) as well as the nonoverlapping areas for lumen, vessel wall, and LRNC are listed for each MR reader. The measurements of the luminal area

showed very high correlation and interobserver agreement (R = 0.996, ICC = 0.99), although the readers were slightly inaccurate with a mean underestimation of -2%. The readers were equally accurate in their delineations (mean nonoverlapping area of 9%). For the vessel wall area, the measurements also correlated and agreed well (R = 0.96, ICC = 0.94). Readers were less accurate in both delineation (mean nonoverlapping area of 21%) and area quantification (mean overestimation of +15%). For the LRNC area, the readers again showed good agreement and correlation (R = 0.95, ICC = 0.94) but were inaccurate, being negatively biased in quantifying the area (mean underestimation of -24%). Readers showed equally poor delineation accuracy for LRNCs (mean nonoverlapping area between 37% and 40% for all readers). For the minimum FC thickness, we found that MR reader measurements had a mediocre correlation and agreement (R = 0.71, ICC = 0.69). For FCs thinner than 0.62 mm, readers severely overestimated the thickness with a large mean relative error and standard deviation: +201% ± 217% (Table 2). For FCs thicker than 0.62 mm, measurements were more accurate and precise, with a relative error of only -6% ± 15%. Although FCs thinner than 0.31 mm (in-plane reconstructed voxel size) were measured with a severe overestimation and large spread, they were notably rarely (10%) quantified thicker than 0.62 mm (Figure 8C). In contrast to the minimum thickness, the average FC thickness yielded a smaller relative measurement error (+65% ± 63% versus +175% ± 191%). It also correlated better with the ground truth and yielded higher agreement (R = 0.81, ICC = 0.79).

**Table 2**
Relative error in minimum FC thickness measurements and nonoverlapping area for lumen, vessel wall, and LRNC per MR reader.

| Reader | Error in FC thickness [%] (caps < 0.62 mm) | Error in FC thickness [%] (caps > 0.62 mm) | Nonover-lapping area: Lumen [%] | Nonover-lapping area: Vessel wall [%] | Nonover-lapping area: LRNC [%] |
|---|---|---|---|---|---|
| 1 | +163 ± 182% | -13 ± 17% | 10 ± 4% | 19 ± 6% | 40 ± 9% |
| 2 | +262 ± 265% | -8 ± 15% | 9 ± 3% | 25 ± 11% | 37 ± 7% |
| 3 | +178 ± 203% | +4 ± 14% | 9 ± 4% | 19 ± 7% | 39 ± 9% |
| Mean | +201 ± 217% | -6 ± 15% | 9 ± 4% | 21 ± 8% | 39 ± 8% |

Values are presented as the mean error ± standard deviation. The chosen thickness cut-off value of 0.62 mm equals the in-plane acquisition voxel size.

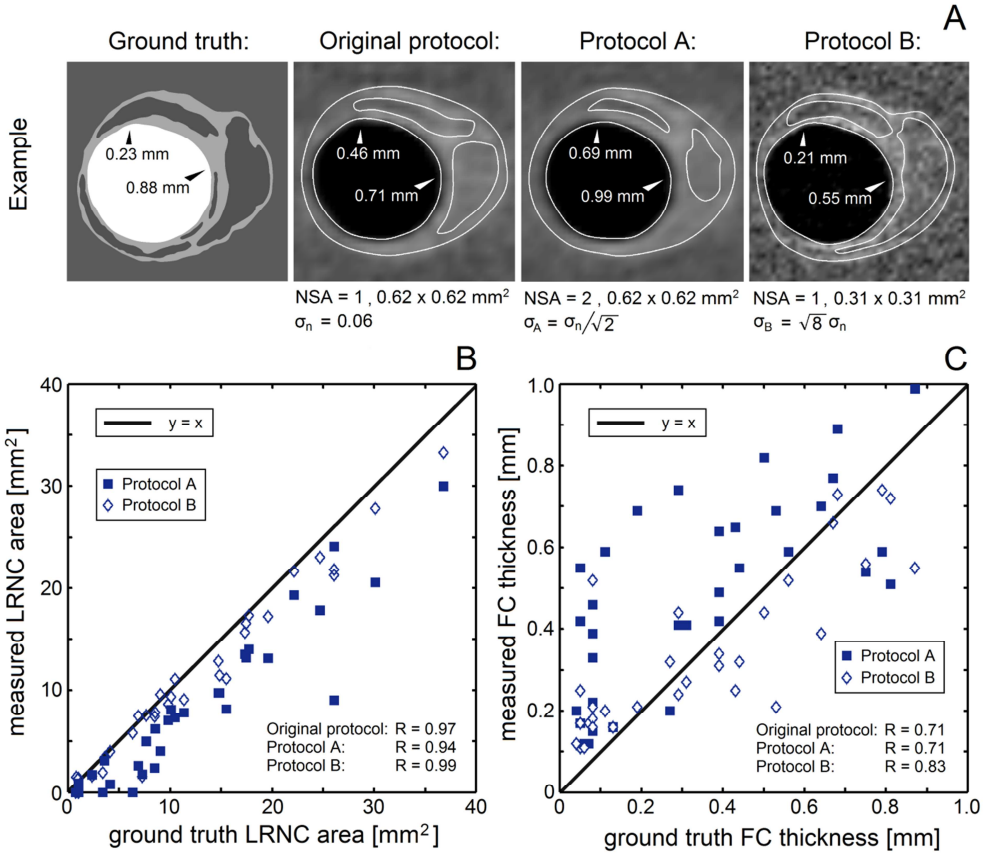


**Figure 9.** Exploring the trade-off between scan time, resolution, and SNR by simulating two modifications (protocols A and B) of the original protocol. (A) Reader segmentation example and protocol details. (B) Measured LRNC area as a function of ground truth value. (C) Measured minimum FC thickness as a function of ground truth value. $p < 10^{-3}$ for all R.

### Trade-off between scan time, resolution, and SNR

The results are shown in Figure 9. Protocol A did not lead to a statistically significant improvement in measurement error of LRNC area or in minimum FC thickness and yielded R = 0.94 and R = 0.71, respectively. Protocol B led to significant improvements and yielded R = 0.99 and R = 0.83, respectively. The mean percentage error for LRNC area improved to -11% ± 18% (compared with -26% ± 21% for the original protocol for this MR reader and -36% ± 17% for protocol A). The sensitivity in detecting LRNCs improved for protocol B to 42 out of 47, while protocol A showed

no improvement with 34 out of 47. Noticeably, protocol B led to an underestimation of the minimum FC thickness of caps $>$ 0.31 mm (-21% $\pm$ 17%).

# DISCUSSION

Carotid MRI is a promising noninvasive method for assessing plaque composition *in vivo*. However, the lack of a ground truth on a submillimeter scale has made it impracticable to assess the accuracy in segmentation of plaque components, most importantly for small but crucial components such as the FC. Our study took a novel approach by numerically simulating a current carotid MRI protocol using the open-source high-performance JEMRIS, allowing for submillimeter ground truth comparison. To our knowledge, this study is the first that circumvents typical histological validation by utilizing carotid MRI simulations for this purpose. We were able to simulate images that corresponded very well to clinical patient images for manual segmentation purposes. We subsequently quantified the accuracy and precision in plaque segmentation and minimum FC thickness as well as luminal, LRNC and vessel wall area measurements. We additionally explored the trade-off between scan time, resolution, and SNR.

## MRI simulations

We implemented a clinical T1W CE pulse sequence in JEMRIS in a manner that avoided unnecessary complexity, reduced simulation time, and provided a best-case imaging scenario for our plaque quantification study. Using this simulated protocol and a set of patient images, we derived apparent $T_1$ relaxation times of plaque components through an inverse mapping approach. Evaluation with patient MR images showed that the simulated MR protocol provided very similar image contrast, SNR, spatial resolution, and intensity gradients over plaque components. The approximated MR protocol, as well as its subsequent numerical simulation in JEMRIS, thus did not induce a significant change in image appearance. Additionally, the choice to simulate a best-case imaging scenario by neglecting arterial pulsating motion and by assuming a 2D axially uniform morphology and minimal noise did not result in an unrealistic image appearance.

Although a number of physical phenomena were not modeled in the simulations, they appeared to be of minor influence:

1. Chemical shift. In the clinical MR protocol, spectral presaturation with inversion recovery (SPIR) is used to suppress perivascular fat, and regional saturation

technique (REST) slabs are used for subcutaneous fat. The LRNC does not behave like these adipose tissues [55], hence for these components no significant ghosting artifacts should occur, because they are either suppressed or insensitive to chemical shift. Phantom validation experiments with the clinical protocol did not show any significant influence on signal homogeneity from the SPIR and QIR prepulses or the nearby placed REST slabs.

2. Magnetic susceptibility. It might be expected that magnetic susceptibility differences in the neck anatomy, especially air cavities, would have an influence on image quality. However, in practice, no significant image artifacts were observed in the ROI, not even when using a sensitive gradient echo sequence.
3. Eddy currents. These are handled quite well in modern MRI systems by the eddy current pre-emphasis, whereas any remaining currents should be small and insignificant.
4. $T_2$*. The used TSE pulse sequence is insensitive to $T_2$* effects.
5. $B_1$ homogeneity. The ROI is small and close to the isocenter of the transmit body coil where the optimal $B_1$ uniformity should result in small flip angle deviations. Additionally, a TSE pulse sequence is insensitive to these small deviations.

We found high similarity between simulated images and patient images for manual segmentation purposes, even though we modeled delineated, homogenized plaque components and focused on the LRNC by omitting calcium and intraplaque hemorrhage in the simulations. Note that simulated images were not validated to be identical to patient *in vivo* images in every aspect. This would in practice require the use of histology, which has practical limitations such as the presence of deformation artifacts, difficulties in registration, and the lack of knowledge of the possible heterogeneous distribution of tissue $T_1/T_2$ relaxation times within a plaque. An additional T1W turbo field echo (TFE) protocol revealed intraplaque hemorrhage in only one patient image, whereas presence of calcium caused a notable difference in one case: patient 3 (Figure 3C). The calcified LRNC in this case explains the lower LRNC intensity in the patient image compared with its simulated counterpart. With regard to the pixel intensity histograms of plaque components, we observed a lower standard deviation in intensities in simulated images. This can be explained by the use of homogenized tissues in the simulations. The contrast of FCs and LRNCs in patient images depends strongly on presence of collagen, loose matrix and inflammatory cells for fibrous or calcified tissues, and localized intraplaque hemorrhage for LRNCs, all leading to a higher standard deviation in patient images [7,12,25]. Another contribution to the higher standard deviation could be the fact that partial volume effects and PSF

signal spreading raised the pixel intensity levels inside LRNCs close to the inaccurately segmented borders to high intensity fibrous tissue. These effects could also explain the higher mean pixel intensity of LRNCs and lower mean intensity for fibrous tissue in the histograms compared with the values derived from the $T_1$ relaxation time study. This is because in the latter, only ROIs well inside and distant from possible component edges were used.

To our knowledge, no existing MR $T_1$ mapping methods have yet been applied to directly measure vessel wall $T_1$ *in vivo* at 3.0T. Our approach of determining $T_1$ relaxation times by normalization to the adjacent SCM muscle could result in inaccuracies, due to factors such as $B_1$ inhomogeneities and coil sensitivity profiles, as well as to differences in proton density and $T_2$. These inaccuracies (which have led us to use the term *apparent* values) are reflected in the large standard deviations reported. Investigations such as ours, also considering the fact that $T_1$ measurements at different field strengths or from *ex vivo* samples may differ significantly [56,57], thus prompt the need for studies on *in vivo* $T_1$ mapping of carotid plaques at 3.0T. It should be noted that the $T_1$ times obtained in this study fall within realistic ranges when taking these studies into consideration.

As already indicated, there are two key assumptions inherent in the simulation approach implemented in this study. The implications of these assumptions require careful consideration. First, the partial volume averaging effects of a nonuniform axial morphology within a 2-mm slice are not negligible and could restrict tissue characterization and decrease the accuracy of *in vivo* segmentation. Second, such characterizations and segmentations may also be significantly impaired by the simplifying assumption of homogenized plaque components. For both of these oft-used assumptions in carotid MRI, the simulation methodology presented in this study could provide important insight into their influence on carotid MR image interpretation.

### Quantification of plaque components

MR readers exhibited high correlations and interobserver agreement for luminal area, vessel wall area, and LRNC area. Luminal area and LRNC area were underestimated, however, whereas vessel wall area was overestimated. Measured LRNC area has been compared with histology measurements in previous studies, which confirmed our findings with respect to the good correlation and agreement [12,25]. While these and most other studies have only assessed correlation with histology, intra- or interreader agreement, and/or reproducibility, our novel method of simulating MRI led us to quantify segmentation accuracy and precision directly by means of ground truth comparison. We found a relatively large inaccuracy in LRNC segmentation, in correspondence with earlier reports [28]. Another one of our key findings, LRNC area

underestimation, has also been reported [11]. This underestimation could be attributed to intravoxel partial volume effects and PSF signal spreading of high-intensity fibrous tissue, causing low-intensity LRNC regions to appear smaller and high-intensity fibrous tissue regions larger. Our methods and findings are relevant for imaging of other plaque components for segmentation and quantification; for example, the apparent increase of hyperintense intraplaque hemorrhage on time-of-flight and T1W scans, or the apparent reduction of hypointense calcium regions on T1W, T2W, and proton density scans [7,17]. If automated segmentation algorithms are validated or parametrically fine-tuned merely to agree with manual segmentations [14,15], then inaccuracies from consistent over- or underestimations would remain unnoticed and uncorrected for. MRI simulations as introduced in this study have the potential to play a crucial role in improvement and validation of (automatic) segmentation. They could be widely applicable to other fields besides carotid MRI.

Our study was inspired by the question of how accurately FCs thinner than ~1 mm can be quantified by carotid MRI. This question remained unanswered due to the lack of adequate *in vivo* ground truth comparison methods [24,28]. While CE T1W imaging facilitates a qualitative assessment of FC status, it could be problematic for quantitative measurements, because hyperintense FCs can appear thicker due to PSF signal spreading and partial volume effects. Although overestimation of minimum FC thickness could have been foreseen based on the limited in-plane spatial acquisition resolution (0.62 mm) alone, our method enabled us to quantify this inaccuracy. We observed that the accuracy and precision for caps thinner than 0.62 mm are too poor for reliable thickness quantification (error of +201% ± 217%). The measurements of caps slightly thicker than 0.62 mm were relatively much more precise and accurate (-6% ± 15%), which is remarkable given the ~1-mm width of the PSF. However, some caution is in order. First, all our findings reflect the upper limit in a best-case imaging scenario. Second, numerous thin caps were measured to be thicker than 0.62 mm, which could result in a possible false-negative vulnerability assessment. The inaccuracy and poor precision in quantifying minimum FC thickness at this spatial resolution raise concern regarding the reliability of carotid MRI-based biomechanical FEA stress models of vulnerable thin cap plaques, because those models are very sensitive to minimum FC thickness [28,33,35,53]. An interesting finding in this study was that the JEMRIS simulations correctly simulated Gibbs artifacts (ringing) in the measurement direction. This occasionally caused FCs oriented along the phase direction to appear more intense. A low-pass k-space filter, as used in clinical systems, counteracts this phenomenon. The influence of this artifact on FC thickness quantification, in combination with k-space filtering, should be subject of future studies.

The present study was designed using a set of 33 realistic histology-based cross sections displaying a wide variety of plaques. A parameter study using a single simulated (idealized) lesion would provide more insight in the exact sources of error in measurements. However, for manual reader segmentation as investigated in this study, the latter approach would likely result in dependent measurements of an MR reader due to a priori knowledge and a learning effect, rendering a statistical analysis problematic. The current approach also incorporates the wide range of complex morphologies plaques can have that would be missed when using a single or idealized plaque model. This makes the results of this study directly clinically applicable.

### Trade-off between scan time, resolution, and SNR and future research

To illustrate the potential of MRI simulations and the role they can play in improving MRI in general, we used the simulations to explore trade-offs in protocol design. Comparisons between enhanced SNR or increased resolution when doubling the scan time showed that only the latter provided better segmentation results. Despite the decreased SNR, a higher resolution apparently leads to better visualization of small plaque features and structures, such as thin FCs and small LRNCs. Thus, when improving current carotid MRI protocols, scan time could be better invested in increasing the resolution, while sacrificing some SNR, if the initial SNR is sufficiently high as was the case here. We found that SNR (when sufficiently high) was not the limiting factor in measurement accuracy in this study, suggesting small plaque features were obscured by the spatial resolution and not by noise. The identification of an optimal combination of scan protocol parameters for any particular purpose (e.g., scan time reduction, increased interreader agreement and reproducibility, tissue characterization, automatic segmentation, etc.), is an area in which further research using MRI simulations could prove fruitful. This would provide direct feedback to scan protocol and pulse sequence development, or even for MR system design, to optimize MR imaging in a controllable, time- and cost-effective way [58,59]. JEMRIS simulations can be extended by implementing multicontrast protocols and by including arterial pulsating motion, $T_2$* effects, $B_0$ field inhomogeneity, slice-selective RF pulses, three-dimensional sample models, and nonlinear gradients.

## CONCLUSIONS

MRI simulations provide realistic *in vivo* carotid MR images that can be used to quantify the accuracy and precision in plaque component segmentation, in particular of submillimeter FCs. We found that carotid MRI can quantify plaques with regard to the

lumen, vessel wall area, and LRNC area but has limitations in FC thickness quantification. Numerically simulating *in vivo* MRI proves a feasible methodology to improve scan protocol design and to address clinical imaging-based questions by providing a ground truth comparison.

## ACKNOWLEDGEMENTS

We thank Peter van der Meulen, Liesbeth Geerts, Wim Prins (Philips Healthcare, Best, the Netherlands), and Bram Coolen (Academic Medical Center, Amsterdam, the Netherlands) for useful discussions. We also thank Jeroen Sonnemans and Gilion Hautvast (formerly of Philips Healthcare, Best, the Netherlands) for performing MR segmentations and Kim van Gaalen (Erasmus Medical Center, Rotterdam, the Netherlands) for histological processing.

## REFERENCES

1. Falk E. Pathogenesis of atherosclerosis. J Am Coll Cardiol 2006;47:C7-12.
2. Mughal MM, Khan MK, DeMarco JK, Majid A, Shamoun F, Abela GS. Symptomatic and asymptomatic carotid artery plaque. Expert Rev Cardiovasc Ther 2011;9:1315-1330.
3. Roger VL, Go AS, Lloyd-Jones DM et al. Heart disease and stroke statistics - 2012 update: a report from the American Heart Association. Circulation 2012;125:e2-e220.
4. Li F, Yarnykh VL, Hatsukami TS et al. Scan-rescan reproducibility of carotid atherosclerotic plaque morphology and tissue composition measurements using multicontrast MRI at 3T. J Magn Reson Imaging 2010;31:168-176.
5. Kerwin WS, Canton G. Advanced techniques for MRI of atherosclerotic plaque. Top Magn Reson Imaging 2009;20:217-225.
6. Watanabe Y, Nagayama M. MR plaque imaging of the carotid artery. Neuroradiology 2010;52:253-274.
7. Underhill HR, Hatsukami TS, Fayad AZ, Fuster V, Yuan C. MRI of carotid atherosclerosis: clinical implications and future directions. Nat Rev Cardiol 2010;7:165-173.
8. Wang J, Balu N, Canton G, Yuan C. Imaging biomarkers of cardiovascular disease. J Magn Reson Imaging 2010;32:502-515.
9. Cappendijk VC, Kessels AGH, Heeneman S et al. Comparison of lipid-rich necrotic core size in symptomatic and asymptomatic carotid atherosclerotic plaque: initial results. J Magn Reson Imaging 2008;27:1356-1361.
10. Kwee RM, van Oostenbrugge RJ, Prins MH et al. Symptomatic patients with mild and moderate carotid stenosis: plaque features at MRI and association with cardiovascular risk factors and statin use. Stroke 2010;41:1389-1393.
11. Hofman JMA, Branderhorst WJ, ten Eikelder HMM, Cappendijk VC, Heeneman S, Kooi ME, Hilbers PAJ, ter Haar Romeny BM. Quantification of atherosclerotic plaque components using *in vivo* MRI and supervised classifiers. Magn Reson Med 2006;55:790-799.
12. Saam T, Ferguson MS, Yarnykh VL, Takaya N, Xu D, Polissar NL, Hatsukami TS, Yuan C. Quantitative evaluation of carotid plaque composition by *in vivo* MRI. Arterioscler Thromb Vasc Biol 2005;25:234-239.
13. Liu F, Xu D, Ferguson MS, Chu B, Saam T, Takaya N, Hatsukami TS, Yuan C, Kerwin WS. Automated *in vivo* segmentation of carotid plaque MRI with morphology-enhanced probability maps. Magn Reson Med 2006;55:659-668.

14. Sakellarios AI, Stefanou K, Siogkas P et al. Novel methodology for 3D reconstruction of carotid arteries and plaque characterization based upon magnetic resonance imaging carotid angiography data. Magn Reson Imaging 2012;30:1068-1082.
15. van 't Klooster R, Naggara O, Marsico R, Reiber JHC, Meder JF, van der Geest RJ, Touze E, Oppenheim C. Automated versus manual *in vivo* segmentation of carotid plaque MRI. Am J Neuroradiol 2012;33:1621-1627.
16. Steinman DA, Thomas JB, Ladak HM, Milner JS, Rutt BK, Spence JD. Reconstruction of carotid bifurcation hemodynamics and wall thickness using computational fluid dynamics and MRI. Magn Reson Med 2002;47:149-159.
17. Sadat U, Teng Z, Gillard JH. Biomechanical structural stresses of atherosclerotic plaques. Expert Rev Cardiovasc Ther 2010;8:1469-1481.
18. Li Z, Howarth S, Trivedi RA, U-King-Im JM, Graves MJ, Brown A, Wang L, Gillard JH. Stress analysis of carotid plaque rupture based on *in vivo* high resolution MRI. J of Biomech 2006;39:2611-2622.
19. Tang D, Teng Z, Canton G, Yang C, Ferguson M, Huang X, Zheng J, Woodard PK, Yuan C. Sites of rupture in human atherosclerotic carotid plaques are associated with high structural stresses. An *in vivo* MRI-based 3D fluid-structure interaction study. Stroke 2009;40:3258-3263.
20. Gao H, Long Q, Graves M, Gillard JH, Li Z. Carotid arterial plaque stress analysis using fluid–structure interactive simulation based on *in vivo* magnetic resonance images of four patients. J of Biomech 2009;42:1416-1423.
21. Hatsukami TS, Ross R, Polissar NL, Yuan C. Visualization of fibrous cap thickness and rupture in human atherosclerotic carotid plaque *in vivo* with high-resolution magnetic resonance imaging. Circulation 2000;102:959-964.
22. Yuan C, Zhang S, Polissar NL, Echelard D, Ortiz G, Davis WJ, Ellington E, Ferguson MS, Hatsukami TS. Identification of fibrous cap rupture with magnetic resonance imaging is highly associated with recent transient ischemic attack or stroke. Circulation 2002;105:181-185.
23. Mitsumori LM, Hatsukami TS, Ferguson MS, Kerwin WS, Cai J, Yuan C. *In vivo* accuracy of multisequence MR imaging for identifying unstable fibrous caps in advanced human carotid plaques. J Magn Reson Imaging 2003;17:410-420.
24. Kwee RM, Engelshoven JMA, Mess WH et al. Reproducibility of fibrous cap status assessment of carotid artery plaques by contrast-enhanced MRI. Stroke 2009;40:3017-3021.
25. Cai J, Hatsukami TS, Ferguson MS, Kerwin WS, Saam T, Chu B, Takaya N, Polissar NL, Yuan C. *In vivo* quantitative measurement of intact fibrous cap and lipid-rich necrotic core size in atherosclerotic carotid plaque: comparison of high-resolution, contrast-enhanced magnetic resonance imaging and histology. Circulation 2005;112:3437-3444.
26. Kerwin WS, Zhao X, Yuan C, Hatsukami TS, Maravilla KR, Underhill HR, Zhao X. Contrast-enhanced MRI of carotid atherosclerosis: dependence on contrast agent. J Magn Reson Imaging 2009;30:35-40.
27. Trivedi RA, U-King-Im J, Graves MJ, Horsley J, Goddard M, Kirkpatrick PJ, Gillard JH. MRI-derived measurements of fibrous-cap and lipid-core thickness: the potential for identifying vulnerable carotid plaques in vivo. Neuroradiology 2004;46:738-743.
28. Gao H, Long Q, Graves M, Gillard JH, Li Z. Study of Reproducibility of human arterial plaque reconstruction and its effects on stress analysis based on multispectral *in vivo* magnetic resonance imaging. J Magn Reson Imaging 2009;30:85-93.
29. Adame IM, van der Geest RJ, Wasserman BA, Mohamed MA, Reiber JHC, Lelieveldt BPF. Automatic segmentation and plaque characterization in atherosclerotic carotid artery MR images. MAGMA 2004;16:227-234.
30. Redgrave JN, Gallagher P, Lovett JK, Rothwell PM. Critical cap thickness and rupture in symptomatic carotid plaques: the Oxford plaque study. Stroke 2008;39:1722-1729.
31. Qian D, Bottomley PA. High-resolution intravascular magnetic resonance quantification of atherosclerotic plaque at 3T. J Cardiovasc Magn Reson 2012;14:20.
32. Saba L, Potters F, van der Lugt A, Mallarini G. Imaging of the fibrous cap in atherosclerotic carotid plaque. Cardiovasc Intervent Radiol 2010;33:681-689.
33. Gao H, Long Q. Effects of varied lipid core volume and fibrous cap thickness on stress distribution in carotid arterial plaques. J Biomech 2008;41:3053-3059.
34. Teng Z, Sadat U, Ji G, Zhu C, Young VE, Graves MJ, Gillard JH. Lumen irregularity dominates the relationship between mechanical stress condition, fibrous-cap thickness, and lumen curvature in carotid atherosclerotic plaque. J Biomech Eng 2011;133:034501-1-4.

35. Akyildiz AC, Speelman L, van Brummelen H, Gutiérrez MA, Virmani R, van der Lugt A, van der Steen AFW, Wentzel JJ, Gijsen FJH. Effects of intima stiffness and plaque morphology on peak cap stress. BioMed Eng OnLine 2011;10:25.
36. Speelman L, Akyildiz AC, den Adel B et al. Initial stress in biomechanical models of atherosclerotic plaques. J Biomech 2011;44:2376-2382.
37. U-King-Im JM, Tang TY, Patterson A et al. Characterization of carotid atheroma in symptomatic and asymptomatic patients using high resolution MRI. J Neurol Neurosurg Psychiatry 2008;79:905-912.
38. Young VE, Patterson AJ, Sadat U et al. Diffusion-weighted magnetic resonance imaging for the detection of lipid-rich necrotic core in carotid atheroma *in vivo*. Neuroradiology 2010;52:929-936.
39. Groen HC, van Walsum T, Rozie S et al. Three-dimensional registration of histology of human atherosclerotic carotid plaques to *in vivo* imaging. J Biomech 2010;43:2087-2092.
40. Coombs BD, Rapp JH, Ursell PC, Reilly LM, Saloner D. Structure of plaque at carotid bifurcation: high-resolution MRI with histological correlation. Stroke 2001;32:2516-2521.
41. Stöcker T, Vahedipour K, Pflugfelder D, Shah NJ. High-performance computing MRI simulations. Magn Reson Med 2010;64:186-193.
42. Yarnykh VL, Yuan C. $T_1$-insensitive flow suppression using quadruple inversion-recovery. Magn Reson Med 2002;48:899-905.
43. Yuan C, Kerwin WS, Ferguson MS, Polissar N, Zhang S, Cia J, Hatsukami TS. Contrast-enhanced high resolution MRI for atherosclerotic carotid artery tissue characterization. J Magn Reson Imaging 2002;15:62-67.
44. Wasserman BA, Casal SG, Astor BC, Aletras AH, Arai AE. Wash-in kinetics for gadolinium-enhanced magnetic resonance imaging of carotid atheroma. J Magn Reson Imaging 2005;21:91-95.
45. Robson MD, Gore JC, Constable RT. Measurement of the point spread function in MRI using constant time imaging. Magn Reson Med 1997;38:733-740.
46. Gudbjartsson H, Patz S. The Rician distribution of noisy MRI data. Magn Reson Med 1995;34:910-914.
47. Sijbers J, den Dekker AJ. Maximum likelihood estimation of signal amplitude and noise variance from MR data. Magn Reson Med 2004;51:586-594.
48. Stanisz GJ, Odrobina EE, Pun J, Escaravage M, Graham SJ, Bronskill MJ, Henkelman RM. $T_1$, $T_2$ relaxation and magnetization transfer in tissue at 3T. Magn Reson Med 2005;54:507-512.
49. Biasiolli L, Lindsay AC, Choudhury RP, Robson MC. *In vivo* $T_2$ mapping of atherosclerotic plaques in carotid arteries. J Cardiovasc Magn Res 2012;14:P134.
50. Clarke LP, Velthuizen RP, Camacho MA, Heine JJ, Vaidyanathan M, Hall LO, Thatcher RW, Silbiger ML. MRI segmentation: methods and applications. Magn Res Imag 1995;13:343-368.
51. Kass M, Witkin A, Terzopoulos D. Snakes: active contour models. Int J Comp Vision 1988;321-331.
52. van Engelen A, Niessen WJ, Klein S, Groen HC, Verhagen HJM, Wentzel JJ, van der Lugt A, de Bruijne M. Multi-feature-based plaque characterization in *ex vivo* MRI trained by registration to 3D histology. Phys Med Biol 2012;57:241-256.
53. Nieuwstadt HA, Akyildiz AC, Speelman L, Virmani R, van der Lugt A, van der Steen AFW, Wentzel JJ, Gijsen FJH. The influence of axial image resolution on atherosclerotic plaque stress computations. J Biomech 2013;46:689-695.
54. Hashemi RH, Bradley GW, Lisanti CJ. MRI: The basics. 400 pages. Lippincott Williams & Wilkins, Philadelphia, 2010.
55. Toussaint J, LaMuraglia GM, Southern JF, Fuster V, Kantor HL. Magnetic resonance images lipid, fibrous, calcified, hemorrhagic, and thrombotic components of human atherosclerosis *in vivo*. Circ 1996;94:932-938.
56. Morrisett J, Vick W, Sharma R, Lawrie G, Reardon M, Ezell E, Schwartz J, Hunter G, Gorenstein D. Discrimination of components in atherosclerotic plaques from human carotid endarterectomy specimens by magnetic resonance imaging *ex vivo.* Magn Reson Imaging 2003;21:465-474.
57. Degnan AJ, Young VE, Tang TY, Gill AB, Graves MJ, Gillard JH, Patterson AJ. *Ex vivo* study of carotid endarterectomy specimens: quantitative relaxation times within atherosclerotic plaque tissues. Magn Reson Imaging 2012;30:1017-1021.
58. Kwan RK, Evans AC, Pike GB. MRI simulation-based evaluation of image-processing and classification methods. IEEE Trans Med Imaging 1999;18:1085-1097.
59. Baum G, Menezes G, Helguera M. Simulation of high-resolution magnetic resonance images on the IBM Blue Gene/L supercomputer using SIMRI. Int J Biomed Imag 2011;2011:305968.

# Atherosclerotic plaque fibrous cap assessment under an oblique scan plane orientation in carotid MRI

3

**Abstract** | Carotid MRI is used to noninvasively assess atherosclerotic plaque fibrous cap (FC) status, which is closely related to ischemic stroke. Acquiring anisotropic voxels improves in-plane visualization, however, an oblique scan plane orientation could then obscure a FC (i.e., contrast below the noise level) and thus impair a reliable status assessment. To quantify this, we performed single-slice numerical simulations of a clinical 3.0T, 2D T1-weighted, black-blood, contrast-enhanced pulse sequence with various voxel dimensions: in-plane voxel size of 0.62 x 0.62 $mm^2$ and 0.31 x 0.31 $mm^2$, slice thickness of 1, 2, and 3 mm. Idealized plaque models (FC thickness of 0.5, 1, and 1.5 mm) were imaged at various scan plane angles (0° - 40° in steps of 10°), and the FC contrast was quantified. We found that when imaging thin FCs with anisotropic voxels, the FC contrast decreased when the scan plane orientation angle increased. However, a reduced in-plane voxel size at the cost of an increased slice thickness often led to enhanced FC contrast even in the presence of scan plane orientation angles of up to 40°. It can be concluded that while isotropic-voxel imaging eliminates the issue of scan plane obliqueness, it comes at the cost of reduced FC contrast, thus likely decreasing the reliability of FC status assessment in carotid MRI. If scan plane orientation obliquity at the slice of interest is moderate (<40°) or otherwise diminished through careful scan planning, voxel anisotropy could increase FC contrast and, in effect, increase the reliability of FC status assessment.

**This chapter is based on:** Nieuwstadt HA, van der Lugt A, Kassar ZAM, Breeuwer M, van der Steen AFW, Gijsen FJH. Atherosclerotic plaque fibrous cap assessment under an oblique scan plane orientation in carotid MRI. Quantitative Imaging in Medicine and Surgery 2014;4:216-224.

## INTRODUCTION

Carotid magnetic resonance imaging (MRI) is used to noninvasively image atherosclerotic plaques at the carotid bifurcation [1,2]. Of particular relevance are rupture-prone, vulnerable plaques, which are morphologically constituted of a large lipid-rich necrotic core (LRNC) covered by a thin fibrous cap (FC) [3,4]. Carotid plaque rupture is a major cause of transient ischemic attacks and ischemic strokes. The principal advantage of carotid MRI is its high soft-tissue contrast, which allows visualization of individual plaque components [5,6]. Black-blood, contrast-enhanced MRI sequences assist in FC visualization by enhancing the FC signal relative to the adjacent LRNC [7-9]. However, quantitative thickness measurements of FCs are prone to error due to the limited in-plane voxel size with respect to FC thickness [10-12]. Instead, a more straightforward and more reliable qualitative assessment of FC status (e.g., thick, thin, and ruptured) *in vivo* through carotid MRI has been proven to be clinically highly relevant [13-19].

Most clinical protocols today employ two-dimensional (2D) multi-slice sequences and acquire anisotropic voxels [20]. With anisotropic voxels, one can reach a smaller in-plane voxel size while maintaining the same voxel volume and signal-to-noise ratio (SNR) because of a relatively larger slice thickness [21]. Recent advances in 3D carotid MRI pulse sequence design enable isotropic-voxel plaque imaging [22]. Irrespective of the acquisition methodology (i.e., 2D or 3D), the choice of a relatively smaller in-plane voxel size will facilitate visualization of in-plane plaque features –such as thin fibrous caps– by reducing in-plane partial volume effects and point-spread function (PSF) signal spreading [10,11]. On the downside, axial partial volume effects in anisotropic voxels can not only be caused by plaque morphological variations in the slice-select direction within a slice [23,24], but also by an oblique scan plane orientation in relation to the localized FC orientation [25]. In clinical practice, the slice-select direction is typically aligned with the common carotid axis proximal to the bifurcation, using a localizer on an MR angiography scout scan in a sagittal view (Figure 1). A plaque could therefore be imaged at an angle, which, on top of the already limited in-plane resolution, might decrease FC contrast, thus preventing a reliable status assessment. A FC is often the smallest feature of a plaque, making it the most susceptible to obliquity artifacts. In addition, a plaque is usually present at locations with large geometrical variations or vessel angulations [26,27]. An oblique scan plane orientation affects carotid wall area measurements and could influence FC imaging [28]. Whether or not imaging at a certain angle would obscure a FC and prevent its differentiation from the adjacent LRNC depends on numerous factors, such as the scan protocol, tissue relaxation times, FC thickness, in-plane resolution, slice thickness, and SNR. In this

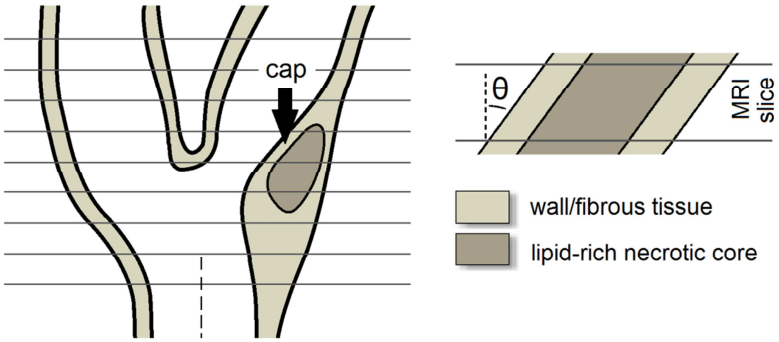


**Figure 1.** Illustration of a longitudinal cross-section of a carotid bifurcation and MRI slice positioning. Slices from 2D carotid MRI protocols are aligned along the common carotid artery axis, which can cause an oblique scan plane orientation (imaging at an angle $\theta$) at the slice covering the FC, obscuring the FC and impairing a reliable status assessment.

study, we took into account all of these factors for a typical 2D contrast-enhanced T1-weighted pulse sequence and quantified the influence of scan plane obliquity and voxel dimensions on FC contrast.

## METHODS

We performed numerical MRI simulations of a typical 2D carotid MRI protocol on idealized plaque models and varied the cap thickness ($d$), the acquired in-plane voxel size, the slice thickness ($\delta$), and the scan plane orientation angle ($\theta$). The advantage of MRI simulations is that they allow a perfectly controlled environment where single parameters can be varied, which is impracticable in a patient study. For a reliable FC status assessment, the FC contrast should be sufficiently high in relation to the adjacent LRNC contrast and the SNR. We therefore quantified the effects of the aforementioned parameters on FC contrast. Because we focused on scan plane obliquity, axial plaque morphological variations were not taken into account. Scan plane obliquity was confined to the direction of relevance: the short axis of the FC (i.e., the FC thickness direction). Each methodological step will now be discussed in more detail.

### Trigonometric model

Before commencing the MRI simulations, it was important to gain a feeling for the combined effects of $\theta$, $\delta$, and $d$ on the spatial distribution of FC tissue within a slice in the direction of angulation ($x$). We therefore created a simple analytical 1D

trigonometric model (Figure 2A). To maintain generality at this point, we confined ourselves to a geometrical analysis and focused on $\lambda(x)$: the fraction [%] of tissue at location $x$ occupied by the FC. Location B is given by $\delta\tan(\theta)$, and location C by $d/\cos(\theta)$. Also note that apparent FC thickness increased with a factor $1/\cos(\theta)$. These simple geometrical relationships helped explain some observations from the MRI simulations.

### Idealized plaque models

Three idealized carotid plaque models with a single LRNC and no other components were created, each with only a different FC thickness: 0.5, 1, and 1.5 mm. Although FCs of vulnerable carotid plaques can be thinner than 0.5 mm [10,29], we did not include these, because they would fall below the typical in-plane acquired voxel size of current clinical carotid MRI protocols, and would become obscured regardless of scan plane obliquity [16]. The lumen diameter (4.5 mm), outer wall diameter (9.0 mm), LRNC shape, LRNC size (14 mm$^2$), and LRNC width (2.4 mm) of the idealized models were kept unaltered and were based on typical dimensions of diseased carotid arteries. The modeled plaque tissues were fibrous tissue, LRNC, and the sternocleidomastoid muscle (used as background), and were assigned $T_1$ relaxation

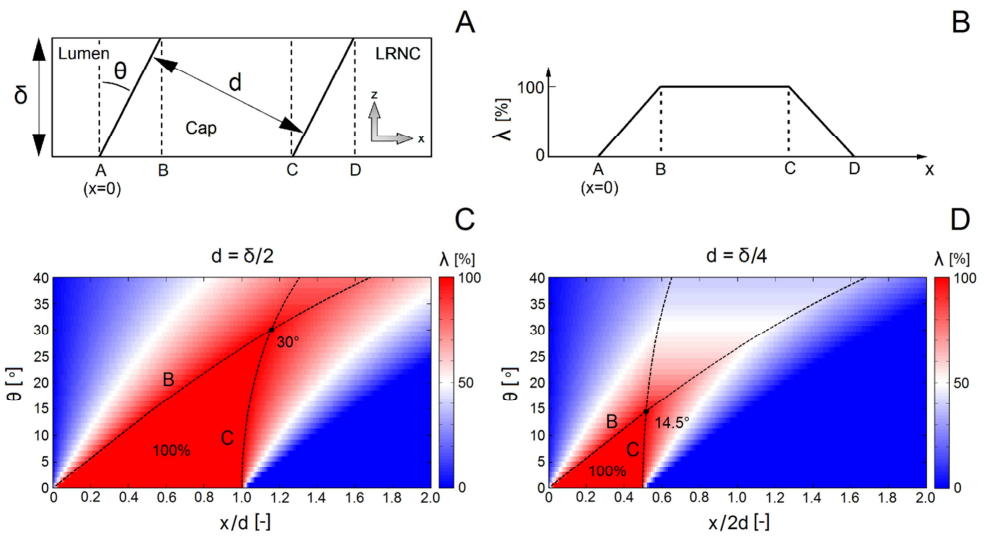


**Figure 2.** (A) A 1-dimensional trigonometric model illustrates the effects of the scan plane angle ($\theta$), slice thickness $\delta$, and cap thickness $d$ on $\lambda(x)$: the fraction of tissue occupied by the FC within a slice. (B) Sketch of $\lambda(x)$ for a certain $\theta$, (C) $\lambda(x,\theta)$ for $d = \delta/2$, and (D) $\lambda(x,\theta)$ for $d = \delta/4$.

times of 680 ms, 1220 ms, and 1412 ms respectively, and a fixed $T_2$ of 50 ms for the MRI simulations [11]. The models were angulated from 0° to 40° in steps of 10° with respect to the axial axis. The direction of the FC thickness was aligned with the phase direction in the MRI simulations and likewise was the direction of scan plane obliquity. This choice was made because Gibbs ringing artifacts manifesting predominantly in the frequency (measurement) direction could influence tissue intensity at the edge of the lumen [11,28].

### MRI simulations

A standard clinically applied 3.0T, 2D T1-weighted turbo spin-echo, contrast-enhanced, black-blood pulse sequence used for FC imaging was implemented in the Jülich Extensible MRI Simulator (JEMRIS) [30]. A detailed description of this particular implementation including an evaluation with patient images can be found in [11]. The simulated pulse sequence used non-selective radio frequency pulses, which eliminated the need for slice selection and spoiler gradients, resulting in single slice simulations. The repetition and echo timings were 800 ms and 10 ms, respectively. The simulated sequence covered a field-of-view of 37 x 37 $mm^2$ with a matrix size of 60 x 60 which yielded the same in-plane acquisition voxel size as the original clinical protocol: 0.62 x 0.62 $mm^2$. The reduced field-of-view was obtained by decreasing the number of shots while keeping both the turbo-spin echo factor (equal to 10) and k-space filling order (centric) unaltered. A reconstructed voxel size of 0.31 x 0.31 $mm^2$ was achieved after zero-padding of the k-space prior to Fourier transforming. The slice thickness of the original clinical protocol was $\delta = 2$ mm. For this study, we additionally simulated slice thicknesses of 1 and 3 mm. A modified protocol with a smaller in-plane acquired voxel size of 0.31 x 0.31 $mm^2$ (0.16 x 0.16 $mm^2$ reconstructed) was also simulated. Such changes in voxel sizes would affect the SNR and/or scan time in clinical systems according to the SNR equation. Because our simulations yielded noise-free images, our FC contrast findings can be assessed post-hoc for any arbitrary SNR levels. The actual measure for resolving small features in MRI is the PSF, and its importance is the reason we performed MRI simulations instead of simply geometrical re-sampling [11]. The full-width at half-maximum of the PSF in the phase direction (which was the direction of angulation) in the image space was 1.1 mm for the original 0.62 x 0.62 $mm^2$ protocol and 0.55 mm for the modified 0.31 x 0.31 $mm^2$ protocol. The simulations were performed with a high spin-discretization, with an average of ~8000 simulated spins per voxel. Black-blood imaging was simulated by defining no magnetization of the luminal area. Motion artifacts were not simulated.

### Analysis

For each resulting noise-free (1/SNR = 0) simulated carotid MR image, the FC contrast was computed. The FC contrast was defined as the maximum FC intensity relative to the minimum intensity of the adjacent LRNC, and therefore computed with the following contrast-to-tissue equation: ($I_{cap,max}$ - $I_{LRNC,min}$) / $I_{LRNC,min}$ [31]. Note that the theoretical upper-limit of the FC contrast, $C_{FC,max}$, can be derived from the repetition time (TR) and the apparent $T_1$ relaxation times (tissues had identical $T_2$ times) of LRNC and fibrous tissues:

$$C_{FC,max} = \frac{\exp\left(\frac{-TR}{T1_{LRNC}}\right) - \exp\left(\frac{-TR}{T1_{fibrous}}\right)}{1 - \exp\left(\frac{-TR}{T1_{LRNC}}\right)}. \quad (1)$$

With the modeled tissue $T_1$ relaxation times, the theoretically maximum FC contrast with no partial volume effects or PSF signal spreading was equal to 0.44. The SNR was defined as the reciprocal of the coefficient of variation. This definition enabled a direct comparison between FC contrast and 1/SNR, because if the FC contrast would be lower than 1/SNR (i.e., the relative noise level), the FC would likely be obscured. We also asked one (blinded) MRI reader (Z.K.) to measure the FC thickness on a set of images with $\delta$ = 2 mm and with added noise (SNR = 16.7), in the situation where the FC was not judged as obscured by that reader. The images were presented in randomized order on five separate occasions.

## RESULTS

### Trigonometric model

We first studied our 1D geometrical model. In Figure 2, we graph two cases: $d = \delta/2$ (Figure 2C) and $d = \delta/4$ (Figure 2D) for $\theta$ = 0° to 40°. We defined a critical angle, $\theta_c = \sin^{-1}(d/\delta)$, when B = C (Figure 2B). This critical angle represents the smallest angle at which less than 100% at any location $x$ is occupied by FC tissue. For $d = \delta/2$, $\theta_c$ = 30°, and for $d = \delta/4$, $\theta_c$ = 14.5°. So, interestingly, in the limit of a hypothetical in-plane voxel size $\ll d$, no obscurement of the FC should occur for $\theta < 30°$ in the case of $d = \delta/2$. However, for $d = \delta/4$, the critical angle dropped to only 14.5°. Because this is just a geometrical analysis, the critical angle –a simple

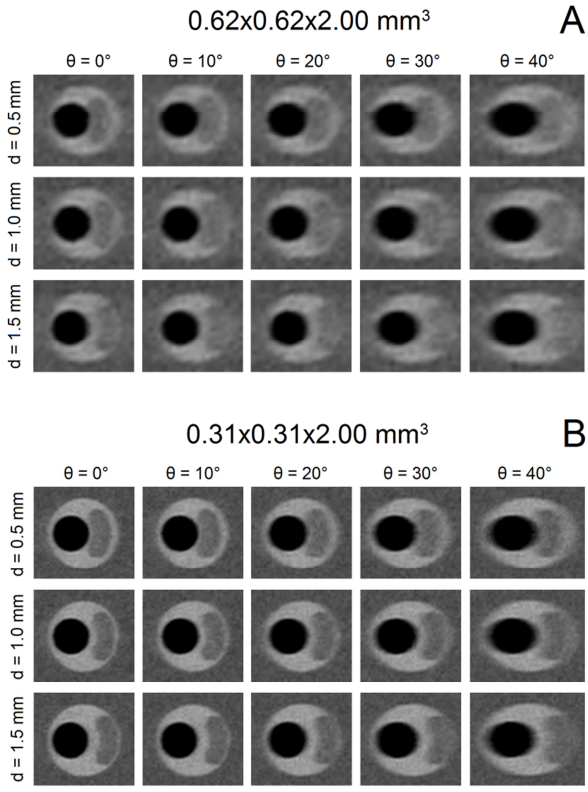


**Figure 3.** Simulated MR images for the case of $\delta = 2$ mm. Each plaque model with different FC thicknesses ($d = 0.5$, 1, and 1.5 mm) is imaged at five angles (0° to 40°). (A) Voxel size of 0.62 x 0.62 x 2.00 mm³, (B) voxel size of 0.31 x 0.31 x 2.00 mm³. Rician distributed noise was added to these example images to yield a typical SNR of 16.7 [11].

indicative but rather strict measure– does not directly translate to MR imaging, where the in-plane voxel size (typically ~$d$), PSF, and SNR play significant roles as well.

## MRI simulations

Simulated MR images for the case of $\delta = 2$ mm are shown in Figure 3. The scan plane obliquity angle $\theta$ was found to have a strong effect on the appearance of FCs in certain configurations of the parameters studied. A cap of 0.5 mm thickness was already indistinguishable at $\theta = 0°$ for an in-plane acquired voxel size of 0.62 x 0.62 mm², while a cap of 1.0 mm (hardly visible at $\theta = 0°$) became obscured at 40°. For an acquired in-plane voxel size of 0.31 x 031 mm², a cap of 0.5 mm, clearly visible at $\theta = 0°$, was obscured at $\theta = 40°$. A FC of 1.5 mm thickness remained visible up to

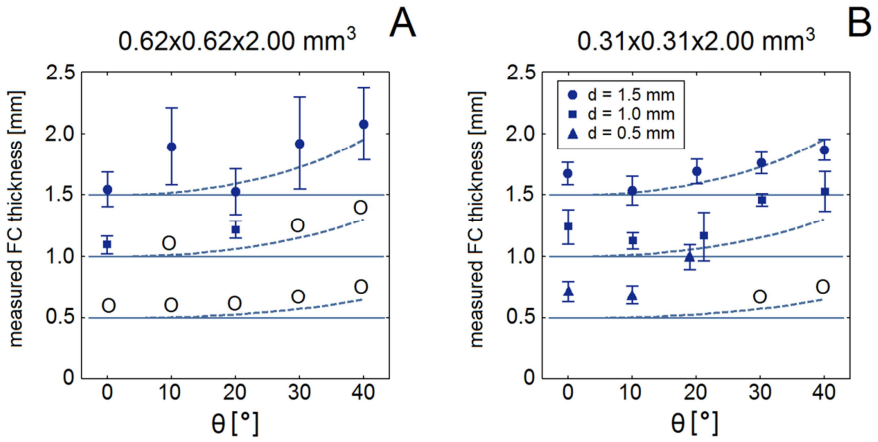


**Figure 4.** Manual FC thickness measurements ($n = 5$, mean ± standard deviation indicated) on images in Figure 3 (SNR = 16.7, $\delta = 2$ mm). The dotted grey curves represent $d/\cos(\theta)$: the apparent FC thickness. FCs judged as obscured by the MRI reader are indicated with an O ('obscured') and no thickness measurements were performed. (A) Data for a voxel size of 0.62 x 0.62 x 2.00 mm$^3$, (B) data for a voxel size of 0.31 x 0.31 x 2.00 mm$^3$. Legend in (B) also applies to (A).

$\theta = 40°$. In general, thicker FCs appeared to be largely insensitive to scan plane obliquity, especially when imaged at the higher in-plane resolution. Increasing $\theta$ led to a reduction in FC contrast. FC contrast was clearly higher for thicker caps and for the 0.31 x 0.31 mm$^2$ protocol, due to reduced in-plane partial volume effects.

The results of the manual FC thickness measurements (for the case with $\delta = 2$ mm and SNR = 16.7) are shown in Figure 4. In general, the overestimation of FC thickness increased for increasing $\theta$. For example, the thickness of a 1.5 mm FC was measured as 1.55 ± 0.14 mm for $\theta = 0°$, and as 2.08 ± 0.29 mm for $\theta = 40°$ with the original 0.62 x 0.62 mm$^2$ protocol. For the modified 0.31 x 0.31 mm$^2$ protocol, the thickness of a FC of 1.5 mm was measured as 1.67 ± 0.09 mm for $\theta = 0°$, and as 1.87 ± 0.08 mm for $\theta = 40°$.

The FC contrast as a function of $\theta$ for all plaque models and scan parameters with 1/SNR = 0 is shown in Figure 5. FC contrast became less dependent on $\theta$ for larger $d$, smaller $\delta$, or a larger in-plane voxel size (thus approaching isotropic voxels). In fact, FC contrast even slightly increased for increasing $\theta$ in the $\delta = 1$ mm case. In general, a thicker FC, or the use of a high in-plane resolution (anisotropic) protocol, led to significantly increased FC contrast. These two factors, in many cases, outweighed the influence of scan plane obliquity on FC contrast. Figure 5 provides quantitative data on how the FC contrast depends on the studied scan parameters. With the SNR

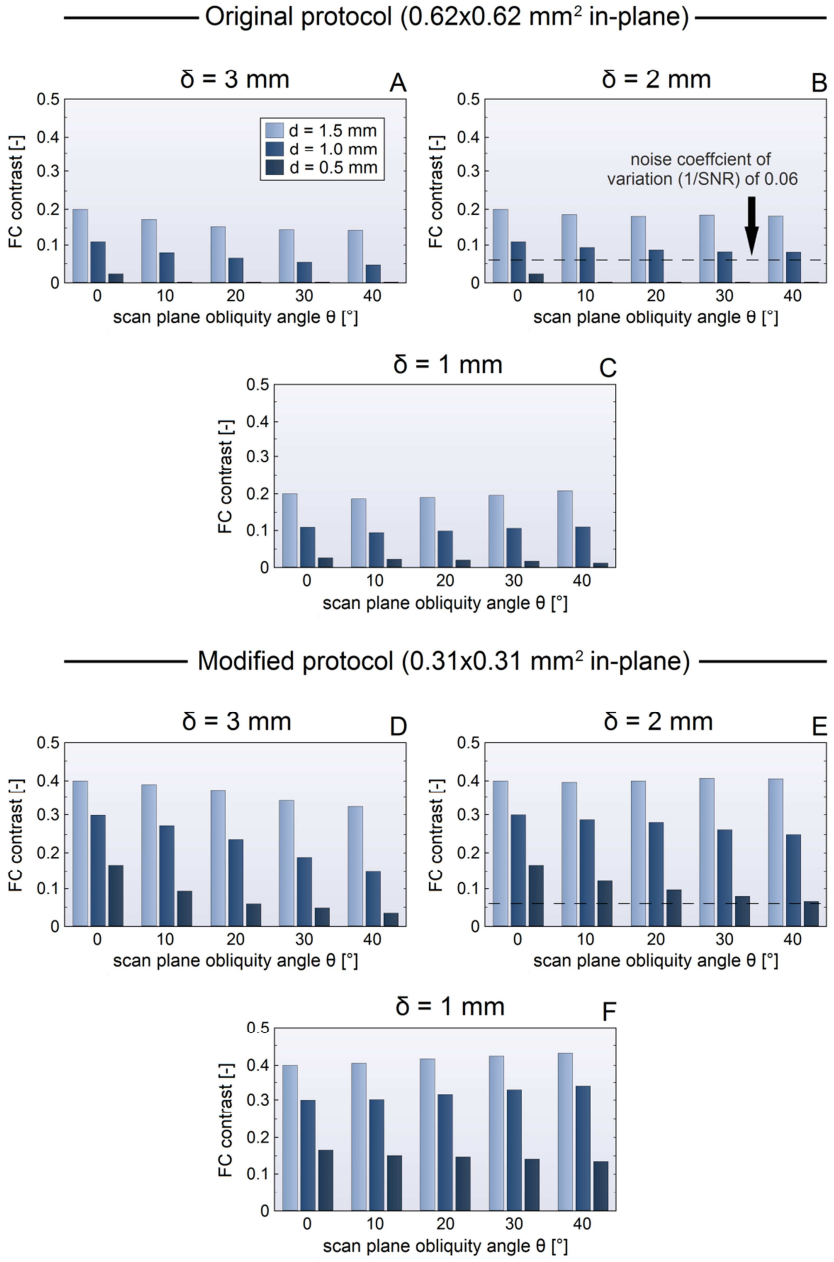


**Figure 5.** FC contrast is shown as a function of the scan plane angle ($\theta$). Each graph (A-F) contains data for a specific slice thickness ($\delta$) and in-plane acquired voxel size. Legend in (A) applies to all six graphs. The dotted horizontal line in (B,E) represents the 1/SNR line for the example SNR = 16.7.

and imaging parameters known, it is now possible to determine which FCs would become indistinguishable. For example, consider the case where SNR = 16.7 and $\delta$ = 2 mm. When imaged with an acquired voxel size of 0.62 x 0.62 x 2.00 mm$^3$ at $\theta$ = 40°, the contrasts of FCs of 0.5 mm and 1.0 mm thickness were in the order of 1/SNR (or lower), shown as the dotted line in Figure 5B. This was also true for a FC of 0.5 mm imaged with an acquired voxel size of 0.31 x 0.31 x 2.00 mm$^3$ at $\theta$ = 40°. These FCs would likely be obscured, preventing a reliable qualitative assessment of their status. At $\theta$ = 0°, only the contrast of a FC of 0.5 mm thickness imaged with an acquired voxel size of 0.62 x 0.62 x 2.00 mm$^3$ fell below 1/SNR. And indeed, these findings corresponded with what we previously determined from Figure 3, and were largely in line with the MRI reader decisions.

## DISCUSSION

We investigated the influence of an oblique scan plane orientation in combination with voxel dimensions on FC contrast (i.e., FC intensity relative to the adjacent LRNC) for a typical 2D clinical T1-weighted, black-blood, contrast-enhanced carotid MRI protocol. The use of MRI simulations allowed full scan parameter control and precise knowledge of the plaque geometry, FC thickness, and tissue relaxation times.

Using higher voxel anisotropy or imaging thinner FCs led to a larger influence of scan plane obliquity on FC contrast. The latter is of particular concern because the thinner the FC gets, the more vulnerable the plaque becomes [32]. Nevertheless, our simulations showed that the in-plane voxel size and the FC thickness strongly determine FC contrast, and, most interestingly, often outweigh scan plane obliquity for angles up to 40°. FC signal intensity strongly increases if the FC is covered by more voxels when considering out-of-voxel PSF signal spreading. Our findings for different in-plane acquired voxel sizes at no scan plane obliquity ($\theta$ = 0°) are thus already interesting in and of themselves. We found that, on average, the measured FC thickness increased for increasing $\theta$, as expected from the increase in apparent thickness. An oblique scan plane orientation (or a larger in-plane voxel size) decreases intensity gradients at plaque component interfaces (blurred edges), which affects segmentation accuracy [33]. An elaborate analysis of the overestimation of mm-scale thickness features under scan plane orientation obliquity is given in [28]. All FCs with a contrast <1/SNR were judged by the MRI reader as obscured while all FCs with a contrast >2/SNR were judged as visible. Out-of-voxel PSF signal spreading caused FC contrast to slightly increase with $\theta$ in the cases where $d \geq \delta$. When imaging any FC at an angle with a finite slice thickness $\delta$, the total amount of FC tissue present in the slice (the integral of $\lambda(x)$) increases. If the FC intensity profile would be modeled as

the convolution of the PSF($x$) and $\lambda(x)$, one would indeed find a slight increase in peak FC intensity with respect to $\theta = 0°$ for the combinations of parameters for which an increase in FC contrast was observed in the MRI simulations. When approaching near isotropic voxels in clinical systems, PSF signal spreading in the slice-select direction or slice overlapping would attenuate this FC intensity enhancement. For clinically applied MRI, alterations in the field-of-view and/or voxel dimensions impact the total scan time and/or SNR (not FC contrast, being a relative measure) according to the SNR equation. An advantage of our methodology was that the simulated images were free of noise, which allows the assessment of FC contrast data reported in our study for arbitrary SNR levels.

Isotropic resolution carotid MR imaging –which is increasingly being used– renders the issue of scan plane obliquity obsolete and it is currently claimed to be favorable for imaging small features [22,23]. However, our simulations suggest otherwise: isotropic imaging can actually lead to reduced FC contrast when the FC thickness is less than the PSF width, which is usually the case. Because FC thickness is a predominantly in-plane feature, anisotropic voxels can provide higher FC contrast. While we found that an oblique scan plane orientation reduces FC contrast, we observed that increasing the in-plane resolution (while decreasing the slice thickness) still yielded considerably higher FC contrast even at moderate (<40°) scan plane obliquity. This supports the use of anisotropic voxels for FC imaging. In 3D sequences, the number of slice-select phase encoding steps can be lowered to achieve anisotropic imaging, which could also extend to a reduction in scan time and/or noise. We also demonstrated that a properly aligned scan direction at the slice containing the plaque can significantly increase FC contrast, which calls for further investigation into the improvement of scan planning in carotid MRI for FC status assessment in clinical practice, and into the possibility of *a priori* estimation of FC orientation. Interestingly, our simulations showed that the combination of merely geometrical angulations and finite voxel imaging can obscure even relatively thick FCs (>0.5 mm) in carotid MRI. This obscurement could lead to a false evaluation of FC absence (or thinning) in potentially stable lesions.

A number of assumptions and simplifications were made. Motion artifacts [34] or influences from imperfect blood signal suppression [35], which could contribute to obscuring the FC in addition to scan plane obliquity, were not modeled. Furthermore, a uniform $B_1$ homogeneity was assumed with fixed repetition and echo times in the protocol, and $T_1$ relaxation times for FC and LRNC tissue were not varied. Note that while these parameters influenced FC contrast (equation 1), they did not affect the relationship with scan plane angle. In the simulations, perfect (uniform) slice excitation was assumed with no influence from other slices (i.e., no cross-talk in case of 2D

protocols, or no axial PSF or Gibbs ringing effects in case of 3D protocols). Such effects were not simulated because they are highly protocol-specific. We did not model axial FC morphological variations within a slice. These variations can be substantial, as reported in previous studies [22-24], and should be subject of further investigation. Plaque tissues were modeled as homogeneous, given the large differences in biological structure between FCs and LRNCs [3]. A FC is typically well defined in contrast-enhanced MRI as the consequence of different relaxation times of fibrous tissue with gadolinium-uptake and the underlying LRNC [8,9]. However, the FC-LRNC interface is not always sharp-edged as assumed in our study. Because the FC thickness measurements were performed on idealized models, those results cannot be directly translated to actual *in vivo* MRI. The advantage of MRI simulations was that we could investigate solely scan plane obliquity without obstructions from any of the aforementioned effects; however, these matters could also influence FC status assessment in practice.

## CONCLUSIONS

While isotropic-voxel carotid MRI eliminates the issue of scan plane obliqueness, the relatively larger in-plane voxel size could cause FC contrast reduction. In our simulations, a smaller in-plane voxel size at the cost of a larger slice thickness (i.e., voxel anisotropy) often enhanced FC contrast even in the presence of scan plane orientation angles up to 40°. If scan plane orientation obliquity at the slice of interest is moderate (<40°) or otherwise diminished through careful scan planning, the acquisition of anisotropic voxels could significantly enhance FC contrast which, in effect, could improve the reliability of FC status assessment.

## ACKNOWLEDGEMENTS

We would like to thank Tom Geraedts (Philips Healthcare, Best, the Netherlands) for useful discussions.

## REFERENCES

1. Toussaint J, LaMuraglia GM, Southern JF, Fuster V, Kantor HL. Magnetic resonance images lipid, fibrous, calcified, hemorrhagic, and thrombotic components of human atherosclerosis in vivo. Circ 1996;94:932-938.
2. Cai JM, Hatsukami TS, Ferguson MS, Small R, Polissar NL, Yuan C. Classification of human carotid atherosclerotic lesions with in vivo multicontrast magnetic resonance imaging. Circ 2002;106:1368-1373.

3. Virmani R, Burke AP, Farb A, Kolodgie FD. Pathology of the vulnerable plaque. J Am Coll Cardiol 2006;47:C13-18.
4. Li ZY, Howarth SP, Tang T, Gillard JH. How critical is fibrous cap thickness to carotid plaque stability? A flow-plaque interaction model. Stroke 2006;37:1195-1199.
5. Saam T, Ferguson MS, Yarnykh VL, Takaya N, Xu D, Polissar NL, Hatsukami TS, Yuan C. Quantitative evaluation of carotid plaque composition by *in vivo* MRI. Arterioscler Thromb Vasc Biol 2005;25:234-239.
6. Underhill HR, Hatsukami TS, Fayad AZ, Fuster V, Yuan C. MRI of carotid atherosclerosis: clinical implications and future directions. Nat Rev Cardiol 2010;7:165–173.
7. Yuan C, Kerwin WS, Ferguson MS, Polissar N, Zhang S, Cai J, Hatsukami TS. Contrast-enhanced high resolution MRI for atherosclerotic carotid artery tissue characterization. J Magn Reson Imaging 2002;15:62-67.
8. Wasserman BA, Smith WI, Trout HH, Cannon RO, Balaban RS, Arai AE. Carotid artery atherosclerosis: *in vivo* morphologic characterization with gadolinium-enhanced double-oblique MR imaging initial results. Radiology 2002;223:566-573.
9. Cai J, Hatsukami TS, Ferguson MS, Kerwin WS, Saam T, Chu B, Takaya N, Polissar NL, Yuan C. *In vivo* quantitative measurement of intact fibrous cap and lipid-rich necrotic core size in atherosclerotic carotid plaque: comparison of high-resolution, contrast-enhanced magnetic resonance imaging and histology. Circulation 2005;112:3437-3444.
10. Redgrave JN, Gallagher P, Lovett JK, Rothwell PM. Critical cap thickness and rupture in symptomatic carotid plaques: the Oxford plaque study. Stroke 2008;39:1722-1729.
11. Nieuwstadt HA, Geraedts TR, Truijman MT, Kooi ME, van der Lugt A, van der Steen AF, Wentzel JJ, Breeuwer M, Gijsen FJ. Numerical simulations of carotid MRI quantify the accuracy in measuring atherosclerotic plaque components *in vivo*. Magn Reson Med 2014;72:188-201.
12. Schär M, Kim WY, Stuber M, Boesiger P, Manning WJ, Botnar RM. The impact of spatial resolution and respiratory motion on MR imaging of atherosclerotic plaque. J Magn Reson Imaging 2003;17:538-544.
13. Hatsukami TS, Ross R, Polissar NL, Yuan C. Visualization of fibrous cap thickness and rupture in human atherosclerotic carotid plaque *in vivo* with high-resolution magnetic resonance imaging. Circulation 2000;102:959-964.
14. Takaya N, Yuan C, Chu B, Saam T, Underhill H, Cai J, Tran N, Polissar NL, Isaac C, Ferguson MS, et al. Association between carotid plaque characteristics and subsequent ischemic cerebrovascular events: a prospective assessment with MRI--initial results. Stroke 2006;37:818-823.
15. Yuan C, Zhang SX, Polissar NL, Echelard D, Ortiz G, Davis JW, Ellington E, Ferguson MS, Hatsukami TS. Identification of fibrous cap rupture with magnetic resonance imaging is highly associated with recent transient ischemic attack or stroke. Circulation 2002;105:181-185.
16. Kwee RM, van Engelshoven JM, Mess WH, ter Berg JW, Schreuder FH, Franke CL, Korten AG, Meems BJ, van Oostenbrugge RJ, Wildberger JE, Kooi ME. Reproducibility of fibrous cap status assessment of carotid artery plaques by contrast-enhanced MRI. Stroke 2009;40:3017-3021.
17. Kwee RM, van Oostenbrugge RJ, Mess WH, Prins MH, van der Geest RJ, ter Berg JW, Franke CL, Korten AG, Meems BJ, van Engelshoven JM, Wildberger JE, Kooi ME. MRI of carotid atherosclerosis to identify TIA and stroke patients who are at risk of a recurrence. J Magn Reson Imaging 2013;37:1189-1194.
18. Saba L, Potters F, van der Lugt A, Mallarini G. Imaging of the fibrous cap in atherosclerotic carotid plaque. Cardiovasc Intervent Radiol 2010;33:681-689.
19. Ota H, Yu W, Underhill HR, Oikawa M, Dong L, Zhao X, Polissar NL, Neradilek B, Gao T, Zhang Z, Yan Z, Guo M, Zhang Z, Hatsukami TS, Yuan C. Hemorrhage and large lipid-rich necrotic cores are independently associated with thin or ruptured fibrous caps: an *in vivo* 3T MRI study. Arterioscler Thromb Vasc Biol 2009;29:1696-1701.
20. Wang J, Balu N, Canton G, Yuan C. Imaging biomarkers of cardiovascular disease. J Magn Reson Imaging 2010;32:502–515.
21. Luk-Pat GT, Gold GE, Olcott EW, Hu BS, Nishimura DG. High-resolution three-dimensional *in vivo* imaging of atherosclerotic plaque. Magn Reson Med 1999;42:762-771.
22. Balu N, Yarnykh VL, Chu B, Wang J, Hatsukami T, Yuan C. Carotid plaque assessment using fast 3D isotropic resolution black-blood MRI. Magn Reson Med 2011;65:627-637.
23. Balu N, Chu B, Hatsukami TS, Yuan C, Yarnykh VL. Comparison between 2D and 3D high-resolution black-blood techniques for carotid artery wall imaging in clinically significant atherosclerosis. J Magn Reson Imaging 2008;27:918-924.

24. Coombs BD, Rapp JH, Ursell PC, Reilly LM, Saloner D. Structure of plaque at carotid bifurcation: high-resolution MRI with histological correlation. Stroke 2001;32:2516-2521.
25. Balu N, Kerwin WS, Chu B, Liu F, Yuan C. Serial MRI of carotid plaque burden: influence of subject repositioning on measurement precision. Magn Reson Med 2007;57:592-599.
26. Lee SW, Antiga L, Spence JD, Steinman DA. Geometry of the carotid bifurcation predicts its exposure to disturbed flow. Stroke 2008;39:2341-2347.
27. Slager CJ, Wentzel JJ, Gijsen FJ, Schuurbiers JC, van der Wal AC, van der Steen AF, Serruys PW. The role of shear stress in the generation of rupture-prone vulnerable plaques. Nat Clin Pract Cardiovasc Med 2005;2:401-407.
28. Antiga L, Wasserman BA, Steinman DA. On the overestimation of early wall thickening at the carotid bulb by black blood MRI, with implications for coronary and vulnerable plaque imaging. Magn Reson Med 2008;60:1020-1028.
29. Qian D, Bottomley PA. High-resolution intravascular magnetic resonance quantification of atherosclerotic plaque at 3T. J Card Magn Reson 2012;14:20.
30. Stöcker T, Vahedipour K, Pflugfelder D, Shah NJ. High-performance computing MRI simulations. Magn Reson Med 2010;64:186-193.
31. Li B, Dong L, Chen B, Ji S, Cai W, Wang Y, Zhang J, Zhang Z, Wang X, Fang J. Turbo fast three-dimensional carotid artery black-blood MRI by combining three-dimensional MERGE sequence with compressed sensing. Magn Reson Med. 2013;70:1347-1352.
32. Loree HM, Kamm RD, Stringfellow RG, Lee RT. Effects of fibrous cap thickness on peak circumferential stress in model atherosclerotic vessels. Circ Res 1992;71:850-858.
33. Greenman RL, Wang X, Ngo L, Marquis RP, Farrar N. An assessment of the sharpness of carotid artery tissue boundaries with acquisition voxel size and field strength. Magn Reson Imaging 2008;26:246-253.
34. Boussel L, Herigault G, de la Vega A, Nonent M, Douek PC, Serfaty JM. Swallowing, arterial pulsation, and breathing induce motion artifacts in carotid artery MRI. J Magn Reson Imaging 2006;23:413-415.
35. Dong L, Wang J, Yarnykh VL, Underhill HR, Neradilek MB, Polissar N, Hatsukami TS, Yuan C. Efficient flow suppressed MRI improves interscan reproducibility of carotid atherosclerosis plaque burden measurements. J Magn Reson Imaging 2010;32:452-458.

# A computer-simulation study on the effects of MRI voxel dimensions on carotid plaque lipid-core and fibrous cap segmentation and stress modeling

# 4

**Abstract** | The benefits of a decreased slice thickness in carotid MRI for atherosclerotic plaque component quantification accuracy and biomechanical peak cap stress analysis have not yet been investigated because of practical limitations. In order to provide a methodology that allows such an investigation, numerical simulations of a T1-weighted, contrast-enhanced, slice-selective 2D MRI sequence were employed. Both the slice thickness (2 mm, 1 mm, and 0.5 mm) and the in plane acquired voxel size (0.62 x 0.62 $mm^2$ and 0.31 x 0.31 $mm^2$) were varied. This virtual MRI approach was applied to 8 histology-based 3D patient carotid atherosclerotic plaque models. We found that a decreased slice thickness did not result in major improvements in lumen, vessel wall, and lipid-rich necrotic core size measurements. At 0.62 x 0.62 $mm^2$ in-plane, only a 0.5 mm slice thickness resulted in improved minimum fibrous cap thickness measurements (a 2 – 3 fold reduction in measurement error) and only marginally improved peak cap stress computations. Acquiring voxels of 0.31 x 0.31 $mm^2$ in-plane, however, led to either similar or significantly larger improvements in plaque component quantification and computed peak cap stress. In conclusion, this study provides evidence that for currently used 2D carotid MRI protocols, a decreased slice thickness might not be more beneficial for plaque measurement accuracy than a decreased in-plane voxel size. The MRI simulations performed indicate that not a reduced slice thickness, but the acquisition of anisotropic voxels with a relatively smaller in-plane voxel size improves carotid plaque quantification and peak cap stress computation.

**This chapter is based on:** Nieuwstadt HA, Kassar ZAM, van der Lugt A, Breeuwer M, van der Steen AFW, Wentzel JJ, Gijsen FJH. A computer-simulation study on the effects of MRI voxel dimensions on carotid plaque lipid-core and fibrous cap segmentation and stress modeling. *PLOS ONE*, accepted, 2015.

## INTRODUCTION

Carotid magnetic resonance imaging (MRI) is an established modality to image atherosclerotic plaques at the common carotid artery bifurcation [1-3]. MRI is the only currently available, noninvasive modality to visualize the fibrous cap (FC) and components such as the lipid-rich necrotic core (LRNC) with high contrast, allowing for plaque segmentation [4-6]. Segmentation data can be used to quantify plaque components and to compute the peak cap stress –a biomechanical marker for rupture risk– via finite element analysis (FEA) [7-10].

While three-dimensional (3D) carotid MRI protocols with isotropic spatial resolution have recently been introduced [11-14], the majority of current clinical protocols remain slice-selective, two-dimensional (2D) sequences [15]. In 2D protocols, anisotropic voxels are acquired with a slice thickness larger than the in-plane acquired voxel size. A slice thickness of 2–3 mm is most commonly used [3,16,17]. Acquiring anisotropic voxels can improve the signal-to-noise ratio (SNR) and/or decrease the total scan time while maintaining a small in-plane voxel size to facilitate visualization in a cross-sectional plane [6,18]. It is commonly argued that a decreased slice thickness (or isotropic acquisition) would improve imaging by reducing the influence of axial intravoxel partial volume effects caused by axial morphological variations of a plaque within a slice in the slice-select direction [12,17,19]. However, decreasing the slice thickness requires a sacrifice in SNR and/or scan time, so careful considerations are called for when making such trade-offs [20]. For example, a study by Balu et al. found no difference in measurements of the lumen area, vessel wall area and wall thickness when comparing protocols with slice thicknesses of 0.7 mm (3D, isotropic) and 2 mm (2D, anisotropic) [12]. For more crucial, vulnerable plaque parameters like LRNC size, minimum FC thickness, and peak cap stress, the potential benefits of a decreased slice thickness in MRI have not been investigated.

The reason why such investigations have not yet been performed lies in the fact that they require a methodology that provides a direct comparison with a ground truth (i.e., the exact underlying geometry) and where the isolated influence of changes in the acquired voxel dimensions can then be studied in detail. A controlled environment would be needed where other parameters (e.g., noise, motion, and image registration) are kept unaltered and where scan duration, due to running many protocols, does not pose severe practical limitations on patient inclusion. During recent years, numerous studies demonstrated that numerical "virtual" MRI is an effective new methodology to achieve such a controlled environment [21-23]. Through modeling MR physics (i.e., solving the Bloch equations) guided by scanner-properties, the input geometry with pre-assigned MR properties (e.g., magnetization, relaxation times), and the pulse sequence, one can computer simulate an *in vivo* MR image. Due to advances in

computer power and the developments of open-source software packages, MRI simulations are increasingly being used to answer clinical image-based questions [23-25].

In a previous study, we performed numerical simulations of a 2D, contrast-enhanced, T1-weighted carotid MRI protocol [25] using the Jülich Extensible MRI Simulator (JEMRIS) [26]. In this current study we adopted a similar approach. We created a set of 3D ground truth carotid plaque models from histological patient data and performed numerical MRI simulations. We focused on slice thickness and intravoxel partial volume effects which, in turn, affect segmentation accuracy. We quantified the impact of a decreased slice thickness on (1) the measurement error of the lumen area, vessel wall area, LRNC area, and minimum FC thickness and on (2) the error in computed peak cap stress. To study the combined influence of in-plane resolution and slice thickness, we repeated the aforementioned investigation with a reduced in-plane voxel size.

## METHODS

### Histology

Histological data were used to create a set of sufficiently realistic 3D computer models of carotid plaque geometries to serve as ground truth input sample models for the MRI simulations. Atherosclerotic specimens, obtained at carotid endarterectomy, were decalcified and embedded in paraffin for histological processing. Cross-sectional slices of 5 μm thickness were obtained at 1 mm intervals, and an Elastica van Gieson stain was applied. Histological data from eight (n = 8) patients met our requirements, which were: (1) the presence of at least three successive, largely undeformed and undamaged, cross sections which (2) covered at least one large LRNC with a FC. Micron resolution digitized microscopy images of the histology cross-sections were manually segmented for LRNC and fibrous tissue.

### Geometry reconstructions

The eight 3D patient plaque models were constructed by vertically stacking the three histology segmentations with intervals of 1 mm and interpolating the contour data in the axial direction ($z$-direction) with smooth surfaces defined by non-uniform rational basis splines (Gambit, Fluent Inc., ANSYS, Canonsburg, Pennsylvania, USA) [27], as shown in Figure 1. The contours were aligned by the luminal center of gravity. Prior to simulating MRI, the ground truth models were computationally inflated to 100 mmHg using 3D FEA (see section “Finite Element Analysis”). This deformation was applied because the histological sections were not fixated under physiological pressure.

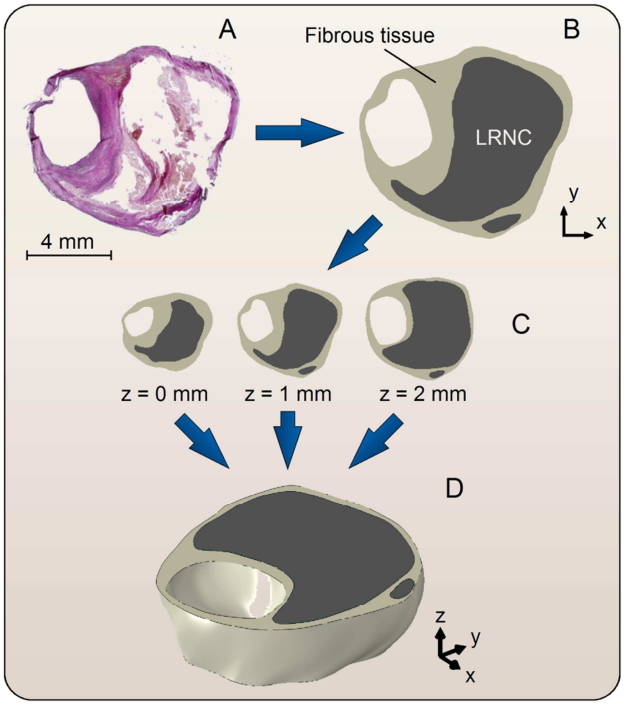


**Figure 1.** The reconstruction procedure of a 2-mm thick 3D ground truth carotid plaque model illustrated using an example. (A) Histological section, (B) segmentation of the microscopy image, (C) combination of three cross sections, and (D) reconstructed, interpolated, 3D ground truth plaque model.

### MRI simulations

A typical clinically applied 3.0T 2D T1-weighted turbo spin-echo, contrast-enhanced, black-blood pulse sequence used to image the FC and LRNC, [16], was implemented in JEMRIS, an open-source numerical Bloch-equation solver [26]. Full details on this specific implementation and an evaluation of *in vivo* MRI simulations have been previously described [25]. The original protocol had an in-plane acquired voxel size of 0.62 x 0.62 mm$^2$ (size adopted in clinical practice) and repetition/echo times of 800 ms/10 ms respectively. Through k-space zero padding, a reconstructed (interpolated) voxel size of 0.31 x 0.31 mm$^2$ was achieved. The simulated pulse sequence was modified through the definition of non-selective radio frequency pulses and the removal of slice-select and spoiler gradients, which resulted in single slice simulations. Three slice thicknesses were simulated: 0.5 mm, 1 mm, and 2 mm, the latter being the slice thickness of the clinically applied protocol. Because the simulated

pulse sequence was not slice-selective the input 3D plaque geometries were altered to simulate MRI with a certain slice thickness: for a 2-mm slice, the entire 3D plaque ground truth model, from $z = 0$ mm to $z = 2$ mm, was used as input. For a 1-mm slice, the 3D ground truth model only between $z = 0.5$ mm and $z = 1.5$ mm was used, and for a 0.5-mm slice only between $z = 0.75$ mm and $z = 1.25$ mm. A protocol modification with a doubling of the phase-acquisition steps resulted in a reduced in-plane acquisition voxel size of 0.31 x 0.31 $mm^2$ (0.16 x 0.16 $mm^2$ reconstructed). Hence, a total of 6 scan protocols were simulated in this study: two in-plane acquired voxel sizes (original protocol 0.62 x 0.62 $mm^2$, modified protocol 0.31 x 0.31 $mm^2$) each with three slice thicknesses (2 mm, 1 mm, and 0.5 mm). The smallest simulated acquired voxel size was 0.31 x 0.31 x 0.5 $mm^3$ (volume of 0.05 $mm^3$) which is, currently, far from achievable in a clinical setting. The largest voxel size was 16 times larger, 0.62 x 0.62 x 2 $mm^3$ (volume of 0.77 $mm^3$), and was identical to the voxel size from the original, clinically applied protocol. Noise was superimposed in post-processing to yield an SNR of 16.7 [25]. Because we were interested in *solely* the influence of voxel dimensions we chose specifically to not vary the SNR. Fibrous tissue, LRNC, and the background (sternocleidomastoid muscle) were modeled with $T_1$ relaxation times of 680 ms, 1220 ms, and 1412 ms, respectively, and a $T_2$ of 50 ms (incorporating gadolinium uptake). Perfect blood signal suppression was presumed and motion effects were not simulated. The simulated MR images were presented in randomized order, on pre-set contrast-brightness settings to an experienced, blinded, MR reader (Z.K.) for manual segmentation. To avert learning-effects, the lower in-plane resolution images (original protocol) were presented first.

### Finite element analysis

Tissues were modeled as homogeneous, isotropic, hyperelastic and incompressible using a nonlinear Neo-Hookean constitutive model. The material constants were 167 kPa for fibrous tissue and 1 kPa for LRNC [28]. FEA computations were performed in Abaqus (Abaqus Standard, 6.11, Dassault Systèmes Simulia Corp., Providence, Rhode Island, USA). Details on meshing and initial/boundary conditions were described previously [27]. The 3D histology-based ground truth models were deformed to an *in vivo* shape by loading them with a static intraluminal pressure of 100 mmHg before they were used for MRI simulations. The contours from the MR reader segmentations on the single-slice images were converted to 2D models (plane strain formulation). For the stress computations both the 3D (ground truth) and 2D (MRI segmentations) models were loaded with a systolic pressure of 125 mmHg. The initial stresses present in the MRI segmentation models were computed with the backward incremental method [29].

### Analysis

We first studied the geometries of the ground truth models. Three metrics for axial morphological variations in a given slice thickness were defined: (1) the relative area difference between the top and bottom cross sections, (2) the relative nonoverlapping area between those same top and bottom cross sections, and (3) the maximum in-plane ($x$, $y$) shift of the center of gravity. The latter was applied to only the LRNC because the models were defined with an axially aligned luminal center of gravity. For each metric, the absolute value was taken. We then performed the MRI simulations and obtained the lumen area, vessel wall area, LRNC area, minimum FC thickness and peak cap stress from the segmentations. To allow a comparison of a 2D segmentation with the underlying 3D ground truth we normalized for slice thickness by using the ground truth slice averaged area (i.e., volume within the simulated 3D ground truth slice divided by its thickness) instead of volumes. The minimum FC thickness was defined as the shortest distance between LRNC tissue and the lumen. The maximum principal stress was used as the scalar stress measure. For all the aforementioned parameters the relative error was computed with respect to the ground truth value, and a paired Student's t-test was applied to test for statistically significant differences in the mean (significant if $p < 0.05$). Data are shown as the mean ± standard deviation.

## RESULTS

### Ground truth plaque models

Three examples of the 3D ground truth plaque models are shown in Figure 2. All eight models covered a wide range of plaque dimensions. For the 2-mm models, the slice-averaged area for the lumen was 13.4 ± 6.6 mm$^2$ (range 5.8 – 24.9 mm$^2$), for the vessel wall 38.6 ± 11.5 mm$^2$ (range 25.2 – 57.4 mm$^2$), and for the LRNC 15.8 ± 9.7 mm$^2$ (range 6.0 – 34.6 mm$^2$). The minimum FC thickness was 0.27 ± 0.20 mm (range 0.10 – 0.67 mm). In Figure 3, the three metrics for axial morphological variations (area difference, nonoverlapping area, and center of gravity) are shown in box plots as a function of the slice thickness.

### Plaque component measurements

The example in Figure 4 shows a 3D ground truth plaque model, the simulated *in vivo* carotid MR images, and their segmentations. The ground truth model encompassed one main LRNC covering the entire 2-mm axial distance and various smaller LRNCs at $z = 1$ mm and $z = 2$ mm. Segmentation inaccuracies appeared to be mostly

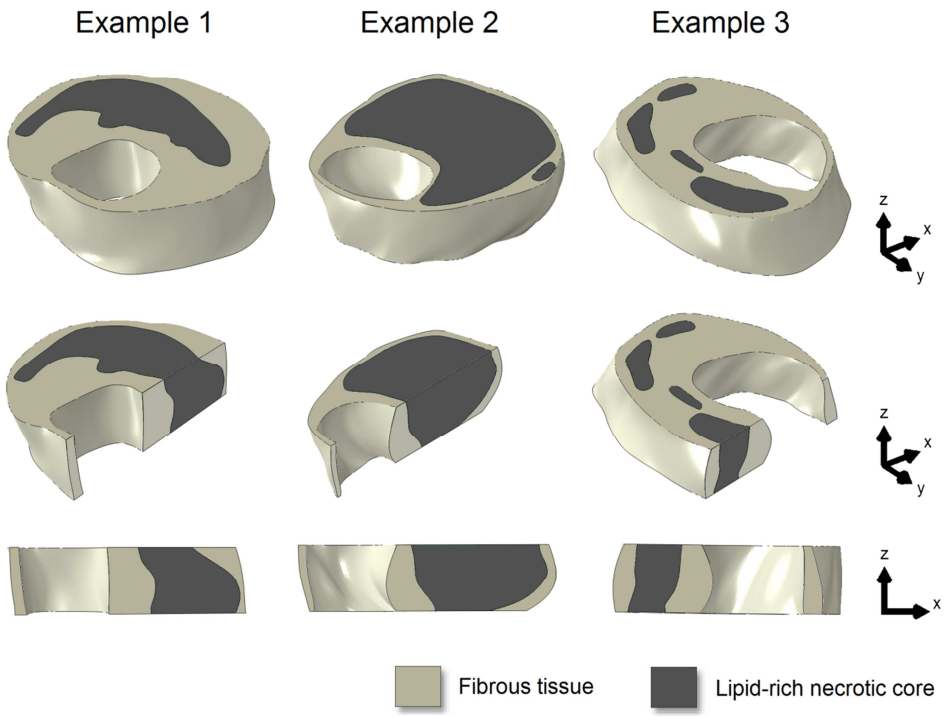


**Figure 2.** Three examples of the 3D ground truth plaque models (top row). Longitudinal cross-sectional views (middle and bottom rows) illustrate axial morphological variations.

attributable to the limited in-plane resolution, not the slice thickness. The modified MRI protocol (0.31 x 0.31 $mm^2$ in-plane) provided more in-plane detail which resulted in (1) a more accurate segmentation, (2) the positive identification of one additional smaller LRNC at $z = 1$ mm, and (3) more profound axial partial volume effects, making delineation accuracy more dependent on slice thickness. Due to reduced axial partial volume effects when the slice thickness was decreased, the contrast between the FC and LRNC tissues locally increased, improving FC visualization.

For all eight models, the measurement errors of all geometrical parameters for both in-plane voxel sizes and each slice thickness are shown in box plots in Figure 5. The lumen and LRNC areas were, on average, underestimated while the vessel wall area and minimum FC thickness were overestimated. When measuring the lumen area, vessel wall area, and LRNC area, no major improvements were observed when the slice thickness was decreased (for 0.62 x 0.62 $mm^2$ in-plane). On the other hand, we found larger, statistically significant, improvements when decreasing the in-plane voxel size for any given slice thickness, as well as substantial reductions in error spread (i.e.,

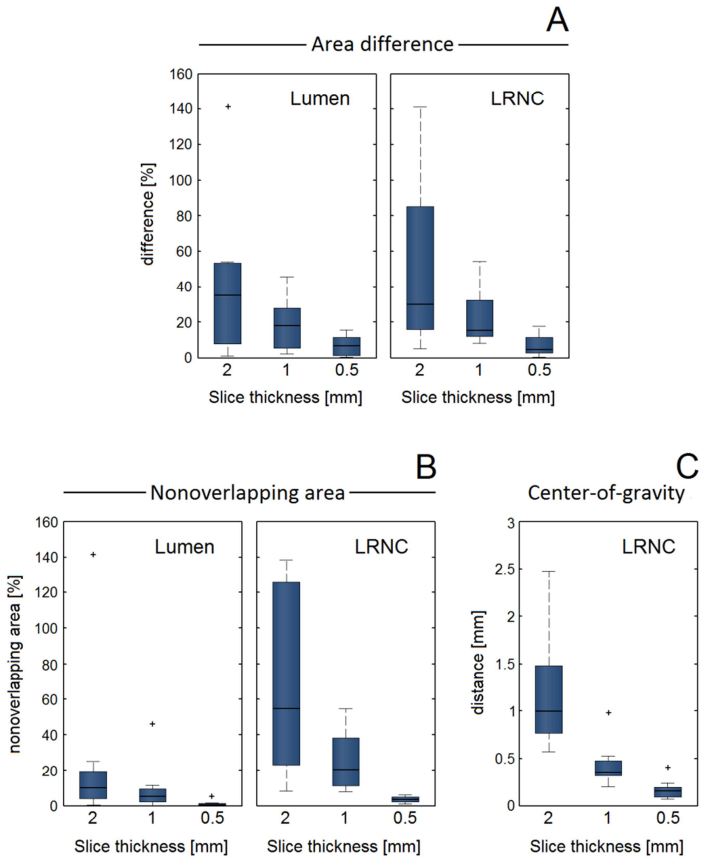


**Figure 3.** Three metrics quantify the axial geometrical variations in the ground truth models as a function of slice thickness. (A) Relative area difference between slice top and bottom cross sections for lumen and LRNC, (B) relative nonoverlapping area between slice top and bottom cross sections for lumen and LRNC, and (C) maximum in-plane shift of the center of gravity within the slice (C). Whiskers in the box plots represent maximum/minimum data points not considering outliers, which are marked by plus (+) symbols.

increased precision) for all geometrical parameters. The minimum FC thickness was the only parameter for which the error significantly improved when only the slice thickness was reduced. This occurred for a 0.5-mm slice thickness versus a 2-mm slice for the original protocol ($p = 0.05$), and versus a 1-mm slice for the modified protocol ($p < 0.01$). The measurement error for minimum FC thickness significantly improved from $+238\% \pm 200\%$ for 0.62 x 0.62 x 2 mm$^3$ voxels to only $+35\% \pm 50\%$ for 0.31 x 0.31 x 0.5 mm$^3$ voxels ($p < 0.01$). We found no significant correlations

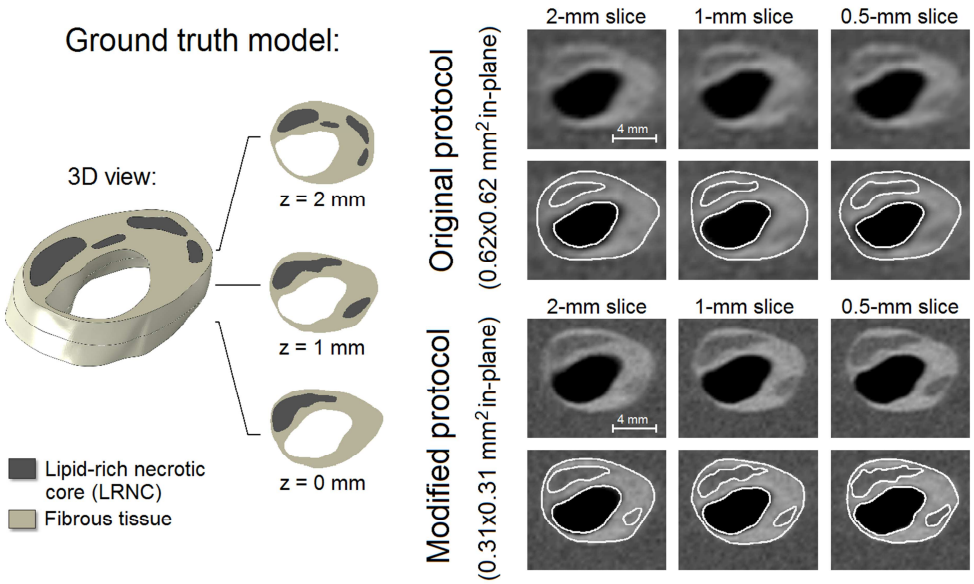


**Figure 4.** An example of a 3D ground truth input model (left) with its 6 simulated *in vivo* carotid MR images with different voxel dimensions and segmentation (right). Axial domain of the simulated geometry for a 2-mm slice: z = 0 to 2 mm, for a 1-mm slice: z = 0.5 to 1.5 mm, and for a 0.5-mm slice: z = 0.75 to 1.25 mm

between the geometrical axial variation metrics in the ground truth models and the measurement errors in MRI.

The fact that a highly anisotropic 0.31 x 0.31 x 2 $mm^3$ voxel has the same volume (0.19 $mm^3$) as a near isotropic 0.62 x 0.62 x 0.5 $mm^3$ voxel allowed an evaluation regarding voxel anisotropy. LRNC area measurements were far more accurate and precise when acquiring the highly anisotropic voxels instead of near isotropic voxels: an error of -6% ± 13% versus -23% ± 24% ($p$ = 0.03). This indicates that LRNC variations were largest in-plane. Acquiring the highly anisotropic voxels also improved the mean measurement error of the lumen (-5% anisotropic versus -11% isotropic, $p$ = 0.16) and vessel wall (+11% versus +19%, $p$ = 0.17) areas. While not statistically significant, the low $p$-values imply trends. For minimum FC thickness, there was no difference (+88% versus +96%, $p$ = 0.77), indicating that axial and in-plane FC variations were comparable.

### Plaque stress computations

The example in Figure 6 shows the stress distributions in a 3D ground truth plaque model and in the corresponding 2D models based on MRI segmentations. In the 3D

model a heterogeneous stress distribution was present, with high plaque stresses in the mid-cap (thin) and plaque shoulders (high luminal curvature). The ground truth peak cap stress was 174 kPa (at $z = 0.92$ mm). The MRI-based models exhibited a similar

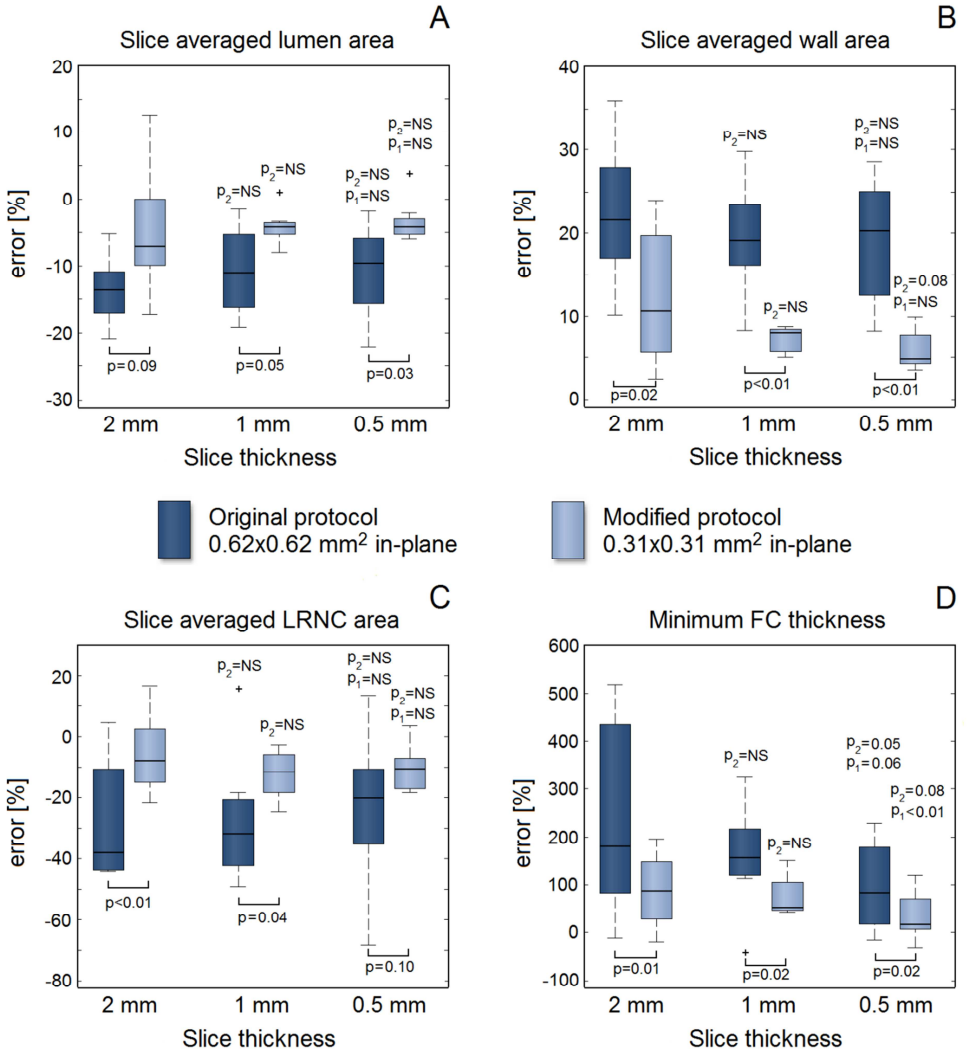


**Figure 5.** Relative error in measured value with respect to the ground truth for the geometrical parameters studied: (A) lumen area, (B) wall area, (C) LRNC area, and (D) minimum FC thickness. Whiskers in the box plots represent maximum/minimum data points not considering outliers, which are marked by plus (+) symbols. The *p*-values with respect to the 2-mm and 1-mm slice data are indicated with $p_2$ and $p_1$, respectively. A *p*-value is denoted as NS (not significant) if $p > 0.10$.

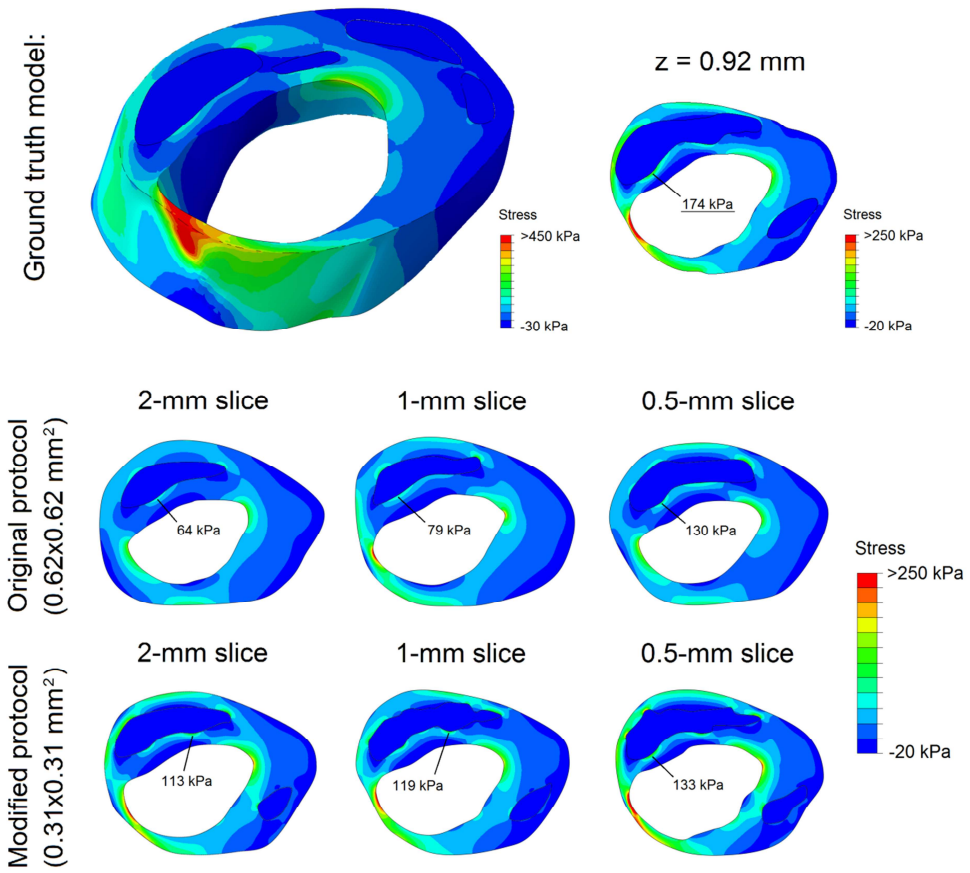


**Figure 6.** Stress distribution in an example 3D ground truth model (top row) and the stress distributions in its 6 2D MRI segmentation models (middle and bottom rows). The location and magnitude of the peak cap stress is indicated in each model.

stress distribution, but with a severe peak cap stress underestimation. A thinner segmented FC yielded a higher stress and, in effect, a reduced underestimation. The underestimation of peak cap stress (related to FC thickness overestimation [28]) decreased for a reduced slice thickness and/or a reduced in-plane voxel size.

For all eight models, the error of the MRI segmentation model peak cap stress is shown in Figure 7 for both the original (0.62 x 0.62 mm$^2$) and the modified protocol (0.31 x 0.31 mm$^2$) as a function of the slice thickness. The peak cap stress was severely underestimated, with a large imprecision (i.e., large error spread). The interquartile ranges indicate no improvements in precision for a decreased slice thickness or in-plane voxel size. A decreased slice thickness only improved the mean

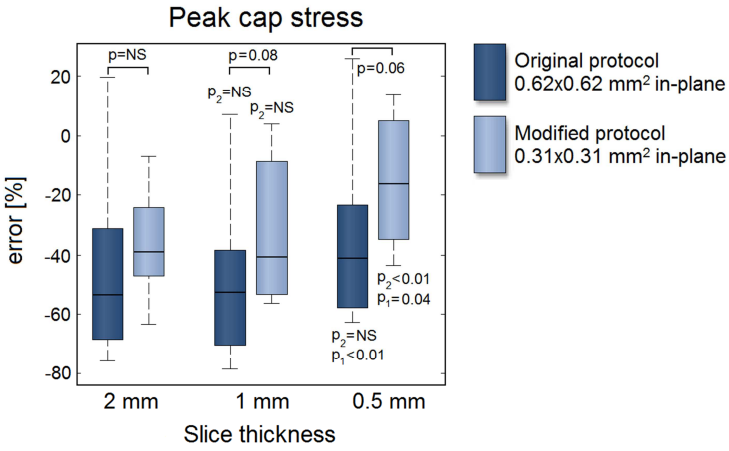


**Figure 7.** Relative error in the MRI segmentation model predicted peak cap stress with respect to the ground truth peak cap stress as a function of slice thickness. For details, see caption of Figure 5.

error when 0.5-mm slices were acquired, while a reduced in-plane voxel size (for any given slice thickness) always resulted in larger improvements. The low $p$-values ($p = 0.08$ for a 1-mm slice and $p = 0.06$ for a 0.5-mm slice) indicate trends. The smallest voxel size (0.31 x 0.31 x 0.5 mm$^3$) yielded an error of -15% ± 22% versus an error of -45% ± 32% for the largest voxel size (0.62 x 0.62 x 2 mm$^3$) ($p < 0.01$). Interestingly, acquiring highly anisotropic voxels (0.31 x 0.31 x 2 mm$^3$) instead of near isotropic voxels (0.62 x 0.62 x 0.5 mm$^3$) with the same volume had little effect on the peak cap stress error (-36% ± 18% anisotropic versus -35% ± 30% isotropic, $p = 0.89$).

## DISCUSSION

In this study, we investigated the degree to which axial intravoxel partial volume effects, associated with acquiring a specific slice thickness, contribute to errors in atherosclerotic plaque component measurements and peak cap stress computations in carotid MRI. A simulated, virtual MRI approach allowed direct quantification of measurement error in a controlled environment where only the voxel dimensions were varied.

### General observations

For a typical clinical in-plane acquired voxel size of 0.62 x 0.62 mm$^2$, a decreased slice thickness did not significantly improve measurements of the lumen, vessel wall and

LRNC size, but it did have a beneficial effect on the accuracy of minimum FC thickness measurements. Furthermore, only a 0.5-mm slice led to a relatively marginal improvement in the error in computed peak cap stress. A reduction in the in-plane voxel size to 0.31 x 0.31 $mm^2$, however, led to similar or often larger improvements. LRNC measurements improved when anisotropic voxels were acquired instead of isotropic voxels of the same volume (error of -6% ± 13% versus -23% ± 24%, $p = 0.03$). Similar trends were observed for the other parameters studied. Our findings provide evidence that current 2D carotid MRI protocols for plaque quantification appropriately sacrifice axial resolution to reduce scan time and/or noise. The commonly used argument that a standard 2-mm slice thickness limits imaging therefore only applies to small, localized features such as the FC. Consequently, 3D carotid MRI protocols could be modified by reducing the slice-select phase-encoding steps (i.e., transitioning from isotropic to anisotropic voxels), thus reducing scan time. We confirmed the reports of Balu et al. with regard to the unimproved vessel wall and lumen measurements [11,12], and, by virtue of our simulation methodology, studied more crucial, vulnerable plaque parameters. A ground truth comparison as employed in our study allowed a quantification of measurement accuracy, the absence of which was a limitation in most previous studies which only assessed reproducibility [9,11,12,18,30]. The observed overestimations (wall area and FC thickness) and underestimations (lumen area, LRNC area, and peak cap stress) were in line with previous reports [25,28,31-33]. A recent study by van Wijk et al., also found that higher voxel anisotropy improved wall measurements [18]. In a previous study, we reported the large inaccuracy in minimum FC measurements [25], while assuming a uniform axial morphology within a slice. The findings from the present study show that intraslice axial FC variations lead to a much larger inaccuracy in measured FC thickness than previously reported [25].

The analysis of the ground truth models using the axial variation metrics illustrates that plaques can exhibit large variations on relatively small longitudinal length scales, as earlier qualitatively elucidated by Coombs et al. [17]. Axial variations rapidly decreased when the slice thickness was reduced. Although indicative, the axial variation metrics were quite strict when linked to MRI segmentation because they only use data on the axial boundaries of a slice. Gradual intensity changes due to partial volume effects in an MRI slice will lead to a correct 'slice-averaged' segmentation, and thus to a relatively precise measurement of the component volume. Indeed, with regard to MRI slice thickness, volumetric plaque components are inherently more forgiving than, for instance, minimum FC thickness, which is a very localized parameter both in-plane and axially. The lack of any correlation between the axial variation metrics and

measurement errors also suggests that segmentation accuracy is more influenced by the in-plane voxel size than by the slice thickness.

### Clinical implications

In clinical practice, alterations in voxel dimensions affect scan time and SNR. A decrease in voxel size would either result in an increased scan time, a lower SNR, or a combination of both. Scan time and SNR were not the focus of this study and therefore not investigated. A trade-off can easily become more complicated than the mere application of the standard SNR equation when considering, for example, 3D versus 2D protocols [34], motion artifacts [35], and imperfect black-blood signal suppression [30,36]. Note that we found that, even with an *unaltered* SNR, a decreased slice thickness was often not beneficial. In a previous study, we explored the trade-off between scan time, SNR and in-plane resolution, and found that SNR was less limiting than the resolution for manual segmentation [25]. However, Rhonen et al. investigated the effects of SNR and in-plane resolution in an *ex vivo* study using thin histological slices, and concluded that SNR had a large impact on automated tissue classification [20]. While our study provides relevant data, the true clinical benefit when trading-off voxel dimensions against scan time, noise, motion-artifacts and blood signal suppression needs to be investigated in further studies [31]. We purposely imposed a relatively high SNR to create MR images that on the one hand were as realistic as possible, but in which, on the other hand, noise would not be the weakest link [25]. We restricted ourselves by focusing on only partial volume effects caused by finite voxel dimensions, because these effects are a critical and often addressed (but insufficiently studied) issue in carotid MRI studies [10,12,17,28,34,37]. We did therefore not study additional possible benefits of a decreased slice thickness in clinical practice such as improved axial image matching in longitudinal studies, improved retrospective multi-planar reformatting [11,12], easier registration to histology slices [17,38], and a decreased sensitivity to a localized oblique scan plane orientation [32]. A reduction in slice thickness would serve a double benefit for plaque FEA since it would also increase the axial sampling resolution for 3D multislice-based plaque FEA [27].

### Study limitations

Eight representative carotid plaques were used. From a statistical point of view our study was exploratory: the sample size was not sufficiently large to corroborate the statistical significance of relatively small differences between means. Nevertheless, such small changes are immaterial for practical applications, especially when considered in conjunction with the observed large spread in errors. Intraplaque hemorrhage was

absent in the histological sections, and decalcification inhibited the inclusion of calcifications in the ground truth models. For small calcifications, isotropic imaging can be beneficial [11,12]. The 3D ground truth models were created by interpolating histology slices which had a 1-mm axial spacing. This is a limitation considering the fact that the MRI slice thickness was in the same order of magnitude. However, the examples shown in Figures 1, 2 and 4 indicate the presence of axial variations on sub-millimeter scales (due to the 3D spline interpolation). In addition, the examples do not evidence critical axial under sampling. By aligning the luminal center of gravity of the histological sections, we assumed no oblique scan plane orientation at the slice of interest (for details, see [32]). For the MRI, the imposed SNR was relatively high, motion was neglected, and homogeneous components were used. These factors, when combined, make the errors we report in this study representative for a best-case imaging scenario. Only single-slice simulations were performed with uniform axial excitation, neglecting influences from adjacent slices. This choice was made because such influences (e.g., cross talk in 2D sequences or point spread function effects in the slice-select phase direction in 3D sequences) can be highly protocol-specific. For a detailed discussion regarding the MRI simulations using JEMRIS, we refer to our previous work [25]. Residual stresses, heterogeneity and collagen/elastin fiber directionality were not included in the biomechanical models [39], but this did not compromise the comparisons which involved solely geometrical differences.

## CONCLUSIONS

This study provides evidence that measurements of the lumen, vessel wall or LRNC size in carotid MRI do not majorly improve when decreasing the slice thickness, even if the SNR remains unaltered. For minimum FC thickness and the closely related peak cap stress magnitude, a decreased slice thickness was beneficial, but not more than a decreased in-plane voxel size. Our simulations indicate that it is not a decreased slice thickness, but the acquisition of anisotropic voxels that improves plaque quantification in a clinical setting.

## ACKNOWLEDGEMENTS

We thank Maxime Verschuuren for geometrical analyses, Henk Smit for insightful discussions, and Kim van Gaalen for histological processing.

## REFERENCES


1. Yuan C, Mitsumori LM, Beach KW, Maravilla KR. Carotid atherosclerotic plaque: noninvasive MR characterization and identification of vulnerable lesions. Radiology 2001;221:285-99.
2. Cai JM, Hatsukami TS, Ferguson MS, Small R, Polissar NL, Yuan C. Classification of human carotid atherosclerotic lesions with in vivo multicontrast magnetic resonance imaging. Circulation 2002;106:1368-1373.
3. Underhill HR, Hatsukami TS, Fayad AZ, Fuster V, Yuan C. MRI of carotid atherosclerosis: clinical implications and future directions. Nat Rev Cardiol 2010;7:165-173.
4. Toussaint J, LaMuraglia GM, Southern JF, Fuster V, Kantor HL. Magnetic resonance images lipid, fibrous, calcified, hemorrhagic, and thrombotic components of human atherosclerosis in vivo. Circulation 1996;94:932-938.
5. Cai J, Hatsukami TS, Ferguson MS, Kerwin WS, Saam T, Chu B, Takaya N, Polissar NL, Yuan C. *In vivo* quantitative measurement of intact fibrous cap and lipid-rich necrotic core size in atherosclerotic carotid plaque: comparison of high-resolution, contrast-enhanced magnetic resonance imaging and histology. Circulation 2005;112:3437-3444.
6. Li F, Yarnykh VL, Hatsukami TS, Chu B, Balu N, Wang J, Underhill HR, Zhao X, Smith R, Yuan C. Scan-rescan reproducibility of carotid atherosclerotic plaque morphology and tissue composition measurements using multicontrast MRI at 3T. J Magn Reson Imaging 2010;31:168-76.
7. Cheng GC, Loree HM, Kamm RD, Fishbein MC, Lee RT. Distribution of circumferential stress in ruptured and stable atherosclerotic lesions. A structural analysis with histopathological correlation. Circulation 1993;87:1179-87.
8. Li ZY, Howarth S, Trivedi RA, U-King-Im JM, Graves MJ, Brown A, Wang L, Gillard JH. Stress analysis of carotid plaque rupture based on in vivo high resolution MRI. J Biomech 2006;39:2611-2622.
9. Gao H, Long Q, Graves M, Gillard JH, Li Z. Study of Reproducibility of human arterial plaque reconstruction and its effects on stress analysis based on multispectral *in vivo* magnetic resonance imaging. J Magn Reson Imaging 2009;30:85-93.
10. Tang D, Teng Z, Canton G, Yang C, Ferguson M, Huang X, Zheng J, Woodard PK, Yuan C. Sites of rupture in human atherosclerotic carotid plaques are associated with high structural stresses: an in vivo MRI-based 3D fluid-structure interaction study. Stroke 2009;40:3258-3263.
11. Balu N, Chu B, Hatsukami TS, Yuan C, Yarnykh VL. Comparison between 2D and 3D high-resolution black-blood techniques for carotid artery wall imaging in clinically significant atherosclerosis. J Magn Reson Imaging 2008;27:918-924.
12. Balu N, Yarnykh VL, Chu B, Wang J, Hatsukami T, Yuan C. Carotid plaque assessment using fast 3D isotropic resolution black-blood MRI. Magn Reson Med 2011;65:627-637.
13. Liu W, Balu N, Sun J, Zhao X, Chen H, Yuan C, Zhao H, Xu J, Wang G, Kerwin WS. Segmentation of carotid plaque using multicontrast 3D gradient echo MRI. J Magn Reson Imaging 2012;35:812-819.
14. Li B, Dong L, Chen B, Ji S, Cai W, Wang Y, Zhang J, Zhang Z, Wang X, Fang J. Turbo fast three-dimensional carotid artery black-blood MRI by combining three-dimensional MERGE sequence with compressed sensing. Magn Reson Med 2013;70:1347-1352.
15. Watanabe Y, Nagayama M. MR plaque imaging of the carotid artery. Neuroradiology 2010;52:253-274.
16. Truijman MT, Kooi ME, van Dijk AC, de Rotte AA, van der Kolk AG, Liem MI, Schreuder FH, Boersma E, et. al. Plaque At RISK (PARISK): prospective multicenter study to improve diagnosis of high-risk carotid plaques. Int J Stroke 2014;9:747-754.
17. Coombs BD, Rapp JH, Ursell PC, Reilly LM, Saloner D. Structure of plaque at carotid bifurcation: high-resolution MRI with histological correlation. Stroke 2001;32:2516-2521.
18. van Wijk DF, Strang AC, Duivenvoorden R, Enklaar DJ, van der Geest RJ, Kastelein JJ, de Groot E, Stroes ES, Nederveen AJ. Increasing spatial resolution of 3T MRI scanning improves reproducibility of carotid arterial wall dimension measurements. MAGMA 2014;27:219-226.
19. González Ballester MA, Zisserman AP, Brady M. Estimation of the partial volume effect in MRI. Med Image Anal 2002;6:389-405.
20. Ronen RR, Clarke SE, Hammond RR, Rutt BK. Resolution and SNR effects on carotid plaque classification. Magn Reson Med 2006;56:290-295.

21. Hackländer T, Mertens H. Virtual MRI: a PC-based simulation of a clinical MR scanner. Acad Radiol 2005;12:85-96.
22. Benoit-Cattin H, Collewet G, Belaroussi B, Saint-Jalmes H, Odet C. The SIMRI project: a versatile and interactive MRI simulator. J Magn Reson 2005;173:97-115.
23. Xanthis CG, Venetis IE, Aletras AH. High performance MRI simulations of motion on multi-GPU systems. J Cardiovasc Magn Reson 2014;4:16-48.
24. Klepaczko A, Szczypiński P, Dwojakowski G, Strzelecki M, Materka A. Computer simulation of magnetic resonance angiography imaging: model description and validation. PLoS One 2014;9:e93689.
25. Nieuwstadt HA, Geraedts TR, Truijman MT, Kooi ME, van der Lugt A, van der Steen AF, Wentzel JJ, Breeuwer M, Gijsen FJ. Numerical simulations of carotid MRI quantify the accuracy in measuring atherosclerotic plaque components in vivo. Magn Reson Med 2014;72:188-201.
26. Stöcker T, Vahedipour K, Pflugfelder D, Shah NJ. High-performance computing MRI simulations. Magn Reson Med 2010;64:186-193.
27. Nieuwstadt HA, Akyildiz AC, Speelman L, Virmani R, van der Lugt A, van der Steen AFW, Wentzel JJ, Gijsen FJH. The influence of axial image resolution on atherosclerotic plaque stress computations. J Biomech 2013;46:689-695.
28. Nieuwstadt HA, Speelman L, Breeuwer M, van der Lugt A, van der Steen AF, Wentzel JJ, Gijsen FJ. The influence of inaccuracies in carotid MRI segmentation on atherosclerotic plaque stress computations. J Biomech Eng 2014;136:021015-1-9.
29. Speelman L, Akyildiz AC, den Adel B, Wentzel JJ, van der Steen AF, Virmani R, van der Weerd L, Jukema JW, Poelmann RE, van Brummelen EH, Gijsen FJ. Initial stress in biomechanical models of atherosclerotic plaques. J Biomech 2011;44:2376-2382.
30. Balu N, Kerwin WS, Chu B, Liu F, Yuan C. Serial MRI of carotid plaque burden: influence of subject repositioning on measurement precision. Magn Reson Med 2007;57:592-599.
31. Schär M, Kim WY, Stuber M, Boesiger P, Manning WJ, Botnar RM. The impact of spatial resolution and respiratory motion on MR imaging of atherosclerotic plaque. J Magn Reson Imaging 2003;17:538-544.
32. Antiga L, Wasserman BA, Steinman DA. On the overestimation of early wall thickening at the carotid bulb by black blood MRI, with implications for coronary and vulnerable plaque imaging. Magn Reson Med 2008;60:1020-1028.
33. Hofman JMA, Branderhorst WJ, ten Eikelder HMM, Cappendijk VC, Heeneman S, Kooi ME, Hilbers PAJ, ter Haar Romeny BM. Quantification of atherosclerotic plaque components using in vivo MRI and supervised classifiers. Magn Reson Med 2006;55:790-799.
34. Luk-Pat GT, Gold GE, Olcott EW, Hu BS, Nishimura DG. High-resolution three-dimensional in vivo imaging of atherosclerotic plaque. Magn Reson Med 1999;42:762-771.
35. Al-Kwifi O, Kim JK, Stainsby J, Huang Y, Sussman MS, Farb RI, Wright GA. Pulsatile motion effects on 3D magnetic resonance angiography: implications for evaluating carotid artery stenoses. Magn Reson Med 2004;52:605-611.
36. Dong L, Wang J, Yarnykh VL, Underhill HR, Neradilek MB, Polissar N, Hatsukami TS, Yuan C. Efficient flow suppressed MRI improves interscan reproducibility of carotid atherosclerosis plaque burden measurements. J Magn Reson Imaging 2010;32:452-458.
37. Yuan C, Kerwin WS. MRI of atherosclerosis. J Magn Reson Imaging 2004;19:710-719.
38. Groen HC, van Walsum T, Rozie S, Klein S, van Gaalen K, Gijsen FJ, Wielopolski PA, van Beusekom HM, de Crom R, Verhagen HJ, van der Steen AF, van der Lugt A, Wentzel JJ, Niessen WJ. Three-dimensional registration of histology of human atherosclerotic carotid plaques to in-vivo imaging. J Biomech 2010;43:2087-2092.
39. Holzapfel GA, Mulvihill JJ, Cunnane EM, Walsh MT. Computational approaches for analyzing the mechanics of atherosclerotic plaques: A review. J Biomech 2014;47:859-869.

# The influence of axial image resolution on atherosclerotic plaque stress computations

5

**Abstract** | Biomechanical models are used extensively to study risk factors, such as peak stress, for vulnerable atherosclerotic plaque rupture. Typically, 3D patient-specific arterial models are reconstructed by interpolating between cross-sectional contour data which have a certain axial sampling, or image, resolution. The influence of the axial sampling resolution on computed stresses, as well as the comparison of 3D with 2D simulations, is quantified in this study. A set of histological data of four atherosclerotic human coronary arteries was used which were reconstructed in 3D with a high sampling (HS) and low sampling (LS) axial resolution, and 4 slices were treated separately for 2D simulations. Stresses were calculated using finite element analysis (FEA). High stresses were found in thin cap regions and regions of thin vessel walls. Low stresses were found inside lipid-rich necrotic cores and media and adventitia layers. Axial sampling resolution was found to have a minor effect on general stress distributions, peak plaque/cap stress locations, and the relationship between peak cap stress and minimum cap thickness. Axial sampling resolution did have a profound influence on the error in computed magnitude of peak plaque/cap stresses (±15.5% for HS versus LS geometries and ±24.0% for HS versus 2D geometries for cap stresses). The findings of this study show that axial under sampling does not significantly influence the qualitative stress distribution. However, high axially sampled 3D models are needed when accurate computation of peak stress magnitude is required.

**This chapter is based on:** Nieuwstadt HA, Akyildiz AC, Speelman L, Virmani R, van der Lugt A, van der Steen AFW, Wentzel JJ, Gijsen FJH. The influence of axial image resolution on atherosclerotic plaque stress computations. Journal of Biomechanics 2013;46:689-695.

## INTRODUCTION

Atherosclerosis is characterized by plaque formation in the arterial wall [1]. Plaque rupture may lead to thromboembolism, possibly causing acute myocardial infarctions and ischemic strokes [2,3]. Rupture prone plaques, termed vulnerable plaques, generally consist of a large necrotic core separated from the lumen by a thin macrophage infiltrated fibrous cap [4,5].

To improve clinical decision making for medical treatment, much attention has been focused on understanding vulnerable plaque rupture. The biomechanical approach treats plaque rupture as an event of mechanical failure, where stresses in the cap lead to its rupture if they exceed the cap strength [6-9]. Finite element analysis (FEA) is often used to provide insight into the stress distribution in plaques and the dependence of plaque stress on morphological and geometrical factors such as cap thickness, necrotic core size, luminal curvature and microcalcifications [10-20]. In addition to contributing to understanding of plaque rupture [21], biomechanical modeling also shows potential for noninvasive identification of vulnerable plaques using novel risk-stratification criteria [13].

Reliable stress assessment using FEA critically depends on accurate reconstruction of the plaque geometry. The plaque geometry is typically obtained with invasive or noninvasive imaging methods such as magnetic resonance imaging (MRI) [12,15,22-24], x-ray computed tomography (CT) [18,20], optical coherence tomography (OCT) [25], intravascular ultrasound (IVUS) [26-28], and histology [10,29-32]. In the case of two-dimensional (2D) FEA simulations, plaque components are delineated in cross sectional images, and a plane strain analysis is performed. For three-dimensional (3D) simulations, cross sectional images are predominantly obtained from MRI volume data which typically consist of anisotropic voxels with an in-plane resolution being in the order of 5–10 times higher than the axial resolution (voxel dimensions of 0.2–0.6 mm in-plane versus 1–2 mm axial) [33]. The 3D geometry is reconstructed by axially stacking cross sectional segmented contours with a distance which will be referred to in this study as the axial sampling resolution. For contours derived from volume image data, the axial sampling resolution is equal to the axial voxel dimension while for contours based on histology it is equal to the slice distance. Upon stacking the contours, interpolation is used to generate the 3D arterial geometry.

This study aimed to quantify the influence of axial sampling resolution on computed peak plaque and cap stress using FEA. This was done by performing stress simulations on a set of histology-based atherosclerotic arterial segments. Each segment was reconstructed in 3D using a high axial resolution and a low axial resolution. For each segment, also 2D simulations were performed and compared with the 3D models.

# METHODS

## Histology

To investigate the influence of axial sampling resolution on computed stresses, we needed a data set of diseased arteries with a sufficiently high resolution that could serve as a gold standard. We used a histological set of human coronary arteries with an axial slice distance of 0.5 mm. We selected 4 arterial segments with a length of 3 mm (7 slices). The selection criteria were such that each segment contained at least one large necrotic core and at least one thin cap. Before sectioning, the arteries were decalcified and perfusion fixated with formalin at 100 mmHg and stained with a Movat pentachrome staining to enable segmentation of the plaque components. Manual segmentation of the lumen, necrotic cores, media and adventitia layers was performed (Figure 1).

## Geometry reconstructions

To reconstruct the 3D geometries the slices were stacked vertically by alignment of the luminal center of gravity. For each arterial segment a reference geometry using all 7

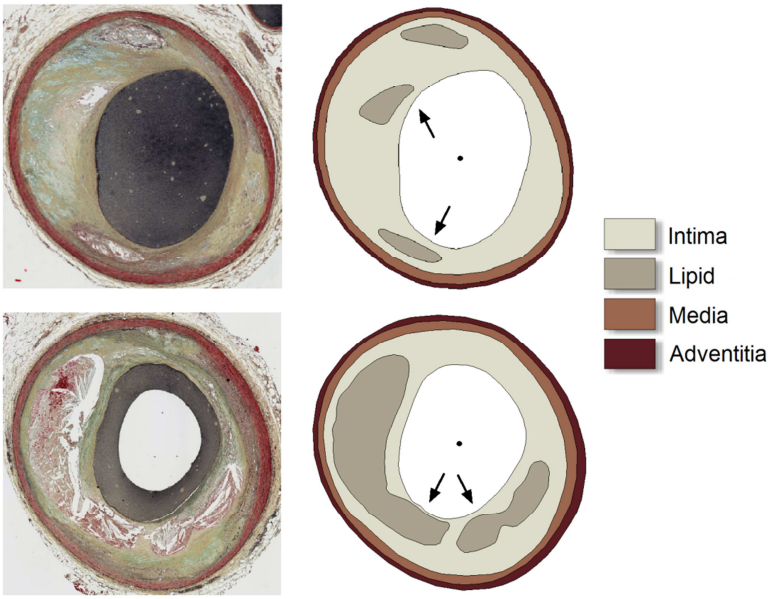


**Figure 1.** Histological cross sections and their delineated contours. Cap regions are indicated by black arrows.

histological slices spaced 0.5 mm apart was created, referred to as the high sampling (HS) model. A low sampling (LS) geometry was created to mimic the noninvasive, *in vivo*, imaging situation which had only 4 slices spaced 1.0 mm apart. The most extreme case of low axial sampling would be the use of only one single slice, thus resulting in a 2D formulation. To investigate and compare results of this lowest possible sampling resolution with the HS models, 4 2D models were created from the same 4 slices used for the LS geometry (Figure 2). Non-uniform rational basis spline interpolation in Gambit (Fluent Inc., ANSYS, Canonsburg, Pennsylvania, USA) was used to interpolate between slices. To avoid reading out values at the boundary of the simulated domain, an additional top and bottom end slice were added to each 3D model before geometrical interpolation.

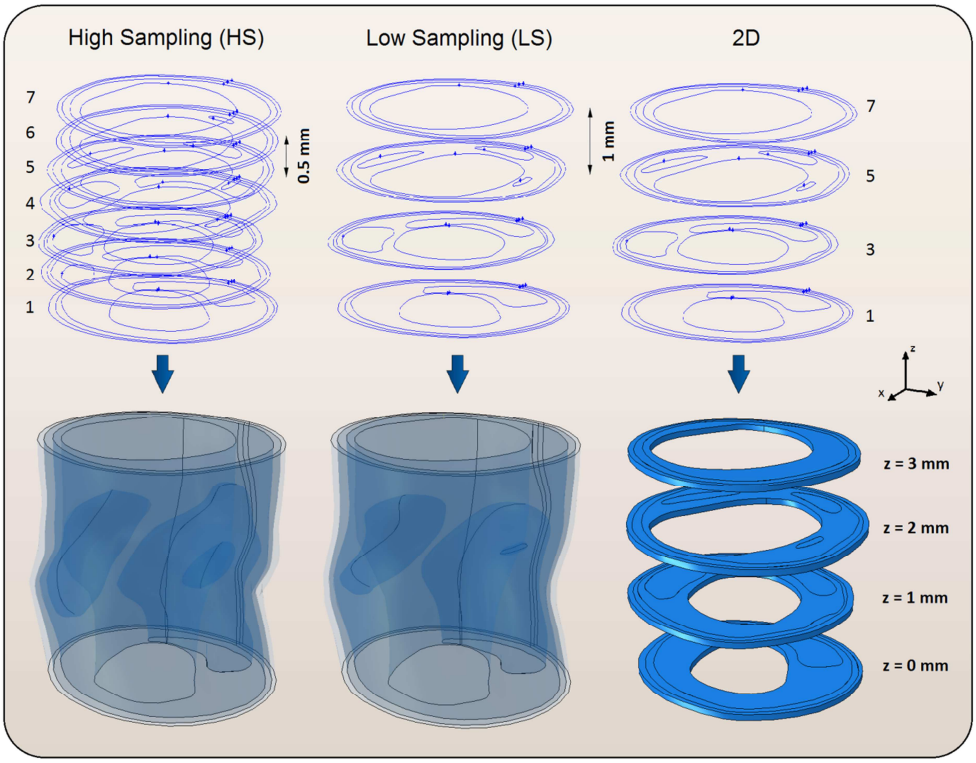


**Figure 2.** Geometry reconstruction procedure (segment 4 used as example). Contours shown in top row result in the models in the bottom row. HS uses all 7 histological cross sections (slice distance 0.5 mm) to re-create the 3D artery geometry, whereas for LS only 4 cross sections are used. 2D simulations are performed on the same 4 cross sections as used for LS.

## Finite element analysis

All tissues were assumed to be homogeneous, hyperelastic, and incompressible. The intima and lipid core tissues were assumed to be isotropic and modeled with the neo-Hookean material model. The media and adventitia tissues were modeled with an anisotropic material model [34]. The same material constants were used as in Akyildiz et al. [10] and are listed in Table 1. All FEA computations were performed using Abaqus (Version 6.11.1, Dassault Systèmes Simulia Corp., Providence, Rhode Island, USA). The models for the 2D simulations were meshed with four-node linear hybrid elements (~100 000 elements). For 3D simulations, four-node linear hybrid tetrahedral elements were used. All 3D meshes were created using an iterative adaptive remeshing procedure allowing for small elements in high stress regions while keeping the total mesh size below two million elements. All models contained at least 3 layers of elements in every thin cap and yielded mesh independent solutions. The initial stress was calculated using the backward incremental method [30,35]. A static intraluminal pressure of 15 kPa (~110 mmHg) was applied as the loading condition for all models. The 2D models were based on a plane strain assumption whereas the boundary conditions for the 3D models consisted in restraining the $z$-component of the deformation at the axial boundaries.

## Analysis

The maximum principal stress, stress-$P_1$ [kPa], was used as the stress scalar quantity in this study [22]. Quantitative comparisons were performed only at cross sections matching the slices used to create the HS models. Four out of seven of these slices were *shared* in all models (HS, LS and 2D) while the other three represented *interpolated* cross sections for the LS models and did not occur as 2D models (Figure 2). The peak *plaque* stress refers to the maximum stress in a cross sectional plane at a particular $z$-

**Table 1**
Material constants of the plaque components.

| Tissue type | Material constant(s) |
|---|---|
| Media | $\mu$ = 2.24 kPa, $k_1$ = 65.76 kPa, $k_2$ = 76.87, $\phi$ = 50.89°, and $\kappa$ = 0.27 |
| Adventitia | $\mu$ = 5.86 kPa, $k_1$ = 2069.42 kPa, $k_2$ = 394.28, $\phi$ = 52.54°, and $\kappa$ = 0.2 |
| Lipid | $C$ = 1 kPa |
| Intima | $C$ = 167 kPa |

height. The peak *cap* stress specifically refers to the maximum stress in a cap region in a plane. Computed stresses for HS were compared with LS and 2D cases using Bland Altman plots which plot the relative difference [%] as a function of the mean of two values. Mean slice curvatures in the $z$-direction (axial direction) were numerically calculated from the 3D FEA mesh, by inverting the radius of the osculating circle through three vertically interpolated aligned mesh nodes around the slice and averaging for the entire lumen wall circumference. A non-parametrical one-tailed Mann-Whitney $U$ test was used for comparison between groups of data where a $p$-value $< 0.01$ was considered significant.

## RESULTS

### Qualitative stress distribution

Longitudinal stress plots are shown in Figure 3. Within the reference geometry of each arterial segment, the HS case, we found a highly heterogeneous stress distribution along the luminal wall. High stresses were found in the cap regions, regions of high luminal

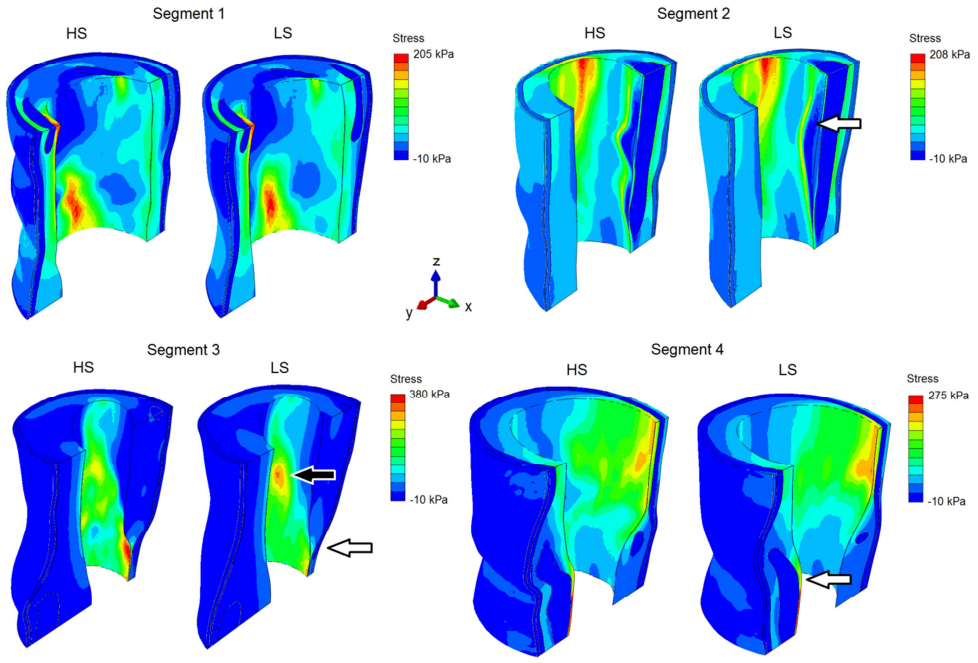


**Figure 3.** Plaque stress distribution shown on longitudinal cuts through each segment for the HS and LS case. Arrows mark regions of interest.

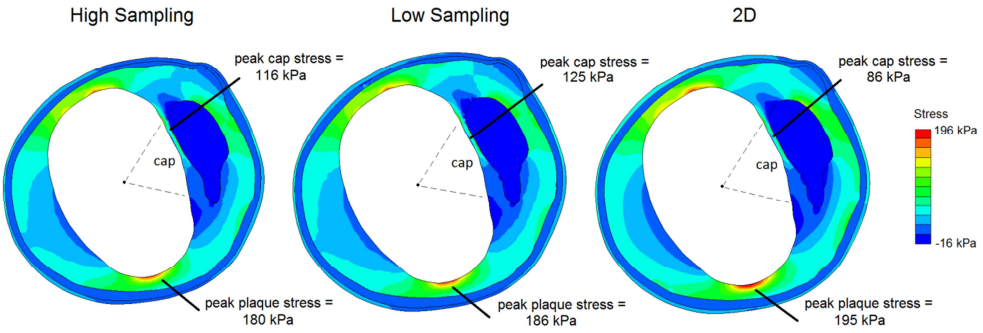


**Figure 4.** Example of a cross sectional stress distribution resulting from all three sampling cases (slice 7 from segment 2, cap thickness 44 μm).

curvature and in thin vessel walls at the plaque shoulder areas. Low stresses were found in the soft necrotic cores and in thick intima regions. Overall, peak stresses varied largely, from 205 kPa (segment 1) to 380 kPa (segment 3). When observing the LS cases, we first noticed axial smoothing of geometrical plaque features (indicated by the white arrows) leading to local vessel wall thickening or thinning. From a qualitative perspective, lower axial sampling did not appear to influence the general stress distribution except for the case of segment 3 (black arrow). At this location, local geometrical changes were observed in both the curvatures of the geometrical plaque features and in the thickness of the arterial wall.

### Peak plaque stress

An example of the stress distribution in a shared cross section is shown in Figure 4. The cross section contained one necrotic core with a thin cap, leading to a highly heterogeneous stress distribution. The peak plaque stress was found in a region where the in-plane luminal wall curvature was relatively high and the vessel wall was thin. For lower sampling, the qualitative stress distribution and the location of peak plaque stress remained the same. The computed magnitude of the peak plaque stress was influenced however by lower sampling: for LS the peak plaque stress was higher (186 kPa versus 180 kPa) and for 2D also higher (195 kPa versus 180 kPa). We observed a similar trend for all other cross sections: the qualitative stress distribution, as well as the location of peak plaque stress, was unaffected by lower sampling, but the magnitude of peak plaque stress was significantly influenced. In Figure 5, plots show the relative difference between peak plaque stress computed from the HS model and that of both the LS and 2D models as a function of their averaged value. For the 16 shared cross sections from LS geometries, the magnitude of the peak plaque stress

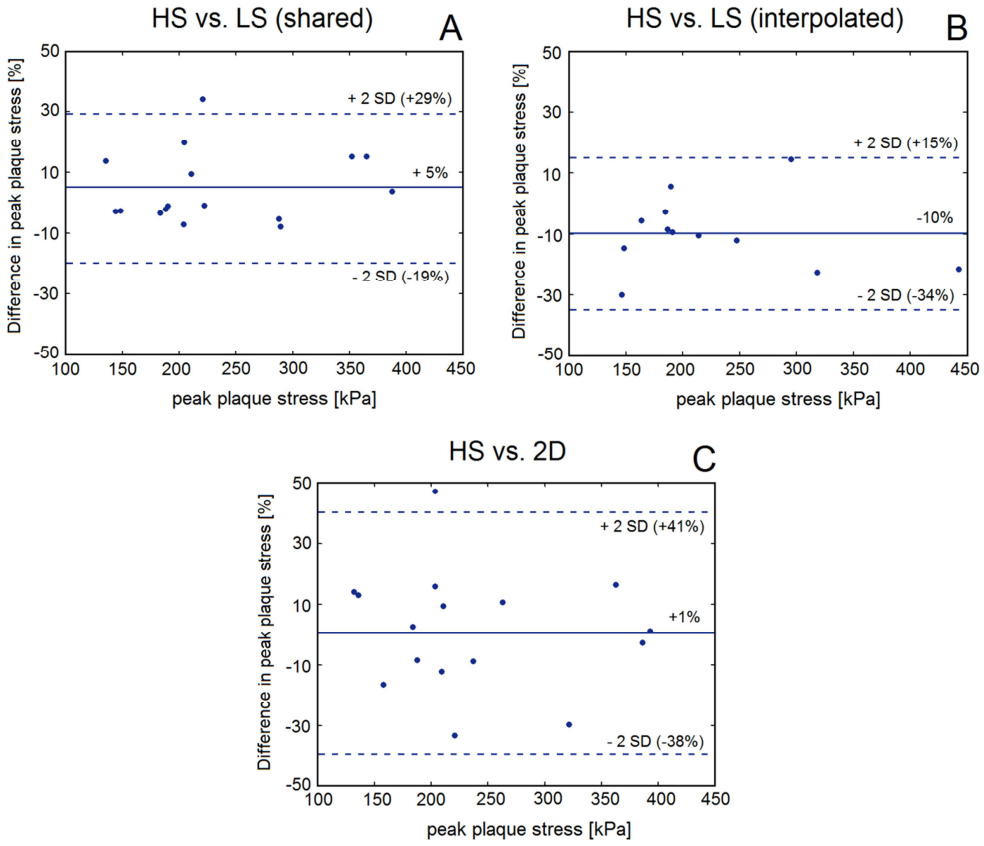


**Figure 5.** Bland Altman plots showing the relative difference in peak plaque stress for shared slices of LS compared to HS (A), interpolated slices of LS to HS (B) and 2D to HS (C) as a function of the average peak plaque stress.

compared with that of the HS models deviated +4.9 ± 11.9% ($p$ = 0.34, range [-8%, +34%]). For the 12 interpolated cross sections from the LS geometries the difference with the HS geometries was larger: -9.7 ± 12.1% ($p$ = 0.29, range [-30%, +15%]). For the 16 2D cases the difference was +1.2 ± 19.8% ($p$ = 0.46, range [-33%, +47%]). The mean in the latter case was small, which indicates that there was no systematic bias. Although statistical tests for the mean showed no statistical significance, the error and range (19.8% and 47% respectively) were large, indicating a significant decrease in the accuracy of calculated peak plaque stress when performing 2D simulations instead of 3D HS.

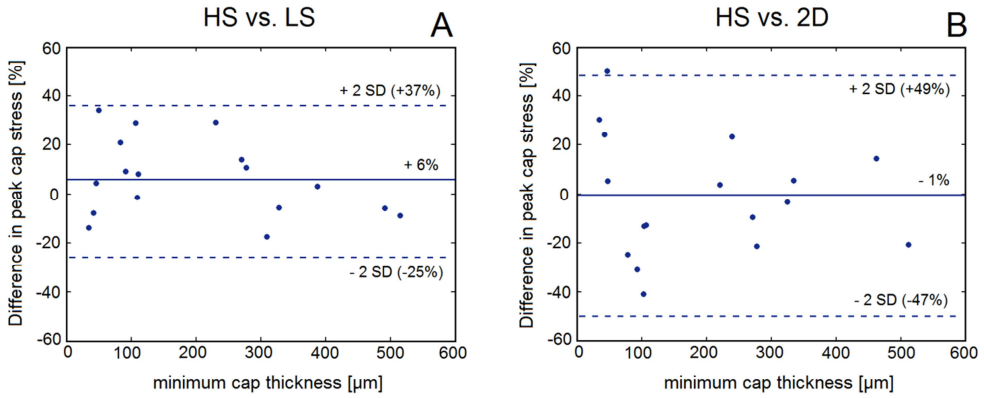


**Figure 6.** Relative difference in peak cap stress for shared slices of LS compared to HS (A), and 2D compared to HS (B) as a function of minimum cap thickness.

### Peak cap stress

The magnitude of the peak *cap* stress in the example cross section in Figure 4 also changed for lower axial sampling. For LS, the peak cap stress was 8% higher (125 kPa versus 116 kPa) and for 2D it was 26% lower (86 kPa versus 116 kPa). This again followed the general trend that the accuracy of the calculated peak cap stress significantly decreased for lower sampling, but without a clear systematic bias. In Figure 6, the relative difference in peak cap stress is plotted as a function of cap thickness for all caps present in the shared cross sectional slices studied. From the 17 cap regions identified, it was found that the peak cap stress in the LS case deviated +6 ± 15.5% ($p$ = 0.37, range [-17%, +34%]) from the HS case, and in the 2D case it deviated -1.2 ± 24.0% ($p$ = 0.45, range [-41%, +50%]). It is apparent from the plots that the minimum cap thickness was not a predictor for whether LS models would either under- or overestimate the peak cap stress; however, as Figure 6B shows, smaller cap thicknesses led to a larger range in errors in computed stresses for 2D models.

### Cap thickness – peak cap stress relationship

Although lower sampling caused significant changes in the absolute magnitude of peak stresses, we questioned whether parametrical relationships, such as the relationship between peak cap stress and minimum cap thickness, were influenced by lower sampling. In Figure 7 we plot this relationship for the HS, LS, and 2D models. This revealed that the relationship was unaffected by lower sampling. For thin caps (mean thickness of 71 µm), the mean peak cap stress for HS was 139 ± 57 kPa and for thick caps (mean thickness of 349 µm) 62 ± 27 kPa ($p < 0.01$). For LS this same

difference was observed: thin caps 120 ± 42 kPa and thick caps 60 ± 19 kPa ($p < 0.01$). Finally, for 2D simulations there was also a significant difference between the two groups: thin caps 123 ± 44 kPa and thick caps 61 ± 26 kPa ($p < 0.01$).

### Luminal wall curvature – peak plaque stress relationship

To gain insight into why lower sampling led to a wide, but unbiased, spread in peak plaque and cap stresses, we quantified the effect of axial sampling resolution on the average luminal wall $z$-curvature per cross section studied. Luminal wall axial curvature was chosen due to it being the most obvious geometrical parameter influenced by axial sampling resolution. In Figure 8 we plot the computed difference in average luminal $z$-curvature per slice between HS and LS geometries against the difference in computed peak plaque stress for that slice. Slice mean luminal $z$-curvature magnitudes were found to be in the range of 1.4 - $3.9 \cdot 10^{-4}$ µm$^{-1}$ (mean $2.4 \cdot 10^{-4}$ µm$^{-1}$), which are a factor 10 lower than typical in plane ($x$, $y$) curvatures (found to be in the order of $1 \cdot 10^{-3}$ µm$^{-1}$). Comparing LS to HS, the mean difference in curvature was -8 ± 34%, range [-51%, +70%] which indicates that luminal wall $z$-curvature, on average, tends to decrease for lower sampling. However, a positive or negative change in luminal wall $z$-curvature could not be correlated to an under- or overestimation in peak plaque stress.

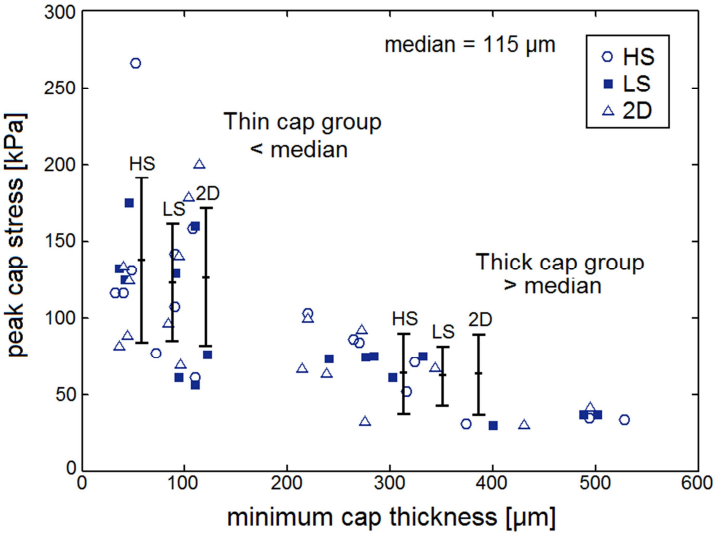


**Figure 7.** Peak cap stress as a function of minimum cap thickness for all three sampling cases.

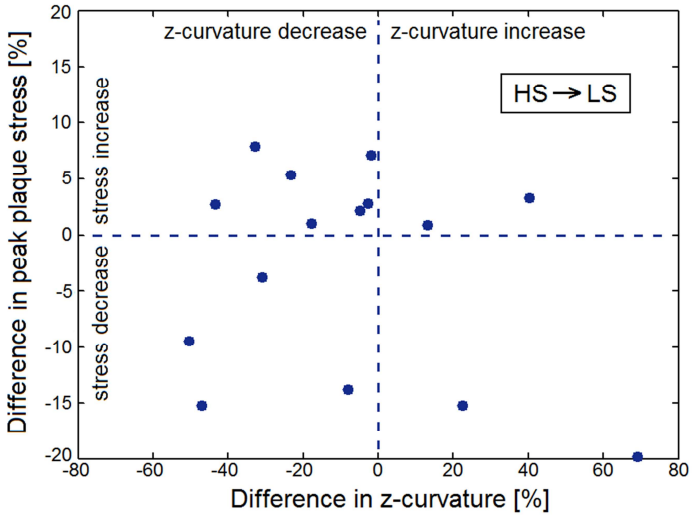


**Figure 8.** Difference in peak plaque stress as a function of difference in slice mean luminal wall *z*-curvature when comparing LS to HS.

## DISCUSSION

Biomechanical FEA is an increasingly used method to study vulnerable plaque rupture risk [7], thus it is vital that its constituents and their effects on model outcomes are well understood. This study focused on the geometry reconstruction step and quantified the influence of axial sampling on peak stresses. Results showed that lower sampling had a small influence on the qualitative stress distribution in plaques and on the location of peak stresses. The 3D qualitative stress distribution was found to be unaffected, suggesting that an axial sampling resolution of 1 mm is sufficient to capture the general geometrical features of atherosclerotic arterial segments. However, regarding the accuracy of calculated peak cap stresses, lower sampling did have a profound influence. Although lower sampling did not lead to a systematic bias in computed peak cap stresses (+6% and +1% for HS versus LS and HS versus 2D, respectively), it did lead to a larger error in calculated values (15.5% for HS versus LS up to 24.0% for HS versus 2D).

In order to understand the geometrical changes induced by lower sampling and their correlation with over- or underprediction of peak stresses, geometrical analyses were performed. While lower axial sampling led to geometrical axial smoothing, a decrease in axial curvature failed to correlate with lower peak stresses as would, at first hand, be expected from a mechanical perspective. Furthermore, the cap thickness turned out to be an inadequate predictor for a bias in computed peak stress differences.

It was also observed that lower sampling models did not include some small necrotic cores and other local morphological plaque features present in HS models, due to the resolution limit of 1.0 mm. It can be noted that LS models typically lead to an underestimation of lipid core axial length, illustrated in Figure 2. This underestimation can be up to 1 slice distance (1.0 mm) and could be significant if the missed geometrical information would have revealed a thin cap. With regard to spline interpolation, lower sampling can lead to both a locally thinner or thicker cap or vessel wall and a higher or lower axial curvature, either increasing or decreasing peak stresses. Combined, these geometrical effects lead to a complex interplay of parameters altered by lower sampling which causes a larger, but unbiased, error in computed peak stresses in shared slices. This error was larger for interpolated slices, implying that stresses in solely non-interpolated cross sections should be considered for 3D plaque stress computations.

The most extreme form of under sampling would be the use of single slice information, thus resulting in a 2D model. The comparison of 2D models with 3D resulted in the observation that absolute stress values from 2D simulations deviated significantly from the HS models: up to 48% for peak cap stresses. In a study by Ohayon et al. [36], a similar discrepancy in peak stress was found when comparing 2D simulations with 3D based on intravascular ultrasound data from one coronary arterial segment. Biased stress over prediction and difference in peak stress location for 2D models found in that study could be attributed to the use of a fine and a coarse mesh for 2D and 3D models respectively, whereas our study employed a similar mesh density for both models. An additional difference is that our study used decalcified tissue, which might be a smoothing factor. Although the 2D to 3D model comparison is valuable for this particular study on axial sampling resolution, it is of importance to note that this comparison cannot be translated directly into *in vivo* 2D and 3D stress simulations. This is because our study did not take any circumferential or axial residual stresses for 3D and 2D models into account. Residual stresses have been shown to have a crucial impact on peak plaque and cap stresses as well as on comparisons between 2D and 3D models [31,37,38]. Residual stresses are thus a vital constituent for accurate plaque stress modeling *in vivo*. Unfortunately, residual stresses are currently unobtainable from *in vivo* data used for noninvasive FEA-based plaque vulnerability assessment studies for which this study would be of relevance [7]. To truly investigate the outcome of patient-specific 2D and 3D plaque model comparisons, further studies should include residual stresses.

This work showed the possibility of using histology for 3D biomechanical plaque models, allowing contours based on a high axial and in-plane resolution and enabling the inclusion of thin media and adventitia layers, all in contrast to using *in vivo*

imaging data such as MRI. The use of histology, however, also led to certain limitations of this study. Decalcification was applied during histological processing which resulted in the fact that our study could not include macro- or microcalcifications into the models. The possible effects of decalcification on the outcome of this study remain unknown and should be investigated in future research by for instance utilizing additional µCT imaging. It has been shown that the presence of microcalcifications in the cap can increase the peak cap stress 2 to 5 fold, which is significantly larger than stress magnitude changes reported in this study [19,20]. A minimum axial resolution of 6.7 µm would be required for adequate reconstruction of microcalcifications to evaluate their effect on local peak cap stresses [20]. This resolution is beyond the currently available noninvasive imaging modalities. In case of microcalcifications, the results of this study still provide valuable insight into the cap background stress. Furthermore, axially aligned stacking of the cross sectional contours neglected the lumen centerline curvature, which might influence results. However, it is reasonable to assume that this curvature is small compared to axial changes of geometrical plaque features, and is thus of little influence on the plaque stresses.

## CONCLUSIONS

Axial sampling resolution was found to have a minor influence on general stress distributions and on the peak plaque/cap stress locations. Also, the relationship between peak cap stress and minimum cap thickness was found to be unaffected by lower sampling. Lower sampling did, however, have a major influence on the accuracy of the computed magnitude of peak plaque/cap stresses. Therefore, it can be concluded that high sampled 3D models are required for accurate plaque vulnerability assessment using stress magnitude as a measure for rupture risk.

## REFERENCES

1. Virmani R, Kolodgie FD, Burke AP, Farb A, Schwartz SM. Lessons from a sudden coronary death: a comprehensive morphological classification scheme for atherosclerotic lesions. Arterioscler Thromb Vasc Biol 2000;20:1262-1275.
2. Falk E, Shah PK, Fuster V. Coronary plaque disruption. Circulation 1995;92:657-671.
3. Yuan C, Zhang S, Polissar NL, Echelard D, Ortiz G, Davis JW, Ellington E, Ferguson MS, Hatsukami TS. Identification of fibrous cap rupture with magnetic resonance imaging is highly associated with recent transient ischemic attack or stroke. Circulation 2002;105:181-185.
4. Schaar JA, Muller JE, Falk E, Virmani R, Fuster V, Serruys PW, Colombo A, Stefanadis C, Ward Casscells S, Moreno PR, Maseri A, van der Steen AF. Terminology for high-risk and vulnerable coronary artery plaques. Report of a meeting on the vulnerable plaque, June 17 and 18, 2003, Santorini, Greece. Eur Heart J 2004;25:1077-1082.
5. Virmani R, Burke AP, Farb A, Kolodgie FD. Pathology of the vulnerable plaque. J Am Coll Cardiol 2006;47:C13-18.

6. Loree HM, Kamm RD, Stringfellow RG, Lee RT. Effects of fibrous cap thickness on peak circumferential stress in model atherosclerotic vessels. Circ Res 1992;71:850-858.
7. Sadat U, Teng Z, Gillard JH. Biomechanical structural stresses of atherosclerotic plaques. Expert Rev Cardiovasc Ther 2010;8:1469-1481.
8. Redgrave JN, Gallagher P, Lovett JK, Rothwell PM. Critical cap thickness and rupture in symptomatic carotid plaques. Stroke 2008;39:1722-1729.
9. Tang D, Teng Z, Canton G, Yang C, Ferguson M, Huang X, Zheng J, Woodard PK, Yuan C. Sites of rupture in human atherosclerotic carotid plaques are associated with high structural stresses: an in vivo MRI-based 3D fluid-structure interaction study. Stroke 2009;40:3258-3263.
10. Akyildiz AC, Speelman L, van Brummelen H, Gutiérrez MA, Virmani R, van der Lugt A, van der Steen AF, Wentzel JJ, Gijsen FJ. Effects of intima stiffness and plaque morphology on peak cap stress. Biomed Eng Online 2011;10:25.
11. Gao H, Long Q, Graves M, Gillard JH, Li ZY. Study of reproducibility of human arterial plaque reconstruction and its effects on stress analysis based on multispectral in vivo magnetic resonance imaging. J Magn Reson Imaging 2009;30:85-93.
12. Sadat U, Teng Z, Young VE, Li ZY, Gillard JH. Utility of magnetic resonance imaging-based finite element analysis for the biomechanical stress analysis of hemorrhagic and non-hemorrhagic carotid plaques. Circ J 2011;75:884-889.
13. Sadat U, Teng Z, Young VE, Graves MJ, Gaunt ME, Gillard JH. High-resolution magnetic resonance imaging-based biomechanical stress analysis of carotid atheroma: a comparison of single transient ischaemic attack, recurrent transient ischaemic attacks, nondisabling stroke and asymptomatic patient groups. Eur J Vasc Endovasc Surg 2011;41:83-90.
14. Vengrenyuk Y, Carlier S, Xanthos S, Cardoso L, Ganatos P, Virmani R, Einav S, Gilchrist L, Weinbaum S. A hypothesis for vulnerable plaque rupture due to stress-induced debonding around cellular microcalcifications in thin fibrous caps. Proc Natl Acad Sci 2006;103:14678-14683.
15. Teng Z, Sadat U, Ji G, Zhu C, Young VE, Graves MJ, Gillard JH. Lumen irregularity dominates the relationship between mechanical stress condition, fibrous-cap thickness, and lumen curvature in carotid atherosclerotic plaque. J Biomech Eng 2011;133:034501.
16. Teng Z, Sadat U, Li Z, Huang X, Zhu C, Young VE, Graves MJ, Gillard JH. Arterial luminal curvature and fibrous-cap thickness affect critical stress conditions within atherosclerotic plaque: an in vivo MRI-based 2D finite-element study. Ann Biomed Eng 2010;38:3096-3101.
17. Creane A, Maher E, Sultan S, Hynes N, Kelly DJ, Lally C. Prediction of fibre architecture and adaptation in diseased carotid bifurcations. Biomech Model Mechanobiol 2011;10:831-843.
18. Creane A, Maher E, Sultan S, Hynes N, Kelly DJ, Lally C. Finite element modelling of diseased carotid bifurcations generated from in vivo computerized tomographic angiography. Comput Biol Med 2010;40:419-429.
19. Rambhia SH, Liang X, Xenos M, Alemu Y, Maldonado N, Kelly A, Chakraborti S, Weinbaum S, Cardoso L, Einav S, Bluestein D. Microcalcifications increase coronary vulnerable plaque rupture potential: a patient-based micro-CT fluid-structure interaction study. Ann Biomed Eng 2012;40:1443-1454.
20. Maldonado N, Kelly-Arnold A, Vengrenyuk Y, Laudier D, Fallon JT, Virmani R, Cardoso L, Weinbaum S. A mechanistic analysis of the role of microcalcifications in atherosclerotic plaque stability: potential implications for plaque rupture. Am J Physiol Heart Circ Physiol 2012;303:619-628.
21. Gao H, Long Q, Das SK, Sadat U, Graves M, Gillard JH, Li ZY. Stress analysis of carotid atheroma in transient ischemic attack patients: evidence for extreme stress-induced plaque rupture. Ann Biomed Eng 2011;39:2203-2212.
22. Kock SA, Nygaard JV, Eldrup N, Fründ ET, Klaerke A, Paaske WP, Falk E, Yong Kim W. Mechanical stresses in carotid plaques using MRI-based fluid–structure interaction models. J Biomech 2008;41:1651-1658.
23. Li ZY, Tang T, U-King-Im J, Graves M, Sutcliffe M, Gillard JH. Assessment of carotid plaque vulnerability using structural and geometrical determinants. Circ J 2008;72:1092-1099.
24. Huang X, Teng Z, Canton G, Ferguson M, Yuan C, Tang D. Intraplaque hemorrhage is associated with higher structural stresses in human atherosclerotic plaques: an in vivo MRI-based 3d fluid-structure interaction study. Biomed Eng Online 2011;9:86.
25. Chau AH, Chan RC, Shishkov M, MacNeill B, Iftimia N, Tearney GJ, Kamm RD, Bouma BE, Kaazempur-Mofrad MR. Mechanical analysis of atherosclerotic plaques based on optical coherence tomography. Ann Biomed Eng 2004;32:1494-1503.

26. Ohayon J, Teppaz P, Finet G, Rioufol G. In-vivo prediction of human coronary plaque rupture location using intravascular ultrasound and the finite element method. Coron Artery Dis 2001;12:655-663.
27. Kural MH, Cai M, Tang D, Gwyther T, Zheng J, Billiar KL. Planar biaxial characterization of diseased human coronary and carotid arteries for computational modeling. J Biomech 2012;45:790-798.
28. Baldewsing RA, de Korte CL, Schaar JA, Mastik F, van der Steen AF. Finite element modeling and intravascular ultrasound elastography of vulnerable plaques: parameter variation. Ultrasonics 2004;42:723-729.
29. Huang H, Virmani R, Younis H, Burke AP, Kamm RD, Lee RT. The impact of calcification on the biomechanical stability of atherosclerotic plaques. Circulation 2001;103:1051-1056.
30. Speelman L, Akyildiz AC, den Adel B, Wentzel JJ, van der Steen AF, Virmani R, van der Weerd L, Jukema JW, Poelmann RE, van Brummelen EH, Gijsen FJ. Initial stress in biomechanical models of atherosclerotic plaques. J Biomech 2011;44:2376-2382.
31. Ohayon J, Dubreuil O, Tracqui P, Le Floc'h S, Rioufol G, Chalabreysse L, Thivolet F, Pettigrew RI, Finet G. Influence of residual stress/strain on the biomechanical stability of vulnerable coronary plaques: potential impact for evaluating the risk of plaque rupture. Am J Physiol Heart Circ Physiol 2007;293:H1987-H1996.
32. Vengrenyuk Y, Kaplan TJ, Cardoso L, Randolph GJ, Weinbaum S. Computational stress analysis of atherosclerotic plaques in apoE knockout mice. Ann Biomed Eng 2010;38:738-747.
33. Yuan C, Kerwin WS. MRI of Atherosclerosis. J Magn Reson Imaging 2004;19:710-719.
34. Gasser TC, Ogden RW, Holzapfel GA. Hyperelastic modelling of arterial layers with distributed collagen fibre orientations. J R Soc Interface 2006;3:15-35.
35. de Putter S, Wolters BJ, Rutten MC, Breeuwer M, Gerritsen FA, van de Vosse FN. Patient-specific initial wall stress in abdominal aortic aneurysms with a backward incremental method. J Biomech 2007;40:1081-1090.
36. Ohayon J, Finet G, Treyve F, Rioufol G, Dubreuil O. A three-dimensional finite element analysis of stress distribution in a coronary atherosclerotic plaque: In-vivo prediction of plaque rupture location. Biomech Appl to Comp Assist Surg 2005;225-241.
37. Cilla M, Peña E, Martínez MA. 3D computational parametric analysis of eccentric atheroma plaque: influence of axial and circumferential residual stresses. Biomech Model Mechanobiol 2012;11:1001-1013.
38. Tang D, Yang C, Zheng J, Woodard PK, Sicard GA, Saffitz JE, Yuan C. 3D MRI-based multicomponent FSI models for atherosclerotic plaques. Ann Biomed Eng 2004;32:947-960.

# The influence of inaccuracies in carotid MRI segmentation on atherosclerotic plaque stress computations

# 6

**Abstract** | Biomechanical finite element analysis (FEA) based on *in vivo* carotid magnetic resonance imaging (MRI) can be used to assess carotid plaque vulnerability noninvasively by computing peak cap stress. However, the accuracy of MRI plaque segmentation and the influence this has on FEA has remained unreported due to the lack of a reliable submillimeter ground truth. In this study, this influence is quantified using novel numerical simulations of carotid MRI. Histological sections from carotid plaques from 12 patients were used to create 33 ground truth plaque models. These models were subjected to numerical computer simulations of a currently used clinically applied 3.0T T1-weighted black-blood carotid MRI protocol (in-plane acquisition voxel size of 0.62 x 0.62 $mm^2$) to generate simulated *in vivo* MR images from a known underlying ground truth. The simulated images were manually segmented by three MRI readers. FEA models based on the MRI segmentations were compared with the FEA models based on the ground truth. MRI-based FEA model peak cap stress was consistently underestimated, but still correlated (R) moderately with the ground truth stress: R = 0.71, R = 0.47 and R = 0.76 for the three MRI readers respectively ($p < 0.01$). Peak plaque stretch was underestimated as well. The peak cap stress in thick-cap, low-stress plaques was substantially more accurately and precisely predicted (error of 12 ± 44 kPa) than the peak cap stress in plaques with caps thinner than the in-plane acquisition voxel size (error of 177 ± 168 kPa). It can be concluded that for reliable MRI-based FEA to compute the peak cap stress of carotid plaques with thin caps, the current clinically used in-plane acquisition voxel size (~0.6 mm) is inadequate. FEA plaque stress computations would be considerably more reliable if they would be used to identify thick-cap carotid plaques with low stresses instead.

**This chapter is based on:** Nieuwstadt HA, Speelman L, Breeuwer M, van der Lugt A, van der Steen AFW, Wentzel JJ, Gijsen FJH. The influence of inaccuracies in carotid MRI segmentation on atherosclerotic plaque stress computations. Journal of Biomechanical Engineering 2014;136:021015.

## INTRODUCTION

Atherosclerosis is a chronic cardiovascular disease in which plaques cause focal vessel wall thickening at flow-disturbed regions such as the carotid bifurcation [1]. Rupture prone, vulnerable plaques are constituted of a large lipid-rich necrotic core (LRNC) separated from the lumen by a thin fibrous cap (FC) [2]. Vulnerable plaques are of particular interest due to the fact that they can remain asymptomatic until FC rupture occurs followed by thrombus formation. For carotid plaques, this thrombosis is a cause of ischemic stroke, which ranks among the leading causes of morbidity and mortality worldwide [3]. Patients with a symptomatic carotid artery and >70% stenosis need to be treated to prevent an ipsilateral carotid territory ischemic stroke [4]. Although interventions through carotid endarterectomy (CEA) or stenting based on degree of stenosis criteria have been shown to be beneficial, these operative procedures are costly and carry some risk [5,6]. In addition, a significant fraction of the surgical interventions performed are possibly on stable, nonvulnerable carotid plaques, putting patients at unnecessary operative risk [7].

From a biomechanical perspective, plaque rupture occurs when the peak cap stress exceeds the local tissue strength, appointing stress as a more suitable marker for plaque vulnerability than merely the degree of stenosis or plaque composition [8-10]. This approach led to the extensive use of finite element analysis (FEA) to compute the stress/strain distribution within plaques [11]. FEA proves useful in determining geometrical risk factors associated with higher peak cap stresses and thus a higher rupture risk. For example, thinner FCs lead to higher peak cap stresses [12-14]. Recent studies suggested that peak plaque stretch can be related to plaque vulnerability as well. A localized high strain (from diastolic to systolic phase) in a plaque may expose possible neovasculature to large deformations. These localized high stretch conditions could cause damage to small neovessels in the plaque which in turn could trigger intraplaque hemorrhage [15,16]. Carotid magnetic resonance imaging (MRI) is the method of choice to obtain the plaque composition and geometry *in vivo* noninvasively through image segmentation [17,18]. This makes MRI-based FEA a promising methodology to better assess patient-specific carotid plaque vulnerability noninvasively, and numerous studies have utilized MRI-based FEA for carotid plaques [11,15,19-22].

At this point, a critical question has remained largely unaddressed: how accurately can the plaque geometry be recovered from *in vivo* carotid MRI, and what influence does this have on computed stresses? The current clinically achievable resolution of *in vivo* MRI is a limiting factor in measuring submillimeter features such as thin FCs, which are especially present in vulnerable plaques [11,15,19,23,24]. This raises concern, because the sensitivity of biomechanical FEA plaque models to FC

thickness is very high [13,14,25,26]. A careful evaluation of the accuracy and precision of MRI-based FEA plaque stress computations is therefore indispensable.

The difficulty in answering this question lies in the lack of an adequate ground truth (i.e., knowledge of the actual underlying geometry) needed to evaluate MRI plaque segmentation accuracy on a submillimeter level. A comparison between histological sections obtained after *in vivo* MRI of *the same vessel*, as is typically performed, is unreliable on a submillimeter scale due to deformation artifacts induced by histopathological processing (e.g., shrinkage), difficulties in registration, and axial partial volume effects in MRI. To circumvent these issues, we took an opposite approach in this study. We started out with a set of realistic carotid plaque models of which we knew the exact shape (ground truth), and then imaged these plaques with carotid MRI. We did this in a computational setting by using numerical simulations of an *in vivo* carotid MRI protocol which we introduced in a recent study [24]. With MRI simulations, we could generate a two-dimensional (2D) *in vivo* carotid MRI slice from an input, ground truth, carotid plaque model using a specified clinical carotid MRI pulse sequence. The segmentation on a simulated MR image could directly be compared with the ground truth carotid plaque model on a submillimeter scale. To create a set of realistic ground truth carotid plaque models, microscopy images of histological sections were used because they have a high resolution with staining for plaque components. The earlier mentioned limitations of histological processing did not apply anymore because we did not compare a histological section of a vessel with any imaging data of that same vessel as it once was *in vivo*. We used histology merely to create a set of realistic carotid plaque models for the MRI simulations. Through this MRI simulation approach, we investigated the influence of carotid MRI segmentation on plaque FEA by quantifying the correlation between the MRI model predicted peak cap stress and the ground truth peak cap stress.

## METHODS

An overview of this study's methodology is illustrated in Figure 1. Histological cross sections were manually segmented on µm-resolution microscopy images and converted to 2D computational FEA plaque models. The deformed carotid plaque geometries at 13.3 kPa (100 mmHg) were defined as the ground truth models, of which *in vivo* MR images were numerically simulated. These computer generated MR images were manually segmented by three readers to form MRI models. The ground truth models and the MRI models were then subjected to a FEA, yielding different results only because of differences in geometry/morphology. Each methodological step will now be discussed in detail.

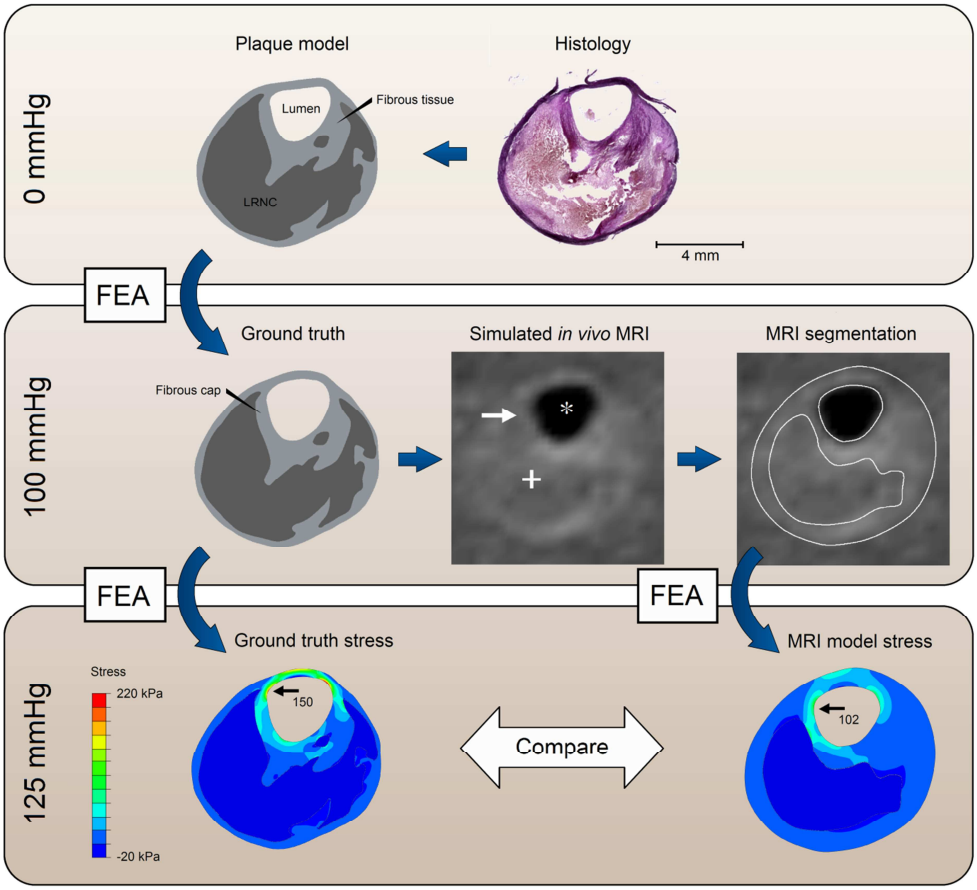


**Figure 1.** Methodology of the study. Each horizontally layered block represents an increasing arterial pressure of 0, 100 and 125 mmHg. Minimum FC thickness location and peak cap stress are indicated in ground truth and MRI models. In the simulated *in vivo* MR image, (+) indicates LRNC, (*) indicates lumen, and the white arrow the FC location. In the stress maps, black arrows indicate location and magnitude (in kPa) of the peak cap stress.

## Histology

We chose to use µm-resolution histological data to create a set of realistic ground truth carotid plaque models. We obtained 33 undamaged histological sections of excised plaques (>70% stenosis) from 12 patients which had been scheduled for CEA. The plaques were decalcified, embedded in paraffin, sliced at intervals of 1 mm with a thickness of 5 µm, and stained with an Elastica van Gieson staining to distinguish

between the relevant plaque components (for details, see [27]). Fibrous tissue and LRNC were manually delineated on the µm-resolution microscopy images by one expert (K.v.G.). These histological sections provided us with highly accurate plaque component segmentations, which could then serve as ground truth models. The histological plaque cross sections each had a different morphology and each had at least 1 LRNC with a FC $<$ 1 mm. The limitations of histological processing preventing a reliable comparison with actual MRI of the same vessel as it once was *in vivo,* as described in our introduction, did not apply anymore. High-resolution histological sections were used in this study only to create realistic ground truth plaque models for the MRI simulations and not for the aforementioned comparison.

### Finite element analysis

To create the ground truth plaque models, the histology segmentations were converted to 2D plaque models and the deformed, pressurized, *in vivo* shapes were computed using FEA (Abaqus Standard 6.11, Dassault Systèmes Simulia Corp., Providence, Rhode Island, USA). Fibrous tissue and LRNC were modeled as homogeneous, incompressible, isotropic materials, using a neo-Hookean model: $W = C(I_1 - 3)$, where $W$ is the strain energy density function and $I_1$ the first invariant of the deformation tensor. The material constant $C$ was set to 167 kPa for fibrous tissue and 1 kPa for LRNC [14,26]. The 2D FEA models were meshed with an average of 50 000 four-node linear hybrid quadrilateral elements. A plane strain assumption was used. The loading condition required to recover the *in vivo* plaque shape consisted of a static intraluminal pressure of 13.3 kPa (100 mmHg). The resulting deformed geometries, referred to as the ground truth plaque models, were used as input for the MRI simulations. After manual MRI segmentation, the MRI models and the ground truth models were subjected to a systolic pressure of 16.7 kPa (125 mmHg) with FEA. The MRI plaque models involved an initially pressurized geometry at 13.3 kPa; thus adequate prestress conditions needed to be taken into account for the MRI models. To achieve that, the backward incremental method was used to compute the initial prestress present in the MRI models [28]. For more details on the FEA procedure see [26].

### MRI simulations

The Jülich extensible MRI simulator (JEMRIS) was used for the MRI simulations [29]. The software provides pulse sequence implementation and, by solving the Bloch equations, a subsequent numerical MRI simulation of a given input sample model. The sample model consists of the geometry with the MRI material properties (relaxation times $T_1$, $T_2$ and M0). The model is discretized to a finite number of spins, of which the

responses in spatial signal intensity are computed, resulting in a computer generated MR image. For this study, a typical clinically applied 3.0T 2D T1-weighted turbo spin-echo, contrast enhanced, black-blood pulse sequence designed to image the FC, was simulated [24]. The simulated protocol had the following scan parameters: repetition/echo times of 800 ms/10 ms, respectively, a reduced field-of-view of 37 x 37 $mm^2$, a matrix size of 60 x 60 resulting in an in-plane acquisition voxel size of 0.62 x 0.62 $mm^2$, an interpolated reconstructed voxel size of 0.31 x 0.31 $mm^2$ after standard k-space zero-padding, and an imposed signal-to-noise ratio of 16.7. A best case imaging scenario was chosen with a high signal-to-noise ratio, absence of any motion artifacts, and the ideal case of an axially uniform plaque morphology over a single slice thickness (the clinical protocol had a slice thickness of 2 mm). The latter choice allowed us to use 2D, cross-sectional, plaque sample models, for which we used histological sections. Because of this 2D approach for MRI we could discard the now redundant slice selection gradients and replaced the selective radio frequency pulses by full excitation pulses in the simulated pulse sequence. Fibrous, LRNC and background tissues were modeled and given apparent $T_1$ relaxation times of 680 ms, 1220 ms and 1412 ms respectively, and a fixed $T_2$ of 50 ms. The resulting MR images were independently segmented by three expert MRI readers (M.B., G.H. and J.S.) blinded to the ground truth. For more details regarding the MRI simulation procedure see [24].

### Modification of the MRI protocol to improve FEA reliability

In our earlier study, we explored how the clinical MRI protocol could be modified in order to improve plaque segmentation accuracy. In that study, we found that when a doubling of the scan time was invested in doubling the in-plane spatial resolution (although decreasing the signal-to-noise ratio), FC thickness measurements improved [24]. In this current study, we investigated if that specific modified protocol with a double resolution (in-plane acquisition voxel size of 0.31 x 0.31 $mm^2$) but with more noise (a signal-to-noise ratio of 5.9) and more scan time would improve MRI-based FEA reliability as well. All other scan parameters were kept unaltered.

### Analysis

The maximum principal stress was used as the stress measure. The peak cap stress, confined to only the cap region, was obtained from the FEA models. The peak value of the maximum principal stretch within the entire diseased plaque region was used for the peak plaque stretch [15]. Note that peak cap stress and peak plaque stretch are different physical quantities and do not need to be situated at the same location. Previous studies suggested that peak cap stress can be related to geometrical

parameters such as minimum FC thickness, the maximum in-plane luminal wall curvature at the cap region (here referred to as the peak cap curvature), and the LRNC area [14,30-32]. These geometrical parameters were therefore obtained from the ground truth and MRI models. Peak cap stress, peak plaque stretch and minimum FC thickness results were analyzed separately for caps thicker and thinner than 0.62 mm (the MRI in-plane acquisition voxel size) present in the ground truth models. The Pearson correlation coefficient (R) was used to compute correlations (significant when $p < 0.01$). The single measure intraclass correlation coefficient (ICC) was used to assess the agreement (absolute) between MR readers. A nonparametrical one-tailed Mann–Whitney $U$ test was used for comparisons between groups of data where $p < 0.01$ was considered significant (S). Unless otherwise indicated, data are shown as the mean value ± standard deviation (SD) or are shown as the mean value (min, max) in the case of measurements from the three MRI readers.

## RESULTS

Prior to reporting the results for all plaque models, we will first discuss two examples that reflect the general trends observed. In the first example (Figure 2), the ground

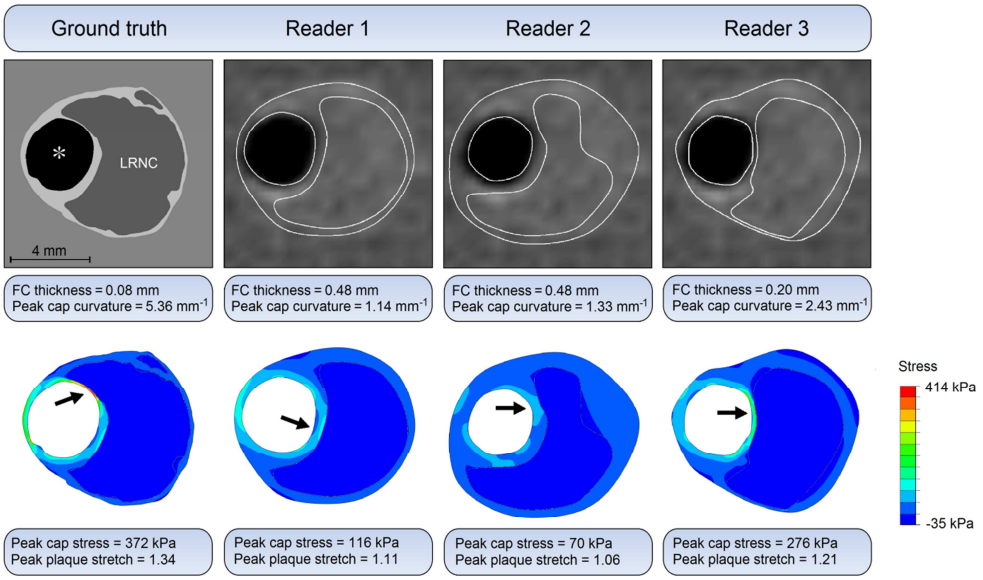


**Figure 2.** Example 1: thin cap, high peak cap stress case. Ground truth model and stress map (first column), and the three MR reader segmentations and MRI model stress maps (columns 2 through 4). (*) indicates lumen, black arrows show the location of peak cap stress.

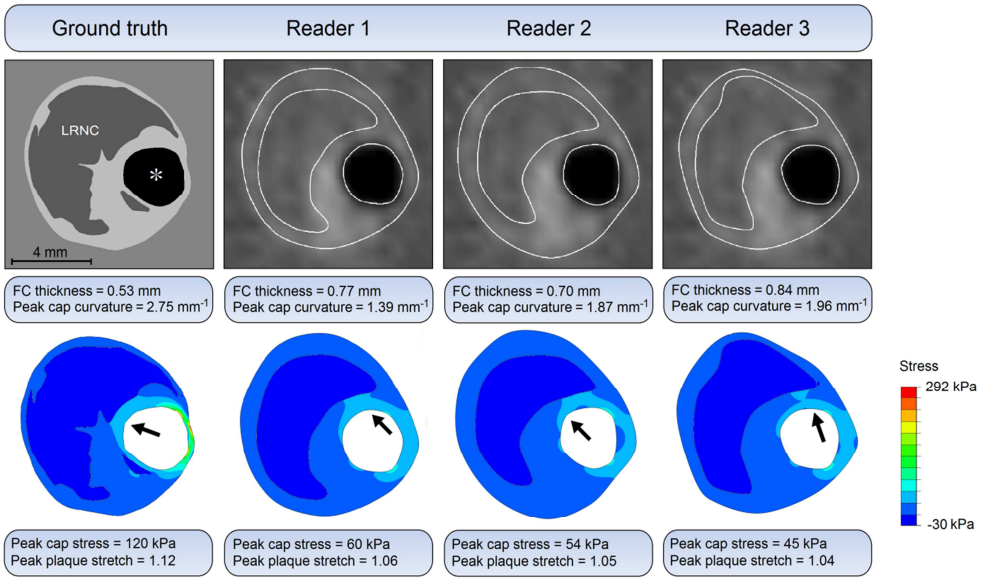


**Figure 3.** Example 2: thick cap, low peak cap stress case. Ground truth model and stress map (first column), and the three MR reader segmentations and MRI model stress maps (columns 2 through 4). (*) indicates lumen, black arrows show the location of peak cap stress.

truth plaque model has a very thin FC (0.08 mm) and a large LRNC (30.1 $mm^2$). In the MRI segmentation, the FC was severely overestimated in thickness by all three readers, resulting in a mean relative error of +383% (min, max: +150%, +600%). Furthermore, component edges were smoothed in the MRI models due to the limited spatial resolution, resulting in severe underestimation of peak cap curvature with a mean relative error of -70% (-88%, -55%). Intravoxel partial volume averaging effects of low intensity LRNC mixed with higher intensity fibrous tissue are the most likely cause of underestimation of LRNC size: error of -24% (-21%, -7%). The FEA results show high localized stresses in the load-bearing FC and thin vessel walls, and low stresses in the LRNC. Peak cap stress magnitude was underestimated by all MRI models with a mean relative error of -59% (-81%, -26%). The peak cap stress location was relatively accurately predicted. Peak plaque stretch was underestimated with a mean relative error of -16% (-21%, -10%). In the second example (Figure 3), the ground truth model had a thicker FC (0.53 mm), resulting in a lower peak cap stress in the ground truth. Cap thickness was quantified more accurately and precisely by the MRI readers, yielding a mean relative error of +45% (+32%, +58%). The peak cap stress was again systematically underestimated with a mean relative error of -56% (-63%, -50%), although with a smaller absolute difference (mean absolute error

of -67 kPa for the second example versus -218 kPa for the first example). Peak plaque stretch was again underestimated with a mean relative error of -6% (-7%, -5%).

### MRI model peak cap stress relation to ground truth peak cap stress

Figure 4A shows the MRI model peak cap stress plotted against the ground truth model peak cap stress. The MRI models were found to systematically underestimate the peak cap stress. This underestimation was less severe for low stress plaques. The MRI model peak cap stress correlated moderately with the ground truth stress: R = 0.71, R = 0.47 and R = 0.76 for the three MRI readers, respectively (all $p < 0.01$). Due to differences in segmentation, the MRI models exhibited weak interreader agreement in peak cap stress prediction: ICC = 0.55 ($p < 0.01$). The average peak cap stress derived from the three reader MRI models also correlated with the ground truth, yielding an R = 0.76 ($p < 0.01$). In Figure 4B, the absolute difference between the MRI model peak cap stress and the ground truth model peak cap stress is plotted as function of ground truth minimum FC thickness. Thicker cap plaques in general lead to lower stresses and consequently to a smaller difference between the MRI model peak cap stress and the ground truth value. That difference improved from -177 ± 168 kPa (mean ± SD) for plaques with FCs thinner than

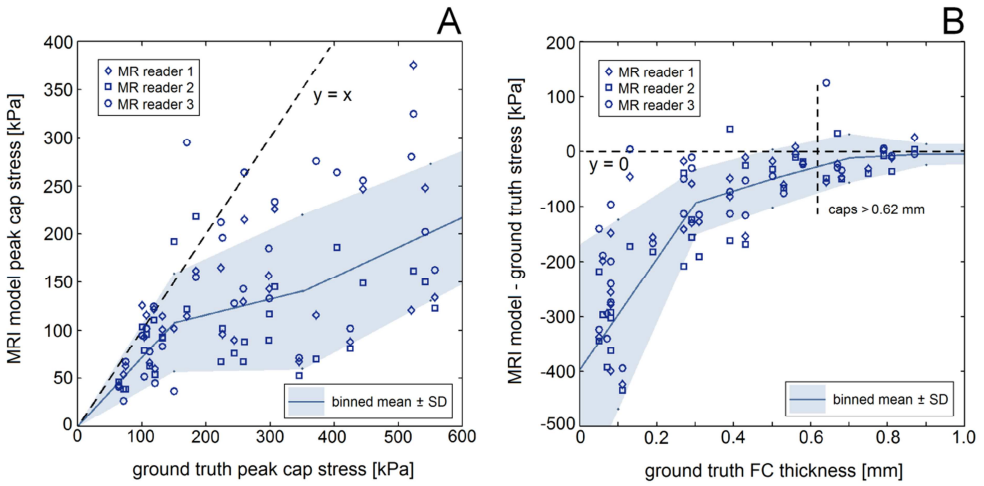


**Figure 4.** (A) Peak cap stress in MRI models as a function of peak cap stress in ground truth models for the three MR readers. Bin size is 200 kPa. (B) Difference in computed peak cap stress between MRI models and ground truth models as a function of ground truth minimum FC thickness. Bin size is 0.2 mm.

0.62 mm (the MRI in-plane acquisition voxel size) to only -12 ± 44 kPa for plaques with FCs thicker than 0.62 mm.

### Geometrical parameters

The geometrical parameters studied are shown in the box plots, grouping all data, in the top row of Figure 5 (ground truth versus MRI models). Similar trends were

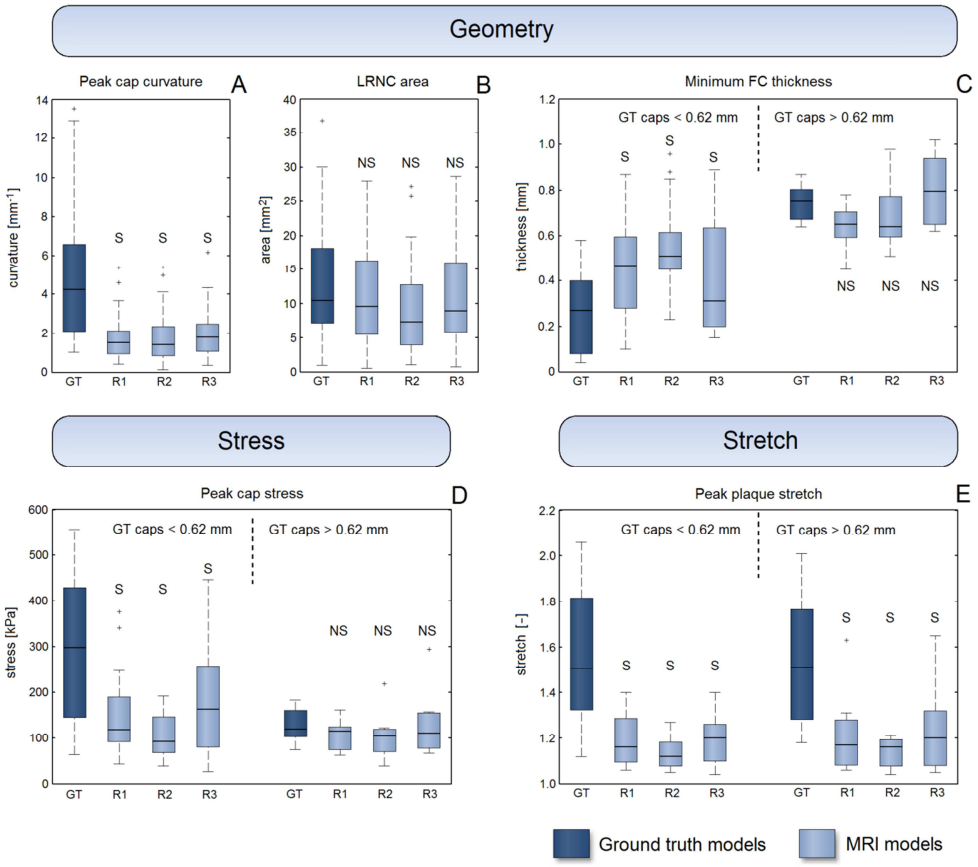


**Figure 5.** Box plots showing grouped data for all plaque models: ground truth versus MRI models. GT = ground truth, R = reader, (+) indicates an outlier, (S) indicates significance with respect to the ground truth data distribution, $p < 0.01$, (NS) indicates no significance. Whiskers mark the extreme data points not considering outliers. (A-C) Geometrical parameters studied, (D) peak cap stress and (E) peak plaque stretch. For (C-E), data are split into two groups with a ground truth minimum FC thickness smaller (left) and larger (right) than 0.62 mm (MRI in-plane acquisition voxel size).

observed for all three MRI readers. Peak cap curvature (Figure 5A) was consistently underestimated in the MRI models ($p < 0.01$). LRNC area (Figure 5B) was underestimated less severely ($p$ = NS). Minimum FC thickness (Figure 5C) for plaques with caps < 0.62 mm ($n = 25$) was consistently overestimated ($p < 0.01$) whereas the minimum FC thickness for plaques with caps > 0.62 mm ($n = 8$) was measured more accurately ($p$ = NS).

### Peak cap stress relation to geometrical parameters

Peak cap stress (Figure 5D) was underestimated in MRI models for plaques with caps < 0.62 mm ($p < 0.01$), but more accurately predicted for caps > 0.62 mm ($p$ = NS). Within solely the ground truth models, FC thickness was the only geometrical parameter studied that significantly correlated with peak cap stress: R = -0.75 ($p < 0.01$). Within solely the MRI models, also only measured FC thickness correlated with peak cap stress, but more weakly: R = -0.48 ($p < 0.01$) for reader 1, R = -0.25 ($p$ = NS) for reader 2, and R = -0.51 ($p < 0.01$) for reader 3. A comparison between the ground truth and the MRI models showed that none of the studied geometrical parameters in the ground truth correlated significantly with MRI model peak cap stress. But for the other way around, ground truth peak cap stress correlated with measured FC thickness in the MRI models: R = -0.63, R = -0.70 and R = -0.57 for readers 1–3 (all $p < 0.01$).

### Peak plaque stretch relation to peak cap stress

Peak plaque stretch (Figure 5E) was found to be severely underestimated in MRI models, with no notable improvement for caps > 0.62 mm ($p < 0.01$ for both groups). Recall that peak plaque stretch can be located within the entire plaque area, whereas peak cap stress is confined to only the cap, and they are different physical quantities. Within solely the ground truth models, peak plaque stretch correlated significantly with peak cap stress: R = 0.50 ($p < 0.01$). Peak plaque stretch did not correlate significantly with any of the geometrical parameters studied. Within solely the MRI models, again peak plaque stretch only correlated significantly with peak cap stress: R = 0.52 ($p < 0.01$), R = 0.44 ($p = 0.02$) and R = 0.57 ($p < 0.01$) for readers 1–3. A comparison between the ground truth and the MRI models showed that the MRI model peak plaque stretch did not correlate significantly with the ground truth peak plaque stretch. The MRI model peak plaque stretch correlated weakly with the ground truth peak cap stress: R = 0.46 ($p = 0.02$), R = 0.16 ($p$ = NS) and R = 0.47 ($p = 0.01$) for readers 1–3.

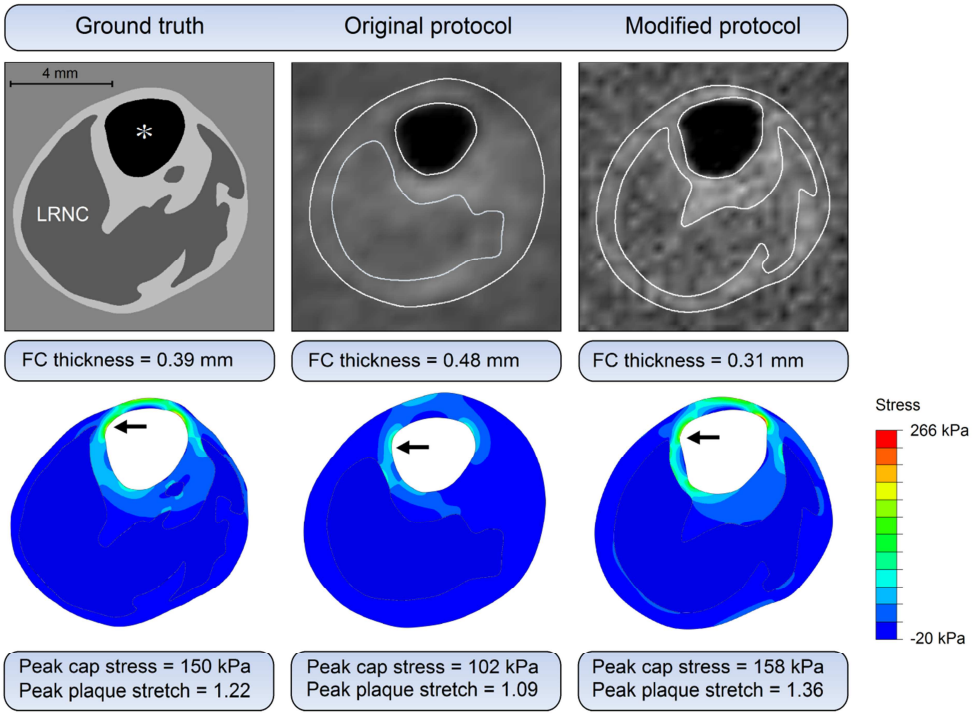


**Figure 6.** Example of the modified MRI protocol data. Ground truth model and stress map (first column). Segmentation and stress maps for the original protocol (second column) and the modified protocol (third column). (*) indicates lumen, black arrows show the location of peak cap stress.

### Modification of the MRI protocol to improve FEA reliability

In the example shown in Figure 6, the modified protocol (with a doubling of the resolution) resulted in improvements with respect to LRNC segmentation, FC thickness quantification, and peak cap stress prediction. Qualitatively, a better segmentation and a more similar stress distribution were obtained. For all plaque models, peak cap stress was underestimated less for high stress plaques (Figure 7A). There was, however, no improvement in the correlation between the MRI model peak cap stress and the ground truth stress: $R = 0.69$ ($p < 0.01$). The difference between the MRI model peak cap stress and ground truth stress as a function of cap thickness (Figure 7B) decreased with respect to the original protocol (see Figure 4B), yielding a higher accuracy for plaques with thinner caps. Interestingly, peak cap stress in plaques with caps $> 0.31$ mm (the MRI in-plane acquisition voxel size for the modified protocol)

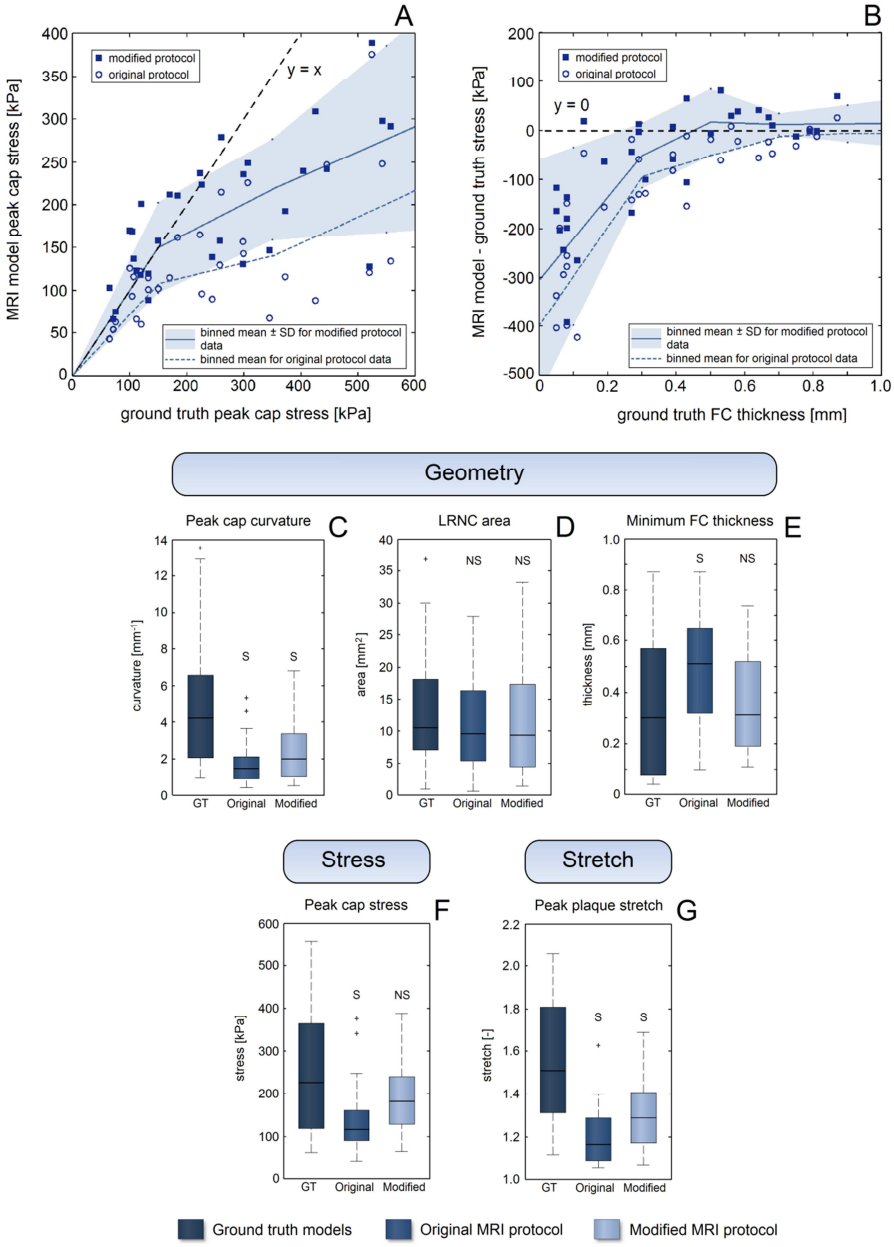


**Figure 7.** (A) Peak cap stress in MRI models as a function of peak cap stress in ground truth models for the original and the modified protocol. Bin size is 200 kPa. (B) Difference in computed peak cap stress between MRI models and ground truth models as a function of ground truth minimum FC thickness. Bin size is 0.2 mm. (C-G) Box plots showing grouped data of all parameters studied, for details see caption of Figure 5.

was now overestimated in 56% (9/16) of those cases. The grouped data (box plots in Figures 7C-G) show that the modified protocol yielded improvements with regard to the parameters studied. The MRI model peak cap stretch still did not correlate significantly with the ground truth peak cap stretch.

## DISCUSSION

As for any biomechanical analysis, knowledge of three fundamental aspects is required for reliable plaque stress computations: the constitutive laws, the loading/boundary conditions, and the geometry [33]. This study focused on the latter with regard to MRI-based carotid plaque FEA and utilized MRI simulations to provide a direct ground truth comparison. This makes it the first study that quantified the accuracy and precision of MRI-based plaque FEA when it comes to plaque segmentation. Our five key findings are:

1. MRI-based carotid plaque models consistently underestimate peak cap stress.
2. However, peak cap stress predicted by MRI-based plaque FEA models still correlates with the ground truth peak cap stress, although this correlation is relatively weak.
3. The thinner the cap becomes, the worse the reliability of MRI-based plaque FEA gets.
4. There is no correlation between MRI model peak plaque stretch and ground truth peak plaque stretch; there is, however, a weak correlation with peak cap stress.
5. A doubling of the MRI protocol scan time and spatial in-plane resolution (to an acquired in-plane voxel size of 0.31 x 0.31 $mm^2$) reduces the underestimation of peak cap stress, but does not significantly improve the correlation between the MRI model peak cap stress and the ground truth peak cap stress.

We found that the outcome of carotid plaque FEA depends strongly on the underlying MRI protocol and image segmentation. For the clinical MRI protocol that was studied, the limited in-plane resolution and likely other contributions such as noise and insufficient component contrast negatively influenced plaque segmentation accuracy [24]. Due to intravoxel partial volume effects and point-spread function signal blurring, the thickness of FCs thinner than the in-plane voxel size was severely overestimated and imprecisely measured. In addition, LRNC size and peak cap curvature were underestimated, explaining findings (1-3). Previous FEA studies warned of the possible influence of the limited currently achievable acquisition voxel size in clinical carotid

MRI with regard to FC thickness [11,19], but were unable to provide any quantification of error. Although lower than favorable, our study did show a significant correlation between the MRI-based predicted peak cap stress and the ground truth, which supports the numerous previous studies that utilized carotid MRI-based plaque FEA. Because a ground truth comparison is not required for the mere assessment of the agreement between different readers or different methods, an earlier FEA study by Gao et al. [19] investigated interreader agreement which yielded results similar to the ones in our study. Another study by Adame et al. [34] compared manually measured FC thickness on MRI with automatic segmentation and found good agreement, although only plaques with thick caps (0.5–3 mm) were studied. In our study, we found severe systematic biases (overestimation of cap thickness, underestimation of stress), which would otherwise remain unnoticed in any study on interreader agreement or manual versus automatic MRI segmentation. Regarding finding (4), computed peak plaque stretch in the MRI models fell within the (low) range reported in a previous study by Teng et al. [15]. Interestingly, while they are fundamentally different in definition, peak plaque stretch correlated with peak cap stress. So if peak cap stress is a marker for plaque vulnerability, then so might peak plaque stretch be. Plaque stretch can be measured *in vivo* for example by ultrasound elastography [35]. Higher resolution MRI protocols with a smaller acquisition voxel size can provide more detailed plaque imaging, particularly regarding small features on a submillimeter scale such as thin FCs which are crucial for reliable biomechanical modeling [36,37]. In our study, modifying the MRI protocol by halving the acquisition voxel size to 0.31 x 0.31 $mm^2$ indeed yielded improvements despite an increase in noise, finding (5), suggesting that MRI voxel size is a likely cause of the errors in predicted peak cap stress. But since no improvement in correlation was found for the modified MRI protocol, even greater advances in carotid MRI hardware/protocol design are indispensable for reliable identification of thin-cap, high-stress plaques through MRI-based FEA.

Although the MRI simulations were previously evaluated to provide realistic images with regard to plaque segmentation [24], there are a number of simplifications in this study that need to be addressed. The ground truth models are 2D, they contain only idealized homogenized plaque components and they lack incorporation of *in vivo* anisotropic constitutive relations and incorporation of residual stresses, which all combined inhibit the knowledge of the true *in vivo* stress. Also, a histological specimen obtained from CEA might not reflect the true vessel morphology and stress/strain configuration, because media and adventitia layers were absent and thus not modeled. The ground truth stress value is therefore logically not the actual, true stress in the 3D *in vivo* patient plaque but merely in the ground truth plaque model used for the simulated MR imaging and subsequent FEA. This, of course, works greatly to our

advantage: since the ground truth models are defined in the way we chose, the MRI-based models do not need to account for any of the aforementioned issues. As such, these simplifications do *not* play a role here with regard to the comparison between an MRI-based FEA model and our reference ground truth model. These simplifications are therefore not limitations with regard to the comparisons we made, which involved only differences in plaque morphology/geometry. It has to be noted that due to the use of homogenized components, sharp tissue borders might elevate local peak stretch/stress levels in the ground truth models. Calcium and intraplaque hemorrhage were not included in the ground truth models. Calcifications were omitted due to decalcification in histological processing, which also led to the absence of any microcalcifications in the ground truth models. Note that microcalcifications would be, due to their small size, undetectable with current clinical carotid MRI protocols [38]. We used histological sections to create realistic ground truth carotid plaque models, but other high resolution imaging modalities (intravascular ultrasound, optical coherence tomography, *ex vivo* µm-resolution MRI, etc.) could just as well be used. Future studies could take such an approach in the case of a non-simulated MRI setting, and image a plaque with MRI combined with a second, high resolution (invasive) imaging modality serving as a ground truth. In our study, we chose to model a best-case MR imaging scenario. This meant: (1) no plaque axial variations within an MRI slice and thus no axial partial volume effects by using 2D cross-sectional plaque geometries, (2) a high signal-to-noise ratio and (3) no motion artifacts. In effect, the errors for FEA we reported in this study are representative for a best-case imaging scenario. Note that the use of 2D MRI simulations led us to the use of 2D FEA. In a previous study, we investigated in detail the differences between 2D and 3D plaque FEA with regard to computed peak stress [26]. Since JEMRIS simulations can be extended to 3D as well, future studies should be able to quantify the negative influence of a 3D plaque morphology on MR imaging and subsequent FEA in a similar simulated MRI setting. This would be of particular relevance for 2D MRI protocols which often acquire anisotropic voxels leading to a slice thickness much larger than the in-plane voxel size. In our study we used only manual MRI segmentation; future studies should investigate the reliability of MRI-based carotid plaque FEA with regard to automated segmentation [39].

In this study, we found that thick-cap plaques (> acquisition voxel size) were measured profoundly more accurately than thin-cap plaques, and it is to be expected that even thicker caps (our plaque dataset contained only caps < 1 mm) can be quantified even more reliably. It should be noted that these low-stress plaques with >70% stenosis in our dataset had been surgically removed through CEA, while the low peak cap stress indicates that these plaques might have been stable. Changing one's perspective, one can deduce that carotid MRI-based FEA could be useful in reliably

identifying the most stable, low-stress plaques instead of the high-stress ones. This in turn might reduce the high number of costly and risky operative interventions on potentially nonvulnerable carotid plaques [7,40]. Further biomechanical studies and subsequent clinical trials have to be performed to test this hypothesis.

## CONCLUSIONS

For reliable MRI-based FEA of thin-cap carotid plaques, the current clinically achievable acquired in-plane voxel size (~0.6 mm) is inadequate. The thinner the FC becomes (thus the higher the peak cap stress), the worse the reliability of MRI-based FEA gets. Because thick FCs can be quantified more accurately, carotid MRI-based FEA stress computations would be considerably more reliable if they would be used to identify low-stress carotid plaques instead.

## ACKNOWLEDGEMENTS

We thank Jeroen Sonnemans and Gilion Hautvast (formerly of Philips Healthcare, Best, the Netherlands) for performing MRI segmentations, and Kim van Gaalen (Erasmus Medical Center, Rotterdam, the Netherlands) for histological processing.

## REFERENCES

1. Slager CJ, Wentzel JJ, Gijsen FJH, Schuurbiers JCH, van der Wal AC, van der Steen AFW, Serruys PW. The role of shear stress in the generation of rupture-prone vulnerable plaques. Nat Clin Pract Cardiovasc Med 2005;2:401-407.
2. Virmani R, Burke AP, Farb A, Kolodgie FD. Pathology of the vulnerable plaque. J Am Coll Cardiol 2006;47:C13-18.
3. Go AS, et al. Heart disease and stroke statistics - 2013 update: a report from the American heart association. Circulation 2013;127:e6-e245.
4. Rothwell PM, Eliasziw M, Gutnikov SA, Fox AJ, Taylor DW, Mayberg MR, Warlow CP, Barnett HJM. Analysis of pooled data from the randomised controlled trials of endarterectomy for symptomatic carotid stenosis. Lancet 2003;361:107-116.
5. Rerkasem K, Rothwell PM. Systematic review of the operative risks of carotid endarterectomy for recently symptomatic stenosis in relation to the timing of surgery. Stroke 2009;40:e564-e572.
6. Yadav JS, et al. Protected carotid-artery stenting versus endarterectomy in high-risk patients. New Engl J Med 2004;351:1493-1501.
7. Barnett HJM, et al. Benefit of carotid endarterectomy in patients with symptomatic moderate or severe stenosis. New Engl J Med 1998;339:1415-1425.
8. Richardson PD, Davies MJ, Born GVR. Influence of plaque configuration and stress distribution on fissuring of coronary atherosclerotic plaques. Lancet 1989;2:941-944.
9. Loree HM, Kamm RD, Stringfellow RG, Lee RT. Effects of fibrous cap thickness on peak circumferential stress in model atherosclerotic vessels. Circ Res 1992;71:850-858.
10. Ohayon J, Teppaz P, Finet G, Rioufol G. In-vivo prediction of human coronary plaque rupture location using intravascular ultrasound and the finite element method. Coron Artery Dis 2001;12:655-663.

11. Sadat U, Teng Z, Gillard JH. Biomechanical structural stresses of atherosclerotic plaques. Expert Rev Cardiovasc Ther 2010;8:1469-1481.
12. Tang D, Yang C, Zheng J, Woodard PK, Saffitz JE, Petruccelli JD, Sicard GA, Yuan C. Local maximal stress hypothesis and computational plaque vulnerability index for atherosclerotic plaque assessment. Ann Biomed Eng 2005;33:1789-1801.
13. Gao H, Long Q. Effects of varied lipid core volume and fibrous cap thickness on stress distribution in carotid arterial plaques. J Biomech 2008;41:3053-3059.
14. Akyildiz AC, Speelman L, van Brummelen H, Gutiérrez MA, Virmani R, van der Lugt A, van der Steen AF, Wentzel JJ, Gijsen FJ. Effects of intima stiffness and plaque morphology on peak cap stress. Biomed Eng Online 2011;10:1-13.
15. Teng Z, Sadat U, Wang W, Bahaei NS, Chen S, Young VE, Graves MJ, Gillard JH. Intraplaque stretch in carotid atherosclerotic plaque - an effective biomechanical predictor for subsequent cerebrovascular ischemic events. PLoS One 2013;8:e61522.
16. Teng Z, He J, Degnan AJ, Chen S, Sadat U, Bahaei NS, Rudd JH, Gillard JH. Critical mechanical conditions around neovessels in carotid atherosclerotic plaque may promote intraplaque hemorrhage. Atherosclerosis 2012;223:321-326.
17. Underhill HR, Hatsukami TS, Fayad AZ, Fuster V, Yuan C. MRI of carotid atherosclerosis: clinical implications and future directions. Nat Rev Cardiol 2010;7:165-173.
18. Li F, Yarnykh VL, Hatsukami TS et al. Scan-rescan reproducibility of carotid atherosclerotic plaque morphology and tissue composition measurements using multicontrast MRI at 3T. J Magn Reson Imaging 2010;31:168-176.
19. Gao H, Long Q, Graves M, Gillard JH, Li ZY. Study of reproducibility of human arterial plaque reconstruction and its effects on stress analysis based on multispectral in vivo magnetic resonance imaging. J Magn Reson Imaging 2009;30:85-93.
20. Li Z, Howarth S, Trivedi RA, U-King-Im JM, Graves MJ, Brown A, Wang L, Gillard JH. Stress analysis of carotid plaque rupture based on *in vivo* high resolution MRI. J of Biomech 2006;39:2611-2622.
21. Tang D, Teng Z, Canton G, Yang C, Ferguson M, Huang X, Zheng J, Woodard PK, Yuan C. Sites of rupture in human atherosclerotic carotid plaques are associated with high structural stresses: an *in vivo* MRI-based 3D fluid-structure interaction study. Stroke 2009;40:3258-3263.
22. Sadat U, Teng Z, Young VE, Graves MJ, Gaunt ME, Gillard JH. High-resolution magnetic resonance imaging-based biomechanical stress analysis of carotid atheroma: a comparison of single transient ischaemic attack, recurrent transient ischaemic attacks, nondisabling stroke and asymptomatic patient groups. Eur J Vasc Endovasc Surg 2011;41:83-90.
23. Redgrave JN, Gallagher P, Lovett JK, Rothwell PM. Critical cap thickness and rupture in symptomatic carotid plaques: the Oxford plaque study. Stroke 2008;39:1722-1729.
24. Nieuwstadt HA, Geraedts TR, Truijman MTB, Kooi ME, van der Lugt A, van der Steen AFW, Wentzel JJ, Breeuwer M, Gijsen FJH. Numerical simulations of carotid MRI quantify the accuracy in measuring atherosclerotic plaque components *in vivo*. Magn Reson Med 2014;72:188-201.
25. Finet G, Ohayon J, Rioufol G. Biomechanical interaction between cap thickness, lipid core composition and blood pressure in vulnerable coronary plaque: impact on stability or instability. Coron Artery Dis 2004;15:13-20.
26. Nieuwstadt HA, Akyildiz AC, Speelman L, Virmani R, van der Lugt A, van der Steen AFW, Wentzel JJ, Gijsen FJH. The influence of axial image resolution on atherosclerotic plaque stress computations. J Biomech 2013;46:689-695.
27. Groen HC, van Walsum T, Rozie S et al. Three-dimensional registration of histology of human atherosclerotic carotid plaques to *in vivo* imaging. J Biomech 2010;43:2087-2092.
28. Speelman L, Akyildiz AC, den Adel B et al. Initial stress in biomechanical models of atherosclerotic plaques. J Biomech 2011;44:2376-2382.
29. Stöcker T, Vahedipour K, Pflugfelder D, Shah NJ. High-performance computing MRI simulations. Magn Reson Med 2010;64:186-193.
30. Li ZY, Tang T, U-King-Im J, Graves M, Sutcliffe M, Gillard JH. Assessment of carotid plaque vulnerability using structural and geometrical determinants. Circ J 2008;72:1092-1099.
31. Teng Z, Sadat U, Li Z, Huang X, Zhu C, Young VE, Graves MJ, Gillard JH. Arterial luminal curvature and fibrous-cap thickness affect critical stress conditions within atherosclerotic plaque: an *in vivo* MRI-based 2D finite-element study. Ann Biomed Eng 2010;38:3096-3101.

32. Teng Z, Sadat U, Ji G, Zhu C, Young VE, Graves MJ, Gillard JH. Lumen irregularity dominates the relationship between mechanical stress condition, fibrous-cap thickness, and lumen curvature in carotid atherosclerotic plaque. J Biomech Eng 2011;133:034501.
33. Humprey JD. Cardiovascular solid mechanics: cells, tissues, and organs. 757 pages. Springer, New York, 2002.
34. Adame IM, van der Geest RJ, Wasserman BA, Mohamed MA, Reiber JHC, Lelieveldt BPF. Automatic segmentation and plaque characterization in atherosclerotic carotid artery MR images. MAGMA 2004;16:227-234.
35. Ribbers H, Lopata RG, Holewijn S, Pasterkamp G, Blankensteijn JD, de Korte CL. Noninvasive two-dimensional strain imaging of arteries: validation in phantoms and preliminary experience in carotid arteries *in vivo*. Ultrasound Med Biol 2007;33:530-540.
36. Jahnke C, Dietrich T, Paetsch I, Koehler U, Preetz K, Schnackenburg B, Fleck E, Graf K, Nagel E. Experimental evaluation of the detectability of submillimeter atherosclerotic lesions in ex vivo human iliac arteries with ultrahigh-field (7.0 T) magnetic resonance imaging. Int J Cardiovasc Imaging 2007;23:519-527.
37. Balu N, Yarnykh VL, Chu B, Wang J, Hatsukami T, Yuan C. Carotid plaque assessment using fast 3D isotropic resolution black-blood MRI. Magn Reson Med 2011;65:627-637.
38. Rambhia SH, Liang X, Xenos M, Alemu Y, Maldonado N, Kelly A, Chakraborti S, Weinbaum S, Cardoso L, Einav S, Bluestein D. Microcalcifications increase coronary vulnerable plaque rupture potential: a patient-based micro-CT fluid-structure interaction study. Ann Biomed Eng 2012;40:1443-1454.
39. Liu W, Balu N, Sun J, Zhao X, Chen H, Yuan C, Zhao H, Xu J, Wang G, Kerwin WS. Segmentation of carotid plaque using multicontrast 3D gradient echo MRI. J Magn Reson Imaging 2012;35:812-819.
40. Farrell B, Fraser A, Sandercock P, Slattery J, Warlow, CP. Randomised trial of endarterectomy for recently symptomatic carotid stenosis: final results of the MRC European Carotid Surgery Trial (ECST). Lancet 1998;351:1379-1387.

# Local mechanical characterization of atherosclerotic plaques – combination of ultrasound displacement imaging and inverse finite element analysis

7

**Abstract |** Biomechanical models have the potential to predict plaque rupture. Accurate material properties of plaque components are a prerequisite for model reliability. This study aims to estimate these material properties by combining ultrasound strain imaging and inverse finite element modeling. Iliac arteries with plaques were excised from 6 atherosclerotic pigs and subjected to an inflation test with pressures ranging from 10 to 120 mmHg. The arteries were imaged with high frequency 40 MHz ultrasound. Deformation maps of the plaques were reconstructed by cross correlation of the ultrasound radiofrequency data. Subsequently, the arteries were perfusion fixed for histology, and wall, intima, and calcifications were annotated. The histological data were non-uniformly registered to the ultrasound data to construct a finite element model of the plaques. Upon solving the inverse problem and minimizing their cumulative difference, the computed and measured displacements showed an excellent agreement, implying that the finite element models were able to capture local inhomogeneities within the plaque. Non-linear stiffening of both the wall and the intima was observed. The artery wall was markedly stiffer than the intima (877 ± 459 kPa versus 100 ± 68 kPa at 100 mmHg). The large spread illustrates the wide variation amongst plaques. We demonstrated the feasibility of a mixed experimental-numerical approach to determine the material properties of individual atherosclerotic plaque components. We conclude that, due to the observed variations, plaque-specific mechanical properties are required to increase stress-simulation accuracy.

**This chapter is based on:** Akyildiz AC, Hansen HHG, Nieuwstadt HA, Speelman L, de Korte CL, van der Steen AFW, Gijsen FJH. Local mechanical characterization of atherosclerotic plaques - combination of ultrasound displacement imaging and inverse finite element analysis. Submitted.

## INTRODUCTION

Atherosclerotic plaques are characterized by a local thickening of the arterial vessel wall, mainly caused by lipid and inflammatory cell infiltration, smooth muscle cell migration and proliferation and extracellular matrix buildup [1]. Some atherosclerotic plaques have a higher chance of causing clinical events and are called thin cap fibroatheromas or vulnerable plaques. Vulnerable plaques are morphologically characterized by a large lipid core and a relatively thin fibrous cap, separating the lipid core from the lumen [2]. Rupture of the cap exposes the content of the lipid core to the blood stream leading to intraluminal thrombosis. Thrombosis triggered by plaque rupture is the predominant cause of myocardial infarction and stroke [3].

Means of accurately predicting plaque rupture-risk are lacking. Biomechanical studies showed that high stress regions in atherosclerotic plaques correspond to rupture locations [4,5]. The rationale behind this is that rupture occurs when the stress at a certain location inside the cap exceeds the local cap strength. Biomechanical models that are used to compare computed cap stresses with cap strength have the potential to improve plaque rupture risk assessment [6]. For accurate stress calculations, biomechanical plaque models not only rely strongly on the plaque geometry, but also on the material properties of plaque components [7,8]. However, experimental data for plaque properties are scarce and available data span a wide range [9,10].

One of the underlying reasons of that wide spread in the experimental data is that commonly applied testing methods, including uniaxial tensile testing, generally involve destructing the plaque. By assessing atherosclerotic plaques with *in vivo* deformation measurements or *ex vivo* inflation tests, the structural integrity of the tissue is not compromised. *Ex vivo* inflation tests have been widely used to estimate material properties of healthy vessels [11,12]. Generally, the deformation of the outer border of the vessel wall was measured. The vessel was modeled as a thin walled cylinder and the material properties were obtained by solving the problem analytically [13-15]. Due to the complex morphology of atherosclerotic plaques, determination of the material properties cannot be done analytically and requires more advanced approaches such as inverse finite element (FE) analysis.

With inverse FE analysis, material properties can be estimated by adjusting material parameters in the FE simulations iteratively and minimizing the difference between the computed and measured deformations. The feasibility of this methodology was demonstrated using synthetic, simulated inflation test data as input [16-20]. Some research groups used the inverse FE based on global plaque deformation measurements, using either intravascular ultrasound or magnetic resonance imaging [21]. The main drawback of using global deformation measurements is that the underlying FE model cannot incorporate multiple plaque components. Baldewsing et al. applied intravascular

ultrasound to obtain local deformation measurements, and they were able to demonstrate the feasibility of the method to generate elasticity maps of coronary plaques [22]. The latter study focused on *in vivo* applications to determine the material properties for small incremental strain values, and the shape of individual plaque components was restricted to reduce the degrees of freedom. A study by Beattie et al. subjected aortic segments to *ex vivo* inflation tests to determine material properties using microscopy techniques to measure local displacements [23]. While this technique proved effective, it limits future utilization in a clinical setting.

In this study a novel hybrid approach was developed for mechanical characterization of atherosclerotic plaques based on *ex vivo* inflation tests. The method combines high resolution ultrasound deformation measurements and histology-derived plaque morphological information with inverse FE analysis to compute the local, nonlinear material properties of atherosclerotic plaque components. The approach was applied to characterize advanced atherosclerotic plaques from porcine iliac arteries.

## METHODS

The methodology of this study consists of three main parts: *ex vivo* inflation tests, FE modeling, and estimation of material properties of plaque components (Figure 1). The individual steps are explained below in details.

### *Ex vivo* inflation tests

Atherosclerotic iliac arteries (n = 6) were collected from diabetic pigs that were on a high cholesterol diet. Streptozotocin-induced diabetic pigs (~45 kg) were fed supplemental (40% of dietary energy) saturated fat/cholesterol, unsaturated fat or starch for 10 weeks. The pigs showed substantial amounts of atherosclerotic lesions in the arterial system. Details of this animal model can be found in [24].

Immediately after sacrificing the animals, iliac arteries were excised and snap-frozen in liquid nitrogen. Arteries were stored at -80° C until the day of inflation experiments. For the experiments, the arteries were thawed to room temperature and cannulated. The side branches were closed by sutures. Based on the estimated *in vivo* length, the arteries were stretched 20% in longitudinal direction and preconditioned between 80 and 120 mmHg ten times. In the inflation experiments, the intraluminal pressure was increased first from 10 mmHg to 120 mmHg in a quasi-steady nature. The tests were conducted in a custom built vessel perfusion system at room temperature.

Deformation of the atherosclerotic vessel wall during the inflation test was imaged with a Vevo® 2100 ultrasound system (FUJIFILM VisualSonics, Inc., Toronto,

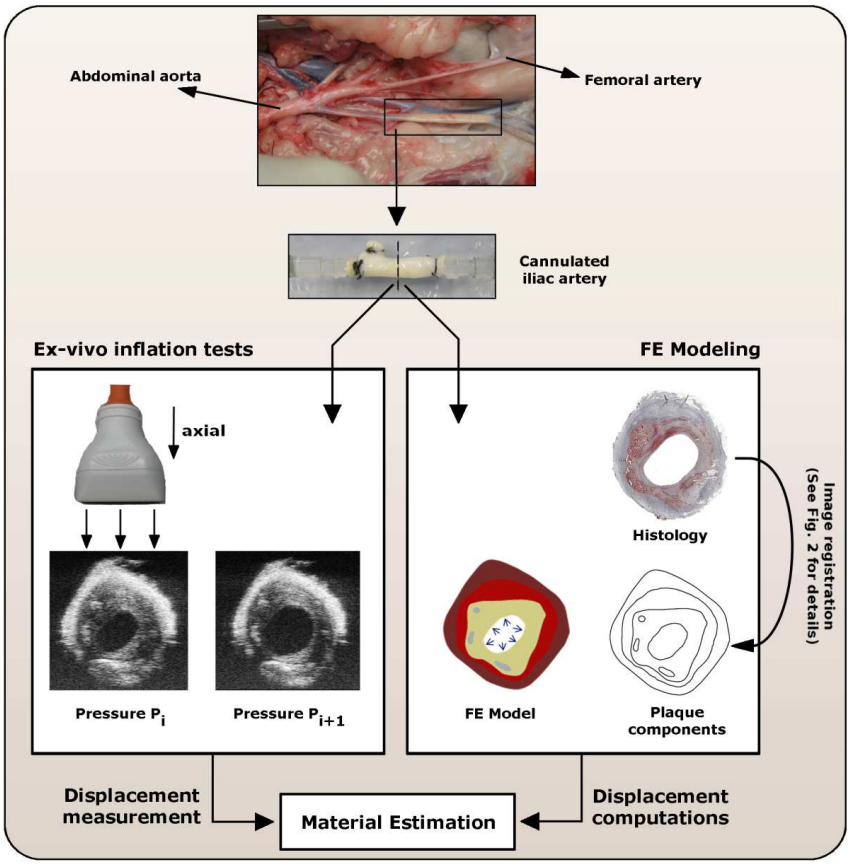


**Figure 1.** Methodology of the study consists of three main parts: *ex vivo* inflation tests, FE modeling, and estimation of material properties.

Canada) using a high frequency linear array transducer (MS550D with center frequency = 40 MHz). Before the inflation experiments, a 3D reconstruction of the segment was generated by stacking a series of 2D B-mode images using a 3D motor stage. A location with a substantial atherosclerotic plaque, at least 10 mm away from either cannula, was identified visually. The location was marked with a tissue marker pen on the outside of the vessel to match it to subsequent histology preparation. Transversal cross-sectional B-mode ultrasound images and radiofrequency (RF) data were recorded at this location at each pressure step.

The RF data enable us to calculate the axial (along the ultrasound lines) and lateral (in the direction perpendicular to ultrasound lines) displacements on the transversal plaque cross-section with high precision. Due to the availability of phase

and amplitude information in axial direction, the displacement estimate in this direction will be more accurate than in the lateral direction. The displacement estimation is performed in three iterations with a coarse-to-fine 2D cross-correlation method using RF data, explained in detail in [25]. The displacement estimation method was originally developed for clinical ultrasound scanners using center frequencies up to 10 MHz, but here applied for high-frequency scanners for the first time. In the first iteration, template and search kernel sizes of 3850 x 715 $\mu m^2$ (axial x lateral) and 7700 x 935 $\mu m^2$ with a kernel overlap of 50% in the axial direction and a kernel overlap of 92% in the lateral direction were used to find a coarse displacement estimate. In the second iteration template and search windows sizes of 60 x 715 $\mu m^2$ and 120 x 935 $\mu m^2$ were used with a window overlap of 75% and 92% in the axial and lateral direction, respectively. In the last iteration local aligning of the data including parabolic interpolation of the cross-correlation peak was performed to obtain accurate subsample displacement estimates. The kernel sizes remained the same in iteration two and three. A median filter of 5 x 5 displacement pixels was applied after each iteration to decrease the amount of outlying displacement values. The final spatial resolution for the displacement estimates was 15 µm in axial direction and 55 µm in the lateral direction.

### Finite element models

Plaque morphology is crucial in FE models if mechanical characterization of individual plaque components is aimed for. However, ultrasound imaging is very limited in providing this information, since it does not provide sufficient contrast between components. To overcome this problem, we used a hybrid approach in which histology images depict the detailed information of different plaque components (Figure 2). To obtain the histological images, the arteries were fixed with formaldehyde for histology at 10 mmHg and 20% longitudinal pre-stretch. Slices of five microns thickness from the imaged plaque cross-section were used for oil red o (ORO) staining, counter stained with hematoxylin. In ORO staining, lipids and fatty acids appear red. The counter-staining hematoxylin stains the nuclei and calcium blue. This staining enabled us to delineate the adventitia, media, intima, calcium, lumen, and the outer border of the vessel wall.

The histological images were slightly different in shape and size than the B-mode images due to histology preparation. To ensure that the plaque morphology in the FE models accurately reflects the plaque morphology in the inflation tests, the histology images were registered to B-mode images. Contours of plaque components delineated on histology images were mapped on ultrasound images (Figure 2C-F) using the image registration software Elastix [26]. First, the lumen contour and the outer

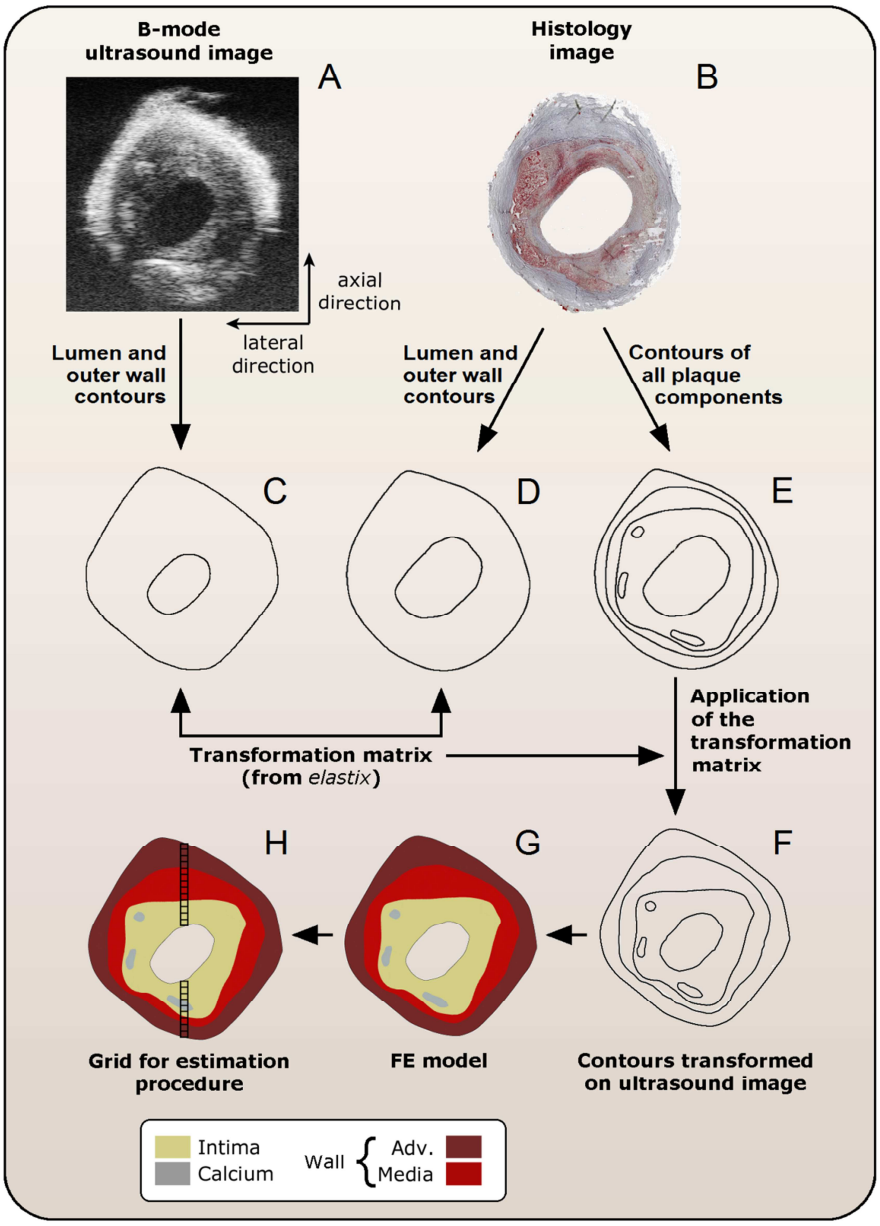


**Figure 2.** Illustration of how the geometry for FE models was obtained. Plaque component borders drawn on histology images were transformed onto the B-mode ultrasound image by the image registration software *Elastix*. Axial (along the ultrasound lines) and lateral (in the direction perpendicular to ultrasound lines) directions are indicated next to the B-mode image.

vessel wall contour were manually drawn both on the ultrasound image obtained at 10 mmHg (Figure 2C) and on the histology image (Figure 2D). Subsequently, the contours on the images were mapped with Elastix. This resulted in a transformation matrix from histology image to ultrasound image for the entire plaque cross-section. Finally, the contours of the plaque components drawn on the histology image (Figure 2E) were transformed onto the ultrasound image (Figure 2F) by using the transformation matrix obtained in the previous step. The transformed histology contours were used to create 2D FE models of the plaques with detailed morphology information (Figure 2G).

Based on the registered histology images, FE models (ABAQUS, version 6.11) were created to simulate the plaque deformation during the inflation tests. The possible nonlinearity in the material behavior of plaque components was modeled with a nonlinear, incompressible neo-Hookean model for all plaque components. The incompressible neo-Hookean material model is characterized by the strain energy density function $W$ defined as $W = C(I_1 - 3)$, where $C$ is the shear modulus and $I_1$ is the first invariant of the left Cauchy-Green deformation tensor. Identical shear moduli were assigned to adventitia and media. This material complex is referred to as "wall" in the rest of the paper. Calcium was assumed to be very stiff ($C = 10^5$ kPa). To prevent rigid body motion in the FE simulations, a very soft and compressible solid buffer layer surrounding the plaque was created and zero-displacement boundary conditions were applied to its outer border. The models were pressurized intraluminally following the protocol of the inflation experiment, and solved using previously developed numerical procedures [7,27].

## Estimation of material properties

A grid search method was employed for the material parameter estimation. The material parameters were altered within a pre-specified range with a constant step size, and all possible combinations of the parameters were simulated. In the estimation procedure, shear moduli of plaque wall and intima were varied between 1 and 400 kPa in the FE models. The measured displacements from the central region of the plaques in the axial direction were used in the estimation procedure to find the optimum material properties. Plaques were located in the test setup such that the thickest plaque section was in this central region. A grid with 100 µm element size (~6x the axial and ~2x the lateral in-plane resolution of ultrasound data) was generated in this plaque region as illustrated in Figure 2H. The total number of elements in the grids varied between 30 and 50 depending on the plaque thickness.

In each grid element, both the computed and measured displacements were averaged. To cover the material nonlinearity in the physiological pressure range, the

displacements from 10 to 80 mmHg (step 1), from 80 to 100 mmHg (step 2), and from 100 to 120 mmHg (step 3) were used in the analysis. An objective function, $F$, to be minimized in the estimation procedure for each pressure step was defined as

$$F = \sum_{j=1}^{n} (u_j^{comp} - u_j^{meas})^2, \quad (1)$$

where $u_j^{comp}$ and $u_j^{meas}$ are the average computed and measured displacements, respectively, similar as done in [23]. In the objection function, $F$, "$j$" represents the grid element number and "$n$" the total number of the grid elements. The FE simulation with the lowest value of the objective function $F$ was considered as the best match to the experimental measurements and the shear moduli used in this FE model were taken as the final estimates of the intima and wall material properties. The estimation procedure was run for all 3 pressure steps separately to enable a shear modulus estimation for each pressure step. The corresponding Young's modulus values, $E$, of the estimated shear moduli were calculated with the formula, $E = 6C$, and reported in the remainder of the paper for an easy comparison with the results reported in literature. The goodness of the parameter estimation for each plaque and each pressure step was evaluated by computing the relative difference between the measured and computed displacement:

$$\Delta u_{rel} = \left[ \left( \frac{\sqrt{F}}{n} \right) < u^{meas} > \right] \times 100\%, \quad (2)$$

where $< u^{meas} >$ represents the average absolute displacement for each pressure step.

## RESULTS

Of the six porcine iliac plaques, two plaques were concentric and four were eccentric. Histology images revealed morphological heterogeneity of the plaques (Figure 3). Atherosclerotic intima contained extracellular lipids and collagen fibers (Figure 3, plaque 4). No lipid pool or necrotic core was present in any of the plaques. All but plaque 1 contained calcium in varying amounts. The calcifications were localized usually near the intima-media interface (Figure 3, plaque 6).

Displacement measurements were successfully performed with the cross correlation technique applied to the RF data from high frequency ultrasound imaging. An example (plaque 3) of the measured displacements from 10 to 80 mmHg in the

axial and lateral directions is shown in the upper panel of Figure 4. Axial displacements showed a smooth profile. As expected, the lateral displacement measurements were less accurate. The corresponding computed displacements (of the simulation with the minimum objective function value) are shown in the lower panel of Figure 4. The principal displacements within the plaque were outwards in the radial direction, which is the expected deformation profile of a pressurized arterial segment.

Figure 5 represents the measured and computed axial displacements in the grid elements (lines A-B and C-D) for all three pressure steps for plaque 3. For pressure step 1, the displacement of point A was measured as +0.20 mm whereas point B displaced by +0.56 mm. This implies that the tissue between point A and B was compressed by 0.36 mm. Similarly, the tissue between the point C and D was compressed by 0.20 mm. The computed displacements showed a very good agreement

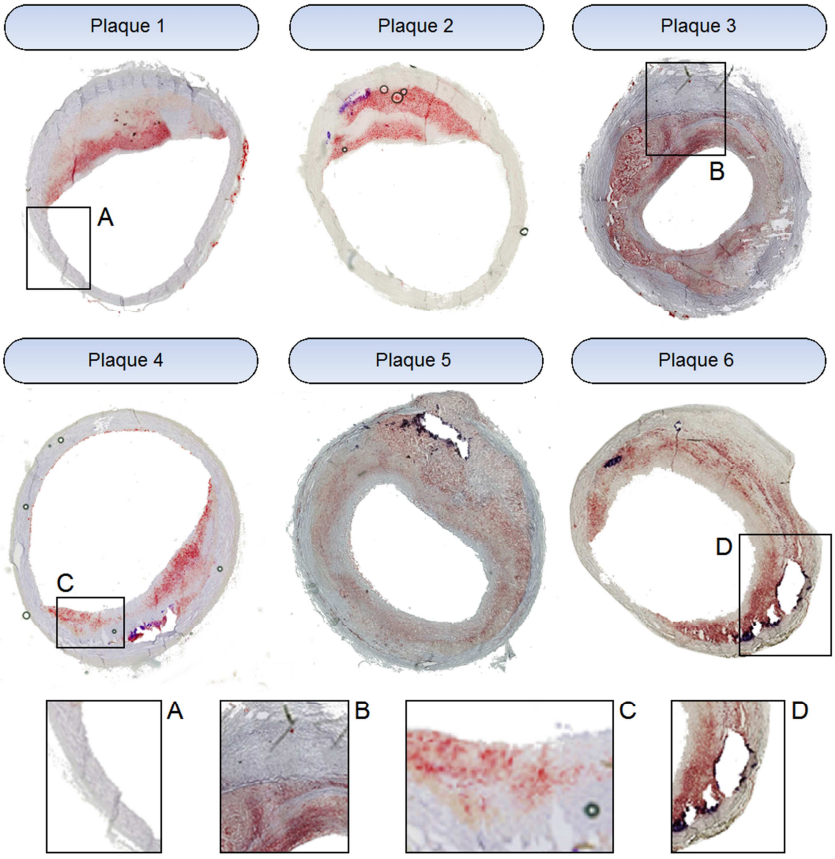


**Figure 3.** Histology images of the atherosclerotic plaques from porcine iliac arteries.

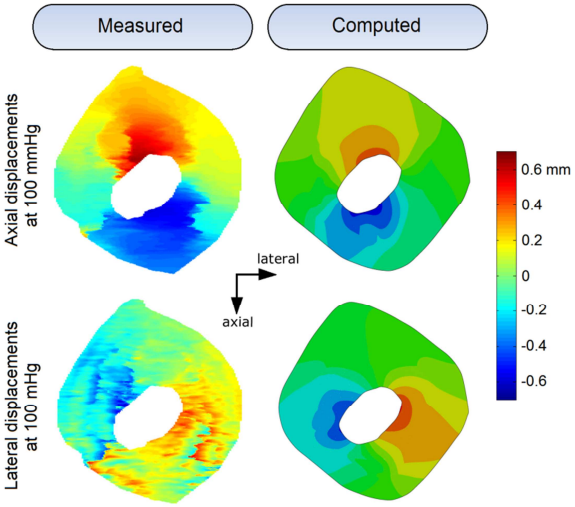


**Figure 4.** Measured (left) and computed (right) displacement maps in the axial direction (parallel to the ultrasound beam) in the top row and lateral direction (perpendicular to the ultrasound beam) in the bottom row for plaque 3 due to intraluminal pressure increase for pressure step 1 (from 10 to 80 mmHg).

with the measured displacements. For this plaque and pressure step 1, the relative difference between the measured and computed displacement, $\Delta u_{rel}$, was 2.3%. Not only the general deformation pattern, but also local deformations were captured with both the ultrasound measurements and FE simulations. The plateau in the measured displacements between the points C and D suggests that this region showed a relatively small compression. Inspection of the histology and ultrasound images confirmed the presence of calcium in this region (Figure 2). For pressure steps 2 and 3, the measured displacements were smaller than for pressure step 1 as the pressure increase for step 2 and 3 was smaller. The tissue region between A and B was compressed by 0.023 mm during pressure step 2 and by 0.019 mm during pressure step 3. The smaller compression in pressure step 2 compared to step 3 indicates that the tissue stiffened as the pressure increased. The $\Delta u_{rel}$ for pressure steps 2 and 3 was 3.2% and 3.9%, respectively.

Table 1 provides the Young's modulus values for atherosclerotic intima and wall for the 6 models and the mean values. Both plaque components showed increasing stiffness with increasing pressure. The mean Young's modulus (± standard deviation) for intima was 24 (±17) kPa for the pressure change from 10 to 80 mmHg, 100 (±68) kPa for the pressure change from 80 to 100 mmHg, and 190 (±187) kPa for the pressure increase from 100 to 120 mmHg. On average, the wall layer was stiffer than the intima for all pressure steps. For plaque wall, the mean Young's modulus

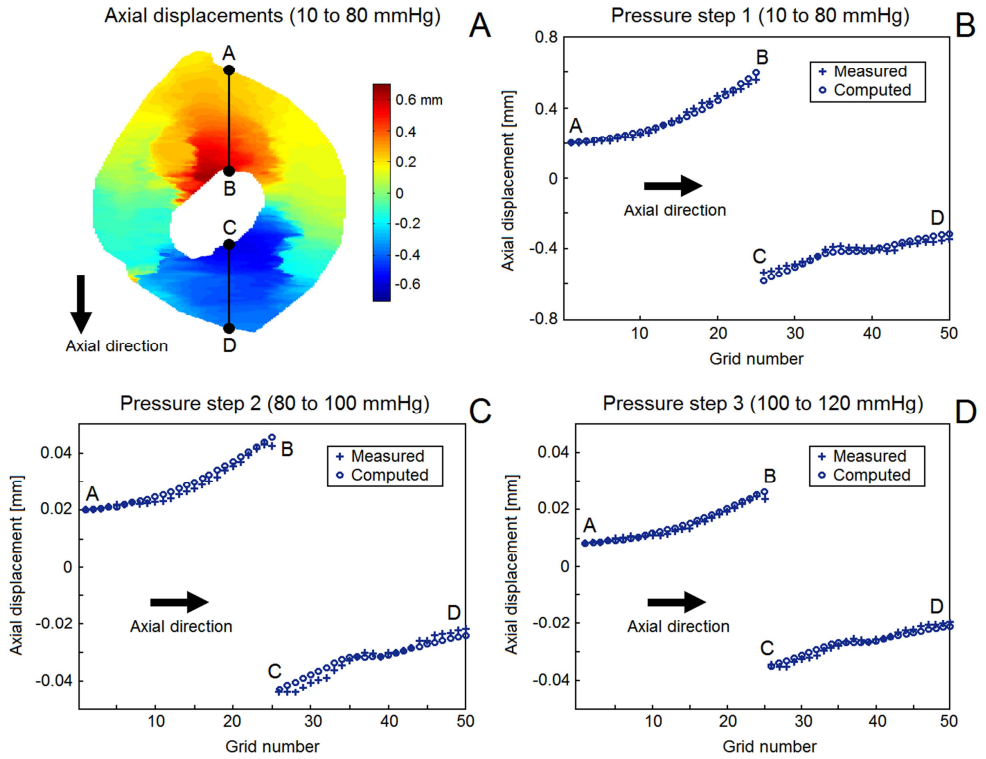


**Figure 5.** Measured ("+") and computed ("o") axial displacements in the midsection of plaque 3 due to intraluminal pressure increase during inflation. Note the difference in the y-axis scaling for the three pressure steps.

values increased from 142 (±108) kPa to 877 (±459) kPa, and then to 1015 (±439) kPa for the same sequence of pressure steps. The estimated stiffness for the individual plaques showed a wide variation but consistent behavior. Two exceptions were observed: for plaque 1 the stiffness of the wall slightly decreased when going from pressure step 2 to step 3. For plaque 4, the intima showed very low stiffness values, hitting the lower limit for pressure steps 2 and 3. For all plaques combined, the average [range] $\Delta u_{rel}$ for pressure steps 1, 2, and 3 were 1.2% [0.5-2.3%], 3.2% [0.9-6.4%], and 3.3% [0.8-6.2%], respectively.

## DISCUSSION

This study presents a new hybrid experimental-numerical approach to determine local mechanical plaque properties. An RF-correlation technique was applied to high

frequency ultrasound data to quantify plaque deformation at a high spatial resolution during inflation. Experiments with intact arteries enabled testing plaques with preserved structural integrity. By registering histology images to ultrasound images unprecedented details on heterogeneous complex plaque morphology were incorporated into the FE models. These models were used in an inverse FE method technique to estimate the material parameters of individual plaque components. This novel technique was utilized to characterize 6 porcine iliac arteries, which contained advanced stage atherosclerosis, from *ex vivo* inflation tests. Accurate quantification of the local displacement distribution is essential for application of inverse methods to map the local properties of complex structures like atherosclerotic plaques. To measure these local displacement fields in the atherosclerotic plaques, a previously developed ultrasound RF cross-correlation technique was applied to high-frequency ultrasound data for the first time. This resulted in displacement maps with an axial resolution of 15 µm, enabling us to image local heterogeneities over spatial scales that are relevant for atherosclerotic plaques. Not only are these high resolution measurements essential for the current application, they will also be essential if we want to study previously reported inhomogeneities within the intima [28].

The excellent agreement between the measured and computed displacement fields was reflected by the small relative differences between the displacement fields, indicating that the underlying plaque model captures the experimental data well. This observation has two implications. The first implication is that the registration between

**Table 1**
Estimated Young's modulus values of the intima and wall of the atherosclerotic plaques

| Plaque | Intima: Step 1 | Intima: Step 2 | Intima: Step 3 | Wall: Step 1 | Wall: Step 2 | Wall: Step 3 |
|---|---|---|---|---|---|---|
| 1 | 48 | 60 | 546 | 108 | 924 | 792 |
| 2 | 18 | 72 | 90 | 36 | 528 | 696 |
| 3 | 30 | 138 | 162 | 48 | 348 | 570 |
| 4 | 6 | 1 | 1 | 186 | 1626 | 1782 |
| 5 | 4 | 186 | 174 | 330 | 1122 | 1164 |
| 6 | 36 | 144 | 168 | 144 | 714 | 1086 |
| Mean ± SD | 24±17 | 100±68 | 190±187 | 142±108 | 877±459 | 1015±439 |

Pressure step 1: 10 to 80 mmHg, Pressure step 2: 80 to 100 mmHg, Pressure step 3: 80 to 100 mmHg. All values in [kPa].

the histology data and the ultrasound data resulted in a good approximation of the underlying plaque geometry. The second implication is that the assumption that the intima can be modeled with a homogeneous material model in the small region of interest we investigated cannot be refuted based on the measurements. Further analyses of the experimental data have to be carried out to investigate whether this observation holds for the complete intima. On average, both the intima and the wall exhibited the expected non-linear behavior [9], the stiffness increased for increasing pressure. Furthermore, the average stiffness values for the wall were higher than the stiffness value for the intima component. This indicates that the arterial wall was the major load bearing structure in these atherosclerotic iliac plaques. The average wall stiffness values are similar to healthy porcine aorta wall properties obtained from previous inflation tests [14,29]. The average intima stiffness values are in the lower range of human data in literature [9], and similar to the compressive stiffness values reported for aortic plaques [30] and to the tensile stiffness for human carotid intima tissue [31]. The average data however cannot conceal the considerable variation in the intima and wall properties. Even in plaques harvested from the same vascular territory from animals of the same age that were exposed to the same diet, stiffness values span a wide range. This implies that for accurate modeling of the stress distribution in atherosclerotic plaques, plaque-specific properties should be used instead of averaged values.

Although this study utilized *ex vivo* inflation experiments, the new hybrid experimental-numerical approach has the potential to be extended to *in vivo* use. The center frequency that was used in this study might still be too high, however with a 20-30 MHz high resolution imaging it would be feasible in non-obese patients. With the recent advances in imaging modalities such as magnetic resonance imaging, morphological information of atherosclerotic plaques can be obtained *in vivo*, in a nondestructive and noninvasive manner. The magnetic resonance imaging data would replace the histology step in the current approach and make the entire method applicable on patients. Especially the application of this method in carotid arteries seems feasible, although heavily calcified plaques are challenging for ultrasound strain imaging due to shading effects.

Some limitations of the method presented in this study should be noted. First, only axial displacements in the mid-section of the plaque were utilized in the minimization procedure. Therefore, only material properties of that specific region were obtained. To obtain the full 2D displacement from ultrasound recordings and improve the robustness of the material estimation algorithm, more advanced displacement estimation techniques are required [32,33], which have not been implemented yet for high frequency ultrasound systems. Second, the software Elastix, which was used to

register histology images to ultrasound images, employs a purely image-based algorithm and does not incorporate any structural, physical information to compute the transformation matrix for the registration. This might lead to some local errors in the registration. However, in our study successful registration for all plaques was confirmed by visual inspection of the measured and computed displacement maps. A representative example can be seen in Figure 5, where a calcified area was identified accurately. Third, possible anisotropic material behavior of intima and wall components was neglected in the study. Yet the isotropic neo-Hookean model, used in FE simulations, resulted in small relative differences between the measured and computed displacement values. More advanced material models can be employed in the FE models if needed. Similarly, the method presented in this paper allows including more components in the FE models if desired. Finally, the inflation procedure leaves the arterial segment intact, which is one of the main advantages of this method. A disadvantage is that, if the plaque is relatively small, the intima will not have a major impact on the displacement field, and as a consequence, the outcome of the minimization procedure will be relatively insensitive to the stiffness of the intima. This might explain the somewhat deviating behavior that was observed for plaque 4.

## CONCLUSIONS

In conclusion, we developed a new hybrid experimental-numerical technique to characterize local mechanical properties of atherosclerotic plaques. The combination of geometrical data from histology and high resolution displacement data from ultrasound was used to quantify the properties of intima and the wall of atherosclerotic iliac arteries from six pigs. Both components exhibited non-linear behavior and, on average, the wall was stiffer than the intima. A large variation in intima elasticity was observed, warranting further research into the relationship between stiffness and compositions of the intima.

## REFERENCES

1. Falk E. Pathogenesis of atherosclerosis. J Am Coll Cardiol 2006;47:C7-12.
2. Schaar JA, Muller JE, Falk E, Virmani R, Fuster V, Serruys PW, Colombo A, Stefanadis C, Ward Casscells S, Moreno PR, Maseri A, and van der Steen AF. Terminology for high-risk and vulnerable coronary artery plaques. Report of a meeting on the vulnerable plaque, June 17 and 18, 2003, Santorini, Greece. Eur Heart J 2004;25:1077-1082.
3. Virmani R, Finn AV, and Kolodgie FD. Carotid plaque stabilization and progression after stroke or TIA. Arterioscler Thromb Vasc Biol 2009;29:3-6.
4. Cheng GC, Loree HM, Kamm RD, Fishbein MC, and Lee RT. Distribution of circumferential stress in ruptured and stable atherosclerotic lesions. A structural analysis with histopathological correlation. Circulation 1993;87:1179-1187.

5. Richardson PD, Davies MJ, and Born GV. Influence of plaque configuration and stress distribution on fissuring of coronary atherosclerotic plaques. Lancet 1989;2:941-944.
6. Holzapfel GA, Mulvihill JJ, Cunnane EM, and Walsh MT. Computational approaches for analyzing the mechanics of atherosclerotic plaques: a review. J Biomech 2014;47:859-869.
7. Akyildiz AC, Speelman L, van Brummelen H, Gutierrez MA, Virmani R, van der Lugt A, van der Steen AF, Wentzel JJ, and Gijsen FJ. Effects of intima stiffness and plaque morphology on peak cap stress. Biomed Eng Online 2011;10:25.
8. Ohayon J, Mesnier N, Broisat A, Toczek J, Riou L, and Tracqui P. Elucidating atherosclerotic vulnerable plaque rupture by modeling cross substitution of ApoE-/- mouse and human plaque components stiffnesses. Biomech Model Mechanobiol 2012;11:801-813.
9. Akyildiz AC, Speelman L, and Gijsen FJ. Mechanical properties of human atherosclerotic intima tissue. J Biomech 2014;47: 773-783.
10. Walsh MT, Cunnane EM, Mulvihill JJ, Akyildiz AC, Gijsen FJ, and Holzapfel GA. Uniaxial tensile testing approaches for characterisation of atherosclerotic plaques. J Biomech 2014;47:793-804.
11. Humphrey JD. Cardiovascular solid mechanics: cells, tissues and organs. New York: Springer 2002.
12. Tian L and Chesler NC. In vivo and in vitro measurements of pulmonary arterial stiffness: A brief review. Pulm Circ 2013;2:505-517.
13. Fung YC and Liu SQ. Determination of the mechanical properties of the different layers of blood vessels in vivo. Proc Natl Acad Sci 1995;92:2169-2173.
14. Kim J and Baek S. Circumferential variations of mechanical behavior of the porcine thoracic aorta during the inflation test. J Biomech 2011;44:1941-1947.
15. Pandit A, Lu X, Wang C, and Kassab GS. Biaxial elastic material properties of porcine coronary media and adventitia. Am J Physiol Heart Circ Physiol 2005;288:H2581-2587.
16. Bouvier A, Deleaval F, Doyley MM, Yazdani SK, Finet G, Le Floc'h S, Cloutier G, Pettigrew RI, and Ohayon J. A direct vulnerable atherosclerotic plaque elasticity reconstruction method based on an original material-finite element formulation: theoretical framework. Phys Med Biol 2013;58:8457-8476.
17. Franquet A, Avril S, Le Riche R, and Badel P. Identification of heterogeneous elastic properties in stenosed arteries: a numerical plane strain study. Comput Methods Biomech Biomed Engin 2011;15:49-58.
18. Karimi R, Zhu T, Bouma BE, and Mofrad MR. Estimation of nonlinear mechanical properties of vascular tissues via elastography. Cardiovasc Eng 2008;8:191-202.
19. Khalil AS, Chan RC, Chau AH, Bouma BE, and Mofrad MR. Tissue elasticity estimation with optical coherence elastography: toward mechanical characterization of in vivo soft tissue. Ann Biomed Eng 2005;33:1631-1639.
20. Le Floc'h S, Ohayon J, Tracqui P, Finet G, Gharib AM, Maurice RL, Cloutier G, and Pettigrew RI. Vulnerable atherosclerotic plaque elasticity reconstruction based on a segmentation-driven optimization procedure using strain measurements: theoretical framework. IEEE Trans Med Imaging 2009;28:1126-1137.
21. Liu H, Canton G, Yuan C, Yang C, Billiar K, Teng Z, Hoffman AH, and Tang D. Using in vivo Cine and 3D multi-contrast MRI to determine human atherosclerotic carotid artery material properties and circumferential shrinkage rate and their impact on stress/strain predictions. J Biomech Eng 2012;134:011008.
22. Baldewsing RA, Danilouchkine MG, Mastik F, Schaar JA, Serruys PW, and van der Steen AF. An inverse method for imaging the local elasticity of atherosclerotic coronary plaques. IEEE Trans Inf Technol Biomed 2008;12:277-289.
23. Beattie D, Xu C, Vito R, Glagov S, and Whang MC. Mechanical analysis of heterogeneous, atherosclerotic human aorta. J Biomech Eng 1998;120:602-607.
24. Koopmans SJ, Dekker R, Ackermans MT, Sauerwein HP, Serlie MJ, van Beusekom HM, van den Heuvel M, and van der Giessen WJ. Dietary saturated fat/cholesterol, but not unsaturated fat or starch, induces C-reactive protein associated early atherosclerosis and ectopic fat deposition in diabetic pigs. Cardiovasc Diabetol 2011;10:64.
25. Lopata RG, Nillesen MM, Hansen HH, Gerrits IH, Thijssen JM, and de Korte CL. Performance evaluation of methods for two-dimensional displacement and strain estimation using ultrasound radio frequency data. Ultrasound Med Biol 2009;35:796-812.

26. Klein S, Staring M, Murphy K, Viergever MA, and Pluim JP. Elastix: a toolbox for intensity-based medical image registration. IEEE Trans Med Imaging 2010;29:196-205.
27. Speelman L, Akyildiz AC, den Adel B, Wentzel JJ, van der Steen AF, Virmani R, van der Weerd L, Jukema JW, Poelmann RE, van Brummelen EH, and Gijsen FJ. Initial stress in biomechanical models of atherosclerotic plaques. J Biomech 2011;44:2376-2382.
28. Chai CK, Akyildiz AC, Speelman L, Gijsen FJ, Oomens CW, van Sambeek MR, van der Lugt A, and Baaijens FP. Local axial compressive mechanical properties of human carotid atherosclerotic plaques-characterisation by indentation test and inverse finite element analysis. J Biomech 2013;46:1759-1766.
29. Lopata RG, Peters MF, Nijs J, Oomens CW, Rutten MC, and van de Vosse FN. Vascular elastography: a validation study. Ultrasound Med Biol 2014;40:1882-1895.
30. Lee RT, Richardson SG, Loree HM, Grodzinsky AJ, Gharib SA, Schoen FJ, and Pandian N. Prediction of mechanical properties of human atherosclerotic tissue by high-frequency intravascular ultrasound imaging. An in vitro study. Arterioscler Thromb 1992;12:1-5.
31. Cunnane EM, Mulvihill JJ, Barrett HE, Healy DA, Kavanagh EG, Walsh SR, and Walsh MT. Mechanical, biological and structural characterization of human atherosclerotic femoral plaque tissue. Acta Biomater 2014;11:295-303.
32. Hansen HH, Lopata RG, Idzenga T, and de Korte CL. Full 2D displacement vector and strain tensor estimation for superficial tissue using beam-steered ultrasound imaging. Phys Med Biol 2010;55:3201-3218.
33. Korukonda S, Nayak R, Carson N, Schifitto G, Dogra V, and Doyley MM. Noninvasive vascular elastography using plane-wave and sparse-array imaging. IEEE Trans Ultrason Ferroelectr Freq Control 2013;60:332-342.

# Carotid plaque elasticity estimation using ultrasound elastography, MRI, and inverse FEA – a numerical feasibility study

8

**Abstract** | The material properties of atherosclerotic plaques govern the biomechanical environment, which is associated with rupture-risk. We investigated the feasibility of noninvasively estimating carotid plaque component material properties through simulating ultrasound (US) elastography and *in vivo* magnetic resonance imaging (MRI), and solving the inverse problem with finite element analysis. 2D plaque models were derived from endarterectomy specimens of 9 patients. Nonlinear neo-Hookean models (tissue elasticity $C_1$) were assigned to fibrous intima, wall (i.e., media/adventitia), and lipid-rich necrotic core. Finite element analysis was used to simulate clinical cross-sectional US strain imaging. Computer-simulated, single-slice *in vivo* MR images were segmented by 2 MR readers. We investigated multiple scenarios for plaque model elasticity, and consistently found clear separations between estimated tissue elasticity values. The intima $C_1$ (160 kPa scenario) was estimated as 125.8 ± 19.4 kPa (reader 1) and 128.9 ± 24.8 kPa (reader 2). The lipid-rich necrotic core $C_1$ (5 kPa) was estimated as 5.6 ± 2.0 kPa (reader 1) and 8.5 ± 4.5 kPa (reader 2). A scenario with a stiffer wall yielded similar results, while realistic US strain noise and rotating the models had little influence, thus demonstrating robustness of the procedure. The promising findings of this computer-simulation study stimulate applying the proposed methodology in a clinical setting.

**This chapter is based on:** Nieuwstadt HA, Fekkes S, Hansen HHG, de Korte CL, van der Lugt A, Wentzel JJ, van der Steen AFW, Gijsen FJH. Carotid plaque elasticity estimation using ultrasound elastography, MRI, and inverse FEA – a numerical feasibility study. Submitted.

## INTRODUCTION

Carotid atherosclerotic plaque rupture can result in ischemic stroke; a major cause of death and disability worldwide [1]. The biomechanical conditions within plaques are closely related to plaque progression [2,3], instability [4,5] and rupture [6-9], the latter being an instance of mechanical failure of a thin fibrous cap overlaying a lipid-rich necrotic core (LRNC) [10].

To compute the stresses inside plaques, knowledge of the geometry, loading conditions and material properties of the various tissues is required. For carotid plaques, the 3D geometry and morphology can be obtained noninvasively with magnetic resonance imaging (MRI) which has high tissue contrast [11,12]. The MRI-derived geometry can be used as input for finite element analysis (FEA) to numerically compute the intraplaque stress distribution *in vivo* [2,13-15]. One of the largest limitations of current MRI-based carotid plaque FEA is the lack of knowledge of the patient-specific mechanical properties of the various tissues, prompting an oversimplified 'one-size-fits-all' approach by assigning literature-based material elasticity (i.e., stiffness) values to plaque components [6,8,9,16]. *In vitro* material testing studies on carotid plaque tissues consistently report differences of multiple orders-of-magnitude in the elasticity between patients [17-22].

Heterogeneous plaque elasticity can be estimated *in vivo* by measuring the strain distribution with ultrasound (US) elastography [23-25], and solving the inverse problem with FEA [16,26,27]. This method has been applied to coronary plaques using invasive intravascular US [28-30]. An major advantage of ultrasound elastography over, for example, MR elastography is the higher spatial resolution. The inverse problem can be solved directly [31,32], but *a priori* knowledge of the plaque geometry and morphology –which US itself poorly provides– reduces nonuniqueness issues, the sensitivity to elastographic noise and resolution, and the degrees of freedom [27,29,30,33-36]. With fewer degrees of freedom, computational power can instead be dedicated to fitting suitable constitutive models, often with numerous parameters themselves [37,38].

In this study, we propose an entirely noninvasive, nonlinear elasticity estimation methodology for carotid plaque components. It consists of imaging the plaque geometry with the various components through MRI, performing US strain imaging [39-42], measuring the systolic and diastolic blood pressures, and solving the inverse problem with FEA. We investigated the feasibility of this methodology (in particular with regard to US strain imaging and MRI) using a fully numerical approach. This allowed a comparison to a known, pre-assigned plaque model elasticity in a controlled setting [26,29-32,35]. We simulated US strain imaging and MRI using a set of histology-derived patient carotid plaque models, solved the inverse problems, and compared the estimated tissue elasticity values with the pre-assigned elasticity.

# METHODS

Histological cross sections were used to create realistic computer patient plaque models (Figure 1). These histology-based plaque models were then used to simulate noninvasive carotid US elastography (images of strain) and to simulate *in vivo* MRI (Figure 2). The inverse FEA problem for tissue elasticity was solved by minimizing the cumulative difference in strains between the simulated US elastogram and the MRI-based plaque FEA model obtained via MRI segmentation. Each step will now be explained in detail.

## Plaque geometry based on histology

We used histological cross sections to create a set of sufficiently realistic 2D plaque models [15] (Figure 1). From excised carotid plaques (>70% stenosis) of 9 patients, one largely-intact cross section (5 µm thickness) was selected per patient resulting in 9 patient plaque models. Sections were decalcified, stained with an Elastica van Gieson staining, and manually delineated for fibrous intima and LRNC [43]. Intima was defined as the intima tissue other than LRNC [15,22]. Because endarterectomy specimens do not include the outer vessel wall layer, a uniform 0.6-mm thick wall was added to the computational models as media/adventitia [44]. Sections were selected for presence of a LRNC >5 $mm^2$.

## Finite element analysis

Tissues were modeled as homogeneous, isotropic, hyperelastic and incompressible with a nonlinear neo-Hookean constitutive model; $W = C_1(I_1 - 3)$, with $W$ the strain

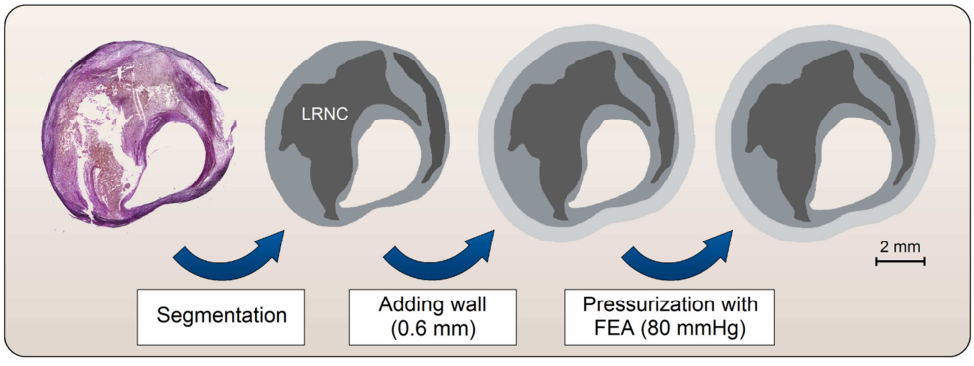


**Figure 1.** Example illustrating the creation of a patient plaque model deformed at 80 mmHg (*in vivo* shape) from a histological cross section. LRNC; lipid-rich necrotic core, FEA; finite element analysis.

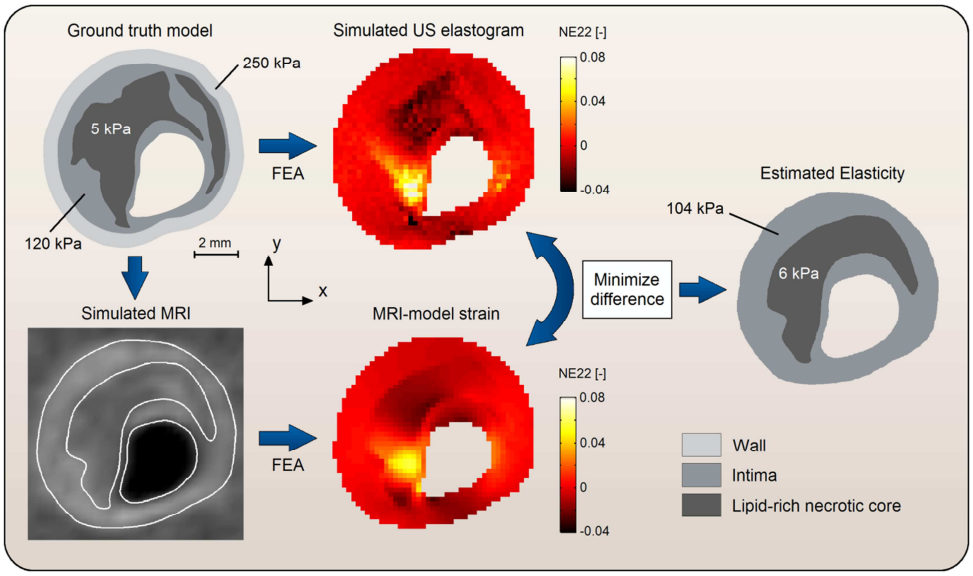


**Figure 2.** Methodology of the study illustrated with an example: patient 1, MR reader 1, stiff wall scenario. A histology-based, "ground truth" carotid plaque model (deformed at 80 mmHg) is used to simulate both an US elastogram and an MR image. The difference in strain is minimized by solving the inverse problem, resulting in an estimation of lipid-rich necrotic core and intima elasticity. Elasticity values are presented as the $C_1$ [kPa] of the neo-Hookean model. Note that axial strain ($y$-direction) is simulated, resulting in negative strain values in the upper and lower part and positive strain values left and right.

energy density function, $I_1$ the first invariant of the deformation tensor, and the constant $C_1$ the elasticity [15]. As an interpretation of $C_1$ we note that for small strains ($\varepsilon \ll 1$), $C_1 \approx E/6$, where $E$ is the Youngs modulus. The 2D plane strain FEA computations were performed in Abaqus (Abaqus Standard, 6.11, Dassault Systèmes Simulia Corp., Providence, Rhode Island, USA), under static loading conditions (blood pressure). We simulated a measured-diastolic pressure of 80 mmHg and measured-systolic pressure of 120 mmHg. The initial stresses and strains present in the MRI-based models (which were based on the deformed histology-based geometries at 80 mmHg luminal pressure) were computed with the backward incremental method [45]. Tissue anisotropy and residual stresses were not modeled.

### US elastography simulations

Each histology-based plaque model was subjected to FEA to compute the spatial strain distribution for 0–80 mmHg, $\varepsilon_{0\text{-}80}(x,y)$, and for 0–120 mmHg, $\varepsilon_{0\text{-}120}(x,y)$. The 80–120

mmHg strain, $\varepsilon_{80\text{-}120} = (\varepsilon_{0\text{-}120} - \varepsilon_{0\text{-}80})/(\varepsilon_{0\text{-}80} + 1)$, was computed, mimicking *in vivo* strains. The $\varepsilon_{80\text{-}120}(x,y)$ field was mapped on the deformed geometry at 80 mmHg luminal pressure. We simulated noninvasive, cross-sectional carotid US strain imaging (i.e., elastography [23-25]) based on Hansen et al. [42], modeling a linear-array transducer with a 9 MHz center frequency, 7 MHz bandwidth, 0.2 mm lateral element pitch, 22.4 (27 dB) system signal-to-noise ratio, and a 0.5 mm cross correlation window length with a 0.2 mm shift. This yielded a 0.2 x 0.2 mm$^2$ resolution elastogram with a strain-dependent elastographic signal-to-noise ratio, SNRe($\varepsilon$), as given in Figure 3. We determined the strain filter, SNRe($\varepsilon$), by combining relationships provided in the literature [46-51]. We used the correlation function from [52, page 276]. Note the characteristic band-pass shape of the strain filter, in which low and high strains lead to increased elastographic noise (lower SNRe) due to, respectively, dominant electronic system noise (Cramer-Rao lower bound) and signal decorrelation effects (Barankin bound). To simulate elastographic strain images, we processed the $\varepsilon_{80\text{-}120}(x,y)$ field in three steps: (1) we extracted only the axial ($y$) engineering (nominal) strain component (NE22) thus removing all shear and lateral strain information, (2) we

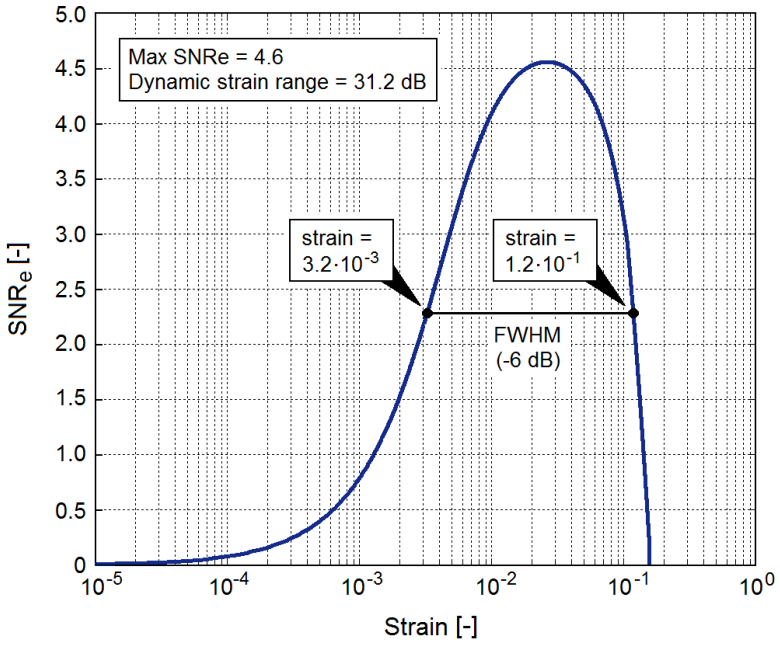


**Figure 3.** The strain-noise relationship (i.e., strain filter), SNRe($\varepsilon$), derived for the modeled US transducer and cross-correlation methodology. This relationship was used when simulating noise in US strain images. FWHM; full width at half maximum

resampled the now scalar strain field to 0.2 x 0.2 mm², and (3) we superimposed Gaussian-distributed elastographic noise according to the SNRe($\varepsilon$) relationship in Figure 3.

### MRI simulations

Each histology-based plaque model (deformed at 80 mmHg pressure using FEA) was subjected to a 2D *in vivo* MRI simulation in the Jülich Extensible MRI Simulator (JEMRIS): an open-source Bloch equation solver [53]. The MRI simulation methodology used in this study is introduced and described in detail in Nieuwstadt et al. [54]. In short, we assigned $T_1$ relaxation times of 680 ms to fibrous tissue (both intima and wall), 1220 ms to LRNC, and 1412 ms to the background, and a constant $T_2$ of 50 ms. We then simulated a typical clinically-applied 3.0T 2D T1-weighted turbo spin-echo, contrast-enhanced, black-blood pulse sequence (0.62 x 0.62 mm² in-plane acquired voxel size interpolated to 0.31 x 0.31 mm², repetition/echo times of 800 ms/10 ms, respectively). Rician distributed noise was added to yield an SNR of 16.7. Motion, axial partial volume effects or imperfect blood signal suppression were not simulated. Resulting images were segmented independently by two blinded, experienced carotid MR readers (Z.K. and M.S.) for fibrous and LRNC tissues to form the MRI-based plaque models. Because the carotid wall (media/adventitia) had similar contrast as the intima (a consequence of similar $T_1$ times), it was also annotated as intima in the MRI models as done in clinical practice [11,12,54].

### Inverse problem

The $\varepsilon_{80\text{-}120}(x,y)$ strain field resulting from each MRI-based model FEA (also assigned neo-Hookean models) was processed to match the simulated US elastograms by extracting only the axial engineering strain component (NE22) and resampling it to 0.2 x 0.2 mm². To estimate the fibrous and LRNC tissue elasticity in the MRI-based models, we followed the same approach as previous studies [28-31,35,55], and minimized a least-squares objective function $f_0$ given by

$$f_0 = \sum_{i=1}^{n} \sqrt{(\varepsilon_{80-120,\text{elastogram}} - \varepsilon_{80-120,\text{MRI model}})^2} \qquad (1)$$

where $i$ represents a 0.2 x 0.2 mm² $\varepsilon_{80\text{-}120}$ strain element. Strain elements from nonoverlapping areas were disregarded. Because we (1) knew the constitutive model (neo-Hookean), (2) dealt with just two parameters ($C_1$ for intima and LRNC) because of the MRI segmentation and (3) knew the pre-defined elasticity values, a grid-scatter

technique consisting of a grid search of the parameter space sufficed here as the optimization method.

### Studied scenarios

The described methodology resulted in 9 patient plaque models for which an US elastogram could be generated, and MRI segmentations from two readers. Based on ranges reported in the literature [21,22], we chose to model two scenarios for the pre-assigned elasticity values of the tissues in the histology-based plaque models:

- **Equal stiffness scenario:**
  $C_1 = 160$ kPa for intima tissue, $C_1 = 160$ kPa for wall tissue, $C_1 = 5$ kPa for LRNC tissue.
- **Stiff wall scenario:**
  $C_1 = 120$ kPa for intima tissue, $C_1 = 250$ kPa for wall tissue, $C_1 = 5$ kPa for LRNC tissue.

An important motivation for choosing these two scenarios is the fact that the wall (media/adventitia) cannot be distinguished from intima in carotid MRI [11,12], while it can be different biomechanically; typically stiffer [56,57]. The equal stiffness scenario allowed the investigation of solely the influence of MRI segmentation. Besides modeling these two scenarios, we performed two additional studies. The first study was an investigation into the influence of elastographic noise. For each US elastogram, we conducted 50 Monte Carlo experiments for the randomly distributed noise according to the SNRe($\varepsilon$) relation (Figure 3) and each time solved the inverse problem. The second study was an investigation into the influence of rotating each histology-model model 90° in-plane, because we simulated US elastography experiments measuring only the axial strain. This rotation simply consisted of extracting the NE11 ($x$-direction strain) instead of the NE22 to generate the scalar strain field $\varepsilon_{80\text{-}120}(x,y)$ for both the elastogram and the MRI model. For both these additional investigations (elastographic noise and 90° in-plane rotation), we used the original MRI segmentations of the MR readers for all 9 plaques and modeled the equal stiffness scenario for the pre-assigned elasticity.

## RESULTS

### Histology-based plaque models

Our dataset of histology-based carotid plaque models obtained from 9 patients displayed a wide range of dimensions. The lumen area (mean ± standard deviation)

was 10.2 ± 10.8 mm², range [1.2, 36.8]. The intima area was 16.0 ± 6.2 mm², range [8.0, 25.3]. The wall area was 15.2 ± 3.2 mm², range [10.3, 21.6]. The LRNC area was 15.1 ± 8.7 mm², range [7.1, 32.8].

### Equal stiffness scenario

In the equal stiffness scenario, we defined $C_1 = 160$ kPa for both the intima and wall in the histology-based models. The results are shown in Figure 4. The estimation methodology always yielded unique solutions of the inverse problem (a single minimum) with relatively accurate estimations. There was a consistently clear separation between plaque intima and LRNC elasticity for all 9 patients. Intima elasticity ($C_1$) was, on average, underestimated: MR reader 1; 125.8 ± 19.4 kPa, range [99.4, 150.0], and MR reader 2; 128.9 ± 24.8 kPa, range [90.4, 173.6]. This is an underestimation for the mean of -19% for reader 1 and -21% for reader 2. For the LRNC, the MR readers showed lower agreement and, on average, slightly overestimated LRNC elasticity: MR reader 1; 5.6 ± 2.0 kPa, range [3.2, 8.6], and MR reader 2; 8.5 ± 4.5 kPa, range [2.8, 15.4]. The estimated $C_1$ for LRNC was more accurate in an absolute sense, but less accurate in a relative sense. We found no statistically significant differences between the means of the two MR readers for the estimated elasticity of both intima ($p = 0.78$) and LRNC ($p = 0.10$) (Student's $t$-test, $n = 9$, $p < 0.05$ considered significant).

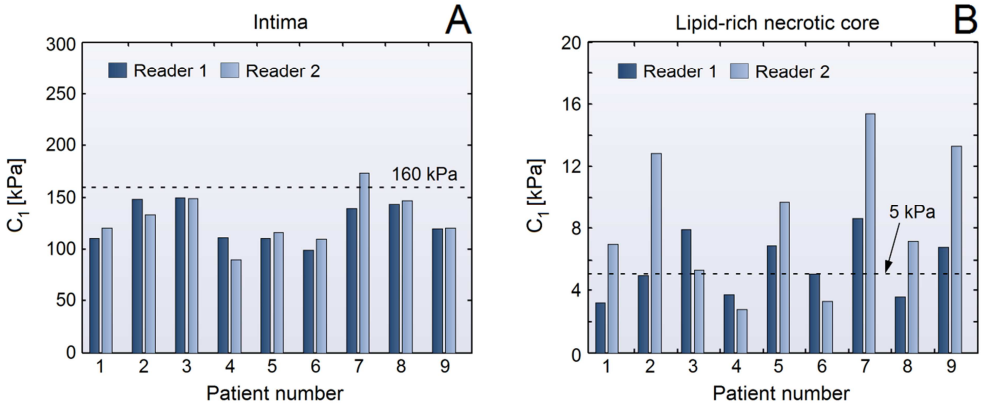


**Figure 4.** Equal stiffness scenario. Estimated $C_1$ for intima (A) and lipid-rich necrotic core (B) tissues shown for each patient plaque per MR reader. Pre-assigned $C_1$ values are shown as dashed lines.

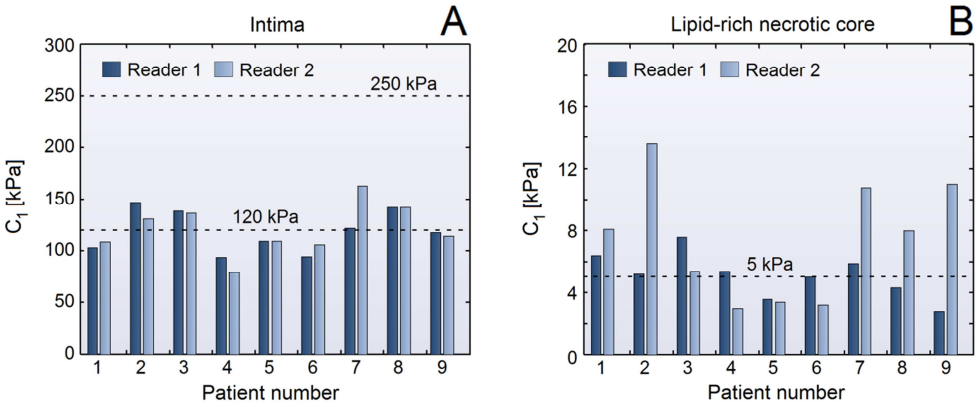


**Figure 5.** Stiff wall scenario. Estimated $C_1$ for intima (A) and lipid-rich necrotic core (B) tissues shown for each patient plaque per MR reader. Pre-assigned $C_1$ values are shown as dashed lines.

### Stiff wall scenario

In the stiff wall scenario, we defined $C_1 = 120$ kPa for intima tissue and $C_1 = 250$ kPa for wall tissue in the histology-based models. The results are shown in Figure 5. The findings were, in general, comparable to the equal stiffness scenario. The estimated elasticity ($C_1$) of the intima in the MRI-based models (in which intima includes histology-based model intima and wall) was close to the pre-assigned intima elasticity; the much stiffer wall had surprisingly little influence. For the stiff wall scenario, we found for the estimated intima $C_1$: MR reader 1; 118.9 ± 20.4 kPa, range [93.8, 147], and MR reader 2; 121.4 ± 24.6 kPa, range [79.0, 163]. The stiff wall did decrease the underestimation of intima stiffness as was observed in the equal stiffness scenario. For the soft LRNC, the estimation accuracy of its $C_1$ was largely unaffected and comparable with the equal stiffness scenario: MR reader 1; 5.1 ± 1.5 kPa, range [2.8, 7.6], and MR reader 2; 7.4 ± 3.9 kPa, range [3.0, 13.6].

### Ultrasound elastography noise

We computed the variance in $C_1$ (LRNC and intima) resulting from the 50 repeated experiments for each plaque (n = 9), and then obtained one average standard deviation ($SD_{avg}$) per reader by taking the squared root of the average of the 9 variances. We found only minor variations in estimated intima elasticity: $SD_{avg} = 3.3$ kPa for reader 1 and $SD_{avg} = 4.4$ kPa for reader 2. There were also only minor variations for estimated LRNC elasticity: $SD_{avg} = 1.1$ kPa for both readers. The

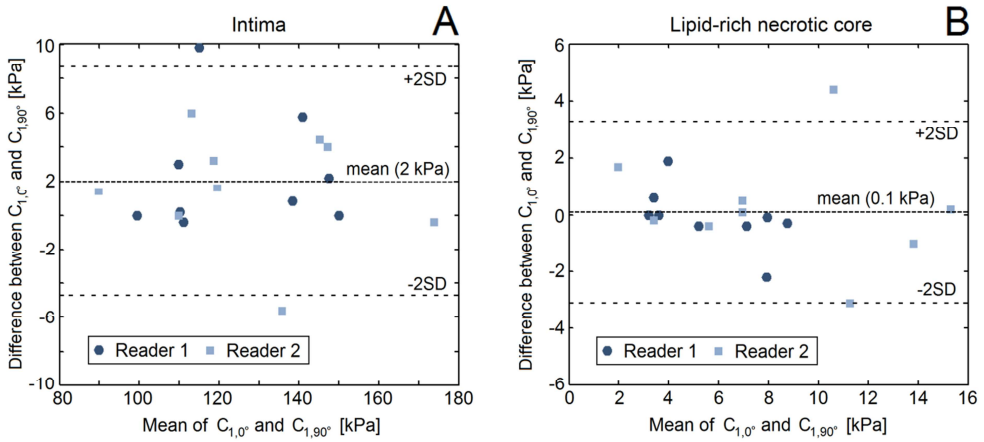


**Figure 6.** Bland Altman plots show the comparison between plaque component elasticity estimated using the original plaque orientation, $C_{1,0°}$, and the 90° in-plane rotation orientation, $C_{1,90°}$. (A) Intima, (B) lipid-rich necrotic core. Pre-assigned $C_1$ values from the equal stiffness scenario were used.

variations in estimated elasticity resulting from US noise were smaller than the variations between plaques and between MR readers in the equal stiffness scenario.

### 90° in-plane rotation

We compared the estimated LRNC and intima $C_1$ values for the original 0° rotation ($C_{1,0°}$) and the 90° rotation ($C_{1,90°}$), shown in Bland Altman plots in Figure 6. There were differences between $C_{1,0°}$ and $C_{1,90°}$ within each plaque model, but these were smaller than the differences between plaques in the equal stiffness scenario study.

## DISCUSSION

The biomechanical environment within atherosclerotic plaques is closely associated with clinical events, which calls for methods to determine the patient-specific plaque mechanical properties. In this simulation study, we numerically demonstrated the feasibility of noninvasively estimating carotid plaque component elasticity with inverse FEA and state-of-the-art black-blood contrast-enhanced *in vivo* MRI and US elastography. The two major advantages of our proposed methodology are that it is noninvasive and that the geometry is obtained *a priori*. We found that the elasticity of intima and LRNC can be estimated relatively precise, although intima elasticity is on average underestimated. A vessel wall (media/adventitia), missed in MRI

segmentation, which was twice as stiff as the intima had relatively little influence. Elastographic noise and measuring only axial strains were found not to be the weakest links in the chain. Remarkably, while resolution-limited (~0.6 mm) MRI segmentation clearly yielded imperfect *a priori* knowledge of plaque geometry (see example in Figure 2) which affected estimation accuracy, it never led to unrealistic elasticity estimations when solving the inverse problem.

The underestimation of intima elasticity is caused by MRI segmentation inaccuracies. MR readers tend to overestimate artery wall thickness and underestimate lumen and LRNC size on contrast-enhanced black-blood MRI [54,58,59]. In the appendix, we provide a demonstration that arterial wall thickness overestimation causes elasticity underestimation. Furthermore, the underestimation of LRNC size places high-strains from LRNCs at locations in the MRI-models incorrectly annotated as intima, causing underestimation of intima elasticity. The elasticity estimation of soft LRNCs was relatively less accurate and more MR reader-dependent. It was, however, still in the correct order of magnitude, which can strongly differ per patient/plaque in practice. Including a stiffer wall (media/adventitia) had little effect on estimated intima elasticity: the combination of the facts that stiffer tissues generally have lower strains and that the wall is located away from the lumen, resulted in a lower weighting in the objective function (equation 1). Nevertheless, a very stiff wall could prevent intima/LRNC deformations when these tissues are (nearly) incompressible. Regarding the 90° rotation investigation, the plaque models were initially randomly oriented, so their variations logically already incorporated orientation-induced variability, leading to the relatively smaller differences within plaques before and after rotation.

We numerically studied the use of US elastography, MRI, and inverse FEA for carotid plaque nonlinear elasticity estimation. When translating our proposed methodology to a clinical setting, practical issues need to be considered. Mismatching in MRI-US image registration and out-of-plane motion in strain imaging [40,60,61] could influence estimation accuracy. These issues can be resolved with multi-modality, non-rigid image registration software (for example Elastix [62]) and 3D strain imaging. Clinical US will be hampered by calcifications which cause shadowing [40,42]. Vulnerable plaques, which are of most interest, have predominantly lipid/fibrous content, and for the calcified plaques one could resort to alternative –although less accurate and lower resolution – strain imaging methods, for example MRI elastography [63]. Furthermore, MRI segmentations do not account for intra-component heterogeneity, and the limited voxel size prevents quantifying local material properties, such as within the thin fibrous cap [20]. This is inherent to current MRI technology. Advances such as 3D pulse sequence design are resulting in smaller acquired voxels [64]. Automated MRI segmentation using tissue classifiers might be beneficial [58,65].

### Limitations

MRI and US strain imaging were simulated for realistic, yet only best-case scenarios. Performing MRI and US in clinical practice would likely decrease the accuracy of elasticity estimation which needs to be quantified in future *in vivo* or *in vitro* studies. The use of decalcified histological specimens from carotid endarterectomy led to the assumption of a 0.6-mm wall thickness and absence of calcifications in the plaque models. When modeling the SNRe, we neglected loss of signal due to penetration depth (~4.5 $dB \cdot cm^{-1}$ for a 9 MHz transducer) and differences in echogenicity of different plaque components. Fibrous material demonstrates higher echo levels than fatty material, leading to a strain filter that is location-dependent. However, because most strains are located in the central part of the strain filter with high SNRe values, this effect will be minimal. Extending this study to 3D would allow investigating constitutive model-fitting to more complex (anisotropic) ground truth tissues, as well as investigating MRI-US registration and longitudinal motion/strains.

## CONCLUSIONS

Noninvasive estimation of carotid plaque component nonlinear elasticity is feasible with *in vivo* MRI and US elastography. The promising findings from this computer-simulation feasibility study stimulate applying, and investigating, the proposed methodology in a clinical setting.

## ACKNOWLEDGEMENTS

We thank Zaid Kassar and Mariana Selwaness (Erasmus Medical Center, Rotterdam, the Netherlands) for MRI segmentations.

## APPENDIX

To gain an appreciation of the effects of overestimating the arterial wall thickness on the estimated elasticity we can resort to the analytical solution for $\varepsilon(r)$ for a linear-elastic (Youngs modulus $E$) thick-walled cylinder [66]. The cylinder has an inner radius $a_1$, outer radius $b_1$, Poisson's ratio $\upsilon$, and inner pressure $P$. The measured radii of the cylinder are given by $a_2$ and $b_2$, leading to a strain distribution $\varepsilon'(r)$ and estimated $E'$. In order to obtain $E'$, we minimize the least-squares objective function:

$$\arg\min_{E'} \int_{\max(a_1,a_2)}^{\min(b_1,b_2)} \sqrt{\left(\varepsilon(r)-\varepsilon'(r)\right)^2}\,dr. \qquad (A.1)$$

The displacement $u(r)$ is given by $u(r) = Ar + Br^{-1}$. The strain is $\varepsilon(r) = du/dr = A - Br^{-2}$, with constants

$$A = \left(\frac{1-\upsilon}{E}\right)\cdot\left(\frac{a^2P}{b^2-a^2}\right), \qquad B = \left(\frac{1+\upsilon}{E}\right)\cdot\left(\frac{a^2b^2P}{b^2-a^2}\right). \qquad (A.2)$$

If we assume $\varepsilon(r) \approx \varepsilon'(r)$ ($a_1 \approx a_2$ and $b_1 \approx b_2$), we leave only the nonlinear term by dropping constant $A$ and we can directly solve $\varepsilon(r) \approx \varepsilon'(r)$. This is a harsh approximation, but it makes the math simple whilst still sufficing for our purpose. We now only need to solve for $B$. Rewriting $\varepsilon(r) \approx \varepsilon'(r)$ yields

$$\frac{E'}{E} \approx \frac{{a_2}^2{b_2}^2({b_1}^2-{a_1}^2)}{{a_1}^2{b_1}^2({b_2}^2-{a_2}^2)}. \qquad (A.3)$$

Let us take $b_1 = 1.2a_1$ as an example. In that case, a 2% underestimation of $a_1$ ($a_2 = 0.98a_1$), leads to a 12% underestimation of $E$ ($E'/E = 0.88$), whilst a 2% overestimation of $b_1$ ($b_2 = 1.02b_1$) leads to an 8% underestimation of $E$. We conclude that: (1) an overestimation of wall thickness leads to an underestimation of $E$, (2) the estimated $E$ is very sensitive to small errors in measured wall thickness, and (3) the estimated $E$ is more sensitive to errors in $a_1$ than in $b_1$ (higher strains at $a_1$, more so if $a_1/b_1 \ll 1$, i.e., a thicker wall).

## REFERENCES


1. Virmani R, Ladich ER, Burke AP, Kolodgie FD. Histopathology of carotid atherosclerotic disease. Neurosurgery 2006;59(5 Suppl 3):S219-227.
2. Tang D, Yang C, Mondal S, Liu F, Canton G, Hatsukami TS, Yuan C. A negative correlation between human carotid atherosclerotic plaque progression and plaque wall stress: *in vivo* MRI-based 2D/3D FSI models. J Biomech 2008;41:727-736.
3. Teng Z, He J, Degnan AJ, Chen S, Sadat U, Bahaei NS, Rudd JH, Gillard JH. Critical mechanical conditions around neovessels in carotid atherosclerotic plaque may promote intraplaque hemorrhage. Atherosclerosis 2012;223:321-326.
4. Huang H, Virmani R, Younis H, Burke AP, Kamm RD, Lee RT. The impact of calcification on the biomechanical stability of atherosclerotic plaques. Circulation 2001;103:1051-1056.
5. Kiousis DE, Rubinigg SF, Auer M, Holzapfel GA. A methodology to analyze changes in lipid core and calcification onto fibrous cap vulnerability: the human atherosclerotic carotid bifurcation as an illustratory example. J Biomech Eng 2009;131:121002.
6. Maldonado N, Kelly-Arnold A, Vengrenyuk Y, Laudier D, Fallon JT, Virmani R, Cardoso L, Weinbaum S. A mechanistic analysis of the role of microcalcifications in atherosclerotic plaque stability: potential implications for plaque rupture. Am J Physiol Heart Circ Physiol 2012;303:H619-628.

7. Sadat U, Teng Z, Gillard JH. Biomechanical structural stresses of atherosclerotic plaques. Expert Rev Cardiovasc Ther 2010;8:1469-1481.
8. Tang D, Teng Z, Canton G, Yang C, Ferguson M, Huang X, Zheng J, Woodard PK, Yuan C. Sites of rupture in human atherosclerotic carotid plaques are associated with high structural stresses: an *in vivo* MRI-based 3D fluid-structure interaction study. Stroke 2009;40:3258-3263.
9. Teng Z, Brown AJ, Calvert PA, Parker RA, Obaid DR, Huang Y, Hoole SP, West NE, Gillard JH, Bennett MR. Coronary plaque structural stress is associated with plaque composition and subtype and higher in acute coronary syndrome: the BEACON I (Biomechanical Evaluation of Atheromatous Coronary Arteries) study. Circ Cardiovasc Imaging 2014;7:461-470.
10. Falk E. Pathogenesis of atherosclerosis. J Am Coll Cardiol 2006;47:C7-12.
11. Saam T, Ferguson MS, Yarnykh VL, Takaya N, Xu D, Polissar NL, Hatsukami TS, Yuan C. Quantitative evaluation of carotid plaque composition by *in vivo* MRI. Arterioscler Thromb Vasc Biol 2005;25:234-239.
12. Underhill HR, Hatsukami TS, Fayad AZ, Fuster V, Yuan C. MRI of carotid atherosclerosis: clinical implications and future directions. Nat Rev Cardiol 2010;7:165-173.
13. Li Z, Howarth S, Trivedi RA, U-King-Im JM, Graves MJ, Brown A, Wang L, Gillard JH. Stress analysis of carotid plaque rupture based on *in vivo* high resolution MRI. J of Biomech 2006;39:2611-2622.
14. Gao H, Long Q, Graves M, Gillard JH, Li ZY. Study of reproducibility of human arterial plaque reconstruction and its effects on stress analysis based on multispectral *in vivo* magnetic resonance imaging. J Magn Reson Imaging 2009;30:85-93.
15. Nieuwstadt HA, Speelman L, Breeuwer M, van der Lugt A, van der Steen AF, Wentzel JJ, Gijsen FJ. The influence of inaccuracies in carotid MRI segmentation on atherosclerotic plaque stress computations. J Biomech Eng 2014;136:021015-1-9.
16. Ohayon J, Finet G, Le Floc'h S, Cloutier G, Gharib AM, Heroux J, Pettigrew RI. Biomechanics of atherosclerotic coronary plaque: site, stability and in vivo elasticity modeling. Ann Biomed Eng 2014;42:269-279.
17. Barrett SR, Sutcliffe MP, Howarth S, Li ZY, Gillard JH. Experimental measurement of the mechanical properties of carotid atherothrombotic plaque fibrous cap. J Biomech 2009;42:1650-1655.
18. Maher E, Creane A, Sultan S, Hynes N, Lally C, Kelly DJ. Tensile and compressive properties of fresh human carotid atherosclerotic plaques. J Biomech 2009;42:2760-2767.
19. Mulvihill JJ, Cunnane EM, McHugh SM, Kavanagh EG, Walsh SR, Walsh MT. Mechanical, biological and structural characterization of in vitro ruptured human carotid plaque tissue. Acta Biomater 2013;9:9027-9035.
20. Chai CK, Akyildiz AC, Speelman L, Gijsen FJ, Oomens CW, van Sambeek MR, van der Lugt A, Baaijens FP. Local axial compressive mechanical properties of human carotid atherosclerotic plaques-characterisation by indentation test and inverse finite element analysis. J Biomech 2013;46:1759-1766.
21. Walsh MT, Cunnane EM, Mulvihill JJ, Akyildiz AC, Gijsen FJ, Holzapfel GA. Uniaxial tensile testing approaches for characterisation of atherosclerotic plaques. J Biomech 2014;47:793-804.
22. Akyildiz AC, Speelman L, Gijsen FJ. Mechanical properties of human atherosclerotic intima tissue. J Biomech 2014;47:773-783.
23. Ophir J, Alam SK, Garra B, Kallel F, Konofagou E, Krouskop T, Varghese T. Elastography: ultrasonic estimation and imaging of the elastic properties of tissues. Proc Inst Mech Eng H 1999;213:203-233.
24. de Korte CL, Pasterkamp G, van der Steen AF, Woutman HA, Bom N. Characterization of plaque components with intravascular ultrasound elastography in human femoral and coronary arteries *in vitro*. Circulation 2000;102:617-623.
25. de Korte CL, Sierevogel MJ, Mastik F, Strijder C, Schaar JA, Velema E, Pasterkamp G, Serruys PW, van der Steen AF. Identification of atherosclerotic plaque components with intravascular ultrasound elastography *in vivo*: a Yucatan pig study. Circulation 2002;105:1627-1630.
26. Karimi R, Zhu T, Bouma BE, Mofrad MR. Estimation of nonlinear mechanical properties of vascular tissues via elastography. Cardiovasc Eng 2008;8:191-202.
27. Doyley MM. Model-based elastography: a survey of approaches to the inverse elasticity problem. Phys Med Biol 2012;57:R35-73.
28. Hamilton AJ, Kim H, Nagaraj A, Mun JH, Yan LL, Roth SI, McPherson DD, Chandran KB. Regional material property alterations in porcine femoral arteries with atheroma development. J Biomech 2005;38:2354-2364.

29. Baldewsing RA, Danilouchkine MG, Mastik F, Schaar JA, Serruys PW, van der Steen AF. An inverse method for imaging the local elasticity of atherosclerotic coronary plaques. IEEE Trans Inf Technol Biomed 2008;12:277-289.
30. Le Floc'h S, Ohayon J, Tracqui P, Finet G, Gharib AM, Maurice RL, Cloutier G, Pettigrew RI. Vulnerable atherosclerotic plaque elasticity reconstruction based on a segmentation-driven optimization procedure using strain measurements: theoretical framework. IEEE Trans Med Imaging 2009;28:1126-1137.
31. Khalil AS, Chan RC, Chau AH, Bouma BE, Mofrad MR. Tissue elasticity estimation with optical coherence elastography: toward mechanical characterization of *in vivo* soft tissue. Ann Biomed Eng 2005;33:1631-1639.
32. Bouvier A, Deleaval F, Doyley MM, Yazdani SK, Finet G, Le Floc'h S, Cloutier G, Pettigrew RI, Ohayon J. A direct vulnerable atherosclerotic plaque elasticity reconstruction method based on an original material-finite element formulation: theoretical framework. Phys Med Biol 2013;58:8457-8476.
33. Barbone PE, Bamber JC. Quantitative elasticity imaging: what can and cannot be inferred from strain images. Phys Med Biol 2002;47:2147-2164.
34. Barbone PE, Oberai AA. Elastic modulus imaging: some exact solutions of the compressible elastography inverse problem. Phys Med Biol 2007;52:1577-1593.
35. Khalil AS, Bouma BE, Kaazempur Mofrad MR. A combined FEM/genetic algorithm for vascular soft tissue elasticity estimation. Cardiovasc Eng 2006;6:93-102.
36. Baldewsing RA, Mastik F, Schaar JA, Serruys PW, van der Steen AF. Young's modulus reconstruction of vulnerable atherosclerotic plaque components using deformable curves. Ultrasound Med Biol 2006;32:201-210.
37. Holzapfel GA, Mulvihill JJ, Cunnane EM, Walsh MT. Computational approaches for analyzing the mechanics of atherosclerotic plaques: a review. J Biomech 2014;47:859-869.
38. Gasser TC, Ogden RW, Holzapfel GA. Hyperelastic modelling of arterial layers with distributed collagen fibre orientations. J R Soc Interface 2006;3:15-35.
39. Ribbers H, Lopata RG, Holewijn S, Pasterkamp G, Blankensteijn JD, de Korte CL. Noninvasive two-dimensional strain imaging of arteries: validation in phantoms and preliminary experience in carotid arteries *in vivo*. Ultrasound Med Biol 2007;33:530-540.
40. McCormick M, Varghese T, Wang X, Mitchell C, Kliewer MA, Dempsey RJ. Methods for robust *in vivo* strain estimation in the carotid artery. Phys Med Biol 2012;57:7329-7353.
41. Khamdaeng T, Luo J, Vappou J, Terdtoon P, Konofagou EE. Arterial stiffness identification of the human carotid artery using the stress-strain relationship *in vivo*. Ultrasonics 2012;52:402-411.
42. Hansen HH, Saris AE, Vaka NR, Nillesen MM, de Korte CL. Ultrafast vascular strain compounding using plane wave transmission. J Biomech 2014;47:815-823.
43. Groen HC, van Walsum T, Rozie S et al. Three-dimensional registration of histology of human atherosclerotic carotid plaques to *in-vivo* imaging. J Biomech 2010;43:2087-2092.
44. Duivenvoorden R, de Groot E, Elsen BM, Laméris JS, van der Geest RJ, Stroes ES, Kastelein JJ, Nederveen AJ. *In vivo* quantification of carotid artery wall dimensions: 3.0-Tesla MRI versus B-mode ultrasound imaging. Circ Cardiovasc Imaging 2009;2:235-242.
45. Speelman L, Akyildiz AC, den Adel B et al. Initial stress in biomechanical models of atherosclerotic plaques. J Biomech 2011;44:2376-2382.
46. Varghese T, Ophir J. A theoretical framework for performance characterization of elastography: the strain filter. IEEE Trans Ultrason Ferroelectr Freq Control 1997;44:164-172.
47. Varghese T, Ophir J. An analysis of elastographic contrast-to-noise ratio. Ultrasound Med Biol 1998;24:915-924.
48. Walker WF, Trahey GE. A fundamental limit on delay estimation using partially correlated speckle signals. IEEE Trans Ultrason Ferroelectr Freq Control 1995;42:301-308.
49. Cespedes I, Insana M, Ophir J. Theoretical bounds on strain estimation in elastography. IEEE Trans Ultrason Ferroelectr Freq Control 1995;42:969-972.
50. Weinstein E, Weiss AJ. Fundamental limitations in passive time-delay estimation--Part II: Wide-band systems. IEEE Trans Ultrason Ferroelectr Freq Control 1984;32:1064-1078.
51. Bilgen M, Insana M. Deformation models and correlation analysis in elastography. J Acoust Soc Am 1996;99:3212-3224.
52. Bendat JS, Piersol AG. Random data: Analysis and measurement procedures. 2nd edition, 566 pages, John Wiley, New York, 1986.

53. Stöcker T, Vahedipour K, Pflugfelder D, Shah NJ. High-performance computing MRI simulations. Magn Reson Med 2010;64:186-193.
54. Nieuwstadt HA, Geraedts TR, Truijman MT, Kooi ME, van der Lugt A, van der Steen AF, Wentzel JJ, Breeuwer M, Gijsen FJ. Numerical simulations of carotid MRI quantify the accuracy in measuring atherosclerotic plaque components in vivo. Magn Reson Med 2014;72:188-201.
55. Beattie D, Xu C, Vito R, Glagov S, Whang MC. Mechanical analysis of heterogeneous, atherosclerotic human aorta. J Biomech Eng 1998;120:602-607.
56. Teng Z, Tang D, Zheng J, Woodard PK, Hoffman AH. An experimental study on the ultimate strength of the adventitia and media of human atherosclerotic carotid arteries in circumferential and axial directions. J Biomech 2009;42:2535-2539.
57. Holzapfel GA, Sommer G, Regitnig P. Anisotropic mechanical properties of tissue components in human atherosclerotic plaques. J Biomech Eng 2004;126:657-665.
58. Hofman JMA, Branderhorst WJ, ten Eikelder HMM, Cappendijk VC, Heeneman S, Kooi ME, Hilbers PAJ, ter Haar Romeny BM. Quantification of atherosclerotic plaque components using in vivo MRI and supervised classifiers. Magn Reson Med 2006;55:790-799.
59. Antiga L, Wasserman BA, Steinman DA. On the overestimation of early wall thickening at the carotid bulb by black blood MRI, with implications for coronary and vulnerable plaque imaging. Magn Reson Med 2008;60:1020-1028.
60. Cinthio M, Ahlgren AR, Bergkvist J, Jansson T, Persson HW, Lindström K. Longitudinal movements and resulting shear strain of the arterial wall. Am J Physiol Heart Circ Physiol 2006;291:H394-402.
61. Golemati S, Gastounioti A, Nikita KS. Toward novel noninvasive and low-cost markers for predicting strokes in asymptomatic carotid atherosclerosis: the role of ultrasound image analysis. IEEE Trans Biomed Eng 2013;60:652-658.
62. Klein S, Staring M, Murphy K, Viergever MA, Pluim JP. Elastix: a toolbox for intensity-based medical image registration. IEEE Trans Med Imaging 2010;29:196-205.
63. Nederveen AJ, Avril S, Speelman L. MRI strain imaging of the carotid artery: present limitations and future challenges. J Biomech 2014;47:824-833.
64. Balu N, Yarnykh VL, Chu B, Wang J, Hatsukami T, Yuan C. Carotid plaque assessment using fast 3D isotropic resolution black-blood MRI. Magn Reson Med 2011;65:627-637.
65. van Engelen A, Niessen WJ, Klein S, Groen HC, Verhagen HJ, Wentzel JJ, van der Lugt A, de Bruijne M. Atherosclerotic plaque component segmentation in combined carotid MRI and CTA data incorporating class label uncertainty. PLoS One. 2014;9:e94840.
66. Humphrey JD, DeLange S. An introduction to biomechanics: solids and fluids, analysis and design. 631 pages, Springer, New York, 2004.

# Carotid plaque morphological classification compared with biomechanical cap stress – implications for an MRI-based assessment

9

**Abstract** | Two approaches to target plaque vulnerability –a histopathological classification scheme and a biomechanical analysis– were compared and the implications for noninvasive risk-stratification of carotid plaques using MRI were assessed. 75 histological plaque cross sections were obtained from carotid endarterectomy specimens from 34 patients (>70% stenosis) and subjected to both a Virmani histopathological classification (thin fibrous cap atheroma with <0.2 mm cap thickness, presumed vulnerable) and a peak cap stress computation (<140 kPa: presumed stable, >300 kPa: presumed vulnerable). To demonstrate the implications for noninvasive plaque assessment, numerical simulations of a typical carotid magnetic resonance imaging (MRI) protocol were performed (0.62 x 0.62 $mm^2$ in-plane acquired voxel size) and used to compute the MRI-based peak cap stress. We found that peak cap stress was generally associated with histological classification. However, only 16/25 plaque cross sections could be labeled as high-risk (peak cap stress>300 kPa and classified as a thin fibrous cap atheroma). 30/50 plaque cross sections could be labeled as low-risk (a peak cap stress<140 kPa and not a thin fibrous cap atheroma). 29 plaques (39%) showed there was a disagreement between both classifications. Because of the limited MRI voxel size in relation to cap thickness, a noninvasive identification of only a group of low-risk, thick-cap plaques was reliable. We conclude that instead of targeting vulnerable plaques, a reliable noninvasive identification of a select group of stable plaques with a thick cap and low stress could be a more fruitful approach to reduce surgical interventions on carotid plaques.

**This chapter is based on:** Gijsen FJH, Nieuwstadt HA, Wentzel JJ, Verhagen HJM, van der Lugt A, van der Steen AFW. Carotid plaque morphological classification compared with biomechanical cap stress – implications for an MRI-based assessment. Submitted.

## INTRODUCTION

To target patients at high risk of a cerebrovascular event, adequate discrimination between vulnerable and stable carotid plaques is important [1]. The current approach of surgical intervention guided by the severity of luminal stenosis is imperfect and unsustainable [2]. Two-thirds of all carotid plaque thromboembolisms result from plaques with less than 60% stenosis and numerous surgeries are needed to prevent just 1 ischemic stroke caused by carotid plaque thromboembolism [2,3]. This carries unnecessary operative risk and costs. Because the degree of stenosis inadequately reflects plaque vulnerability, current research focuses on improving vulnerable plaque identification [4].

One approach to distinguish vulnerable from stable plaques is a morphological classification. Virmani and colleagues introduced a histopathological classification scheme for plaques [5]. Carotid plaques with a thin fibrous cap (<0.2 mm [6,7]) and a distinct lipid-rich necrotic core are classified as 'thin fibrous cap atheroma' and presumed to be at an increased rupture-risk. Plaques classified as 'pathological intimal thickening' (an early stage extracellular lipid pool while mostly fibrous) and as 'fibrous cap atheroma' (similar to a thin fibrous cap atheroma but with a cap >0.2 mm) are considered stable. While this classification scheme is oft-used, it does not always adequately distinguish vulnerable from stable plaques. Not all, and only, thin fibrous cap atheromas are vulnerable: numerous thin fibrous cap atheromas do not rupture, while numerous differently classified plaques do [6].

Another approach to distinguish vulnerable from stable plaques is based on a biomechanical stress analysis [8,9]. Plaque rupture is, in essence, the mechanical failure of the fibrous cap. A biomechanical analysis incorporates morphology, tissue properties and hemodynamics to model the mechanical environment. The peak stress in the fibrous cap computed with finite element analysis is used as a rupture-risk marker. It depends not only on fibrous cap thickness [10,11], but also on, for example, local lumen curvatures, lipid core size, lumen area, and plaque composition [9]. Plaques with a peak cap stress exceeding 300 kPa are presumed to be at an increased rupture-risk [12]. Plaques with a stress lower than 140 kPa are considered stable [12-14]. The efficacy of current biomechanical plaque models to distinguish vulnerable from stable plaques is unknown.

The merit of these two approaches lies in their use of quantitative thresholds which can be assessed through noninvasive imaging. Carotid magnetic resonance imaging (MRI) is currently the only noninvasive imaging modality to obtain the entire plaque geometry/morphology with high soft-tissue contrast in a clinical setting [15]. MRI segmentation data of the vascular wall including plaque components can be used

as input for finite element analysis [8]. However, recent MRI simulation studies addressed limitations of carotid MRI regarding the spatial resolution for thickness measurements of thin fibrous caps [16]. This also has consequences for the reliability of stress computations of thin-cap, high-stress plaques [17]. Numerical computer simulations of MRI can be used as an effective means to investigate *in vivo* MRI segmentation accuracy [18]. Their principal advantage is the availability of a perfectly known ground truth (i.e., the object being imaged) on a submillimeter scale.

This study consists of two parts. In the first part, we acquired carotid plaque cross sections from endarterectomy specimens from patients with >70% stenosis who underwent surgery. We subjected the cross sections to both a histological classification and a peak cap stress computation and investigated the cases of agreement and disagreement. In the second part, we demonstrated the implications for a noninvasive imaging-based risk assessment with MRI. We performed that demonstration with a subset of the plaques using computer simulations of a clinical carotid MRI pulse sequence.

## METHODS

### Histology

Histological cross sections of excised carotid plaques causing more than 70% stenosis (NASCET) from 34 patients who had been scheduled for carotid endarterectomy were used. Written informed consent was obtained from all patients. The plaques were decalcified, embedded in paraffin, sliced at intervals of 1 mm with a thickness of 5 µm, and stained with either an Elastica van Gieson or Resorcine Fuchsine staining to identify fibrous tissue and lipid-rich necrotic core components. These components were manually delineated on µm-resolution microscopy images to create the ground truth plaque models. We randomly selected 25 cross sections morphologically classified as pathological intimal thickening, 25 as fibrous cap atheroma, and 25 classified as thin fibrous cap atheroma. From each patient at least 1 plaque cross section was included.

### Finite element analysis

The spatial stress distributions were computed with Abaqus Standard 6.11 (Dassault Systèmes Simulia Corp., Providence, Rhode Island, USA). Fibrous and lipid-rich necrotic core tissues were modeled as incompressible with a nonlinear neo-Hookean constitutive model (material constant $C_1 = 167$ kPa for fibrous tissue; $C_1 = 1$ kPa for lipid-rich necrotic core) [17]. Each 2D model was meshed with ~50,000 four-node linear

hybrid quadrilateral elements (mesh-independent solutions). The loading condition consisted of a static intraluminal pressure of 16.7 kPa (125 mmHg). The maximum principal stress was used as the scalar stress measure. Prior to MRI simulations, the ground truth models were deformed with finite element analysis by applying 80 mmHg to recover an *in vivo* shape. The initial stresses in the resulting MRI-based plaque models were computed with the backward incremental method [19].

### Noninvasive imaging demonstration: MRI simulations

To demonstrate the influence of MRI-based *in vivo* peak cap stress computations on the agreement with the histological classification of the underlying ground truth plaque, we performed numerical MRI simulations on a subset of the plaques (32 plaque cross sections). These 32 cross sections were used in our previous studies [16,17]. A numerical MRI simulation consists in modeling MRI-physics by solving the Bloch equations for a provided pulse sequence and ground truth computer sample model. The Jülich Extensible MRI Simulator (JEMRIS) was used for simulations [18]. A clinically applied, 2D, T1-weighted, turbo spin-echo, gadolinium contrast enhanced, black-blood sequence on a 3.0T full-body system was simulated (single-slice) [16]. The repetition/echo times were 800 ms/10 ms respectively. A reduced field-of-view of 37 x 37 $mm^2$ was simulated with a matrix size of 60 x 60. This resulted in an in-plane acquisition voxel size of 0.62 x 0.62 $mm^2$, the same as in the clinical protocol (interpolated voxel size of 0.31 x 0.31 $mm^2$ achieved after standard k-space zero-padding). Noise was added in post-processing (signal-to-noise ratio of 16.7). Fibrous, lipid-rich necrotic core, and background tissues were assigned apparent $T_1$ relaxation times of 680 ms, 1220 ms, and 1412 ms respectively (all $T_2 = 50$ ms).

### Analysis

When comparing the means of groups of data, a non-parametrical Mann-Whitney $U$ test was used (significant if $p < 0.05$). To test for correlations, the Pearson correlation coefficient (R) was used (significant if $p < 0.05$). For the demonstration with MRI simulations, the simulated carotid MR images were independently segmented by 3 blinded MRI readers (M.B., J.S., and G.H.). MRI-based plaque models were created from the MR reader segmentations and subjected to finite element analysis. We compared the MRI-based peak cap stress with the histological classification of the ground truth plaque cross section using quartiles for stress. We defined three groups: low stress < first quartile; first quartile < medium stress < third quartile; high stress > third quartile. That definition was done for each MR reader separately.

# RESULTS

## Examples

Three examples of histological plaque cross sections and their stress distributions are shown in Figure 1. The first example (left) is a cross section classified as pathological intimal thickening containing some deep extracellular lipid while having mostly fibrous tissue. The minimum fibrous cap thickness is 1.16 mm and the peak cap stress is 66 kPa. The second example (middle) is a cross section classified as a fibrous cap atheroma containing a large distinct lipid-rich necrotic core with a cap thickness of 0.24 mm and a peak cap stress of 264 kPa. The third example (right) is a cross section classified as a thin fibrous cap atheroma with a cap thickness of 0.12 mm and a peak cap stress of 404 kPa. The plaque cross sections had low stresses in the soft lipid regions and high stresses at the plaque shoulders (high lumen curvature) and at the location of the minimum fibrous cap thickness.

## Peak cap stress is associated with histological classification

The results for all plaque cross sections are shown in Figure 2. On average, cross sections classified as pathological intimal thickening had the lowest stress (median

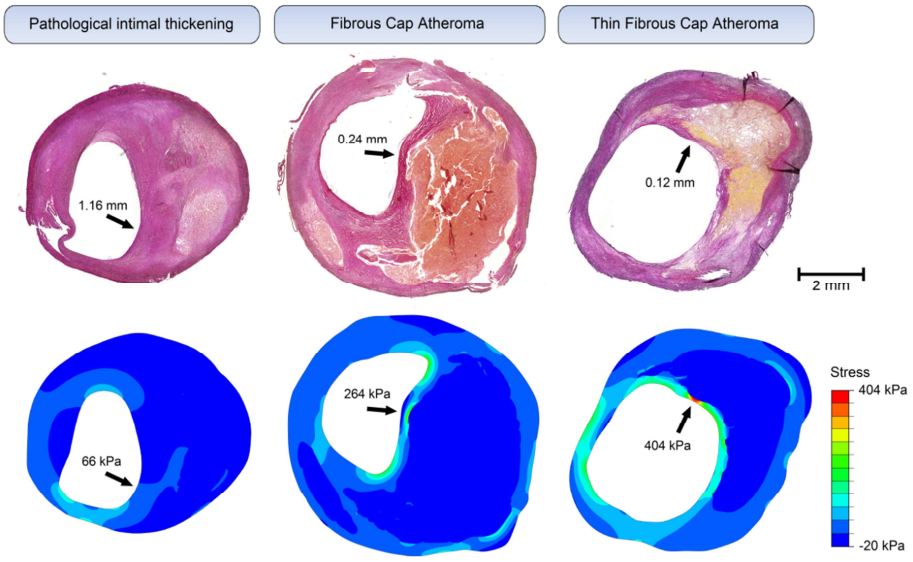


**Figure 1.** Three examples of histological cross sections and their stress distributions computed with finite element analysis. Arrows indicate location of minimum cap thickness and peak cap stress.

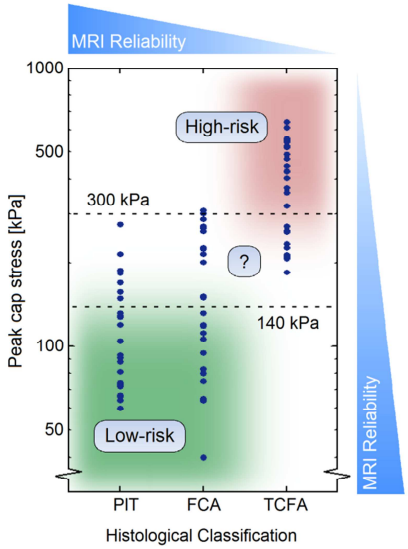


**Figure 2.** Peak cap stress as a function of histological classification. PIT; pathological intimal thickening, FCA; fibrous cap atheroma, TCFA; thin cap fibroatheroma. The blue gradients qualitatively illustrate the reliability of a noninvasive assessment of the variable with MRI. Note the logarithmic scale on the vertical axis.

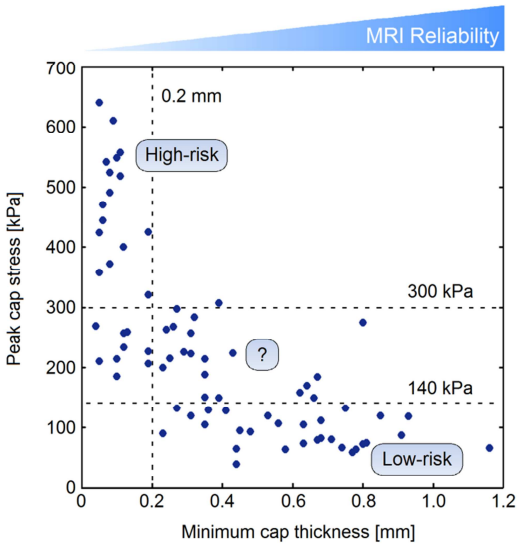


**Figure 3.** Peak cap stress as a function of minimum fibrous cap thickness. Dotted lines indicate the 0.2 mm and the 140/300 kPa thresholds for fibrous cap thickness and peak cap stress, respectively. The blue gradient qualitatively illustrates the reliability of a noninvasive assessment of the variable with MRI.

105 kPa, interquartile range 78 kPa). Cross sections classified as fibrous cap atheroma had a slightly higher stress (median 150 kPa, interquartile range 142 kPa), $p = 0.03$. Cross sections classified as thin fibrous cap atheroma had the highest peak cap stress (median 404 kPa, interquartile range 268 kPa), $p < 10^{-3}$, in comparison with the two other groups. The peak cap stress as a function of the minimum fibrous cap thickness is plotted in Figure 3. There was a significant inverse correlation between peak cap stress and minimum fibrous cap thickness: $R = -0.68$, $p < 10^{-3}$. However, the large spread in the data (especially for caps <0.2 mm) indicates that minimum fibrous cap thickness was not the only parameter influencing peak cap stress.

### High-risk plaques, low-risk plaques, and the cases of disagreement

Despite the aforementioned general association, only a limited number of plaque cross sections showed an agreement between peak cap stress and histological classification.

We found that 64% (16/25) of the thin fibrous cap atheromas had a stress higher than the 300 kPa threshold; we labeled these 16 plaques as high-risk. We also found that 60% (30/50) of the cross sections which were not classified as a thin fibrous cap atheroma had a stress lower than the 140 kPa threshold; we labeled these 30 plaques as low-risk. This left 29 out of 75 plaque cross sections (39%) not belonging to either group as they had a disagreement between both classifications. That group consisted of 9 thin fibrous cap atheromas, 13 fibrous cap atheromas, and 7 pathological intimal thickenings. These plaque cross sections could not be labeled as either high-risk or low-risk.

### Noninvasive imaging: MRI simulations

Of the 32 plaques used for the MRI simulations, 8 (25%) were classified as pathological intimal thickening, 14 (44%) as fibrous cap atheroma, and 10 (31%) as thin fibrous cap atheroma. An MRI-based stress computation resulted in a severely underestimated and imprecise peak cap stress due to overestimation of cap thickness, in particular for plaques with caps <0.62 mm (for details, see [16,17]. The results of the comparison between the MRI-based peak cap stress and the histological classification of the underlying ground truth plaque are shown in Figure 4. In the high stress group (highest 25%) there was a large variation in the classification of the underlying plaque cross sections and large differences between the readers. For reader 1, there were 6 out of 10 thin fibrous cap atheromas present in the high stress group. However, for reader 3, only

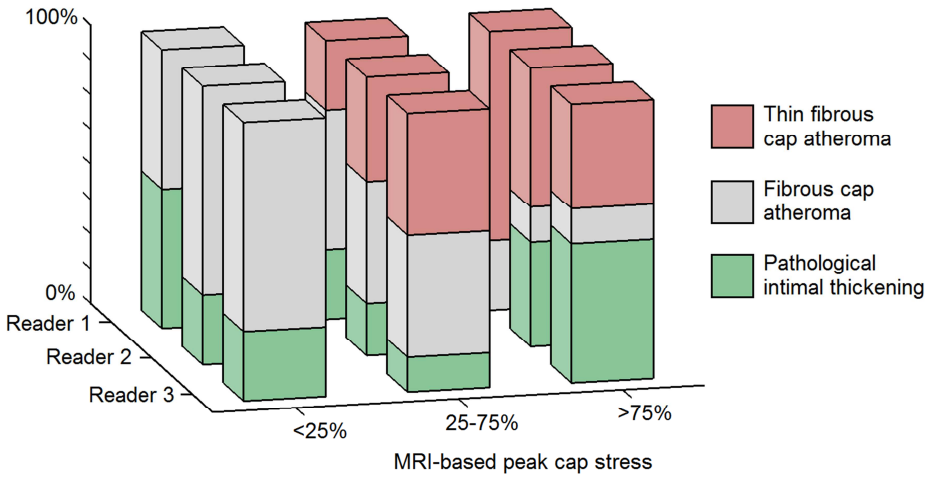


**Figure 4.** MRI-based peak cap stress versus histological classification of the underlying (ground truth) plaque cross section for the three MRI readers.

3 thin fibrous cap atheromas were present in the high stress group which actually contained 4 pathological intimal thickenings. For the low stress group (lowest 25%) there was a higher agreement between MR readers. Only within the low stress group there was a consistent agreement between histological classification and the peak cap stress. For every MR reader, none of the plaques in the low stress group were histologically classified as a thin fibrous cap atheroma (i.e., low-risk). The lowest MRI-based peak cap stress observed in a thin fibrous cap atheroma was 70 kPa (reader 2). Thus, plaque cross sections with an MRI-based peak cap stress <70 kPa were never classified as a thin fibrous cap atheroma for any of the 3 readers. These cross sections were therefore also low-risk. For all readers this was a sizable group: reader 1 identified 7 such plaques, reader 2 identified 10, and reader 3 identified 6.

## DISCUSSION

In order to adequately treat patients at risk of an acute cerebrovascular event, plaque vulnerability needs to be incorporated. In this study, we compared two approaches: a morphological classification and a biomechanical analysis. Although such a comparison has been reported in the literature [20,21,22], our study focused specifically on the cases of agreement and disagreement and their implications instead of on merely general associations. In addition, we also demonstrated the implications for a noninvasive assessment of carotid plaque vulnerability.

In theory it is possible to identify a group of patients with high-risk plaques (i.e., both high peak cap stress and classified as a thin fibrous cap atheroma). There are, however, two practical problems associated with this approach. First: the unreliability of a noninvasive assessment of thin-cap (<0.2 mm) plaques due to the limited voxel size (~0.6 mm) of current carotid MRI inhibits a reliable identification of a group of high-risk plaques in clinical practice. Second: even if sufficiently high-resolution imaging would hypothetically be available, one would still miss many plaques of which it is currently uncertain whether they are vulnerable or stable. We identified numerous thin fibrous cap atheromas with a low peak cap stress and numerous differently classified plaques with a high peak cap stress. These plaques showed a disagreement between the two classification schemes we investigated. This reflects our current inability to identify all, and only all, vulnerable plaques. Not treating vulnerable carotid plaques could result in undertreatment of carotid artery disease patients.

It is in theory also possible to identify a group of patients with low-risk plaques (i.e., both low peak cap stress and not classified as a thin fibrous cap atheroma). The two practical problems associated with the identification of high-risk plaques do not

apply here anymore. First: low-risk plaques typically have thick fibrous caps which can be reliably measured with MRI. This also yields a more reliable peak cap stress computation associated with minimum fibrous cap thickness. Indeed, our demonstration with MRI simulations suggests that only a noninvasive identification of a select group of low-risk plaques is feasible in clinical practice. Although it was not the focus of their study, Esposito-Bauer et al. recently reported a perfect identification of a group of stenosis-inducing stable plaques (58 months event-free) with MRI but an imperfect identification of all, and only all, unstable plaques [23]. Second: instead of focusing on the few patients who would benefit from surgical intervention, it might also be useful and practicable to focus on a group of patients who would *not* benefit. This means a shift of focus from vulnerable plaques to stable plaques. By reliably identifying low-risk plaques and exempting them from surgery, one could also effectively achieve a reduction in the large number of surgical interventions. This hypothesis, the "stable plaque paradigm", needs to be tested in a randomized control trial. We note that in order to improve stable plaque detection, additional parameters such as intraplaque hemorrhage, calcifications, and cap inflammation/strength should be incorporated.

## Limitations

The number of patients used was limited and in some cases multiple cross sections from the same plaques were used. We furthermore selected equal group sizes of differently histologically classified plaques. Our data therefore may not reflect the actual prevalence of entire-plaque classifications in carotid artery disease patients [6]. Such a population-based investigation was beyond this study's scope. Our biomechanical analyses were residual stress-free, static, two-dimensional and used literature-based plaque tissue elasticity values. Microcalcifications (which cannot be noninvasively imaged) and localized tissue strength/elasticity were not incorporated. Note that the aforementioned issues become relatively less influential when targeting thick-cap, low-stress plaques. For example, knowledge of cap strength becomes important only for thinner caps which have peak cap stresses within the range of experimental cap-failure observations (>140 kPa). In the MRI simulations, motion, axial partial volume effects, high image noise, and imperfect blood signal-suppression were neglected, which yielded an ideal-case imaging scenario. This means that thickness measurements of thin caps would be even more unreliable than we determined here. The 70 kPa threshold we introduced in this study is MRI-protocol dependent and does not directly apply to stress modeling based on images from other protocols. In all, we do note that while the limitations and assumptions of this study influence our reported quantitative data, they do not devalue our main arguments and conclusions.

## CONCLUSIONS

The limited spatial resolution of current clinical MRI renders the targeting of thin-cap, high-stress plaques unreliable. Instead of focusing on vulnerable plaques, a reliable identification of stable plaques with a thick fibrous cap might be a more fruitful approach to start reducing carotid surgical interventions.

## ACKNOWLEDGEMENTS

We thank Kim van Gaalen (Erasmus MC, Rotterdam) for histological processing. We thank Marcel Breeuwer (Philips Healthcare, Best), Jeroen Sonnemans and Gilion Hautvast (formerly of Philips Healthcare, Best) for performing MRI segmentations.

## REFERENCES

1. Bentzon JF, Otsuka F, Virmani R, Falk E. Mechanisms of plaque formation and rupture. Circ Res 2014;114:1852-1866
2. Naylor AR. Time to rethink management strategies in asymptomatic carotid artery disease. Nat Rev Cardiol 2011;9:116-124.
3. Rothwell PM, Warlow CP. Prediction of benefit from carotid endarterectomy in individual patients: a risk-modelling study. European Carotid Surgery Trialists' Collaborative Group. Lancet 1999;353:2105-2110.
4. Finn AV, Nakano M, Narula J, Kolodgie FD, Virmani R. Concept of vulnerable/unstable plaque. Arterioscler Thromb Vasc Biol 2010;30:1282-1292.
5. Virmani R, Kolodgie FD, Burke AP, Farb A, Schwartz SM. Lessons from a sudden coronary death: a comprehensive morphological classification scheme for atherosclerotic lesions. Arterioscler Thromb Vasc Biol 2000;20:1262-1275.
6. Redgrave JN, Gallagher P, Lovett JK, Rothwell PM. Critical cap thickness and rupture in symptomatic carotid plaques. Stroke 2008;39:1722-1729.
7. Virmani R, Ladich ER, Burke AP, Kolodgie FD. Histopathology of carotid atherosclerotic disease. Neurosurgery 2006;59:S219-227.
8. Tang D, Teng Z, Canton G, Yang C, Ferguson M, Huang X, Zheng J, Woodard PK, Yuan C. Sites of rupture in human atherosclerotic carotid plaques are associated with high structural stresses: an *in vivo* MRI-based 3D fluid-structure interaction study. Stroke 2009;40:3258-3263.
9. Tang D, Kamm RD, Yang C, Zheng J, Canton G, Bach R, Huang X, Hatsukami TS, Zhu J, Ma G, Maehara A, Mintz GS, Yuan C. Image-based modeling for better understanding and assessment of atherosclerotic plaque progression and vulnerability: data, modeling, validation, uncertainty and predictions. J Biomech 2014;47:834-846.
10. Loree HM, Kamm RD, Stringfellow RG, Lee RT. Effects of fibrous cap thickness on peak circumferential stress in model atherosclerotic vessels. Circ Res 1992;71:850-858.
11. Li ZY, Howarth SP, Tang T, Gillard JH. How critical is fibrous cap thickness to carotid plaque stability? A flow-plaque interaction model. Stroke 2006;37:1195-1199.
12. Cheng GC, Loree HM, Kamm RD, Fishbein MC, Lee RT. Distribution of circumferential stress in ruptured and stable atherosclerotic lesions. A structural analysis with histopathological correlation. Circulation 1993;87:1179-1187.
13. Loree HM, Grodzinsky AJ, Park SY, Gibson LJ, Lee RT. Static circumferential tangential modulus of human atherosclerotic tissue. J Biomech 1994;27:195-204.

14. Lawlor MG, O'Donnell MR, O'Connell BM, Walsh MT. Experimental determination of circumferential properties of fresh carotid artery plaques. J Biomech 2011;44:1709-1715.
15. Underhill HR, Hatsukami TS, Fayad AZ, Fuster V, Yuan C. MRI of carotid atherosclerosis: clinical implications and future directions. Nat Rev Cardiol 2010;7:165-173.
16. Nieuwstadt HA, Geraedts TR, Truijman MT, Kooi ME, van der Lugt A, van der Steen AF, Wentzel JJ, Breeuwer M, Gijsen FJ. Numerical simulations of carotid MRI quantify the accuracy in measuring atherosclerotic plaque components *in vivo*. Magn Reson Med 2014;72:188-201.
17. Nieuwstadt HA, Speelman L, Breeuwer M, van der Lugt A, van der Steen AF, Wentzel JJ, Gijsen FJ. The influence of inaccuracies in carotid MRI segmentation on atherosclerotic plaque stress computations. J Biomech Eng 2014;136:021015-1-9.
18. Stöcker T, Vahedipour K, Pflugfelder D, Shah NJ. High-performance computing MRI simulations. Magn Reson Med 2010;64:186-193.
19. Speelman L, Akyildiz AC, den Adel B, Wentzel JJ, van der Steen AF, Virmani R, van der Weerd L, Jukema JW, Poelmann RE, van Brummelen EH, Gijsen FJ. Initial stress in biomechanical models of atherosclerotic plaques. J Biomech 2011;44:2376-2382.
20. Tang D, Yang C, Zheng J, Woodard PK, Saffitz JE, Petruccelli JD, Sicard GA, Yuan C. Local maximal stress hypothesis and computational plaque vulnerability index for atherosclerotic plaque assessment. Ann Biomed Eng 2005;33:1789-1801.
21. Tang D, Teng Z, Canton G, Hatsukami TS, Dong L, Huang X, Yuan C. Local critical stress correlates better than global maximum stress with plaque morphological features linked to atherosclerotic plaque vulnerability: an *in vivo* multi-patient study. Biomed Eng Online 2009;8:15.
22. Teng Z, Brown AJ, Calvert PA, Parker RA, Obaid DR, Huang Y, Hoole SP, West NE, Gillard JH, Bennett MR. Coronary plaque structural stress is associated with plaque composition and subtype and higher in acute coronary syndrome: the BEACON I (Biomechanical Evaluation of Atheromatous Coronary Arteries) study. Circ Cardiovasc Imaging 2014;7:461-470.
23. Esposito-Bauer L, Saam T, Ghodrati I, Pelisek J, Heider P, Bauer M, Wolf P, Bockelbrink A, Feurer R, Sepp D, Winkler C, Zepper P, Boeckh-Behrens T, Riemenschneider M, Hemmer B, Poppert H. MRI plaque imaging detects carotid plaques with a high risk for future cerebrovascular events in asymptomatic patients. PLoS One 2013;87:e67927.

# 10 Discussion

In this thesis, the feasibility of MRI-based biomechanical stress modeling of carotid atherosclerotic plaques for a noninvasive rupture-risk assessment was investigated. In this chapter we discuss our findings and their implications. The main clinical implication of our findings is discussed separately in the final section, "The stable plaque paradigm".

## CAROTID MAGNETIC RESONANCE IMAGING

Carotid MRI is an established medical imaging modality to diagnose, monitor, and study atherosclerotic carotid artery disease. Its advantages for imaging geometrical and compositional features of carotid plaques are the high soft-tissue contrast by using multi-sequence protocols and the noninvasive nature of the modality. Disadvantages are the long scanning times and, in a practical sense, the relatively high costs. Whether the currently achievable acquired voxel size (~0.6 mm in-plane and ~2 mm slice thickness) can be regarded as a limitation depends on the diagnostic parameters one aspires to determine. For some parameters the spatial resolution suffices, such as for the lumen size, the degree of stenosis, and for qualitative scoring of presence of calcium, intraplaque hemorrhage or lipid-rich necrotic core [1]. However, whether carotid plaque MRI has sufficient spatial resolution for cap imaging and peak cap stress computations was not investigated in detail before.

In **Chapter 2**, we introduce numerical simulations of a carotid MRI protocol to quantify the effects of the in-plane voxel size on the accuracy of plaque segmentation. The novelty of this work is two-fold. The first novelty is the implementation of a clinical protocol in an MRI simulator to answer an imaging-based question related to a diagnosis. The advantages of simulations are the availability of a ground truth, the presence of a perfectly controlled imaging environment, and the fact that extensive patient imaging can be reduced. The second novelty of this work is the presentation of quantitative data on carotid plaque segmentation accuracy and precision. To achieve this, we first obtained cross-sectional histological plaque specimens from twelve patients, assigned MRI material properties to various tissues and performed single-slice MRI simulations. Three experienced MR readers then performed image segmentation and their measurements were compared with the ground truth model data. This allowed a quantification of the systematic errors in plaque measurements using MRI. We were able to show that current clinical MRI can be used to measure the size of the lipid-rich necrotic core, lumen, and vessel wall area of carotid plaques. The lipid-rich necrotic core size was, however, underestimated on average by -24%. These findings provide evidence that MRI is an excellent modality to be used for follow-up studies on plaque progression/regression and to measure the efficacy of pharmaceutical agents, for

example lipid-reducing medication. However, we identified severe limitations for thin fibrous cap thickness quantification. Only the thickness of fibrous caps which were thicker than 0.6 mm (the in-plane acquired voxel size) was reliably measured. Fibrous caps thinner than 0.2 mm (being the cut-off value for a thin fibrous cap atheroma classification) were overestimated in thickness by 100 to 500%.

We not only studied the effects of the in-plane resolution with two-dimensional MRI simulations. We also investigated the influence of the slice thickness on plaque imaging and extended the MRI simulations to a three-dimensional setting. In **Chapter 3**, we applied the MRI simulation methodology to investigate the influence of MRI scan plane angulations and voxel dimensions on fibrous cap contrast. Fibrous cap contrast affects the reliability of a fibrous cap status assessment. A controlled setting with numerical simulations allowed a detailed investigation, using numerous scan protocols with various voxel dimensions to image differently oriented fibrous caps in three-dimensional idealized plaque models. The findings of the study suggest that acquiring anisotropic voxels could increase fibrous cap contrast, even in the presence of localized scan plane orientation obliquity. We also created realistic three-dimensional plaque models based on histological sections to investigate the combined influence of both the slice thickness and in-plane voxel size of an MRI protocol on carotid plaque segmentation. This study is described in **Chapter 4**. The conclusion of the investigation was that acquiring anisotropic voxels could result in improved measurement accuracy of some carotid plaque components. Interestingly, the conclusions from Chapters 3 and 4 contradict earlier claims that novel isotropic imaging (which three-dimensional MRI acquisition allows) in carotid MRI should be preferred [2]. While isotropic imaging reduces axial partial volume effects and allows ideal multiplanar reformatting, the morphological variations of plaques are larger in the cross-sectional plane and better captured with anisotropic voxels when both total scan time and image noise are considered.

To improve MRI of atherosclerotic carotid plaques for fibrous cap thickness quantification, the acquired voxel size needs to be decreased. Various promising approaches are being pursued to achieve this whilst maintaining a sufficiently high image signal-to-noise ratio and short scan duration for clinical feasibility. These approaches include superresolution methods [3], increased field strengths [4,5], improved coil technology, and new pulse sequences [6]. The use of MRI simulations would be an effective approach to investigate the influence of artifacts, to optimize pulse sequences, and to investigate segmentation or image registration accuracy in a controlled environment without needing extensive patient imaging. This could also apply to fields other than carotid plaque imaging, for example brain or heart imaging. While morphological imaging is the classical application of MRI when imaging plaques,

MRI can also be used for functional plaque imaging. Biomechanical parameters such as plaque strain and fibrous cap strength are closely related to plaque rupture-risk. High strains can indicate soft, lipid-rich plaques which tend to be more vulnerable [7]. The cap strength determines at which peak cap stress the plaque will rupture. MRI can be used for the imaging of macrophage content in the fibrous cap with ultrasmall superparamagnetic particles of iron oxides, and for quantifying tissue permeability associated with vasa vasorum and inflammation [8]. Because macrophages affect cap strength, one could thus indirectly measure cap structural integrity *in vivo* [9]. MRI can also be used for direct, noninvasive spatial strain mapping of carotid plaques with displacement encoding, using stimulated echoes pulse sequences [10]. Another interesting research field is quantitative MRI, which goes beyond signal intensity imaging as it directly maps the distribution of tissue relaxation times [11]. This is useful because the signal intensity is not solely determined by tissue properties, but also by many external factors such as a decrease of signals originating more distal from neck receiver coil. Measuring the physical properties of tissues allows a more reliable plaque assessment independent of the image acquisition.

The previously mentioned applications, including morphological carotid plaque imaging, are mostly used in either experimental studies or clinical trials only. Even though MRI itself is, next to CT, an imaging modality to diagnose stroke through a brain scan, it is not an established tool to image carotid artery disease in clinical practice. The latter is currently performed by using ultrasound which suffices to assess merely the degree of stenosis. To image the carotid artery with MRI, a separate neck scan is needed, which would typically be done in a later stage after stroke diagnosis. But if MRI is made the sole standard modality for the initial diagnosis of a stroke, one can add a neck scan to the protocol and thus immediately provide valuable diagnostic information for treatment of carotid plaques to help prevent re-current events.

## PLAQUE BIOMECHANICS

In order to model the stress distribution within atherosclerotic plaques one needs to determine the loading conditions, boundary conditions, plaque geometry, and material properties. In this thesis we focused on the latter two issues. Early work on plaque biomechanics was done with two-dimensional cross-sectional models. Advances in computational power now allow three-dimensional modeling, even incorporating fluid-structure interactions [12]. In **Chapter 5**, we performed finite element analysis on both three-dimensional and two-dimensional models of the same plaques. We found that two-dimensional models suffice to obtain the general cross-sectional stress distribution and to investigate and explore geometrical risk factors associated with

peak cap stress such as in-plane curvatures, sizes of various plaque components, the cap thickness, and other parameters. However, three-dimensional models are needed for reliable absolute peak cap stress computations. Our findings are relevant for future experimental parameter studies because two-dimensional models need fewer pre- and post-processing efforts (easier geometrical reconstruction and meshing) and they require far less computational processing time.

The plaque geometry can be obtained in various ways, depending on the type of study. If one aims to investigate geometrical risk factors through a fundamental study, histological specimens can be used to obtain the plaque geometry with a very high spatial resolution. If one wants to perform an applied noninvasive peak cap stress analysis on a carotid plaque in a patient, MRI can be used. In **Chapter 6** we employed MRI simulations to investigate the influence of MRI segmentation errors related to the spatial resolution on the computed peak cap stress. The minimum fibrous cap thickness greatly influences the peak cap stress, however, it is measured unreliably with MRI if the fibrous cap thickness is smaller than the in-plane voxel size. Fibrous cap thickness overestimation led to peak cap stress underestimation. The computed peak cap stress in plaques with fibrous caps thinner than 0.2 mm (the thin fibrous cap atheroma classification for carotid plaques [13]) was highly imprecise and was underestimated between 100 and 400 kPa. Thus, a meaningful MRI-based peak cap stress computation of a thin fibrous cap atheroma is impossible considering the MRI spatial resolution alone. We found that the computed peak cap stress became increasingly more reliable for plaques with thicker caps. This is the first study to focus on the feasibility of using MRI for a biomechanical analysis as an applied clinical tool by quantifying the influence of MRI segmentation inaccuracies on biomechanical plaque stress modeling.

We determined that the acquired voxel size in MRI has a major influence on the errors in the computed peak cap stress. A decrease in the voxel size would, however, come at the cost of an increased scan time or an increased image noise level. In **Chapter 4**, we investigated the influence of the MRI slice thickness and in-plane voxel size on plaque segmentation accuracy and peak cap stress computations. We found that for the minimum fibrous cap thickness and the closely related peak cap stress magnitude, a decreased slice thickness was beneficial, but not more so than a decreased in-plane voxel size. This suggests that the acquisition of anisotropic voxels (i.e., a slice thickness larger than the in-plane voxel size) could improve biomechanical peak cap stress computations.

In order to compute the peak cap stress, the material properties of the plaque tissues need to be specified. In **Chapter 7**, we present an experimental study in which *ex vivo* ultrasound displacement measurements from inflation tests are combined with

inverse finite element analysis to estimate plaque material properties. The novelty of this work lies in the incorporation of geometrical plaque information obtained from histology of the porcine iliac vessels used for this study, and in the usage of high-frequency, high spatial resolution ultrasound displacement measurements. The advantages of the method lie in the fact that the plaque remains intact during inflation tests which mimics the actual *in vivo* loading, and in the fact that accurate, high-resolution geometrical plaque data from histology are used. Material testing in a physiological setting without damaging the plaque yields more accurate results on the mechanical properties because fibers remain intact [14]. In addition, it facilitates the study of very soft plaque materials, such as the lipid core. It is for these reasons that our approach has the potential to become the method of choice for *ex vivo* material testing of plaques, thus replacing classical tensile testing techniques. The results of the study show a wide variation in tissue elasticity among plaques, even though some plaques are from the same pig and all pigs were fed the same diet. Therefore, merely assigning averaged literature-based values to patient-specific models results in serious inaccuracies in the plaque-specific computed stresses.

There is a need for an estimation of the local plaque mechanical properties if one wants to compute the peak cap stress. Previous research on *in vivo* estimation of plaque mechanical properties mostly relied on invasive, catheter-based, modalities such as intravascular ultrasound or optical coherence tomography. In **Chapter 8**, a new method to noninvasively estimate carotid plaque component elasticity *in vivo* is introduced. The method consists of combining MRI, ultrasound strain imaging, and inverse finite element analysis. We simulated MRI and ultrasound strain imaging on a set of ground truth plaque geometries to demonstrate the feasibility and robustness of the approach by quantifying the accuracy of the elasticity estimation. We found that lipid-rich necrotic core and fibrous tissue elasticity could be estimated relatively accurately, although the stiffness of fibrous tissue was consistently underestimated. Our findings of this simulation study stimulate the application and investigation of the proposed methodology in a clinical setting. An advantage of the method lies in the fact that tissue anisotropy can be accounted for, because any arbitrary constitutive law can be "fitted" to a measured three-dimensional strain distribution. This includes readily available fiber-reinforced structural models. Arteries and atherosclerotic plaque tissues are known to be able to exhibit anisotropic mechanical behavior, which affect the peak cap stress. The anisotropic properties of plaque tissues can differ from those of healthy vessel wall and they can be highly location-dependent [15]. A direct *in vivo* measurement (for example using diffusion tensor imaging) of local fiber orientations which cause the anisotropic behavior is currently impracticable due to long scanning times. However, such knowledge could be important for peak cap stress computation.

Regardless of the imaging resolution, one could depart altogether from the traditional segmentation approach consisting of drawing contours around tissues, because the spatial heterogeneity of biological composition within plaque tissues needs to be accounted for as well. A better approach might be to classify a voxel from the image as a material with known properties, and create a voxel-based finite element model. An example of the influence of variations over very small length scales is the presence of micron-size calcifications in the fibrous cap [16]. Note that incorporating microcalcifications into traditional continuum-mechanics models conflicts with the continuum hypothesis which provides the basis for finite element modeling of plaques. Considering our current knowledge, it might be time to approach the issue of fibrous cap mechanical failure differently. Instead of clinging onto concepts from traditional continuum-mechanics originally devised for macroscopic, non-biological applications, we might be better off starting at a microscopic level and take it from there. It could be helpful to depart from the macroscopic continuum-hypothesis for modeling the mechanical phenomena within very thin fibrous caps where micron-scale processes govern cap rupture, and instead follow an approach of multi-scale modeling. Small length-scale modeling of the (statistical) effects of single-cell interactions, tearing of extracellular matrix or presence of microcalcifications in thin caps may enable us to develop probabilistic fibrous cap rupture models that could be better at predicting which caps will rupture and which will not. On a final note, a promising high spatial resolution imaging modality is optical coherence tomography, which is the only modality with the micron-resolution required to accurately measure fibrous cap thickness [17] *in vivo*. Its disadvantages, however, lie in the facts that it is an invasive, risk-inducing, catheter-based modality and that it cannot accurately image the entire plaque geometry due to the limited penetration depth of light.

While most studies, including ours, nowadays incorporate initial stresses, residual stresses often remain unaccounted for. Their significance is acknowledged, but it is the lack of adequate practical means to assess them *in vivo* that prevents them from being included in patient models [18]. Future studies regarding plaque biomechanics should focus on determining, or estimating, the residual stresses present in plaques. Current *ex vivo* approaches such as measuring the opening angle are imperfect because they reveal some, but likely not all residual stresses present within the entire plaque [19]. Furthermore, in this thesis we investigated the tissue elasticity when examining plaque material properties, however the strength of fibrous cap tissue is equally important. The computed peak cap stress would be of significantly more value as a diagnostic marker for rupture-risk if the cap strength would be known as well. Experimental data on failure mechanics of fibrous caps obtained *ex vivo* span a wide range, which demonstrates that it is important to obtain a patient-specific

strength value. Unfortunately, a direct measurement of cap strength *in vivo* is impossible. Current efforts are directed at estimating plaque-specific cap strength by quantifying related markers such as the degree of inflammation. Only if the cap strength is known can the computed peak cap stress be used as a true marker for plaque-specific rupture-risk stratification.

## THE STABLE PLAQUE PARADIGM

Whilst our fundamental understanding of plaque vulnerability has rapidly evolved, it is evident that the quest for a feasible, practical approach to target all, and only all, vulnerable carotid plaques has to this date been unfruitful. There is ample evidence that plaque vulnerability is closely related to fibrous cap thickness: the thinner the cap, the more vulnerable the plaque. We determined that the current spatial resolution of clinical MRI is insufficient to accurately image thin fibrous caps, with severe consequences. As long as the acquired voxel dimension in carotid MRI does not drop significantly, MRI-based thickness measurements of thin caps will remain unreliable. The implication for peak cap stress computations which we identified in this thesis might be only one manifestation of a more general problem. In the quest for the vulnerable plaque, various other highly-localized features of such very thin caps are inaccurately quantified or estimated, or even neglected. The problem is that features on these small length-scales (e.g., inflammation, microcalcifications, and material properties) might just govern the balance between stability and instability in (thin-cap) plaques. This makes it difficult to noninvasively identify vulnerable plaques without undertreating high-risk patients.

It is much easier to measure something big than it is to measure something small. We have shown in **Chapter 9** that the current image resolution of carotid MRI is sufficient to reliably quantify thick caps which are associated with a stable plaque phenotype. For thick-cap, fibrous-rich plaques, measurement or estimation errors in the previously mentioned markers will be less influential which makes an overall assessment more reliable. We have demonstrated that this is the case for the peak cap stress. Regarding a clinical application, it might be useful to change our mindset. That is, we should consider ceasing our focus on the vulnerable plaques and instead targeting the most stable carotid plaques in order to at least exempt *them* from a surgical intervention. Vulnerable plaque identification in a clinical setting might be, for now, a bridge too far. Instead of trying to identify a smaller cohort of high-risk patients who would benefit from intervention, it might be more effective to reliably identify a smaller cohort of the most low-risk patients with stable plaques who would not benefit from intervention. With this likely more feasible approach, one might just be able to

effectively reduce the unsustainably high number of unnecessary risk- and cost-inducing surgeries on stable carotid plaques while still treating the high-risk carotid artery disease patients. Whether or not our stable plaque hypothesis has any merit will need to be tested in a clinical randomized control trial.

## REFERENCES


1. Underhill HR, Hatsukami TS, Fayad AZ, Fuster V, Yuan C. MRI of carotid atherosclerosis: clinical implications and future directions. Nat Rev Cardiol 2010;7:165-173.
2. Balu N, Yarnykh VL, Chu B, Wang J, Hatsukami T, Yuan C. Carotid plaque assessment using fast 3D isotropic resolution black-blood MRI. Magn Reson Med 2011;65(3):627-637.
3. Plenge E, Poot DH, Bernsen M, Kotek G, Houston G, Wielopolski P, van der Weerd L, Niessen WJ, Meijering E. Super-resolution methods in MRI: can they improve the trade-off between resolution, signal-to-noise ratio, and acquisition time? Magn Reson Med 2012;68:1983-1993.
4. de Rotte AA, Koning W, Truijman MT, den Hartog AG, Bovens SM, Vink A, Sepehrkhouy S, Zwanenburg JJ, Klomp DW, Pasterkamp G, Moll FL, Luijten PR, Hendrikse J, de Borst GJ. Seven-tesla magnetic resonance imaging of atherosclerotic plaque in the significantly stenosed carotid artery: a feasibility study. Invest Radiol 2014;49:749-757.
5. Koning W, de Rotte AA, Bluemink JJ, van der Velden TA, Luijten PR, Klomp DW, Zwanenburg JJ. MRI of the carotid artery at 7 Tesla: Quantitative comparison with 3 Tesla. J Magn Reson Imaging 2014.
6. van Wijk DF, Strang AC, Duivenvoorden R, Enklaar DJ, van der Geest RJ, Kastelein JJ, de Groot E, Stroes ES, Nederveen AJ. Increasing spatial resolution of 3T MRI scanning improves reproducibility of carotid arterial wall dimension measurements. MAGMA 2014;27:219-226.
7. de Korte CL, Pasterkamp G, van der Steen AF, Woutman HA, Bom N. Characterization of plaque components with intravascular ultrasound elastography in human femoral and coronary arteries *in vitro*. Circulation 2000;102:617-623.
8. Kooi ME, Cappendijk VC, Cleutjens KB, Kessels AG, Kitslaar PJ, Borgers M, Frederik PM, Daemen MJ, van Engelshoven JM. Accumulation of ultrasmall superparamagnetic particles of iron oxide in human atherosclerotic plaques can be detected by *in vivo* magnetic resonance imaging. Circulation 2003;107:2453-2458.
9. Lendon CL, Davies MJ, Born GV, Richardson PD. Atherosclerotic plaque caps are locally weakened when macrophages density is increased. Atherosclerosis 1991;87:87-90.
10. Nederveen AJ, Avril S, Speelman L. MRI strain imaging of the carotid artery: present limitations and future challenges. J Biomech 2014;47:824-833.
11. Smit H, Guridi RP, Guenoun J, Poot DH, Doeswijk GN, Milanesi M, Bernsen MR, Krestin GP, Klein S, Kotek G. T1 mapping in the rat myocardium at 7 tesla using a modified CINE inversion recovery sequence. J Magn Reson Imaging 2014;39:901-910.
12. Huang Y, Teng Z, Sadat U, Graves MJ, Bennett MR, Gillard JH. The influence of computational strategy on prediction of mechanical stress in carotid atherosclerotic plaques: comparison of 2D structure-only, 3D structure-only, one-way and fully coupled fluid-structure interaction analyses. J Biomech 2014;47:1465-1471.
13. Redgrave JN, Gallagher P, Lovett JK, Rothwell PM. Critical cap thickness and rupture in symptomatic carotid plaques. Stroke 2008;39:1722-1729.
14. Beattie D, Xu C, Vito R, Glagov S, Whang MC. Mechanical analysis of heterogeneous, atherosclerotic human aorta. J Biomech Eng 1998;120:602-607.
15. Chai CK, Speelman L, Oomens CW, Baaijens FP. Compressive mechanical properties of atherosclerotic plaques - indentation test to characterise the local anisotropic behaviour. J Biomech 2014;47:784-792.
16. Kelly-Arnold A, Maldonado N, Laudier D, Aikawa E, Cardoso L, Weinbaum S. Revised microcalcification hypothesis for fibrous cap rupture in human coronary arteries. Proc Natl Acad Sci 2013;110:10741-10746.

17. Wang Z, Chamie D, Bezerra HG, Yamamoto H, Kanovsky J, Wilson DL, Costa MA, Rollins AM. Volumetric quantification of fibrous caps using intravascular optical coherence tomography. Biomed Opt Express 2012;3:1413-1426.
18. Holzapfel GA, Mulvihill JJ, Cunnane EM, Walsh MT. Computational approaches for analyzing the mechanics of atherosclerotic plaques: a review. J Biomech 2014;47:859-869.
19. Ohayon J, Dubreuil O, Tracqui P, Le Floc'h S, Rioufol G, Chalabreysse L, Thivolet F, Pettigrew RI, Finet G. Influence of residual stress/strain on the biomechanical stability of vulnerable coronary plaques: potential impact for evaluating the risk of plaque rupture. Am J Physiol Heart Circ Physiol 2007;293:H1987-1996.

# Appendix

## Analysis of the dart game – walking into doubles and optimal aiming locations

**Abstract** | In this study a Gaussian distribution is used to model the randomness of darts. With this model, the optimal aiming location and optimal segment can be determined where a dart player should aim in order to expect the highest score. Where the optimal aiming location is depends on the accuracy (skill) of the dart player, which is represented by the standard deviation, $\sigma$, from the Gaussian distribution. In this study an easy method to estimate the (average) $\sigma$ of a dart player has been developed. Also, a certain technique to finish a leg called "walking into a double" has been investigated for different values of $\sigma$, and it has been proved that this technique can significantly increase the chance of successfully finishing a leg in the last turn. Finally, the average $\sigma$ of dart players can be used to rank them based on their average accuracy. This paves the way for a new handicap system in the game of darts.

**This chapter is based on:** Nieuwstadt HA. Analysis of the dart game – walking into doubles and optimal aiming locations. Mathematics Today 2007;43:140-144.

# INTRODUCTION

When throwing darts at a dartboard with the goal of maximizing the score, the question arises as to what the optimal aiming location is. The treble 20 segment yields the highest score of course, but hitting it is difficult for an average player, and the 1 and 5 segments next to the 20 seriously penalize an unsuccessful throw. This means that for many players the treble 20 is not the optimal aiming location [1].

Previous simulation studies with a Gaussian model have already provided an answer to this question [2]. Here a more efficient computational technique is used to refine this analysis and which leads itself to answering other interesting questions concerning optimal dart play. It is possible to calculate expected scores directly by defining a dartboard function, which is a 2D piecewise constant step function with 82 defined values corresponding to the scores associated with each segment of a dartboard. Multiplying this function with a 2D Gaussian distribution centered on a given aiming location and numerically integrating that product yields a direct measure for the expected score when aiming at that location.

The standard deviation $\sigma$ (sigma) of the Gaussian distribution reflects the accuracy of a dart player. This may vary from time to time, from match to match (or from pint to pint), and so it is more meaningful to speak of an average $\sigma$. Once a good estimate of the average $\sigma$ is known (a simple $\sigma$ measurement method will be developed and discussed in this study), not only can the optimal aiming location be determined, but also the step size $\delta$ with which a dart player can best "walk into a double".

# THEORY

## Gaussian Modeling

It is assumed that the probability density functions (PDFs) in the $x$ and $y$ coordinates of where a dart will land on a dartboard can be approximated as Gaussian and that these PDFs are independent, with the standard deviations in the $x$ and $y$ coordinates both equal to $\sigma$ [2,3]. This gives the joint PDF (dart function):

$$f_{dart}(x,y) = \frac{1}{2\pi\sigma^2}\exp\left(-\frac{(x-\mu_x)^2+(y-\mu_y)^2}{2\sigma^2}\right). \quad (1)$$

It is further assumed that the value of $\sigma$ is independent of the aiming location $(\mu_x,\ \mu_y)$, and that each throw is independent of other throws. With $(0,\ 0)$ taken as the aiming location and converting equation (1) into polar coordinate $r$, it then results in the Rayleigh distribution:

$$f_{Rayleigh}(r) = \frac{r}{\sigma^2}\exp\left(-\frac{r^2}{2\sigma^2}\right), \tag{2}$$

which describes the radial distribution of the striking point of a dart from the aiming location. One of the most accurate ways to estimate the $\sigma$ of a dart player is with the maximum likelihood estimator (MLE) for $\sigma$ in equation (2). By throwing $n$ darts to a fixed aiming location and measuring the distance $r_i$ of dart $i$ to that aiming location, the MLE of $\sigma$ is given by:

$$\hat{\sigma}_{ML} = \sqrt{\frac{1}{2n}\sum_{i=1}^{n}(r_i)^2}. \tag{3}$$

## Walking into the double

In a standard "501" dart game (leg) a player must not only achieve a score of exactly 501 before his/her opponent does, but must also finish the game on a double. When a dart player begins a turn (consisting of throwing three darts) and needs to hit a double to win the leg, the dart player can use a technique called "walking into the double". The first dart is aimed a distance $2\delta$ radially outward from the center of the double (Figure 1). If that dart misses the board or bounces out, the second dart is aimed a distance $\delta$ radially outward from the center of the double. If that dart also misses the board or bounces out, the last dart is aimed directly at the center of the double. Let $\alpha_j$ denote the probability that dart $j$ lands outside the dartboard scoring area, and $\beta_j$ the corresponding probability that the dart will land inside the desired double. If a dart

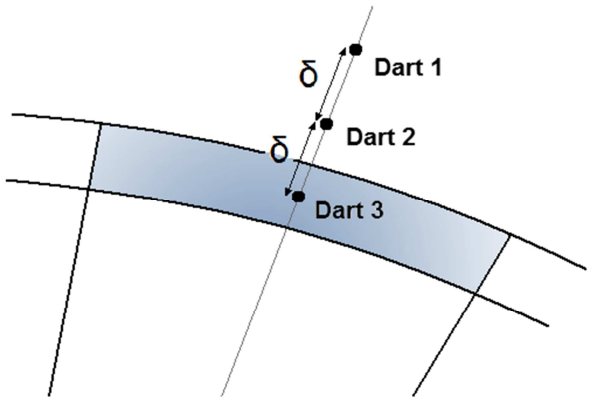


**Figure 1.** Aiming locations for walking into a double with step size $\delta$ (for the double 1).

that hits the dartboard scoring area but not the desired double is considered as a bust, the chance of successfully finishing the turn (and leg), $P_{succes}$, using the walking technique, is

$$P_{succes} = \beta_1 + \alpha_1\beta_2 + \alpha_1\alpha_2\beta_3. \quad (4)$$

## METHODS

The first thing that has to be done is to precisely define the dartboard function. This is done in accordance with the dimensions set out in the official World Darts Federation (WDF) tournament playing rules [4]. All distances are defined in cm, and thus the $\sigma$ from the Gaussian distribution is based on distances in cm. The center of the bullseye is taken as the origin.

### Numerical integration

In this study the product of two 2D functions of $x$ and $y$ has to be integrated. A simple numerical procedure is used to compute that product; a domain of integration [$x$min, $x$max] x [$y$min, $y$max] is subdivided into elemental, sufficiently small areas of width $dx$ and length $dy$:

$$dx = \frac{x\text{max} - x\text{min}}{F}, \; dy = \frac{y\text{max} - y\text{min}}{F}.$$

The coordinates of the center of each small rectangle are determined, and the values of both functions at those coordinates are multiplied with each other. The resulting product is then multiplied with the area of the rectangle, $dxdy$, to give a small volume. The sum of all those elemental volumes will be a measure for the volume of the product of the two functions within the integration boundaries. All integration mentioned in this article is done by this method. $F$ is the integration resolution, which has to be sufficiently large to give an accurate measure of the analytical volume.

### Expected score calculation

The expected score per dart when throwing it at an aiming location ($\mu_x$, $\mu_y$) is the volume of the product of the $f_{dart}(x, y)$ function and the dartboard function. If the expected score is calculated for many different aiming locations distributed uniformly in a rectangular array covering the entire surface of the dartboard, then a graph of the

distribution of expected scores can be constructed showing how these vary with aiming location. This gives an expected score (ES) graph.

Now the optimal segment can be calculated for every value of $\sigma$. The optimal segment is the segment on the dartboard for which aiming for its center provides the highest expected score in comparison to aiming at the center of the other segments. A dartboard consists of 81 different segments (counting the double and single bull segments as a single segment since the aiming location is the same for both). For different values of $\sigma$ in $f_{dart}(x, y)$ the optimal segment can be determined by calculating the expected scores resulting from aiming at the center of all 81 segments, and then determining the aiming location (and thus segment) that yields the highest expected score per dart.

### Estimating σ: the sigma treble estimate (STE) method

Although an estimate for $\sigma$ can be obtained by using the MLE formula given in equation (3), the following alternative approach is somewhat simpler and more convenient. From the fraction of darts, $\theta$, that hit a certain segment while aiming at the center of that segment, the $\sigma$ of a player can be determined. Since the segments of most interest are the treble segments, the dartboard function is replaced by a treble 20 segment function which is zero everywhere expect for the treble 20 segment where it has value 1. The treble 20 segment is used here, but it could be any treble segment, because the dart function is radially symmetric. The aiming location of the dart function is taken as the center of the treble 20. The product of the dart function and the treble 20 segment function that is integrated, is a measure for the expected fraction of darts to land within a treble segment while aiming at the center of that treble segment. For different values of $\sigma$, this fraction can be calculated and plotted. This graph can be used to estimate the $\sigma$ of a player: if a player knows which fraction of his/her darts hit a treble, the graph can be easily used to estimate the corresponding $\sigma$.

### Optimal double walking step size

To determine the optimal value of $\delta$ (of a given $\sigma$) a basic dartboard function is introduced: this function is the same as the dartboard function except that now every scoring segment on the dartboard has value 1. Then a double 20 segment function is defined (it does not matter which double is taken since the dart function is radially symmetric), which is zero everywhere, except for the double 20 segment where it has value 1. Next, the three aiming locations are calculated from the step size $\delta$ (Figure 1). For each aiming location the probability $(1 - \alpha)$ of hitting the dartboard scoring area (integrating the product of the dart function and the basic dartboard function) and

also the probability $\beta$ of hitting the desired double (integrating the product of the dart function and the double 20 segment function) are calculated. Then, using equation (4), the probability of success, $P_{succes}$, can be calculated (which depends on the $\sigma$ and the step size $\delta$ used).

# RESULTS

## Validation of the Gaussian model

To test whether the Gaussian model assumption holds, 816 darts were thrown at a fixed aiming location and the distance $r$ between that aiming location and the location where a dart actually landed was measured. The $\sigma$ was estimated using the MLE, equation (3), which gave a value of 2.69. Figure 2 shows histograms of the observed number of darts and the expected number of darts (Rayleigh distribution, $\sigma = 2.69$) as function of $r$. The data were subjected to a Pearson's chi-squared goodness of fit test. Bin domains were adjusted to result in a constant value of the expected number of darts (91) per bin (9 bins). A $p$-value of 0.92 was found (right tail probability) which gave no reason to reject the null hypothesis that the observed data came from the Gaussian model, equation (1).

## Expected score calculation

For $\sigma = 2.69$ the expected scores have been calculated for 400 x 400 aiming locations. These aiming locations are the points on a grid of 400 steps in the $x$ and $y$ directions

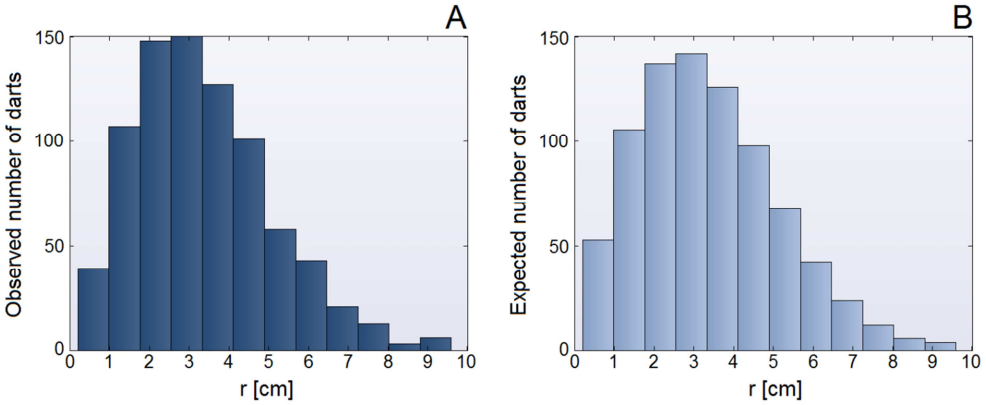


**Figure 2.** Histograms show the observed (A) and expected (B) number of darts ($n$ = 816) to land between indicated, binned, distances from a fixed aiming point.

from -18 cm to 18 cm on the $x$-axis and -18 cm to 18 cm on the $y$-axis. ($F$ = 800, $x$min = $y$min = -18 cm and $x$max = $y$max = 18 cm). The ES-graph is plotted in Figure 3. Then for values of $\sigma$ ranging from 0.50 to 7.00, the expected scores for all 81 aiming locations (centers of all 81 segments) were calculated ($F$ = 2500, $x$min = $y$min = -18 cm and $x$max = $y$max = 18 cm). The segment for which the aiming location gives the highest expected score is the optimal segment for that $\sigma$. The results are summarized in Figure 4.

### Sigma treble estimate (STE) curve

The fraction of darts $\theta$ that land within a treble segment while aiming at the center of that segment has been calculated for different values of $\sigma$ from 0.02 to 3.00 in steps of 0.02 (Figure 5). The treble 20 was used ($x$min = -2.5 cm, $x$max = 2.5 cm, $y$min = 9 cm, $y$max = 11 cm and $F$ = 1000). Figure 5 also shows the fraction of darts that land within the radius of the single bull as a function of $\sigma$. This is obtained analytically by integrating equation (2) from $r$ = 0 to the single bull radius.

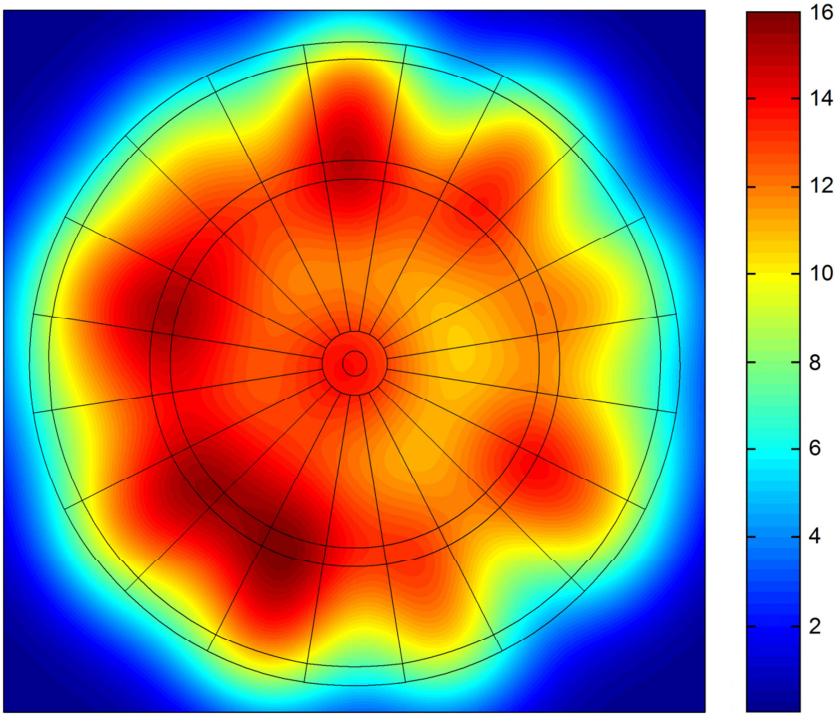


**Figure 3.** ES graph; dependence of expected score per dart on aiming location for $\sigma$ = 2.69.

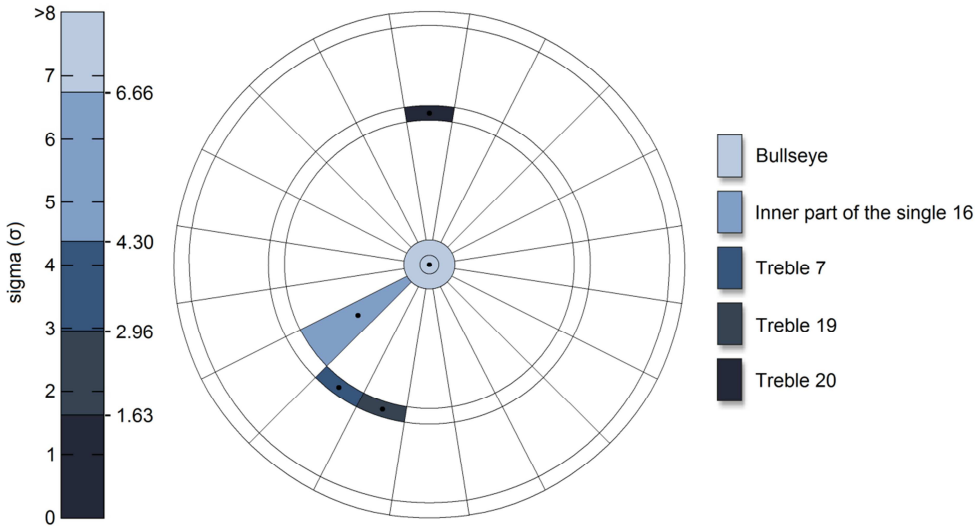


**Figure 4.** Optimal segment based on the sigma ($\sigma$) of a dart player.

### Optimal double walking step size

Four different $\sigma$ values (0.8, 1.2, 1.6, 2.0) have been taken to calculate the probability of success as defined in equation (4) for a range of different step sizes. For the calculation of $(1-\alpha)$ and $\beta$ the same integration parameters have been used: $F = 2500$, $x\text{min} = y\text{min} =$ -18 cm and $x\text{max} = y\text{max} = 18$ cm. For each $\sigma$, the probability of success has been calculated for step sizes $\delta$ ranging from 0.00 cm to 1.50 cm in steps of 0.04 cm (Figure 6A). To quantify the "gain" a dart player can achieve by walking into the double instead of just aiming for its center for every dart in the last turn ($\delta = 0$), the probability of success $P_{0,\sigma}$ for $\delta = 0$ (not walking) and given $\sigma$, is subtracted from the corresponding probability of success for a given step size $\delta \neq 0$ (Figure 6B).

## DISCUSSION AND CONCLUSIONS

This study has illustrated the application of some relatively simple mathematical and statistical techniques to achieve detailed analysis of strategies and tactics in the game of darts. Measurement methods (MLE and STE) that dart players can use to measure their average $\sigma$ have been discussed. Based on this, players can improve two very important aspects of their game: scoring the maximum possible amount of points, and increasing the chance of finishing a leg in the last turn.

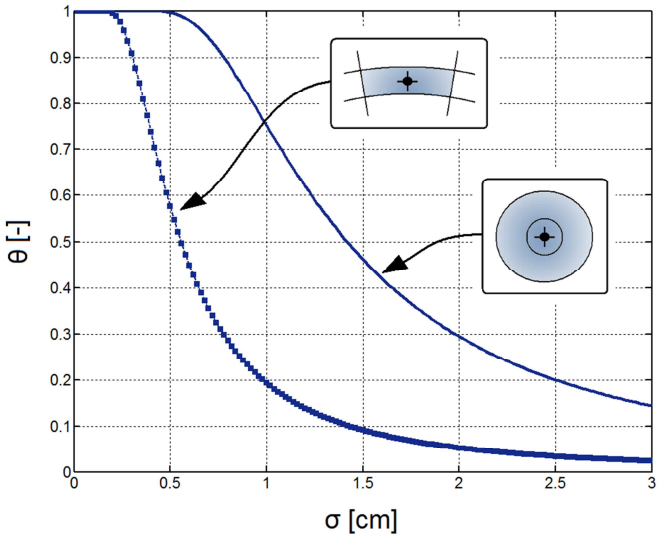


**Figure 5.** STE graph (squares) and bullseye graph (solid line). Expected fraction of darts, $\theta$, to land within the indicated segment as a function of $\sigma$ when aiming at the center of that segment.

While a player could use the MLE formula, equation (3), to estimate the $\sigma$, a simpler and quicker way is to use the STE method. The player should throw at least 200 darts to a treble of his/her choice and calculate the percentage of darts that successfully hit that treble. If this percentage is higher than 5.5% then Figure 5 (curve with squares) can be used to estimate the $\sigma$. Since the $\sigma$ will be different on different occasions, this test should be repeated on several occasions so that the average $\sigma$ can be determined. With the STE method it is also possible to estimate the $\sigma$ of professional dart players based on televised dart matches by just counting the number of successful treble hits and misses. For example, based on all the treble attempts by Mervyn King during the semi-final of the Bavaria Open 2005, his $\sigma$ for that occasion was estimated at 0.87, which is a very typical value for professional dart players. An experienced competition dart player, [5], got an estimated $\sigma$ of 1.48 based on the STE method with 300 darts (competition dart players and good amateur dart players have an average $\sigma$ of roughly between 1 and 3).

To get back to this study: knowing the average $\sigma$, the optimal segment can be determined from Figure 4. This result is in agreement with earlier studies [2,3]. To fully analyze all aiming options, it is possible to make an ES-graph, which shows the expected score for every possible aiming location. The ES-graph for a $\sigma$ of 2.69 (Figure 3) shows for instance that the treble 19 is the optimal segment, which is in agreement

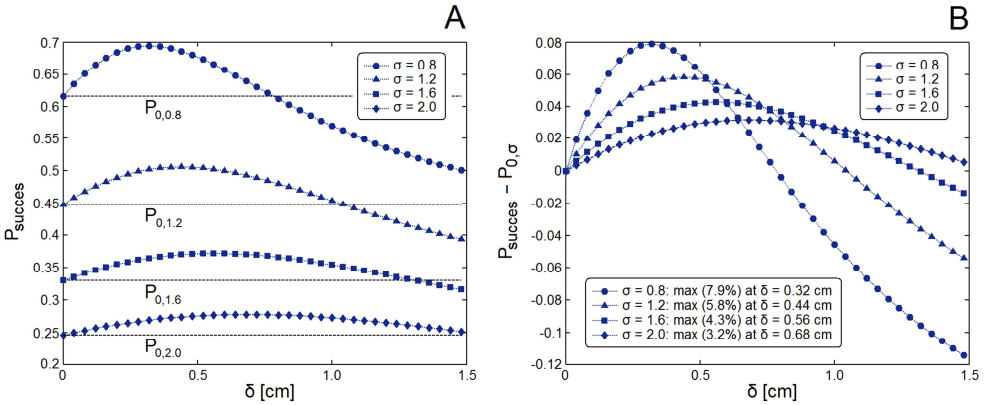


**Figure 6.** Dependence of the probability of success when walking into a double on step size $\delta$ (A) and corresponding gain compared to the probability of success with $\delta = 0$ (B).

with Figure 4. If a player has an average $\sigma$ of 2 or lower, it is advantageous for him/her to use the walking into a double technique when finishing a leg. Figure 6 can be used to determine the optimal step size $\delta$. This study has provided the first mathematical demonstration that walking into a double can improve the chances of successfully finishing a leg in the last turn significantly. For a typical professional dart player with a $\sigma$ of 0.8, walking into a double with a step size of 0.32 cm improves the chance of successfully finishing the leg in the turn by a phenomenal 8%!

Finally, it is worth noting that since $\sigma$ represents the accuracy of a dart player, this suggests a novel way of classifying dart players based on their average accuracy. Observing Figure 4, dart players with a $\sigma < 1.63$ can be called *class A* dart players, dart players for which $1.63 < \sigma \leq 2.96$ can be called *class B* dart players, and any dart player with a $\sigma > 2.96$ a *class C* dart player. This could be construed as a more useful classification than those introduced by [2,3]. It is even possible to classify dart players by their average $\sigma$ based on a certain defined number of matches or tournaments, thus paving the way for a new handicap system in darts. Based on the difference in the average $\sigma$ value of two players, it should be possible to calculate how many extra darts the less good player should get per turn to make the game even or from which score the less good player may begin (for example 401 instead of 501).

## ACKNOWLEDGEMENTS

The author would like to thank Simon Hall, head of marketing for Winmau (Bridgend, U.K.), for showing great interest in this study and many useful discussions, which led

to the writing of this article in the first place. Thanks also to David Swailes (Ph.D), Newcastle University, U.K., for useful discussions, and not to forget David A. Joiner (Ph.D), Kean University, Union, U.S., for introducing the "walking into the double" problem. Finally, thanks go out to Robin Boin, who took the time one evening to throw many darts for measurements at former café De Pet, 's-Gravenzande, the Netherlands.

## REFERENCES

1. Eastway R, Haigh J. How to take a penalty – the hidden mathematics of sport. 192 pages. Robson Books, London, 2005.
2. Aitkenhead M, Pickles B, Norton G, Macmillan K, Nicol GW. Skill-based optimised aiming in darts, Mathematics Today 2007;43:30-32.
3. Kohler D. Optimal strategies for the game of darts. J Opl Res Soc 1982;33:871-884.
4. World Darts Federation (WDF) Playing & Tournament Rules, Seventh Revised Edition, Dave Alderman Co-ordinator, November 1st 2005.
5. Robin Boin, an excellent Dutch competition dart player and once teammate of five-time World Darts Champion Raymond van Barneveld.

# Appendix

# Summary

Carotid atherosclerosis is a common cause of acute ischemic stroke and places a major burden on health-related quality of life worldwide. The current stenosis-degree guidelines to decide on surgical intervention through carotid endarterectomy in order to prevent a future event are imperfect. This is because they target plaque vulnerability insufficiently. To provide an alternative carotid plaque vulnerability assessment, one can compute the biomechanical peak cap stress using noninvasive magnetic resonance imaging (MRI).

In **Chapter 1**, we provide an introduction. Many stenosis-inducing but potentially stable plaques are treated at unnecessary risk and costs, while many plaques inducing no stenosis due to outward remodeling may be prone to rupture but are currently not treated. A biomechanical assessment of the peak cap stress is a promising approach to identify plaque vulnerability, because it combines relevant factors such as morphology and material properties to model the peak cap stress which, in the end, causes rupture. Only MRI can provide sufficient contrast to noninvasively image carotid plaque morphology in three dimensions.

In **Chapter 2**, we investigated the effects of MRI segmentation errors on the quantification of carotid plaque components: the lumen size, the wall size, the lipid-rich necrotic core size, and the minimum fibrous cap thickness. We took a new approach to determine these segmentation errors by numerically simulating an MRI protocol. We created plaque models from histological data of carotid plaques and subjected them to an MRI simulation of a T1-weighted contrast-enhanced protocol. Three MR readers performed segmentation. The lumen, wall, and lipid-rich necrotic core could be measured reliably. However, fibrous caps thinner than the in-plane acquisition voxel size (which was 0.62 mm) were measured inaccurately and overestimated.

In **Chapter 3**, we studied the effects of an oblique scan plane orientation on fibrous cap contrast in carotid MRI. Idealized plaque models were created with varying fibrous cap thickness, rotated between 0° and 40° and subjected to a single-slice carotid MRI simulation. We varied the acquired in-plane voxel size and slice thickness. We found that a reduced in-plane voxel size at the cost of an increased slice thickness often led to enhanced fibrous cap contrast even in the presence of scan plane orientation angles of up to 40°. Thus, if scan plane orientation obliquity at the slice of interest is moderate (<40°) or otherwise diminished through careful scan planning, voxel anisotropy could

increase fibrous cap contrast and, in effect, increase the reliability of fibrous cap status assessment.

In **Chapter 4**, we studied the effects of a decreased slice thickness and/or in-plane voxel size in carotid MRI on atherosclerotic plaque component quantification accuracy and on biomechanical peak cap stress analysis. We studied these effects through an MRI simulation approach. Eight histology-based 3D carotid plaque models were subjected to a simulation of a T1-weighted contrast-enhanced protocol. Interestingly, a decreased slice thickness did not result in major improvements in lumen, vessel wall, and lipid-rich necrotic core size measurements. Acquiring MR images with a higher in-plane resolution (0.31 mm acquired in-plane voxel size) led to similar or significantly larger improvements in plaque component quantification and computed peak cap stress. Thus, the acquisition of anisotropic voxels instead of isotropic voxels could improve carotid plaque quantification.

In **Chapter 5**, we quantified the influence of the axial sampling resolution on computed stresses and we compared three-dimensional plaque stress computations with two-dimensional computations. We obtained histological data from four human coronary plaques and reconstructed the plaques using cross sections with high sampling and low sampling in three dimensions. We also created two-dimensional models. We found that axial undersampling does not influence the qualitative stress distribution significantly and that two-dimensional models can be used to investigate geometrical risk factors in parameter studies. However, three-dimensional models are needed when accurate computation of patient-specific peak stress magnitude is required.

In **Chapter 6**, we studied the influence of MRI plaque segmentation inaccuracies on the computed peak cap stress. This study was an extension of the study in chapter 2. We found that peak cap stress computed with finite element analysis based on carotid MRI data was consistently underestimated. However, it still correlated moderately with the stress in the ground truth histology-based plaque models from which the simulated MR images were created. The peak cap stress in thick-cap, low stress plaques was substantially more accurately and precisely predicted than the peak cap stress in plaques with caps thinner than the acquisition voxel size. We concluded that an in-plane acquisition voxel size of 0.62 mm is inadequate for a reliable MRI-based finite element analysis to compute the peak cap stress of carotid plaques with thin caps.

In **Chapter 7**, we switched our focus to the estimation of plaque tissue elasticity. The reason for this switch of focus lies in the fact that accurate knowledge of plaque

elasticity is also crucial for reliable stress computations. We introduced a hybrid approach for the estimation of plaque tissue elasticity. This approach consists of high-frequency ultrasound displacement measurements and of inverse finite element analysis. We used histological data to obtain detailed knowledge on the plaque geometry. Six porcine iliac arteries were tested in an *ex vivo* inflation testing-setup. The main advantage of the approach lies in the fact that the vessels are loaded in physiological condition and remain intact during the loading. We found that our models captured measured deformation patterns well. In addition, we observed a large variation in the stiffness values when we compared similar tissues from different plaques.

In **Chapter 8**, we developed a method to estimate carotid plaque tissue elasticity noninvasively. The method consists in imaging the carotid plaque geometry with MRI, performing ultrasound strain imaging and solving the inverse problem with finite element analysis. To assess the feasibility of the methodology we took a computational approach and simulated MRI and ultrasound strain imaging on a set of computer plaque models based on histological sections of excised plaques. We investigated multiple scenarios for plaque model elasticity, and consistently obtained accurate estimations of elasticity values of lipid-rich necrotic core and fibrous tissues. The promising findings of this study stimulate the application of the proposed methodology in a clinical setting.

In **Chapter 9**, we compared two approaches to target plaque vulnerability: a morphological classification scheme and a biomechanical analysis. We then assessed the implications of the outcome of the comparison for noninvasive risk-stratification of carotid plaques. We obtained 75 histological plaque cross sections and subjected them to both a peak cap stress computation and a histopathological plaque classification scheme. On a subset of the plaques we performed MRI simulations and we studied the effects of errors in the computed peak cap stress on the aforementioned comparison. While peak cap stress was generally associated with the histopathological classification many plaques exhibited a disagreement between the two classifications. Because of the limited MRI voxel size with regard to cap thickness, a noninvasive identification of only a group of low-risk, thick-cap plaques was reliable. We concluded with the hypothesis that instead of trying to identify all, and only all, vulnerable plaques, a reliable noninvasive identification of stable plaques with a thick cap and low stress might be a more fruitful approach to start reducing surgical interventions on carotid plaques.

In **Chapter 10**, we provided a general discussion. We presented the main conclusions of our studies and put the results in perspective regarding the fields of carotid MRI and

plaque biomechanics. We also provided an outlook for future research. In the last section, we discussed the main clinical implication of our work: “The stable plaque paradigm”.

# Samenvatting

Atherosclerose in de carotis is een veel voorkomende oorzaak van acute beroertes en heeft een grote negatieve invloed op de gezondsheidsgerelateerde levenskwaliteit wereldwijd. De huidige richtlijnen die worden gebruikt om te bepalen of een chirurgische ingreep door middel van een carotis endarterectomie nodig is, zijn gebaseerd op de graad van stenose. Deze richtlijnen hebben echter tekortkomingen omdat de kwetsbaarheid van de plaque onvoldoende wordt meegewogen. Voor een alternatieve evaluatie van carotis plaque kwetsbaarheid kan men de maximale biomechanische kapspanning berekenen met behulp van niet-invasieve magnetische resonantie beeldvorming (MRI).

In **hoofdstuk 1** wordt een introductie gegeven. Plaques die een stenose veroorzaken maar potentieel stabiel zijn worden nu behandeld, met onnodig risico en onnodige kosten tot gevolg - dit terwijl veel plaques die door buitenwaarts remodelleren geen stenose veroorzaken maar wel kunnen scheuren nu niet behandeld worden. Een biomechanische evaluatie van de maximale kapspanning is een veelbelovende manier om plaque kwetsbaarheid in kaart te brengen omdat het relevante factoren zoals de morfologie en materiaaleigenschappen combineert om de maximale kapspanning te modelleren. Het is de kapspanning die uiteindelijk het scheuren van de plaque veroorzaakt. Alleen MRI kan voldoende contrast genereren om niet-invasief de carotis plaque morfologie in drie dimensies af te beelden.

In **hoofdstuk 2** onderzochten wij de effecten van fouten in MRI segmentatie op het kwantificeren van carotis plaquecomponenten: de grootte van het lumen, de wand en de vetrijke kern, en de minimale dikte van de fibreuze kap. Wij onderzochten de effecten van segmentatiefouten op een nieuwe manier, en wel door middel van het numeriek simuleren van een MRI protocol. Wij maakten plaque modellen gebaseerd op histologische data van carotis plaques, en gebruikten deze modellen voor een MRI simulatie van een T1-gewogen, contrast-versterkt protocol. Drie MR lezers segmenteerden de beelden. Van het lumen, de wand en de vetrijke kern waren de resulterende metingen betrouwbaar. Echter, fibreuze kappen dunner dan de in-beeld opgenomen voxelgrootte (deze was 0.62 mm) werden onnauwkeurig gemeten en overschat.

In **hoofdstuk 3** bestudeerden wij de effecten van een gekantelde scan-vlak orientatie op het contrast van de fibreuze kap in MRI van de carotis. Wij maakten geïdealiseerde

plaque modellen met variabele fibreuze kapdikte. Met een rotatie tussen 0° en 40° werden deze afgebeeld met een enkele-plak carotis MRI simulatie. Een gereduceerde in-beeld voxelgrootte ten koste van een grotere plakdikte leidde vaak tot een groter contrast van de fibreuze kap, zelfs als er sprake was van een gekantelde scan-vlak orientatie met hoeken tot 40°. Als de hoek van de scan-vlak orientatie niet zo groot is (<40°), of anderzins is geminimaliseerd door zorgvuldige planning van de scan, dan kunnen anisotrope voxels het contrast van de fibreuze kap verbeteren en daarmee ook de betrouwbaarheid van een evaluatie van de status van de fibreuze kap.

In **hoofdstuk 4** bestudeerden wij de effecten van een kleinere plakdikte en/of in-beeld voxelgrootte in carotis MRI op de nauwkeurigheid van de kwantificatie van atherosclerotische plaquecomponenten en op een biomechanische maximale kapspanningsanalyse. Dit deden wij door middel van MRI simulaties. Acht 3D carotis plaque modellen op basis van histologie werden afgebeeld met een simulatie van een T1-gewogen, contrast-versterkt protocol. Interessant genoeg leidde een verminderde plakdikte niet tot belangrijke verbeteringen in de metingen van het lumen, de wand en de vetrijke kern. Het opnemen van MR beelden met een hogere in-beeld resolutie (0.31 mm opgenomen in-beeld voxelgrootte) leidde tot dezelfde of significant grotere verbeteringen in de kwantificatie van plaquecomponenten en de berekende maximale kapspanning. Het opnemen van anisotrope voxels in plaats van isotrope voxels zou carotis plaque kwantificatie kunnen verbeteren.

In **hoofdstuk 5** kwantificeerden wij de invloed van de axiale bemonsteringsresolutie op berekende spanningen en wij vergeleken drie-dimensionale plaque spanningsberekeningen met twee-dimensionale berekeningen. Wij gebruikten histologische data van vier menselijke coronaire plaques en reconstrueerden deze plaques in drie dimensies door middel van doorsnedes met een hoge bemonstering en een lage bemonstering. Wij maakten ook twee-dimensionale modellen. Wij ontdekten dat een lage axiale bemonstering geen significante invloed heeft op de kwalitatieve spanningsdistributie en dat twee-dimensionale modellen gebruikt kunnen worden om geometrische risicofactoren te onderzoeken in parameterstudies. Echter, drie-dimensionale modellen zijn nodig voor een betrouwbare berekening van de maximale spanning in patient-specifieke modellen.

In **hoofdstuk 6** bestudeerden wij de invloed van onnauwkeurigheden in MRI plaque segmentatie op de berekende maximale kapspanning. Dit onderzoek was een vervolg op de studie beschreven in hoofdstuk 2. We ontdekten dat een eindige elementen analyse model gebaseerd op MRI leidt tot een consistente onderschatting van de maximale

kapspanning. Er was echter wel een matige correlatie met de spanning in de verificatiebasis ('ground truth') histologie-gebaseerde plaque modellen die werden gebruikt voor de MRI simulaties. De maximale kapspanning in dikke kappen met een lage spanning werd aanzienlijk nauwkeuriger en preciezer voorspeld dan de maximale kapspanning in plaques met kappen die dunner waren dan de opgenomen voxelgrootte. Wij concludeerden dat, als we willen dat een MRI-gebaseerde eindige elementen analyse de maximale kapspanning in carotis plaques met een dunne kap betrouwbaar berekent, een in-beeld opgenomen voxelgrootte van 0.62 mm niet voldoende is.

In **hoofdstuk 7** richtten wij onze aandacht op waardeschatting van de elasticiteit van plaque weefsel. Dit deden wij omdat nauwkeurige kennis van plaque elasticiteit ook cruciaal is voor betrouwbare spanningsberekeningen. Wij introduceerden een hybride methode voor het schatten van plaque weefsel elasticiteit. Deze methode bestaat uit hoge-frequentie-echografie verplaatsingsmetingen en een inverse eindige elementen analyse. Wij gebruikten histologische data om gedetailleerde kennis over de plaque geometrie te verkrijgen. Zes iliaca vaten van biggen werden getest in een *ex vivo* inflatie-onderzoeksopstelling. Het voornaamste voordeel van deze methode is dat de vaten werden opgeblazen in fysiologische omstandigheden en onbeschadigd bleven tijdens het opblazen. We ontdekten dat onze modellen de gemeten vervormingspatronen goed konden beschrijven. Ook zagen wij een grote variatie in elasticiteitswaarden bij het vergelijken van dezelfde soorten weefsels afkomstig van verschillende plaques.

In **hoofdstuk 8** ontwikkelden wij een methode om niet-invasief de elasticiteitswaarde van carotis plaqueweefsel te schatten. De methode bestaat uit het afbeelden van de carotis plaque geometrie met MRI, het toepassen van echografie rekmetingen en het oplossen van het inverse probleem met eindige elementen analyse. Om de haalbaarheid van de methode te bepalen gebruikten wij een numerieke aanpak en simuleerden wij MRI en echografie rekmetingen op een aantal computermodellen van plaques die waren gebaseerd op histologische doorsnedes van uitgenomen plaques. We onderzochten meerdere scenario's voor de elasticiteit van de plaque modellen en verkregen telkens nauwkeurige schattingen van de elasticiteitswaarden van de vetrijke kern en de fibreuze weefsels. De veelbelovende bevindingen van deze studie zullen de toepassing van deze methode in een klinische omgeving zeker stimuleren.

In **hoofdstuk 9** vergeleken wij twee manieren voor het detecteren van plaque kwetsbaarheid: een morfologisch classificatieschema en een biomechanische analyse. Daarna bepaalden wij de implicaties van de uitkomst van deze vergelijking voor een

niet-invasieve risicoanalyse van plaques in de carotis. We gebruikten 75 histologische plaque doorsnedes en gebruikten deze voor zowel een berekening van de maximale kapspanning als voor een histopathologische plaqueclassificatie. Op een deel van de plaques voerden wij MRI simulaties uit, en wij bestudeerden het effect van fouten in de berekende maximale kapspanning op de eerdergenoemde vergelijking. Ondanks het feit dat de maximale kapspanning over het algemeen gerelateerd was aan de histopathologische classificatie, zagen wij veel plaques waarbij de twee classificaties niet overeenkwamen. Vanwege de beperkte MRI voxelgrootte met betrekking tot de kapdikte was alleen een niet-invasieve identificatie van een groep plaques met een laag risico en een dikke kap betrouwbaar. Wij sloten dit hoofdstuk af met de hypothese dat in plaats van het identificeren van alle, en enkel alle, kwetsbare plaques, een betrouwbare niet-invasieve identificatie van juist stabiele plaques met dikke kap en lage stress een meer belovende aanpak zou kunnen zijn om de chirurgische ingrepen op plaques in de carotis te verminderen.

**Hoofdstuk 10** bevat een algemene discussie. Daarin presenteerden we de hoofdconclusies van onze studies en plaatsten we de resultaten in perspectief met betrekking tot de onderzoeksvelden van MRI van de carotis en plaque biomechanica. We gaven ook een vooruitblik voor toekomstig onderzoek. In het laatste deel bespraken wij de belangrijkste klinische implicatie van ons werk: “Het stabiele plaque paradigma”.

# Acknowledgements

I am grateful for all the support I have received from the people surrounding me throughout my stays at the Erasmus Medical Center and at Philips Healthcare.

Frank: your professionalism, dedication, and people skills are, at least by my standards, truly unparalleled. Your excellent supervision helped me to become an independent researcher in the best imaginable way. Thank you! Ton: you were always the one who had the broadest view of my PhD project and you made me look at my research from different perspectives. Thank you for being my promotor. Marcel: during my year at Philips Healthcare with you as my supervisor, your never-ending "natural-born" enthusiasm and positivity were the best kind of personal motivators to me. You are an asset to the scientific community. Tom: it was a pleasure working with you at Philips Healthcare on a memorable project. That project was not only predominantly driven by our own curiosities, but also by your knowledge and commitment. I cannot imagine how different this thesis would have looked if we had never met. Aad: you provided me the freedom to ask my own questions and to search for their answers. You gave me very good guidance and, at times, some needed and appreciated advice.

I would also like to take this opportunity to acknowledge the other staff members of the Biomedical Engineering department. Jolanda, Kim vd H, Lambert, Kim G, Hans S, Rorry, Hans B, Gijs, and Nico: thank you for all the support and help. Erna, Gracia, Mieke, and Rita: it was always fun to drop by for a chat and I appreciate your dedicated efforts for my colleagues and myself.

I would like to acknowledge my roommates and colleagues at Philips Healthcare. Jeroen, Gillion, Peter, Raymond, and Steven: it was your presence that made my stay at Philips Healthcare both educational and fun.

Without the help from many (international) collaborators, much work described in this thesis could not have been performed. Stein, Rik, Chris, Tony, Eline, Evelien, Martine, Raf, Wiro, Stefan, Henk, Andres, Diego, Valerio, Mat, Frank B, Frans, Marcel R, Renate, Bram, and Aart: thank you for all the discussions and your advice during meetings and/or visits. Chen-Ket: I want to thank you for making my year-long visit at Eindhoven a good and memorable time. Arna: although we never really were "official" collaborators, our discussions were always insightful. You are a great person to exchange ideas with.

I would like to explicitly credit four PhD students whom I had the pleasure to work closely together with during the past few years. Zaid: I will miss the time when we shared an office room together and routinely broke the silence to play a game of darts. Jelle: I will miss our highly diverse conversations and your excellent sense of humor. You may not realize it, but it brightened up many of my days. Leah: I want to thank you for all the fun and insightful conversations we have had. I really like your thoughtful and clear perspectives on many aspects of life. Ruoyu: simply put, you are among the friendliest persons I know and it was a delight working with you. It is very unfortunate that we only shared an office room for such a short time due to my leaving.

And last but certainly not least, I would like to thank all the (PhD) students I have worked with and from whom I have learned so much. To the (PhD) students I already acknowledged and to Ali, Merih, Mariana, Ayla, Annette, Anouk, Dion, Ruud, Fabian, Bibi, Bahar, Dylan, Maxime, Marco, Mirjam, René, Karthik, Raymon, Quinn, Thessa, Jasper, Bas, Gayle, Sally, Sandra, Tareq, Annelies, Kirsten, Carolien, Klazina, David, Krista, Tom K, Tom v R, Muthu, Ilya, Min, Tianshi, Ying, Deep, Zeynettin, Jacopo, Verya, Alex, and Pieter: you all are the motors driving science forward and I thank you for all the times you provided me with help when I needed it. I was lucky to be surrounded by you to talk not only about work, but also about life in general. It was an honor to have spent time with such enthusiastic, creative, and impressively bright minds.

Harm Nieuwstadt
Rotterdam
November 2014

# Curriculum Vitae

## Harm Aarnout Nieuwstadt

April 29th 1985: born in Utrecht, the Netherlands

## Education

2003 – 2008: B.Sc. Applied Physics
Delft University of Technology, Delft, the Netherlands
2007 – 2010: M.Sc. Applied Physics
Delft University of Technology, Delft, the Netherlands
2004 – 2010: Physics Teaching Licentiate
Science Education and Communication, Delft University of Technology, Delft, the Netherlands
2010 – 2014: Ph.D. Research
Department of Biomedical Engineering. Erasmus University Medical Center, Rotterdam, the Netherlands

## Academic Work Experience

2009 – 2010: Visiting Research Scientist (1.5 years), Department of Biomedical Engineering – Microfluidics. University of Michigan, Ann Arbor, U.S.A.
2012 – 2013: Visiting Research Scientist (1 year), Clinical Science – Magnetic Resonance Imaging. Philips Healthcare, Best, the Netherlands

# Publications

## Articles

Nieuwstadt HA. Analysis of the dart game – walking into doubles and optimal aiming locations. Mathematics Today 2007;43:140-144.

Nieuwstadt HA, Seda R, Li DS, Fowlkes BJ, Bull JL. Microfluidic particle sorting utilizing inertial lift force. Biomedical Microdevices 2011;13:97-105.

Nieuwstadt HA, Akyildiz AC, Speelman L, Virmani R, van der Lugt A, van der Steen AFW, Wentzel JJ, Gijsen FJH. The influence of axial image resolution on atherosclerotic plaque stress computations. Journal of Biomechanics 2013;46:689-695.

Nieuwstadt HA, Geraedts TR, Truijman MTB, Kooi ME, van der Lugt A, van der Steen AFW, Wentzel JJ, Breeuwer M, Gijsen FJH. Numerical simulations of carotid MRI quantify the accuracy in measuring atherosclerotic plaque components in vivo. Magnetic Resonance in Medicine 2014;72:188-201.

Nieuwstadt HA, Speelman L, Breeuwer M, van der Lugt A, van der Steen AFW, Wentzel JJ, Gijsen FJH. The influence of inaccuracies in carotid MRI segmentation on atherosclerotic plaque stress computations. Journal of Biomechanical Engineering 2014;136:021015.

Nieuwstadt HA, van der Lugt A, Kassar ZAM, Breeuwer M, van der Steen AFW, Gijsen FJH. Atherosclerotic plaque fibrous cap assessment under an oblique scan plane orientation in carotid MRI. Quantitative Imaging in Medicine and Surgery 2014;4:216-224.

Nieuwstadt HA, Kassar ZAM, van der Lugt A, Breeuwer M, van der Steen AFW, Wentzel JJ, Gijsen FJH. A computer-simulation study on the effects of MRI voxel dimensions on carotid plaque lipid-core and fibrous cap segmentation and stress modeling. *PLOS ONE*, accepted, 2015.

Nieuwstadt HA, Fekkes S, Hansen HHG, de Korte CL, van der Lugt A, Wentzel JJ, van der Steen AFW, Gijsen FJH. Carotid plaque elasticity estimation using ultrasound elastography, MRI, and inverse FEA – a numerical feasibility study. Submitted.

Gijsen FJH, Nieuwstadt HA, Wentzel JJ, Verhagen HJM, van der Lugt A, van der Steen AFW. Carotid plaque morphological classification compared with biomechanical cap stress – implications for an MRI-based assessment. Submitted.

Akyildiz AC, Speelman L, Nieuwstadt HA, van Brummelen H, Virmani R, van der Lugt A, van der Steen AFW, Gijsen, FJH. The effects of plaque morphology and material properties on peak cap stress in human coronary arteries. Submitted.

Akyildiz AC, Hansen HHG, Nieuwstadt HA, Speelman L, de Korte CL, Gijsen FJH. Local mechanical characterization of atherosclerotic plaques – combination of ultrasound displacement imaging and inverse finite element analysis. Submitted.

## Conference Presentations

Nieuwstadt HA, Li DS, Seda R, Fowlkes BJ, Bull JL. Lift-Force-Driven Microfluidic Droplet Sorting Device. 62nd Annual Meeting of the APS Division of Fluid Dynamics, Minneapolis, Minnesota, USA, November 2009. Podium presentation.

Nieuwstadt HA, Akyildiz AC, Speelman L, Wentzel JJ, Virmani R, van der Steen AFW, Gijsen FJH. Stress Calculations in 3D Reconstructions of Arteries: the Influence of Axial Image Resolution. 6th International Symposium on Biomechanics in Vascular Biology and Cardiovascular Disease, Rotterdam, NL, April 2011. Poster presentation.

Nieuwstadt HA, Akyildiz AC, Speelman L, Wentzel JJ, Virmani R, van der Steen AFW, Gijsen FJH. Stress Calculations in 3D Reconstructions of Arteries: the Influence of Axial Image Resolution. Artery 11 Symposium, Paris, FR, October 2011. Poster presentation.

Nieuwstadt HA, Akyildiz AC, Speelman L, Wentzel JJ, Virmani R, van der Steen AFW, Gijsen FJH. Stress Calculations in 3D Reconstructions of Arteries: the Influence of Axial Image Resolution. 7th International Symposium on Biomechanics in Vascular Biology and Cardiovascular Disease, Atlanta, Georgia, USA, April 2012. Poster presentation.

Nieuwstadt HA, Akyildiz AC, Speelman L, Wentzel JJ, Virmani R, van der Steen AFW, Gijsen FJH. Stress Computations in Atherosclerotic Arteries: the Influence of Axial Image Resolution. ASME 2012 Summer Bioengineering Conference, Fajardo, Puerto Rico, USA, June 2012. Poster presentation.

Nieuwstadt HA, Akyildiz AC, Speelman L, Wentzel JJ, Virmani R, van der Steen AFW, Gijsen FJH. Stress Calculations in 3D Reconstructions of Arteries: the Influence of Axial Image Resolution. 4th Dutch Biomedical Engineering Conference, Egmond aan Zee, NL, January 2013. Poster presentation.

Nieuwstadt HA, Geraedts TR, Truijman MTB, Kooi ME, van der Lugt A, van der Steen AFW, Wentzel JJ, Breeuwer M, Gijsen FJH. Simulating Carotid MRI: How Accurately Can We Quantify Atherosclerotic Plaque Components in Vivo? 4th Dutch Biomedical Engineering Conference 2013, Egmond aan Zee, NL, January 2013. Podium presentation.

Nieuwstadt HA, Wentzel JJ, van der Lugt A, van der Steen AFW, Breeuwer M, Gijsen FJH. Can We Use in Vivo MRI and FEA to Determine Peak Cap Stress in Carotid Plaques? MRI Simulations Provide Answers. 8th International Symposium on Biomechanics in Vascular Biology and Cardiovascular Disease, Rotterdam, NL, April 2013. Poster presentation.

Nieuwstadt HA, Geraedts TR, Truijman MTB, Kooi ME, van der Lugt A, van der Steen AFW, Wentzel JJ, Breeuwer M, Gijsen FJH. Simulating Carotid MRI: How Accurately Can We Quantify Atherosclerotic Plaque Components in Vivo? 8th International Symposium on Biomechanics in Vascular Biology and Cardiovascular Disease, Rotterdam, NL, April 2013. Poster presentation.

Nieuwstadt HA, Geraedts TR, Truijman MTB, Kooi ME, van der Lugt A, van der Steen AFW, Wentzel JJ, Breeuwer M, Gijsen FJH. Numerical Simulations of Carotid MRI: How Accurately Can We Quantify Atherosclerotic Plaque Components in Vivo? ISMRM 21st Annual Meeting & Exhibition, Salt Lake City, Utah, USA, April 2013. Poster presentation.

Nieuwstadt HA, Wentzel JJ, van der Lugt A, van der Steen AFW, Breeuwer M, Gijsen FJH. Can We Use In Vivo MRI and FEA to Determine Peak Cap Stress in Carotid Plaques? MRI Simulations Provide Answers. ASME 2013 Summer Bioengineering Conference, Sunriver, Oregon, USA, June 2013. Podium presentation.

Nieuwstadt HA, Kassar ZAM, van der Lugt A, Breeuwer M, van der Steen AFW, Wentzel JJ, Gijsen FJH. Voxel Size and Anisotropy in Carotid MRI: Impact on Computing Peak Cap Stress. 9th International Symposium on Biomechanics in Vascular Biology and Cardiovascular Disease, Montreal, CA, April 2014. Poster presentation.

Nieuwstadt HA, Kassar ZAM, van der Lugt A, van der Steen AFW, Breeuwer M, Gijsen FJH. Voxel Anisotropy in Carotid MRI: Impact on Fibrous Cap Thickness and Lipid-rich Necrotic Core Size Measurements of Atherosclerotic Plaques. Joint Annual Meeting ISMRM-ESMRMB, Milan, IT, May 2014. Poster presentation.

Nieuwstadt HA, van der Lugt A, van der Steen AFW, Wentzel JJ, Gijsen FJH. MRI and Modeling to Determine Plaque Stress. 7th World Congress of Biomechanics, Boston, USA, July 2014. Podium presentation.

Nieuwstadt HA, Kassar ZAM, van der Lugt A, Breeuwer M, van der Steen AFW, Wentzel JJ, Gijsen FJH. Voxel Size and Anisotropy in Carotid MRI: Impact on Computing Peak Cap Stress. 7th World Congress of Biomechanics, Boston, USA, July 2014. Poster presentation.

Nieuwstadt HA, Kassar ZAM, van der Lugt A, Breeuwer M, van der Steen AFW, Wentzel JJ, Gijsen FJH. Voxel Size and Anisotropy in Carotid MRI: Impact on Computing Peak Cap Stress. 12th International Symposium on Computer Methods in Biomechanics and Biomedical Engineering, Amsterdam, NL, October 2014. Podium presentation.

Nieuwstadt HA, Fekkes S, de Korte CL, Wentzel JJ, van der Steen AFW, Gijsen FJH. Noninvasive, Patient-specific Carotid Plaque Elasticity Estimation Utilizing Ultrasound Elastography, MRI, and Inverse FEA: a Numerical Feasibility Study. 12th International Symposium on Computer Methods in Biomechanics and Biomedical Engineering, Amsterdam, NL, October 2014. Podium presentation.

# PhD Portfolio

| Conference and symposium attendance | Year | ECTS |
|---|---|---|
| - 1st Meeting of the Dutch Virtual Physiological Human Community, Amsterdam, NL | 2011 | 0.3 |
| - 3rd Dutch Biomedical Engineering Conference, Egmond aan Zee, NL | 2011 | 0.6 |
| - 10th Annual Symposium on Trends in Medical Technology: Cardiovascular Imaging (AMC), Amsterdam, NL | 2011 | 0.3 |
| - 6th International Symposium on Biomechanics in Vascular Biology and Cardiovascular Disease, Rotterdam, NL | 2011 | 0.6 |
| - Cardiovascular Research Symposium (TU/e), Eindhoven, NL | 2011 | 0.3 |
| - Artery 11 Symposium, Paris, FR | 2011 | 0.9 |
| - CTMM Annual Meeting 2011 (CTMM), Utrecht, NL | 2011 | 0.3 |
| - 1st Optics in Cardiology Symposium, Rotterdam, NL | 2011 | 0.6 |
| - Holst Memorial Lecture and Symposium (TU/e), Eindhoven, NL | 2011 | 0.3 |
| - Symposium Een Warm Hart (ICIN), Amsterdam, NL | 2012 | 0.3 |
| - 3rd Annual COEUR PhD Day (Erasmus MC), Rotterdam, NL | 2012 | 0.3 |
| - BME Research Day (TU/e), Eindhoven, NL | 2012 | 0.3 |
| - Symposium 35 years 'Laboratorium voor Klinische en Experimentele Beeldverwerking' (LUMC), Leiden, NL | 2012 | 0.3 |
| - ASME 2012 Summer Bioengineering Conference, Fajardo, Puerto Rico, USA | 2012 | 1.2 |
| - Mechanics Symposium on Multi scale Modeling (KIVI NIRIA), Eindhoven, NL | 2012 | 0.3 |
| - NVPHBV Fall Meeting, Eindhoven, NL | 2012 | 0.3 |
| - 4th Dutch Biomedical Engineering Conference, Egmond aan Zee, NL | 2013 | 0.6 |
| - 2nd Optics in Cardiology Symposium, Rotterdam, NL | 2013 | 0.6 |
| - 4th Annual COEUR PhD Day (Erasmus MC), Rotterdam, NL | 2013 | 0.3 |
| - 8th International Symposium on Biomechanics in Vascular Biology and Cardiovascular Disease, Rotterdam, NL | 2013 | 0.6 |
| - STW Annual Conference (STW), Nieuwegein, NL | 2013 | 0.3 |
| - PhD Day 2013 (Erasmus MC), Rotterdam, NL | 2013 | 0.3 |
| - ASME 2013 Summer Bioengineering Conference, Sunriver, Oregon, USA | 2013 | 1.2 |
| - 7th World Congress of Biomechanics, Boston, USA | 2014 | 1.2 |
| - NVPHBV Fall Meeting, Eindhoven, NL | 2014 | 0.3 |

## Courses

| | | | |
|---|---|---|---|
| - | 10th PhD Course 'In Vivo NMR' (Utrecht University), Utrecht, NL | 2011 | 5.0 |
| - | Magnetic Resonance Imaging Course (Philips Healthcare), Best, NL | 2012 | 1.0 |
| - | Summer School on Biomechanics and Modeling in Mechanobiology (Graz University), Graz, AT | 2012 | 5.0 |
| - | Cardiovascular Imaging and Diagnostics (COEUR), Rotterdam, NL | 2013 | 1.0 |
| - | Biostatistics for Clinicians (NIHES), Rotterdam, NL | 2014 | 2.0 |

## Presentations

| | | | |
|---|---|---|---|
| - | Poster presentation – 6th International Symposium on Biomechanics in Vascular Biology and Cardiovascular Disease, Rotterdam, NL | 2011 | 0.2 |
| - | Poster presentation – Artery 11 Symposium, Paris, FR | 2011 | 0.2 |
| - | Podium presentation – COEUR Research Seminar on Imaging Carotid Arteries: Structure and Function (Invited Presentation), Rotterdam, NL | 2011 | 0.2 |
| - | Podium presentation – 3rd Annual COEUR PhD Day, Rotterdam, NL | 2012 | 0.2 |
| - | Poster presentation – 7th International Symposium on Biomechanics in Vascular Biology and Cardiovascular Disease, Atlanta, Georgia, USA | 2012 | 0.2 |
| - | Poster presentation – ASME 2012 Summer Bioengineering Conference, Fajardo, Puerto Rico, USA | 2012 | 0.2 |
| - | Podium presentation – NVPHBV Fall Meeting, Eindhoven, NL | 2012 | 0.2 |
| - | Podium presentation – Medical Imaging Physics Division of the Jülich Research Institute (Invited Presentation), Jülich, DE | 2012 | 0.2 |
| - | Podium and poster presentation – 4th Dutch Biomedical Engineering Conference, Egmond aan Zee, NL | 2013 | 0.4 |
| - | Two poster presentations – 8th International Symposium on Biomechanics in Vascular Biology and Cardiovascular Disease, Rotterdam, NL | 2013 | 0.4 |
| - | Poster presentation – ISMRM 21st Annual Meeting & Exhibition, Salt Lake City, Utah, USA | 2013 | 0.2 |
| - | Podium presentation – 4th Annual COEUR PhD Day, Rotterdam, NL | 2013 | 0.2 |
| - | Podium presentation – COEUR Research Seminar on Carotid Atherosclerotic Plaques: Biomechanics and Imaging (Invited Presentation), Rotterdam, NL | 2013 | 0.2 |
| - | Podium presentation – ASME 2013 Summer Bioengineering Conference, Sunriver, Oregon, USA | 2013 | 0.2 |
| - | Poster presentation – 9th International Symposium on Biomechanics in Vascular Biology and Cardiovascular Disease, Montreal, CA | 2014 | 0.2 |

| | | | |
|---|---|---|---|
| - | Poster presentation – Joint Annual Meeting ISMRM-ESMRMB, Milan, IT | 2014 | 0.2 |
| - | Podium and poster presentation – 7th World Congress of Biomechanics (Invited Presentation), Boston, USA | 2014 | 0.4 |
| - | Podium presentation – NVPHBV Fall Meeting, Eindhoven, NL | 2014 | 0.2 |

## Seminars and workshops

| | | | |
|---|---|---|---|
| - | Research Seminar on Imaging of Atherosclerosis (COEUR), Rotterdam, NL | 2010 | 0.2 |
| - | Research Seminar on Detection of Early Atherosclerosis (COEUR), Rotterdam, NL | 2011 | 0.2 |
| - | Research Seminar on Imaging Carotid Arteries: Structure and Function (COEUR), Rotterdam, NL | 2011 | 0.2 |
| - | Workshop in Image-Based Simulation for Biomechanics, Materials Applications and Reverse Engineering (TU/e), Eindhoven, NL | 2011 | 0.2 |
| - | Research Seminar on Integrity in Science (COEUR), Rotterdam, NL | 2013 | 0.2 |
| - | Research Seminar on Carotid Atherosclerotic Plaques: Biomechanics and Imaging (COEUR), Rotterdam, NL | 2013 | 0.2 |
| - | Research Seminar on Gender Differences in Cardiovascular Disease (COEUR), Rotterdam, NL | 2013 | 0.2 |
| - | Research Seminar on Non-invasive Imaging of Myocardial Ischemia (COEUR), Rotterdam, NL | 2014 | 0.2 |

## Activities

| | | | |
|---|---|---|---|
| - | Lecturing for the Medical Delta (Erasmus MC, LUMC, TU Delft) Minor Program | 2011 | 0.3 |
| - | Supervision of 3 students | 2013 | 5.0 |
| - | PhD committee member of the Cardiovascular Research School Erasmus University Rotterdam (COEUR) | 2013/ 2014 | 1.0 |